Replicating Bone Structure using Apatite-Wollastonite Glass Ceramic

Nilly Hojat

A thesis submitted to the Faculty of Science,

Agriculture and Engineering for the Degree of

Doctor of Philosophy (Integrated)

School of Engineering

Newcastle University

July 2021

Dedicated to my incredible family.

My mother, father, and brother.

Abstract

The aim of this project was to develop three-dimensional porous scaffolds which conformed with the natural properties of the native bone as an *in-vitro* model. This requires in depth knowledge of the biology of the tissue, its morphology and surrounding environment. Many researches focused on developing techniques to produce such highly complex structures which mimic the natural bone *in-vitro*.

This thesis explores techniques for generating repeatable micro and macro porous Apatite-Wollastonite (AW2) scaffolds using Thermally Induced Phase Separation (TIPS) methodology, freeze drying and then a two-step heat treatment process (5°C per minute to 779°C for a 1-hour dwell, then 10°C per minute to 1235°C for a 1-hour dwell). The manufacturing process was optimized to produce scaffolds with high porosity (60 – 76%) by altering the heat treatment process, analysing the distribution of pores and evaluating the mechanical characteristics mimicking bone for an *in-vitro* application. An image processing technique was developed to quantitatively measure the pore size, and its distribution within the AW2 scaffolds using Scanning Electron Microscopy (SEM) images of scaffolds. Open and closed porosity were also measured using Archimedes analysis. Mechanical properties and nutrient diffusion (Glucose release) of the scaffolds were measured and compared against the different scaffold fabrication processes. The scaffolds were designed to be representative of human cancellous bone and to provide a suitable environment for cell adhesion and proliferation of human Osteoblast Cells (HOb).

High number of (over 140) scaffolds were manufactured, and some were further modified by incorporating Fused Filament Fabrication (FFF) printing, and the addition of channels and grooves to further improve open porosity and media flow. Both scaffold types (AW2 and modified AW2) were investigated during 21 days of *in-vitro* tests with human Osteoblast cells, for cell adhesion, infiltration into pores and growth against the controls. Both groups of scaffolds were suitable for nutrient transfer, promoted cellular adhesion (Actin), cellular interaction, extracellular matrix formation (SEM and Energy Dispersive X-ray spectroscopy), and proliferation (Presto Blue).

In conclusion the AW2 scaffolds and modified AW2 scaffolds were successful in the *in-vitro* tests, the porosity and ability to allow for cell-to-cell interaction enabled Osteoblast growth and extracellular matrix formation. Further investigation is required to determine if these scaffolds can potentially be used as an *in-vitro* model for disease modelling and drug testing.

Acknowledgments

I would like to thank Newcastle University, UK, for the opportunity to carry out research here with funding support from EPSRC and Versus Arthritis. Thank you for the support from Centre for Doctoral Training in Additive Manufacturing and 3D printing at the University of Nottingham.

My special thanks to Professor Lidija Siller for supervising, supporting, motivating, and encouraging me during the second half of this PhD journey, especially the past year during the Covid-19 pandemic with remote working. I really appreciate the time, effort, guidance and support you have given me, it has made a lifelong influence on me, especially as you allowed me to explore different methods. Many thanks to Dr Piergiorgio Gentile for your support, feedback, and discussions these past years, I truly appreciate your supports and guidance. To Dr Ana Marina Ferreira-Duarte and Professor Kenny Dalgarno, thank you for the discussions, directions, and conversations regarding the PhD topic and providing lab space in the difficult time during the Covid-19 Pandemic.

Thank you so much to Jen Stewart, who has provided me with a safe space to discuss my thoughts, has provided me with emotional support and been a friend as well as a study support this past year.

A big thank you to the following services for their facilities, training, expertise, and general discussions; NEXUS (Mr Mike Foster), Bioimaging Unit (Dr Rolando Berlinguer Palmini), Electron Microscopy Research Services (Mr Ross Laws), the Strengths Lab (Mr Paul Scott and Mr Graeme Watson) and the BioLab (Dr Stephen Moore).

The biggest thank you and appreciation goes to my amazing family; specifically, my incredible mother Nasrin Nasr and incredible father Ali Hojjat, and my wonderful younger brother Nima Hojat. They have been my biggest support, encouragement and kept me determined during the hardest times. They provided me with full financial support to present at 10th Symposium Biologic Scaffolds for Regenerative Medicine (San Francisco) and TERMIS World Congress (Japan). Also, they have never let me give up on my PhD and encouraged me to keep on fighting.

Thank you to Dr Rohan Bhalekar and Dr Kathryn Chamberlain for being wonderful colleagues but also proving the best friendship and support throughout my time at Newcastle University and beyond (including both your weddings). The endless hours of discussion, and pizza delivery to the office will always be my fondest memories. Thank you to Dr Nicole Kattner for being a close friend from the 1st day and esteemed colleague, our Costa coffee discussions will forever be treasured, and I hope we continue being neighbours for years to come.

Thank you to everyone who has been a part of this long journey, especially during the Covid-19 Pandemic. The WhatsApp messages, voice notes, lab chats, office discussions, lunches and walks around campus have contributed to my experience and will be cherished.

Table of Contents

List of Figures

List of Tables

Chapter 1 – Project Aims and Literature Review

Aim and Objectives

The aim of this study was to generate a repeatable manufacturing process to obtain structurally stable porous Apatite-Wollastonite (AW) scaffolds to replicate bone morphology as an *in-vitro* model. The AW has been largely studied and has been used as a successful material for Tissue Engineering applications.

These scaffolds are required to be suitable for adhesion, and proliferation of Osteoblast cells and enable biomimicry of the bone environment by producing a new extracellular matrix.

The focus of this part of the research is:

- To establish and optimise a method for producing porous scaffolds manufactured from AW2.
- Create a methodology for automatically measuring pore size using Image Analysis.
- Analyse the scaffolds in terms of mechanical properties, open/closed porosity, nutrient diffusion, pore size and its distribution for suitability of the scaffolds for tissue engineering.
- Also analyse the micro and macro pore sizes in relation to scaffold design and manufacturing process for optimizing different steps of the scaffold fabrication process.
- Create an evaluation matrix with all the major factors analysed to allow simple selection of most suitable scaffold for *in-vitro* testing for bone replication.
- Present all the important factors which were critical for scaffold manufacturing collectively in two evaluation matrices, to simplify evaluating the scaffolds using and choosing the most suitable scaffold manufacturing process for bone tissue growth.

Introduction

This thesis describes the main steps required to prepare glass-ceramic material and optimise a scaffold manufacturing technique and investigate these scaffolds *in-vitro* using human osteoblast cells to establish the suitability of scaffolds to replicate bone as an *in-vitro* model. This includes optimising the dioxane:water concentration, choice of cloud point temperature, in addition to the two-step heat treatment process for sintering for Apatite – Wollastonite 2 (AW2) Scaffolds.

The basis of the manufacturing method is based on optimisation of the process to produce porous AW2 scaffolds using Thermally Induced Phase Separation (TIPS), where temperature differences result in changes of material characteristics (Yang et al., 2006). The Thermally Induced Phase Separation method and sintering regimes allow for porous components to be produced. The polymer (Poly Lactic Acid (PLA)) (Guarino and Ambrosio, 2010) is dissolved in a solvent system (Dioxane and Water) to promote phase separation (Ma and Zhang, 2001, Hua et al., 2002, La Carrubba et al., 2008), the AW2 powder is then added to the polymeric solution to facilitate the formation of structurally robust scaffolds. After this application, the slurry content is frozen, freeze-dried, and placed in a furnace to burn-out the polymer to leave a mechanically robust, porous and rough glass-ceramic scaffold resembling bone (Toumpaniari, 2016). A scaffold is mechanically more robust if its compressive strength is high, the process is considered more repeatable if its standard deviations (STD) have less variations.

There are many studies using Apatite-Wollastonite (AW) powder within scaffold fabrication (Kokubo et al., 1982, Kokubo, 1991, Sautier et al., 1994, Yamada et al., 1994, Fujita et al., 2000, Rea et al., 2004, Teramoto et al., 2005, Dyson et al., 2007, Zhang et al., 2009, Lee et al., 2015, Toumpaniari, 2016, Mancuso, 2016, Dziadek et al., 2017, Tcacencu et al., 2018, Fernandes et al., 2018, Rodrigues, 2018, Turnbull et al., 2018, Melo et al., 2019). Toumpaniari (2016) and Rodrigues (2018) have previously used Apatite-Wollastonite 1 (AW1) powder with composition 4.6% MgO, 44.7% CaO, 34% SiO_2, 16.2% P_2O_5, 0.5% CaF_2 and showed that particle sizes 20 – 53 µm produced promising results. For this study, Apatite Wollastonite 2 particles (AW2) with a composition of 3.68% MgO, 44.81% CaO, 35.49% SiO_2, 15.47% P_2O_5, 0.19% CaF_2, 0.02% SrO, 0.09% Fe_2O_3, 0.14% Al_2O_3 and a particle range of 20 – 53 µm was provided to explore its potential and optimise the process considering the previously investigation using

AW1 and different PLA and Dioxane concentrations (Toumpaniari, 2016, Rodrigues, 2018). AW2 is made using a different manufacturing process (confidential process by Glass Technologies Services, GTS), also has a different composition to other AW glasses and therefore behaves differently. Investigation will be carried out to illustrate how the heat treatment process of "green" parts (PLA–AW2 scaffolds), that are produced using TIPS, behave when manufactured with specific concentrations of dioxane:water. Each concentration ratio of dioxane:water and two-step heat treatment process produces scaffolds with different porosities, interconnectivity, and pore distribution, which will then be analysed to identify the most suitable scaffold for bone tissue growth. This technique is utilised to fabricate scaffolds with the desired morphology, and can potentially be scalable for the fabrication of scaffolds of sufficient quantity and quality. The process can be fine-tuned to produce scaffolds with the appropriate morphology and structure for tissue engineering.

Porous AW2 scaffolds were developed using Thermally Induced Phase separation with different heat treatment cycles to obtain pores with different sizes and distributions. The effect of dioxane:water concentration, Cloud Point temperature, cooling method (of moulds), sintering temperature, dwelling time and AW2 particle behaviour on scaffolds was examined. The effect of the two-step heat treatment process on the scaffold's characteristics was analysed for porosity using Scanning Electron Microscopy (SEM), Archimedes' principle, nutrient diffusion, compression and image analysis. The methods section details the methods used to perform the analysis of the scaffolds, which follows with the Results and Discussion section that examines the suitability of the porous AW2 scaffolds for cell attachment and infiltration. Two evaluation matrices present the results of each study performed during scaffold manufacturing process. The matrices are designed to represent the results and discussion both qualitatively and quantitatively.

The next step of this thesis focusses on further improving the interconnectivity of the TIPS manufactured AW2 scaffolds (optimised AW2 scaffolds) by exploring modifications at different stages of the manufacturing process. The established TIPS method was altered with addition of 3D printed parts (using Filament Fused Fabrication printers) which would be removed prior to sintering or 'burnt out' during the sintering process. Modifications post-freeze drying, and post-sintering were investigated further with the repeatable method

determined. The modified AW2 scaffolds underwent validation using scanning electron microscopy, open/closed porosity and mechanical testing. The modified AW2 scaffolds and original AW2 scaffolds were investigated *in-vitro*.

The final step of this thesis focusses on analysing Human Osteoblast cell adhesion, infiltration, viability, proliferation and differentiation. Human Osteoblast Cells were used to assess the suitability of the AW2 scaffolds to mimic the bone environment. This step requires the appropriate procedures to be employed to prepare both the Osteoblast cells and the scaffold, to enable the tissue engineering. Further investigation into cell proliferation, viability and differentiation over a period of 21 days was then required, as extracellular matrix formation is determined by pore size, which enables the transfer of nutrients and waste, migration, distribution, attachment and proliferation of cells within the scaffold (Oh et al., 2007, Oh et al., 2014). Further tests were performed to establish the level of cell adhesion, in addition to cell proliferation and viability on scaffolds in the first 48-hours and seven days respectively. The results of these investigations aid understanding of the suitability of the scaffold as an *in-vitro* model for future bone regeneration. Evaluation of cell morphology is assessed by SEM imaging, and viability via confocal microscopy. Osteoblast cytotoxicity assessment and adhesiveness is also evaluated.

This thesis is organized as follows, Chapter 1 and Chapter 2 focuses on the AW2 scaffold manufacturing process and steps used to optimize the process. It includes a novel image processing algorithm used to measure pore sizes and a new technique for measuring porosity based on Archimedes technique. Chapter 3 presents the results of AW2 scaffold manufacturing process, an evaluation matrix and concluding remarks. Chapter 4 proposes techniques to improve interconnectivity of scaffolds and presents results of two main techniques, imposing interconnectivity during manufacturing process and adding interconnectivity to the AW2 scaffolds, labelled as modified AW2 scaffolds. Chapter 5 focuses on designing cell culture tests and methods used for the *in-vitro* evaluation. The results of *in-vitro* tests are presented in Chapter 5 where the suitability of scaffolds (both optimized AW2 scaffolds and modified AW2 scaffolds) were evaluated based on analysing cell proliferation during 21-days cells culture. The suitability of the scaffolds as a potential *in-vitro* model were also compared against each other with concluding remarks in Chapter 6. Chapter 6 outlines the outcomes and novelty presented in this thesis.

1 Literature Review

Bone has the capacity to self-heal and regenerate itself (Turnbull et al., 2018), however many acquired pathologies including trauma, arthritis, and neoplasm leave patients with bone defects requiring subsequent medical intervention. Interventions include bone grafts, implanting metal substitutes or bone substitute materials to stimulate bone regeneration or aid with stability (Ashman and Phillips, 2013, Thaller et al., 2014). This makes bone one of the most commonly transplanted tissues, with over four million related operations annually (Greenwald et al., 2001, Brydone et al., 2010, Turnbull et al., 2018, Jodati et al., 2020). There are significant limitations in using patients' own bone for implant or artificial implants which has resulted in many researchers investigating alternative methods, with specific attention to making scaffolds that closely mimic the highly complex structure of natural bone as an *in-vitro* model (Turnbull et al., 2018). Bone is a composite material consisting of hydroxyapatite mineral, a mixture of organic materials including lipids, type I collagen and non-collagen proteins and water (Young, 2003, Boskey, 2013). Varieties of bioactive ceramics and glasses are widely used as an *in-vitro* model for human bone growth. These materials have particular properties that encourage direct bonding to human tissues by interfacial reactions. Bioactive glass-ceramics, such as Apatite-Wollastonite (AW) are promising biomaterials that represent mechanical properties comparable to bone with high bioactivity (Kokubo, 1991). Apatite-Wollastonite has been clinically applied in spinal applications, and is widely considered an excellent candidate material for personalised bone implants (Velasco et al., 2015), which morphologically represent bone structure (Henkel et al., 2013).

To create an *in-vitro* model of bone, the material used for fabricating scaffolds should be biocompatible, nontoxic (lack of cytotoxicity), easy to manufacture, biodegradable, osteoconductive, mechanically strong, and should elicit negligible immune response (Lloyd, 2002, Dong et al., 2009, Bose et al., 2012). Biodegradability of scaffolds should be consistent with the level of cell differentiation; otherwise mechanical failure can occur if degradation occurs too quickly or too slowly (Turnbull et al., 2018). The manufacturing process should be optimised to produce scaffolds with appropriate porosity, a good level of interconnectivity between pores, along with a suitable range of pore sizes and distribution. The process of scaffold fabrication should be simple and repeatable. Optimally designed scaffolds should

enable cellular interactions, differentiation and bioactivity, all to enable signalling between cells to promote tissue regeneration.

To fabricate a suitable scaffold, it is essential to ensure that both the pore size and distribution of pores are sufficiently balanced, to retain adequate porosity and interconnectivity, whilst maintaining structural stability within the scaffold (Nordin and Frankel, 2001, Gervaso et al., 2016). A scaffold is deemed structurally stable if no powder residue remains upon handling, and no disintegration occurs when placed in a liquid. This is especially important during the cell test phase of the study. Stability and integrity will be discussed in the discussion.

The internal structure of scaffolds is vital for cell viability, proliferation and encouraging differentiation and fostering tissue growth. An interconnected pore structure with a high overall porosity allows for diffusion of nutrients and oxygen into the scaffold, and diffusion of waste outside of the scaffold. High porosity and interconnectivity aid advance cell migration and improve the available surface area necessary for binding cells to the scaffold surface, and also facilitate interaction with neighbouring tissues (Zeltinger et al., 2001, Hing et al., 2004, Hing et al., 2005, Loh and Choong, 2013). Scaffolds with higher total porosity should lead to a scaffold with larger internal surface area enabling better cell adhesion and proliferation. Suitable pore sizes produce the necessary pore volume which enables the scaffold to accommodate an adequate supply of cells to aid modelling of the bone environment. A compromise that needs to be considered when fabricating scaffolds relates to the fact that an increase in porosity is usually associated with a decrease in mechanical stability and compressive strength, that results in increased difficulty of scaffold manufacture and stability during handling (O'Brien et al., 2005, Loh and Choong, 2013, Gleeson et al., 2010, Prasadh and Wong, 2018).

Many techniques for measuring porosity have been proposed to represent the microstructural characteristics of scaffolds (Amziane et al., 2017). However, research into pore size measurements in scaffolds remains at its infancy, with the majority of published techniques employing manual measurements from images to estimate pore sizes and distribution (Lo Re et al., 2015, Roohani-Esfahani et al., 2017).

Toumpaniari (2016) developed two methods of fabricating scaffolds using AW1. The first method included the casting of dry ceramic powders with a 3D printed Fused Filament

Fabrication (FFF) core mould. This consisted of loose powder combined with FFF negative and FFF core moulds. However, the scaffolds either collapsed or fractured during the sintering process, making them unsuitable for implant application. The second method was based on sintering of green parts that had been produced by TIPS. Two different AW1 particle ranges were explored (20 - 53µm and 54 - 90µm), PLA + Dioxane + AW1 powder were mixed at 40°C for 2 hours prior to being placed into preheated and subsequently into precooled moulds to eventually produce a freeze dried green part, which was then sintered at 1150°C, see Chapter 6.2 of (Toumpaniari, 2016) for details. Analysis of total porosity was presented using Archimedes' principle, however, open porosity and interconnectivity was visually evaluated from SEM images rather than quantitatively (See 3.7.2 in (Toumpaniari, 2016). The measurement of pore sizes or distribution of pores are also missing from Toumpaniari's (2016) study, which makes it difficult to evaluate the suitability of the scaffolds for bone modelling.

Within this chapter, the cloud point temperature was also investigated, along with the ratio of dioxane:water and their effects upon the porosity and mechanical stability of scaffolds. As such, a thermally induced phase separation (TIPS) technique was used in conjunction with Hot Stage Microscopy (HSM) to determine optimum AW2 powder processing and two-step heat treatment process (including sintering temperatures). It also presents a detailed analysis of open porosity and distribution of pore sizes, which allows for the selection of the most suitable scaffold for the requisite application, in this case tissue engineering of an '*in-vitro*' model. Details of the novel image processing technique are presented for quantitatively measured pores sizes, and the number and distribution of pores on the scaffolds. Scaffold Requirements

A key element in tissue engineering is the scaffold, since it enables the fabrication of artificial tissue that mimics natural bone tissue. Bone scaffolds usually have complex structures with a low density, due to the need for high porosity, which is essential for providing a suitable environment for cell attachment, proliferation, and differentiation (osteoinduction & osteoconduction) (Edalat et al., 2012, Polo-Corrales et al., 2014). The scaffold should also support other biomolecules that will eventually enhance the formation of new tissue '*in-vitro*' or in the human body (*in-vivo*). The scaffold should fulfil several requirements including: biocompatibility, ease of manufacture, osteoconductivity, non-carcinogenicity, non-toxicity

(lack cytotoxicity), mechanical strength, and non-antigenicity. Optimal conditions should enable cellular interactions, differentiation, bioactivity, and activation of signalling molecules that promote tissue regeneration. Besides the biomaterial issues, the structure and morphology of the scaffolds are very important. Scaffolds should ideally be highly porous, with suitable pore sizes, pore shapes and pore distribution. They should also have interconnected pores to allow for vascularisation, nutrient transfer, and waste removal. These are all important aspects as they are all usually linked, and modification of one of these parameters during manufacturing typically affects the scaffold properties (Norman et al., 1994).

Once scaffolds have been prepared, other inorganic materials can be incorporated to enhance the chemical properties of the scaffolds, such as the incorporation of growth factors and other biomolecules to aid with the cell component (Martínez-Pérez et al., 2011).

The effect of interconnections on osteoblast cell behaviour were studied on calcium phosphate-based scaffolds with the pore interconnection sizes ranging from 10 µm – 100 µm (Lu et al., 1999). The penetration of cells was studied on these scaffolds at 14 days and 28 days, the results confirmed that osteoblast cells can penetrate within the different interconnection sizes studied, and were able to fully colonise and proliferate inside the pores, with 40 µm being the most favourable size (Lu et al., 1999, Perez and Mestres, 2016).

The next step of this thesis is to grow osteoblast cells on these porous scaffolds with the aim of optimising the process to stimulate bone generation. Such experimentation will help to establish the potential use of these scaffolds as an *in-vitro* model to replicate the bone tissue environment. Methods for tissue culture were designed and are presented Chapter 5 – *In-Vitro* tests with Porous Scaffolds. This includes sterilization, using resazurin and resorufin for cell viability, live-dead test and also establishing calibration curves (Divieto and Sassi, 2015).

This thesis work can be extended to the addition of chondrocytes on the scaffolds as the pore sizes are within the suitable range for chondrocyte differentiation which should have rich productions of collagen II and Glycosaminoglycan (GAG) (Griffon et al., 2006). The study by Griffon et al, showed that after 4 weeks in a bioreactor, the scaffolds with the pore sizes 70µm - 120µm and 10µm - 50µm had chondrocyte differentiation compared to 10µm, this was due to improved diffusion of nutrients and cells within the scaffolds (Griffon et al., 2006).

1.1.1 Pore sizes

Pores are crucial for bone tissue formation as they allow the transfer of nutrients and waste, cell infiltration, attachment and growth within the scaffold (Oh et al., 2007, Gariboldi and Best, 2015). However, the integrity of the internal matrix is also vital, even with a high overall porosity, cell migration can be impeded if the pores are not connected (closed pores) (Loh and Choong, 2013). Both the pore size and porosity, which facilitates cell proliferation and differentiation, are essential parameters in the formation of new tissue as they have a direct impact on the spatial distribution, location and mass transfer of cells, nutrients, oxygen and waste metabolic products.

Pore size is calculated as the area of void space between solid materials and can be calculated in metric units using high resolution SEM. Some studies indicate that scaffolds with a pore size between 100 µm to 350 µm promote osteogenesis (Hulbert et al., 1970, Story et al., 1998), and for scaffolds which are not subject to mechanical loads the porosity should be between 50% to 90% (Whang et al., 1998, Akay et al., 2004, Loh and Choong, 2013) to replicate bone. The recommended corresponding pore sizes differ between authors for different applications ranging from; 150 – 600 µm (Zeltinger et al., 2001), 100 – 400 µm (Burg et al., 2000), 300 – 400 µm (Tsuruga et al., 1997), 200 – 400 µm (Holmes, 1979), 400 – 1200 µm (Hollister, 2005) and over 350 µm (Karageorgiou and Kaplan, 2005). Other studies show that the minimum pore size for significant natural bone tissue ingrowth is between 75µm – 100µm (Hulbert et al., 1970, Klawitter et al., 1976, Murphy et al., 2010), with the optimal range being 100 – 135 µm (Maquet et al., 2000, Murphy et al., 2010). Consideration should be taken for micropores (1 – 75 µm) that are essential for protein adsorption and cell adhesion (Ranucci and Moghe, 1999, Gentile et al., 2012), as the nominal size of a canaliculi diameter is approximately 1 µm (Marieb and Hoehn, 2007, Shah et al., 2016). Hannah et al. (2010) studied the size of lacuna in human bones and concluded that the sizes were approximately 200 μm^3 to 300 μm^3 (Boyde, 1972, Hannah et al., 2010). Therefore, it can be concluded that pore sizes of 20 μm^2 - 30 μm^2 could be suitable for cells to attach fully and allow for nutrient flow.

Lee et al used a pre-osteoblastic cell line M3T3-E1 on 3D-printed scaffolds and showed that a pore size of 500µm had barely any cells after seven days in culture, and concluded that the pore size was too large for cells to interact with the scaffold and each other, under static cell

culturing conditions (Lee et al., 2010). The 500µm pore size did aid in cell infiltration, though did not promote cell adhesion of the pre-osteoblastic cells (Lim et al., 2010, Lee et al., 2010, Perez and Mestres, 2016). Studies by O'Brien et al, concluded that small pore sizes of 95µm showed significant viable cell attachment for osteoblast cells, than those with a larger pore size of 150µm (O'Brien et al., 2005). Despite the research having been conducted both experimentally and computationally, the optimum porosity and pore size for bone regrowth remains unknown, which is likely be due to the multivariable complex nature of scaffolds (their biocompatibility and structure) combined with the complexity of the process of bone regeneration. Osseous tissues boast a biomorphic pattern, characterised by curved surfaces and cross sections, different pore shapes and sizes, and the ability to replicate osseous tissue morphology is very complex (Barrère et al., 2008). Thus demonstrating that pore size and porosity are fundamental to the geometric features in bone regeneration, as they directly contribute to the amount of tissue growth. It can be concluded that scaffolds with higher porosity with both small and large pore sizes, and a higher number of pores with adequate mechanical strength are more suitable for bone tissue regeneration.

Bose et al. (2003) found that pore volume percentage (used as a measure of porosity) affects the compressive strength of porous ceramic scaffolds, they reported a compressive strength range between 0.2MPa and 1.8Mpa depending on pore sizes and porosities (pore volumes) of between 29% and 44%. It was found that porosity had a more profound effect on mechanical properties of the particular ceramics (TCP, tricalcium phosphate ceramics), where compressive strength decreased significantly with an increase in porosity (Bose et al., 2003). The pore sizes within the samples varied between 300µm and 480µm, but there was no conclusive evidence that cell growth behaviour was affected by pore size (Bose et al., 2003). This research shows that there is a need for further investigation into the relationship between pore size and cell growth behaviour (Bose et al., 2003).

As reported throughout this study, researcher have shown that scaffolds with very diverse range of pore sizes have been successfully used for bone generation both for *in-vitro* and/or *in-vivo* applications. The pore sizes range from nanometre scale to millimetre scale, most of which are between 10µm to 350µm (Lagoa et al., 2008, Ratanavaraporn et al., 2011, Grafahrend et al., 2011, Clafshenkel et al., 2012, Li et al., 2013, Shuai et al., 2013, Marí-Buyé et al., 2013, Gao et al., 2014, Polo-Corrales et al., 2014).

1.1.2 Micro-porosity

Microporosity is defined as pores with sizes ranging from a nanometre scale up to 10µm (Perez and Mestres, 2016). Microporosity is a significant contributor to enhancing the ability of cells to attach, proliferate and differentiate, and the osteoinductivity of scaffolds (Perez and Mestres, 2016, Zhang et al., 2018), and also plays a vital role in overall bone regeneration (Perez and Mestres, 2016). Microporosity within a scaffold, and particularly on the surface of a scaffold, enhances the surface area which can improve permeability of scaffolds, provide more protein adsorption sites and subsequently increase the osteoinductivity of the material as this stimulates the osteogenic-related functions of cells (Hing et al., 2005, Rouahi et al., 2006, Polak et al., 2013, Perez and Mestres, 2016, Zhang et al., 2018). Permeability affects the fluid flow and the new tissue ingrowth, it is a result of a combination of factors including; pore size and distribution, pore interconnectivity (open porosity), and pore orientation with respect to the scaffold (Manassero et al., 2016). Total porosity is defined as the sum of the open porosity and closed porosity.

Biomaterials such as hydroxyapatite (HA) are required to be porous for *in-vivo* bone growth (Tsuruga et al., 1997), and contains a high porosity for cell seeding for *in-vitro* applications (Jun et al., 2007, Frohlich et al., 2008). Rouahi et al, found that microporous HA (median pore size of 0.4µm and 12% open porosity) adsorbed 10 times more proteins (in particular Fibronectin and Albumin) than non-microporous HA (Rouahi et al., 2006, Zhang et al., 2018). It is suggested that micropores can induce capillary forces, which aid in anchoring of the cells to the substrate surface but can also cause the cells to become deformed by drawing them into interconnected micropores smaller than the cell itself (Polak et al., 2013, Oh et al., 2014, Zhang et al., 2018).

Polak et al. (2013) hypothesised that in both macro/micro pores self-seeding that is driven by a capillary force may be the basis of this advancement, and with these presented experiments and a mathematical-based model to support their proposed hypothesis. Polak et al. (2013) demonstrated that capillary forces in micropores (5 µm – 50 µm) draw cells through the microporous network with interconnections that are smaller than the cell diameter (Polak et al., 2013). They suggest that microporosities can be tailored to optimise cell infiltration into scaffolds with certain cell-types in mind. This important design feature can be utilised for controlled release of drugs *in-vivo* (Polak et al., 2013). Polak et al. (2013) highlighted that

bone scaffolds that are CaP-based which contain macroporosities of more than 100µm, along with microporosities of 5µm to 50µm have been identified as improving *in-vivo* bone formation, compared to macroporous scaffolds. They have also, in relation to bone regeneration outperformed microporous scaffolds which contained BMP-2. An earlier study showed that smaller pore sizes are better for osteoblastic adhesion, concluding that pores of 95µm are better for initial attachment than larger pores (>150µm) (O'Brien et al., 2005, Perez and Mestres, 2016).

A high microporosity, however, can have a negative impact on the mechanical properties of a scaffold as it will affect its stiffness, strength and toughness, as well as the scaffold's ability to keep its shape and provide necessary structural support for bone formation (Franco et al., 2010, Zhang et al., 2018). Higher porosity is known to be more suitable for tissue growth and it is recognised that a porosity of around 70% for AW scaffolds are suitable as an artificial bone substitute (Teramoto et al., 2005)

1.2 Biomaterials for bone tissue engineering

Over the past few decades, numerous biomaterials have been investigated for 3D scaffolds relating to bone tissue engineering. Biomaterials have been developed to represent both the cartilage and the bone component of joints (osteochondral model). These materials fall into multiple categories, synthetic materials, metals, ceramics, gels, natural scaffolds (corals) and plastics/polymers, some of which have received more attention than others (Hollister, 2005, Polo-Corrales et al., 2014). Some material manufacturing routes are more cost-effective, scalable, easier to source, whilst others are more versatile for scaffold fabrication and have specific characteristics that make them more suitable to particular applications. These characteristics play an important role in the selection of biomaterials and the choice of scaffold fabrication process. A brief overview of some biomaterials including biopolymers, and bioceramic materials used for scaffold fabrication for bone generation are presented.

1.2.1 Biopolymers

Biopolymers can be classified into two groups: naturally derived polymers and synthetic polymers. Naturally derived polymers include polysaccharides, such as chondroitin sulphate, starch, chitosan, alginate, hyaluronic acid and cellulose, and proteins, such as fibrin, collagen, gelatin and silk (Rezwan et al., 2006, Polo-Corrales et al., 2014). Natural polymers tend to have hydrophilic surfaces that encourage cell attachment, proliferation and differentiation,

although they have limitations usually associated with the lack of mechanical properties required for bone scaffolds. There are five different types of collagen found in the body (Types I to V) (Goonoo et al., 2014). Collagen type I, is naturally found in the bone's extra cellular matrix and is commonly used in collagen sponges for bone applications. The collagen sponges are biocompatible as well as biodegradable, though lacking the mechanical strength required for in-vivo applications, making bone scaffold applications limited (He et al., 2005, Harley et al., 2007, Polo-Corrales et al., 2014). Collagen has been modified with different materials to enhance its mechanical properties with some success reported (O'Brien et al., 2007, Serpooshan et al., 2010, Xu et al., 2011). However, there are several issues associated with collagen: cost, solubility, and a lack of commercial sources (Gleeson et al., 2010, Pilia et al., 2013, Polo-Corrales et al., 2014).

Synthetic polymers have also received great attention and they have become the largest family of biopolymers. The physical and mechanical properties of synthetic biopolymers are more predictable and reproducible, in comparison to natural biopolymers (Gleeson et al., 2010, Polo-Corrales et al., 2014, Hajiali et al., 2018). A further advantage of synthetic biopolymers is the high control of impurities and large scale commercial manufacture, resulting in high reproducibility, as well as cost efficiency (Rezwan et al., 2006). Amongst synthetic biopolymers, aliphatic polyesters like polylactic acid (PLA), poly glycolic acid (PGA), poly lactic-coglycolide acid (PLGA) and polycaprolactone (PCL) are the most commonly used for tissue engineering applications (Hutmacher, 2001). These polymers degrade within the body, and their gradual degradation results in the degradation products being removed via natural metabolic pathways. Three-dimensional scaffolds made from these polyesters have been fabricated through numerous techniques individually (e.g. 3D printing) or in conjunction with other materials (such as ceramics) (Li and Chang, 2004, Navarro et al., 2004, Blaker et al., 2005, Charlesharris et al., 2007, Tsigkou et al., 2007). Previous research has identified that alterations in the polymer's molecular weight, crystallinity, thermal transition, polydispersity and melting points all play a part in the scaffold's morphology, degradation and mechanical properties (Maquet et al., 2003, Rezwan et al., 2006, La Carrubba et al., 2008, Yang et al., 2008, Martínez-Pérez et al., 2011, Razak et al., 2012, Li et al., 2013, Toumpaniari, 2016, Barbeck et al., 2017, Burton and Callanan, 2018, Abbasi et al., 2020).

Polylactic acid (PLA) is likely to be the most widely used polymer for tissue engineering and biomedical applications (Wim et al., 2010, Flynt, 2017). PLA is a biodegradable material commonly made from lactic acid; Wallace Carothers in 1932 first polymerised lactide to produce PLA, this method was later patented by DuPont in 1954 (Carothers et al., 1932, Wim et al., 2010). PLA is available in both low and high-density, with high-density PLA primarily used in biomedical areas due to its ability to be safely absorbed biologically.

PLA is made with two possible materials: lactic acid or lactide. PLA is manufactured from renewable sources and is compostable which addresses some problems with waste disposal, and reduced dependence from petroleum-based raw materials. PLA is made using a three-step process: the first step includes biosynthesis of lactic acid from starch, then its conversion to the dimeric cyclic ester of lactic acid (lactide), then ring-opening polymerisation of lactide to convert it to poly-lactic acid. The last step requires a catalyst, heat and a metallic compound as catalyst. Lactic acid is a chiral molecule that exists as two optical isomers, L-lactic acid and D-lactic acid, with the L-isomer being the most common in living organisms. The D-configuration polarises light to the right, whereas the L-configuration, which is also optically active polarises light to the left, as depicted in Figure 1-1. Having two stereoisomeric forms gives rise to four morphologically distinct polymers those being D-PLA, L-PLA, D,L-PLA, and meso-PLA. D-PLA and L-PLA (stereoregular polymers), whereas D,L-PLA is the racemic polymer obtained from a mixture of D- and lactic acid, and meso-PLA can be obtained from D,L-lactide (Rezwan et al., 2006, Razak et al., 2012). Generally, L-PLA is more frequently used as L-lactic acid is a naturally occurring stereoisomer of lactic acid found in nature and is preferred due to its high mechanical strength and toughness (Vainionpää et al., 1987, Gogolewvki, 1992, Gunatillake and Adhikari, 2003). Details of this process could vary depending on the manufacturer of the product, in this study the PLA used was from NatureWorks, Ingeo (4032D PLA) which has a melting point between 150°C – 180°C and a glass transition temperature (Tg) of 55°C – 60°C (Kmetty and Litauszki, 2020, NatureWorks, 2020).

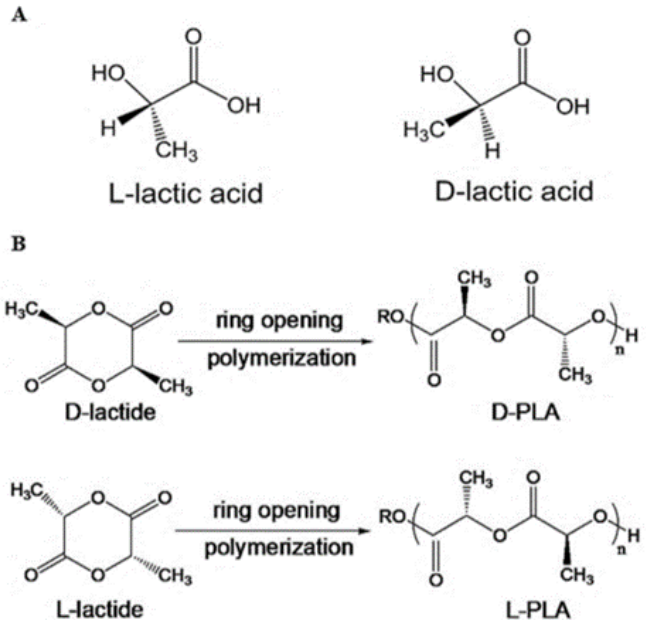

Figure 1-1: A) Stereoisomers of lactic acid and B) Ring-opening polymerisation of lactides. Adapted from (NPTEL, 2014).

Implanting polyesters alone for bone replacement may have its own set of issues, as the degradation products promote increased acidification of the surrounding environments and this can increase the degradation rate of the polyesters, in turn influencing an inflammation response from the surrounding tissue. Highly porous scaffolds made only from polyesters tend to be weaker than their non-porous counterparts. Highly porous polyester scaffolds are weaker in a sense of mechanical tolerances, which can limit their use *in-vivo* for load bearing sites (Harris et al., 1998, Martin and Avérous, 2001, Dhandayuthapani et al., 2011, Gentile et al., 2014, Manavitehrani et al., 2016). There have been studies in relation to incorporating polyesters with bioceramics to increase the mechanical properties and decrease the degradation rate of scaffolds.

1.2.2 Multi-layered scaffolds

Scaffolds with homogeneous material composition known as mono-phasic (single-phased) scaffolds are very common, but depending on application can encounter some limitations especially concerning multi-layered tissues such as osteochondral units (the interface between bone and cartilage) (Xue et al., 2010, Nooeaid et al., 2014, Bernstein et al., 2013, Rodrigues, 2018).

1.2.3 Ceramics for bone tissue engineering

Ceramics are being increasingly used in tissue engineering especially for bone regeneration. They can be grouped into two sub-categories; natural, like natural coral derived apatite's, alumina, and synthetic, like zirconium (Gargiulo et al., 2010, Tran et al., 2011, Divieto and Sassi, 2015, Manassero et al., 2016); for example calcium phosphates such as hydroxyapatite (HA) have a resemblance to the mineral component of bone, whereas bioglass ceramics have a similar strength when bonding to osseous tissue (Kukubo et al., 2003). Bio-ceramics are used in orthopaedics (calcium phosphates) in fracture healing, joint replacements, spinal applications and coatings on metallic bearing couples, and also for periodontal treatment and craniomaxillofacial (Whang et al., 1998, Hollister, 2005).

The most common calcium phosphate ceramics are; hydroxyapatite (HA), calcium sulphate hemihydrate (CSH), gypsum, calcium sulphate dehydrate (CSD), calcium carbonate, dicalcium phosphate (DCP), octacalcium phosphate (OCP), β-tricalcium phosphate (β-TCP), biphasic calcium phosphate (BCP), and β-calcium pyrophosphate (β-CPP) (Bohner et al., 2011, Velasco et al., 2015). Calcium phosphates used either singularly or in combination with other materials (Tzvetanov et al., 2002) have great potential in tissue engineering, as they have the ability to become osteoinductive, and can form strong bonds between a bone interface and biomaterial via increased cellular function (LeGeros, 1993, LeGeros, 2002, Ivanchenko and Pinchuk, 2003, Samavedi et al., 2013). The use of ceramics can promote osteoblast adhesion to the scaffold together with mesenchymal cell migration, which is vital for an *in-vitro* bone model. Hydroxyapatite ($Ca_{10}(PO_4)_6(OH)_2$) is a crystalline calcium phosphate (Guda et al., 2008) which exists in bone and is formed of; calcium ions (Ca^{2+}), orthophosphates (PO_4^{3-}), metaphosphates or pyrophosphates ($P_2O_7^{4-}$), and occasionally hydrogen or hydroxide ions, and can be either natural (bovine or coral) or synthetic (the combination of calcium carbonate and monoammonium phosphate at ambient temperature (Guda et al., 2008). Osteoconductive properties have been observed on some hydroxy apatite (HA) scaffolds, which have led to the onset of the bone regeneration process.

1.2.4 Bio-Glasses

Bioglasses are first introduced as glass compositions which can interact and bond to living bone (Larry Hench 1971). There have been other compositions with the objective of designing

an optimal material for bone regenerating constructs. This includes apatite-wollastonite glass-ceramic (AW2, produced by Glass Technology Services, GTS) used within this thesis.

Bioglasses can incorporate calcium phosphates (CaO, and P_2O_5) and other compounds such as SiO_2, Na_2O, in varying proportions (Velasco et al., 2015). Three-dimensional scaffolds with a wide range of porosities and surface topology characteristics can be made from bioglasses (Velasco et al., 2015). Consequently, they are typically used for maxillofacial reconstruction, otorhinolaryngological reconstruction, periodontal pocket elimination, and alveolar ridge augmentation (Hollister et al., 2005). Bioactive glass can come in the form of '45S5' a conventional silicate (45% $Si0_2$, 24.5% Na_2O, 6% P_2O_5, 24.5% CaO), or either a phosphate or borate-based glass (Mancuso, 2016). The bioglass is bound to the host tissue via a hydroxycarbonate apatite (HCA) layer that interacts with the surrounding collagen and is formed on the surface of the glass. Furthermore, osteogenic cell attachment and proliferation is enhanced by the HCA layer, which is similar to calcium phosphate bioglasses, as it facilitates new bone growth via the adsorption of proteins and growth factors. The interaction between osteoprogenitor cells has a direct influence on the osteoinductivity of the bioglass. In comparison to calcium phosphate, bioglasses benefit from a faster degradation rate (Ravaglioli et al., 2008).

1.2.5 Production of Glass-Ceramics

Shelby (2005) has defined glass as "an amorphous solid that lacks long-range, periodic atomic structure and exhibits a temperature region of glass transformation" (Shelby, 2005). Ceramics are considered as inorganic crystalline grains/materials comprised of at least two chemical elements (Kingery et al., 1976, James, 1995, Callister and Rethwisch, 2018). Glass-ceramics are considered to be polycrystalline materials that are the result of controlled crystallisation of base glass (Rawlings et al., 2006). Glass-ceramics are polycrystalline materials that consist of a mixture of amorphous phase (glass) and crystalline phases (ceramic), which are produced through controlled crystallisation during a two-stage process (Rahaman et al., 2011, Zhao, 2011, Ozdemir, 2020). These are referred to as the nucleation and crystal growth stages (see Figure 1-2), which allows crystals to propagate (Rawlings et al., 2006, Xiao et al., 2008, Fu et al., 2020).

The nucleation stage is a low temperature heat treatment, (around the T_N) to form a high density of nuclei, consisting of large number of smaller size crystals. In this stage, small stable

volumes of the product crystalline phase are formed in the parent glass. Large, oriented crystals in the glass-ceramic microstructure are normally unwanted as this can negatively affect its mechanical properties. When the stable nucleus has formed, the consequent step is the crystal growth stage, which consist of movement of the atoms/molecules from the glass, and into the crystal across the glass-crystal boundary (Rawlings et al., 2006).

Crystal growth step takes place at a higher temperature (Transition Temperature, T_G) than the nucleation step (first step), this higher temperature enables the nuclei to grow at a controlled rate. Differential thermal analysis (DTA) can be used to determine the temperatures of nucleation and crystal growth (Chou et al., 2017). It is well known that mechanical properties of the glass can be changed by controlling the crystallisation process and annealing process (Holland W., 2004, Alharbi, 2016, Mancuso et al., 2017, Deubener and Höland, 2017). The parent glass may be shaped prior to crystallisation employing any glass shaping methods such as casting & forming (McMillan, 1979, Strnad, 1986, Holland W., 2004) or extrusion (Atkinson and McMillan, 1977, Yue et al., 1999, Robert et al., 2000, Rawlings et al., 2006) methods. In this thesis, AW2 Glass Ceramic was purchased from Glass Technology Services (GTS). The AW2 Glass Ceramic was produced at their manufacturing site using a confidential process.

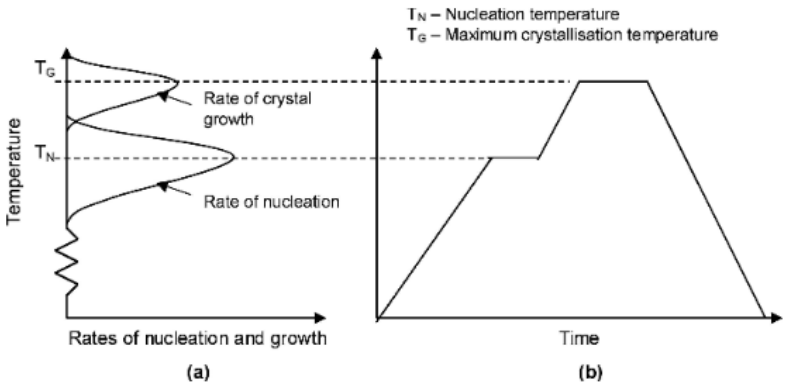

Figure 1-2: Crystallisation of a glass to form a glass-ceramic. (a) rate of nucleation and crystal growth at different temperatures; (b) two-stage heat treatment: temperature versus time for nucleation (T_N) and crystallisation (T_G). Figure from (Rawlings et al., 2006)

Zhang et al explained in detail the preparation of 58S Na_2O-CaO-SiO_2-P_2O_5 bioactive glass and glass ceramics, and investigated the nucleation and crystallisation process in great depth. Bioactive glass-ceramic is a type of bioactive glass after crystallisation with better bioactivity

and higher content of hydroxyapatite (HA) (Zhang et al., 2021). Using a high-temperature melting process, 58S Na_2O-CaO-SiO_2-P_2O_5 bioactive glass was prepared. Their experiments showed that optimal nucleation occurred at 660°C for 1.5 hours and crystallisation 750°C for 2 hours (Zhang et al., 2021). This optimised nucleation and crystallisation process enabled the formation of spherical Hydroxyapatite crystals at the nanoscale which resulted in increased bioactivity after treatment with artificial saliva (Zhang et al., 2021). A study of nucleation and growth of nanocrystals in Glass-Ceramics is presented by Fernandez-Martin et al (Fernandez-Martin et al., 2012). Using a combination of several techniques for Lithium-Aluminium Silicate glass-ceramics, the nucleation occurred during the slower ramp in the 720°C–820°C range and b-quartz crystallisation began in the 820°C–850°C range, with a final 60 minute hold at 930°C for the complete growth process (Fernandez-Martin et al., 2012). This shows that the temperatures and dwell times for the nucleation and crystallisation steps for each glass-ceramic may require optimisation to satisfy the requirements.

1.2.6 Apatite-Wollastonite

AW glass-ceramic is commercially available as Cerabone™ and is successfully used as bioactive glass ceramic for bone replacement. Many researchers have used AW to fabricate scaffolds for Tissue Engineering purposes. This section focusses on reviewing some of the closely related studies using AW (summarised in Table 1-1). (Rea et al., 2004) used Apatite-Wollastonite with high-density polyethylene (AWPEX), different volumes of AW glass ceramic (30% and 50% vol) in conjunction with different median particle sizes 4.5 µm and 7.7 µm, and with different scaffold surface finishes (polished and as-cut). AWPEX was tested with human Saos-2 osteoblast-like cells up to 7 days, to determine the best combination for cell response (Rea et al., 2004). The experiment showed that a polished surface, with 50% AW vol, and larger particle sizes provided an improved cell response (proliferation and differentiation). Similar study by (Tcacencu et al., 2018) gives detailed *in-vitro* and *in-vivo* analysis. Tcacencu et al. (2018) developed an AW/PLA composite structure by overlaying a 3D printed PLA structure (Rodrigues et al., 2016) over an AW disc (Mancuso, 2016) at 12.4% open porosity. The bonded scaffolds were cultured with bone marrow-derived stromal cells (BMSCs) isolated from adult male Sprague-Dawley rats. The result showed that *in-vitro* the scaffolds were cyto-compatible after 48 hours in culture, and the highest alkaline phosphatase (ALP) activity was recorded in AW discs rather than the AW/PLA composites or only PLA alone (Tcacencu et al.,

2018). Tcacencu et al. (2018) also undertook an *in-vivo* assessment with AW/PLA composite structures in rat calvarial defects; the scaffold examined was 2 mm in height (1 mm of PLA and 1 mm of AW). The newly formed bone appeared to be successful *in-vivo*, as tested in the rat model; there was no new bone formation in the PLA only on the scaffolds (Rodrigues et al., 2016, Tcacencu et al., 2018). However, porosity, pore sizes and Youngs modulus were not measured in (Rea et al., 2004) and (Tcacencu et al., 2018)'s research. Such measurements are essential for establishing repeatability of the manufacturing process and ultimately predicting the suitability of scaffolds for bone tissue growth.

Toumpaniari (2016) developed AW1 scaffolds via heat treatment (1150°C) of thermally induced phase separation of PLA-AW1 structures. These resulted in a total porosity of ~82%-86%, with a Young's modulus of 9 MPa (Toumpaniari, 2016). These AW1 scaffolds were used *in-vitro* with 500,000 hTERT Y201 cells per scaffold and had a 100% growth rate after 21 days in a basal medium. Pore sizes were measured via SEM images, but no values are detailed. Also, open porosity and compressive strength of the scaffolds were not reported in the PhD thesis (Toumpaniari, 2016), only total porosity was presented.

(Rodrigues, 2018) performed further studies on AW scaffolds fabricated by Naif Alharbi, as described in (Mancuso, 2016). The AW scaffolds were welded to 3D printed (FFF) PLA structures using two methods; ultrasonic and thermal fusion (details in 4th paragraph, Section 5.1 of (Rodrigues, 2018). The thickness of the AW scaffolds were 2.5 mm and the thickness of PLA was 1~2 mm. The PhD thesis reported successful outcomes following implantation of the scaffold to the scull of a rat with good osteointegration. The shear test indicated that the interfacial strength of the UW AW/PLA scaffold is strong, however, other mechanical tests, like the compression test and Young's modulus, were not performed. At the time of the research there was limitation on sintering temperature due to furnaces being able to achieve a maximum temperature 1200°C, and therefore it was not possible to experiment at higher temperatures (Mancuso, 2016, Rodrigues, 2018).

Kokubo et al. (1982) developed prosthetic scaffolds with AW glass-ceramic and implanted them in rabbit tibia. The scaffolds had very high densities of 99.3% (porosity of 0.7%) and a very high Young's modulus of 103GPa. The scaffolds formed very tight bonds after 8-weeks *in-vivo*, with the surrounding bone and showed no negative reactions with the surrounding tissues even after 25 weeks (Kokubo et al., 1982).

In a more recent study by (Lee et al., 2015) microporous AW scaffolds were made by using; AW particles, at a range of 45 – 90 µm and 0 – 45 µm at a ratio of 3:1 mixed with a 10% acrylic binder, using selective laser sintering (SLS), an additive manufacturing technique. The scaffolds contained a 1 mm cylindrical hole which were cut to the dimensions of 5 x 5 x 2 mm using a precision cut-off machine and sintered in a furnace at 1050°C. The scaffolds were studied *in-vitro* with 2 x 10^6 MSCs (human bone marrow mesenchymal stromal cells) for either 1 or 7 days prior to implanting into them into subcutaneous nude mice. The result showed no significant difference in the amount of osteoid staining in relation to geometry or porosity of the two different scaffold designs (without a hole and with a hole) (Lee et al., 2015). The study also concluded that there was no obvious difference in osteoid formation between un-seeded and seeded cA-W scaffolds by week 8. The results do not necessarily represent the potential of binding to bone tissue. However, the study indicated that dynamic culture may have improved cell proliferation on the scaffolds. Lee et al (2015) agrees with Fujita et al (2000) that over time microporosity allows for more controlled resorption of AW scaffold when implanted *in-vivo*. Although Lee et al (2015) concluded that the macroporosity (central hole) improved early in-growth of cells (within 4-weeks) and matrix deposition within the central channel.

Materials	Manufacturing Technique	Advantages	Limitations	Porosity	Pore Size & measurement Technique	Scaffold size	Youngs Modulus (MPa)	Cell Activity, Number of cells	Cell Growth rate	References
AW + high-density polyethylene composite (AWPEX)	Blending, compounding, centrifugal milling and compression moulding.	Increased cell proliferation on scaffolds with larger AW particles.	Lack of repeatability specially on as-cut scaffolds	Polished surface and as-cut samples	NA	Tile - 1 x 10 x 10 mm^3	NA	Saos-2 human osteoblast-like cells, 4,500 cells per cm^2 3,000 – 25,000 cells per cm^2	From 4,500 to 275,000 cells (cancer cells, high growth rate)	(Rea et al., 2004) (Wang et al., 1994)
AW Frit/powder + PLA (Ceramic – polymer composite)	FFF of PLA structures + indirect 3D printing of AW disks. Thermal bonding of PLA with AW disk	Controlled pore size and porosity for PLA (3D printed) part of scaffold	No compression test was reported	41.85% SE 0.95% Total. 12.4% SE 0.29% open. PLA 60% porous.	NA	PLA Disk - 1 x 8 mm + AW Disk – 1~2 mm x 8 mm	NA	Bone marrow-derived stromal cells (BMSCs) from adult male Sprague–Dawley rat, 10,000 cells/ disc	After 48hours 95% viability	(Tcacencu et al., 2018), (Rodrigues et al., 2016)
AW 1	TIPS	Porous scaffold, reasonable cell growth	No systematic pore size measurement, open porosity, or compressive strength	Total porosity = 82%	Manually measured, categorised as micropore and macropore		9MPa	hTERT Y201 cells, 500,000 cells	100% increase in 21 days in Basal Medium	(Toumpaniari, 2016)
PLA – AW	3D printing PLA bars, and laser cutting the bars. Thermal/US welding of PLA and AW disks	Osseointegration of PLA-AW composite structure in rat model	No compression or Youngs modulus on AW scaffold.	No porosity on AW scaffolds in detail. PLA porosity 52 – 60%	Microporous AW structure. PLA pores 300µm, measured via SEM	AW 2.5mm thick ~6mm diameter	No mechanical tests on PLA-AW scaffolds PLA Youngs	*In-vivo* test in a rat calvarial defect model.	NA (No *in-vitro* test)	(Rodrigues, 2018)

	manufactured by (Mancuso, 2016)		Sintering temp. was limited to 1200°C				modulus 500 – 800 MPa			
Hydroxyapatite + Wollastonite	Sponge replica method and sintering to 1300°C	Excellent bioactive + dissolution properties. Only Large pores.	Small pores not measured. Youngs modulus not given.	88-91% total porosity High interconnectivity without measuring	Small to >500µm, visually using scale bar on SEM images, longer side of pore reported	Cuboid 10 x 10 x 15	Compressive strength 0.21 – 1.02 MPa	NA	NA	(Kunjalukkal Padmanabhan et al., 2013) (Jodati et al., 2020)
Apatite and Wollastonite glass ceramics	Glass powder <44µm pressed in 400kg/m^2 . 1050°C sintered 2-hours	Good compatibility, high compressive strength tight bond with rabbits	Fracture at interface between implant and bone	0.7% porosity Archimedean techniques	<20µm from SEM image and scale bar	10 x 15 x 2 mm	103 GPa Compressive strength 1060 ±60 MPa	*In-vivo* tibia of male rabbits – 8 weeks	NA (*in-vivo*)	(Kokubo et al., 1982)
AW	Selective laser sintering (SLS) of AW powder, then sintering at 1150°C Particles 45-90 and 0-45 at 3:1 ratio	Dynamic culture with 30ml media	*In-vivo* tested performed subcutaneous, not in bone.	Microporosity (<50µ) 25-27%	Microporous <50µm, One macroporous channel of 1 mm	5 x 5 x 2 mm, Hole diameter 1 mm	No Youngs modulus or compressive strength	MSCs extracted from human bone marrow 2,000,000 cells per scaffold	*In-vitro* then transferred to *in-vivo* (subcutaneous in nude mice)	(Lee et al., 2015)
AW 1	AW powder mixed with paraffin wax particles, pressed for moulding. Sintered 1050-1150°C	Good biocompatibility and extensive osteoconductivity	Small pores mentioned but not reported or measured	Porosity of about 70%	250-350 µm – manually via SEM Archimedes	5 x 2 mm	Compressive strength 5MPa	New Zealand rabbit MSC's from bone marrow, 2,000,000 cells per scaffold.	*In-vitro* then transferred *in-vivo* on rabbit's mandible	(Zhang et al., 2009)

AW 2	TIPS using AW2, investigated ratios of dioxane :water. Sintered at temperatures between 1215 - 1250°C	Repeatable method with good mechanical properties, open porosity and pore sizes	High temperature furnace required. Temperature sensitive TIPS method	Open (42%), closed & total (73%) porosity reported.	ImageJ algorithm on SEM images. Micro (10 – 80) + macro pores (80 – 960)	Conical frustrum diameter 8 x 4 mm height	Compressive strength 5±0.4 MPA Young Modulus 126.5 ±20.4MPa	Human Foetal Osteoblast cells (Cell Applications, 406-05f) per scaffold. Preliminary experiment 2.5 $x10^5$ and $5x10^5$ cells. Main experiment used 2 $x10^5$ cells.	See Chapter 5 – In-Vitro tests with Porous Scaffolds of this thesis	Reported in this study/ thesis

Table 1-1: Summary of closely relevant papers which use Apatite-Wollastonite in scaffolds with successful tissue growth either in-vitro or in-vivo. Important parameters are listed in the table.

1.3 Porosity and pore size measurement techniques

Various techniques have been used to measure the porosity and pore sizes of scaffolds. Porosities can be reported as open, closed and/or total porosity. The total porosity is representative of the amount of pore spaces present in the scaffold and can be measured by considering the physical properties of scaffold like the bulk density against the material density (Loh and Choong, 2013). Generally, the total porosity is representative of the pore spaces available in a scaffold, it is considered as the closed porosity plus the open porosity.

Gravimetric is a commonly used technique for total porosity measurement, which uses the apparent density of the scaffold (mass/volume) against the bulk density of the scaffold (Ho and Hutmacher, 2006, Loh and Choong, 2013). This technique cannot measure the open porosity of scaffold (Hu et al., 2002, Maspero et al., 2002, Kim et al., 2004, Ghasemi-Mobarakeh et al., 2007, Guarino et al., 2008). It is a preferred method in materials that cannot withstand mechanical pressures which other porosity determining methods can subject the scaffolds to.

Mercury porosimetry method allows the determination of the total pore volume fraction, the average pore diameter, and pore size distribution of three-dimensional materials/scaffolds (Mayer and Stowe, 1965, Shum et al., 2005, Guarino et al., 2008) by infusing high pressure mercury into the scaffold. This technique is not suitable for many scaffolds as they do not have high enough mechanical integrity and can be destroyed or collapse under the pressure. Also, smaller the pore diameters require higher pressures, and this has to be taken into consideration if this method is utilized. Mercury is very expensive and is toxic and the technique is considered as a sacrificial/destructive technique, therefore the scaffolds cannot be used again (Ghasemi-Mobarakeh et al., 2007, Guarino et al., 2008, Loh and Choong, 2013).

Liquid displacement method is based on Archimedes Principle, it is a simple technique that can be carried out to measure the porosity of scaffolds. This technique uses a liquid that is a not a solvent of the scaffold material like ethanol, and is capable of penetrating into small pores but does not cause size swelling or shrinkage (Shi et al., 2002, Ho and Hutmacher, 2006). In brief, the scaffold will be placed in a holder with a known volume of the displacement liquid and a series of evacuation–repressurisation cycles carried out to force the liquid into the

pores (Shi et al., 2002). The displacement liquid is representative of porosity of the scaffold (Loh and Choong, 2013).

Microcomputed tomography (Micro-CT or μ-CT) imaging can be used to provide more specific information on the internal 3D morphology of scaffolds, which can be used to compute both open and closed porosity as well as pore sizes using specially designed image processing techniques. Micro-CT generates a series of 2D thin images of the scaffolds' internal structure by computing the level of attenuation of x-ray radiation from different angles in a circular form. A stack of 2D images generates a 3D image of the scaffold which can be visualized or used to measure internal structures (Tomlins et al., 2004, Rajagopalan et al., 2005, Loh and Choong, 2013, Bartoš et al., 2018). The resolution of Micro-CT imaging is usually a limiting factor, resolution is approximately 10 micro-meters depending on the device and the scaffold/sample size, which makes small pores unaccounted for, so it is unreliable for measuring micropores and microporosity. Also, Micro-CT can take around 4 hours to scan a single scaffold which can be expensive, although it is a non-destructive method that can be used for fragile scaffolds (Ho and Hutmacher, 2006). However, Micro-CT is used for pore analysis by many researcher (Karageorgiou and Kaplan, 2005, Ho and Hutmacher, 2006, Loh and Choong, 2013, Krieghoff et al., 2019). (Meretoja et al., 2009) used Micro-CT for interconnectivity analysis and pore analysis for continuous phase microporous scaffolds with rat cells in combination with SEM analysis for pore diameter.

SEM has much higher spatial resolution compared to Micro-CT, to less than 10 nm, which makes is a more favourable imaging technique for analysis of the surface of scaffold, including its pore size measurement. However, SEM cannot be used to measure interconnectivity or internal structure. Image processing techniques can be used to measure pore sizes (Tomlins et al., 2004), however it is common to use manual measurement of pores by marking the coordinates of one side of a pore against the coordinate of the other side, and computing the distance. Another method is to use the diameter of pores measured in x-axis and y-axis in SEM images and reporting the distance in each direction (Wei et al., 2005, Shum et al., 2005). Such technique is reports different pore size depending on the orientation of scaffold and therefore is suitable only for scaffolds which have more homogeneous/symmetrical pores.

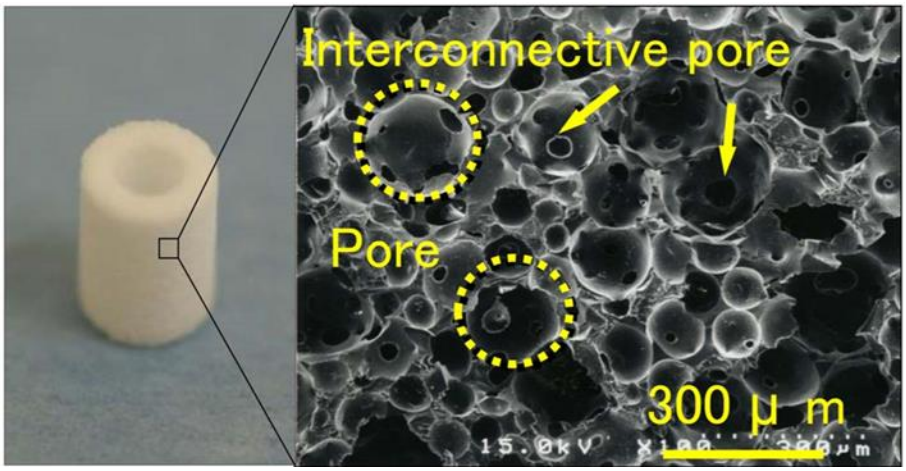

Figure 1-3: (A) Photograph of the prepared IP-CHA (B) A SEM image of the surface. IP-CHA has a systematic arrangement of uniform pores, all of which are connected by a network of smaller interconnected pores (Doi et al., 2012)

Some reports fitted a circle over the pore and measured the diameter of the largest circle which pass through the furthest points on the boundary of the pore and used the diameter of the circle as a representative of pore size, a sample is shown in Figure 1-3 (Doi et al., 2012, Elhadidy et al., 2013, Lo Re et al., 2015). This technique is suitable for circular pores and inevitably will quantify pore sizes larger than the reality (Doi et al., 2012, Turnbull et al., 2018, Bartoš et al., 2018). Section 2.8 presents a novel image processing technique for pore size measurement using SEM images.

1.4 Thermally Induced Phase Separation Scaffolds

Thermally induced phase separation (TIPS) is one of the most commonly used methods in manufacturing processes of scaffolds, due to its capability to produce highly interconnected and porous scaffolds. TIPS is a technique based on a change in temperature which results in a polymetric homogeneous solution to de-mix into a polymer-rich and a polymer-less phase. Owing to the thermodynamic properties of polymer solutions, the de-mixing can be liquid-liquid or solid-liquid (Schugens et al., 1996, He et al., 2009, Mannella, 2012). Solid-liquid usually occurs for binary polymer-solvent mixtures, and liquid-liquid phase separation occurs for ternary polymer/solvent/non-solvent mixtures (Hua et al., 2002). Liquid-liquid phase separation in a ternary polymer/solvent/non-solvent mixture is commonly used in scaffold manufacturing and is based on changing the temperatures (Thermally Induced Phase Separation, TIPS) and/or the composition (Diffusion Induced Phase Separation).

The scaffold architecture is highly influenced by varying the parameters in the process, including polymer type and concentration, starting composition solvent/non-solvent ratio and the sequence of thermal operations. (Conoscenti et al., 2017) showed that if the cooling path is kept constant, then the higher the polymer concentration results in a decrease in the porosity and pore dimension. A study of the pore dimension as a function of temperature and time, showed that at room temperature (25°C) pore sizes are independent of the demixing time, however the demixing time shows significant effects on pore dimensions for temperatures of 30°C and 35°C (Li et al., 2006, Pavia et al., 2008, Conoscenti et al., 2017). Other researchers have adapted the TIPS technique to produce composite scaffold by adding ceramic fillers including: hydroxyapatite, bioglass, keratin (Maquet et al., 2003, Wang et al., 2010, Puglia et al., 2015, Ghersi et al., 2016, Toumpaniari, 2016, Conoscenti et al., 2017) and produced porous scaffold by optimizing the manufacturing process which varies substantially.

1.4.1 Cloud point

The detection of the cloud point is a commonly used method to determine phase boundaries in polymer solutions (van de Witte et al., 1996). A homogeneous polymer solution is cooled down slowly: the suspension will start to become cloudy/turbid when phase separation sets in, this is considered as the cloud point (La Carrubba et al., 2008, Mannella et al., 2013, Ishigami et al., 2014). Traditionally the cloud point is detected visually, therefore this is considered to be a qualitative methodology (Hua et al., 2002, Pavia et al., 2008, Chen et al., 2010, Mannella et al., 2013). Although, to measure the turbidity of solutions more accurately, light transmission approaches have been utilised (Bae et al., 1991, Mannella et al., 2013).

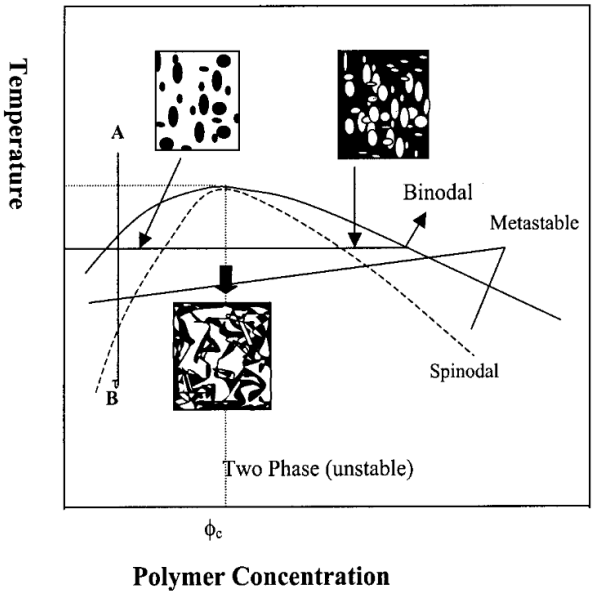

Figure 1-4: Schematic temperature (°C)-composition phase diagram for a binary polymer-solvent system(Hua et al., 2002)

Figure 1-4 displays the spinodal and binodal curves, when quenching temperature is located in the 'unstable zones' an interconnected structure with uniform pores is expected due to the spinodal phase separation (Hua et al., 2002).

1.5 Hot Stage Microscopy

Hot stage microscopy (HSM) was developed by Welch in the 1950s using photographic and digital recordings to visualise the changes in a sample in relation to temperature. The changes in the samples contours in relation to temperature allow for an understanding of the sample's geometry and shape, wettability, viscosity and surface tension (Panna et al., 2016, Mancuso et al., 2017). The modern hot stage microscopes allow for continuous measurements and recording of this data alongside additional software to aid with analysis (Panna et al., 2016). It is important to note that only raw materials are used for hot stage analysis, and this is particularly significant when using ceramics, as it allows for the focus to be on the fusibility of the raw material, allowing determination of ceramic's softening, melting, flow and sintering temperatures (Panna et al., 2016). The data acquired can be analysed in several different ways, including how surface area changes with temperature and rate of temperature (increasing and/or decreasing), which can then be plotted and compared. Furthermore, the particle size of the raw material (AW powder) can affect the sintering temperature as well as the area change observed via HSM.

Chapter 2 – Materials and Methods

2 Materials and Methods

2.1 Materials

Poly Lactic Acid (PLA) (Ingeo 4032D, density 1.24 gcm^{-3}, molecular weight 156.65 g/mol). Dioxane (99.8% purity, Sigma Aldrich). Apatite Wollastonite (AW2) raw powder (3.68% MgO, 44.81% CaO, 35.49% SiO_2, 15.47% P_2O_5, 0.19% CaF_2, 0.02% SrO, 0.09% Fe_2O_3, 0.14% Al_2O_3) was obtained from Glass Technology Services Ltd, (GTS). The AW2 powder contained a variation of particle sizes up to 200 µm in size. Superglue (ASDA stores, UK) and Ethanol (200 proof purity, Sigma Aldrich) were used in this work. Any water mentioned in this methods section was deionised water produced by the Purite 300 water purification system (Purite UK), unless specified otherwise.

2.2 Cloud points analysis

Temperature is an important factor in the manufacture of TIPS scaffolds. To determine the optimum temperature, cloud point analysis was performed. The cloud point refers to the temperature where the material forms a cloudy appearance and begins to be become opaque (Schugens et al., 1996). This temperature plays an important role in the process of manufacturing scaffolds and is used to ensure the separation of the scaffold solution (AW2, Dioxane, water and PLA) does not occur during the manufacturing process.

Polylactic Acid (PLA) at a concentration of 5% w/v was prepared by weighing the PLA (5 g) using a precision balance (Kern ABT220-5D), which was made up to the volume of dioxane and deionised water at a range of different ratios in a Duran bottle. The concentrations of dioxane to water (100 ml) were as follows, 85:15, 87:13, 90:10, 93:07 and 100:00 (v/v) the methods were adapted from (Schugens et al., 1996, Chen et al., 2010). A magnetic stirrer was placed in the Duran bottle containing the PLA Dioxane: water mixture, which was then placed in a water bath at 90˚C and stirred for 2 hours, until all the PLA was dissolved. The Duran bottles containing the PLA dissolved in the solvent mixture solution at the different ratios of dioxane:water was then placed into a water bath at 70˚C and mixed for 10 minutes. The temperature was then lowered at a rate of 1˚C every 2 minutes and visual analysis took place to determine the onset of turbidity of the solutions (n=5). The cloud point is defined as the point where the polymeric solution changes from clear to turbid. This initial experiment was

repeated using a solution of 100:00 dioxane:water at varying concentrations of PLA (3%, 4%, 5%, 6% and 7%) to determine if this influences the cloud point and therefore scaffold morphology.

To obtain a more accurate cloud-point, the experiment was modified slightly by repeating the experiment daily across four days, during which the temperature was lowered at much slower rate of 1˚C every 5 minutes to ensure homogeneity of the temperature. This latter experiment was repeated with the addition of 50% AW2 powder, to investigate if any changes to the cloud point temperature occur. All the samples were subsequently re-heated to 6˚C above their cloud point, and the mixture was then poured into glass moulds, which were then frozen overnight, washed with ethanol and freeze dried and subsequently analysed morphologically. Scaffold preparation is described in more detail in Section 2.3.

2.3 Scaffold Preparation:

2.3.1 AW Powder Milling

Apatite Wollastonite 2 (100 g) with particle sizes greater than 90 μm was milled in a Pulverisette 6 grinder (Fritsch, Germany) for periods of between 1 and 3 minutes at rotational speeds between 380 rpm and 410 rpm. This was repeated until the chosen particle sizes were obtained during sieving as detailed below.

2.3.2 AW Powder Sieving

Milled AW2 powder was sieved in a sieve shaker (Auto Sieve Shaker SV001, Impact, UK), over a period up to a month to obtain particle fractions of <20 μm, 20-53 μm, 54-90 μm and >90 μm (Dyson et al., 2007). A particle size of 20-53 μm was chosen for this study according to previous research (Toumpaniari, 2016, Rodrigues, 2018), which was coded as AW2.

2.3.3 Glass Mould Preparation

Glass petri dishes were covered in non-creased aluminium foil. Superglue was used to attach one end of each glass mould (height 16mm, internal diameter 11mm, external diameter 15mm) to the aluminium foil that's attached to the petri dish. Manual pressure was then applied to ensure the glass moulds were attached to the aluminium foil homogeneously. The petri dishes were then transferred to a fume hood (kept at room temperature) for a minimum of 30 minutes to dry and attach fully.

2.3.4 Dioxane concentrations in scaffolds

The process of generating porous scaffolds using AW2 and PLA beads were used to mimic the bone structure using novel techniques.

Polylactic acid (PLA) beads (5 grams per 100 ml volume; 5% w/v) were dissolved in varying concentrations (85:15, 87:13, 90:10, 93:07 and 100%) of dioxane and deionised water in glass Duran bottles placed at 90°C in a water bath, using a glass beaker filled with water on hot plate (IKA C-MAG HS7), with magnetic stirrer for a period of 2-hours (Figure 2-1). Then 50 grams (g) of AW2 powder was added to the solution held at a temperature 90°C, which was stirred for 10 minutes. This solution was then placed in a water bath at held at 60°C, which was stirred for a period of 1 hour 30 minutes. The temperature was then set at 6°C above the experimentally identified cloud point temperature and was then stirred for a further 20 minutes.

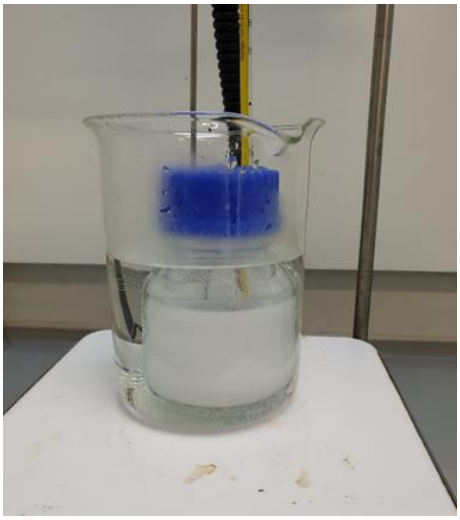

Figure 2-1: Duran bottle with AW2 powder, PLA and Dioxane:Water solution, held in a water bath on a hotplate. Thermometer and temperature loop can also be seen.

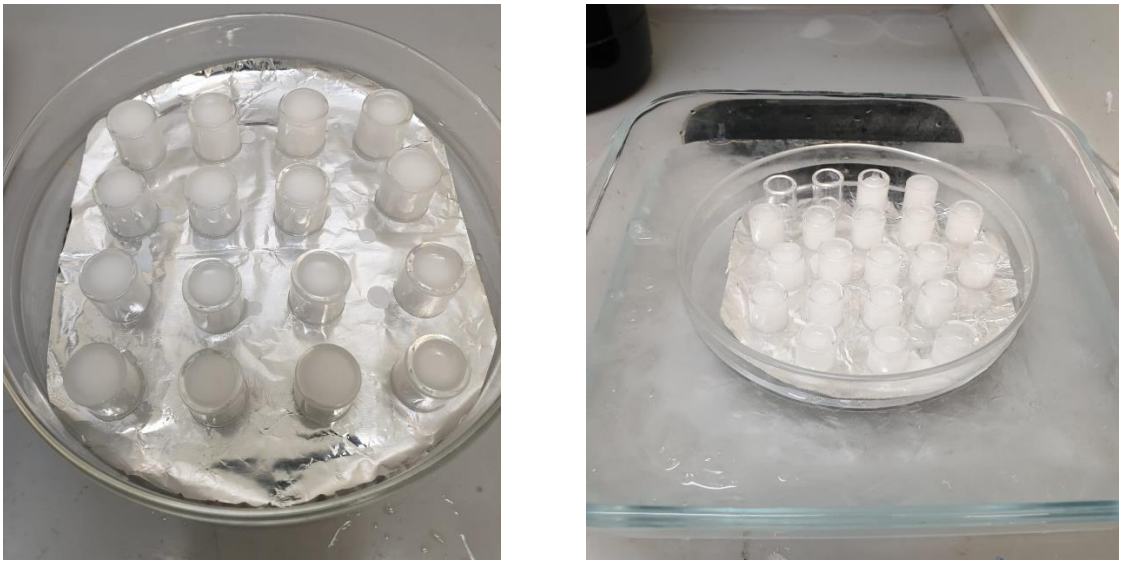

A **B**

Figure 2-2: Glass moulds with AW2, PLA and dioxane:water on a glass petri dish. A) Immediately after pouring at room temperature. B) Partially submerged in Ice-cold water

The solution was then carefully poured into the glass moulds (prepared as in 2.3.3) at room temperature (approx. 21°C), as shown in Figure 2-2A. The glass petri dishes (containing the solution-filled moulds) were left in the room temperature fume hood for 3 minutes. The petri dishes containing the moulds were then partially submerged into an ice-cold water bath for 1 minute as shown in Figure 2-2B, then transferred to a freezer and were frozen at -20°C overnight.

The moulds were removed from the freezer and were then carefully peeled off the aluminium foil; the scaffolds were then pushed out gently using a thick glass rod. The scaffolds were rapidly immersed (fully) into a plastic receptacle filled with a freezer cold (-20°C) ethanol:water solution (80%:20%). This solution was replaced twice daily over four consecutive days.

The scaffolds were removed from the ethanol:water (80%:20%) solution (-20°C), and were then placed into ice-cold (0°C) deionised water for 2-minutes and were stirred gently using a glass rod. The scaffolds were then removed and dried with blue tissue roll, placed onto freezer-cold (-20°C) glass petri dishes and into the freezer for 4-hours.

A B

Figure 2-3: Scaffolds made of AW2, PLA and dioxane:water. A) Scaffold prior to freeze-drying. B) Scaffold post freeze–drying

The scaffolds (as shown in Figure 2-3A) were then freeze-dried for 48 hours (Freeze Dryer - ALPHA 1-2 LD plus; Martin Christ Freeze Dryers, UK), which resulted in porous AW-PLA structures, as shown in Figure 2-3B. After freeze-drying, the scaffolds were stored at room temperature (approximately 20°C) until the sintering stage.

2.4 Hot-Stage Microscopy and Thermal Analysis

Using Misura equipment (Expert System Solutions, Italy) Hot stage microscope (HSM), multiple fractions of the milled AW2 powder were analysed separately to assess thermal behaviour of the powder.

AW2 powder (2g) was thoroughly mixed with deionised water using a small metal spatula to form a relatively stiff paste, which was then inserted into a moulding cylinder (2 mm diameter x 3 mm height), an AW2 cylinder was then carefully removed from the mould. The AW2 cylinder was then placed onto the loading platform, directly in front of the HSM camera for visual analysis, at room temperature (approx. 20°C), with the heating rate set to increase by 10°C per minute, up to a maximum temperature of 1300°C. A heating rate of 5°C per minute was also used for a more accurate comparative study, which yielded the same findings as 10°C per minute.

2.5 Scaffolds shrinkage and material loss due to sintering process

The volume shrinkage that occurs in the scaffolds due to two-step heat treatment was evaluated. The diameter and height of the freeze-dried scaffolds was taken with a digital Mitutoya Calliper, from which the volume was calculated. Post heat-treatment, the scaffolds were of a conical frustum shape, as such, the diameter was measured on both conical shaped ends of the scaffolds, the height of the scaffolds were again measured using the digital calliper (Mitutoyo). The structural stability of the scaffolds was evaluated whilst handling during these measurements.

The scaffolds mass was determined by weighing the samples (using a precision balance - Kern ABT220-5D) 5 times at each stage: post freeze-drying, post heat-treatment, and during the Archimedes protocol.

2.6 Heat Treatment Process of AW2 Scaffolds

To obtain sintered scaffolds, the freeze-dried AW-PLA scaffolds were placed on a platinum foil base (Pt 99.95%) on top of a refractory brick in the middle of the furnace chamber (SNOL10/1300LHM01 Eurotherm 3216).

The heating process was programmed in two consecutive steps:

Step 1 – heating the furnace from room temperature to 779°C, using a heat rate of 5°C per minute, with a dwelling time at 779°C of one-hour.

Step 2 – All scaffolds completed step 1, the heating is then continued at a rate of 10°C per minute, up to a specified temperature, with a dwell time of one-hour. This temperature for step 2 was between 1215°C to 1250°C.

After the two-step heat treatment cycle is complete, the scaffolds remain within the furnace until it reaches room temperature (approximately 20°C). A precision balance is then used to measure the mass (grams) of each scaffold (once cooled) following the two-step heat treatment.

2.7 Morphological analysis of the green and sintered scaffolds using SEM

A Hitachi TM3030 Scanning Electron Microscope (SEM) (Newcastle University) was used for high-resolution imaging of the scaffolds at different stages (post freeze-drying and post heat-treatment). Each sample was initially cleaned with pressurised air to remove any particulates.

Aluminium stubs were coated in double-sided carbon tape and each scaffold was then gently loaded onto the SEM. A digital photo was taken of the loaded sample stage prior to insertion into the SEM. Five areas of view were analysed for each scaffold (horizontally, and vertically). Each scaffold's position was altered to obtain images of the "top" of the scaffold. The images were captured at 15kV and saved as JPG or TIF file formats. Prior to each image being acquired, the magnification was altered to obtain optimally focussed images, with multiple images taken at each magnification.

2.8 SEM image analysis – to measure pore size and distribution

A novel image-processing algorithm was developed to measure the pore sizes from the SEM images. The algorithm consists of many steps including; 1) pixel size unit conversion to metric units; 2) image segmentation; 3) morphological filter to split connected pores; 4) verification step; 5) extract statistics from the detected pores, a schematic is shown in Figure 2-4. ImageJ FIJI (Rasband, 1997, Rasband, 2012, Schneider et al., 2012) was used to implement the algorithm.

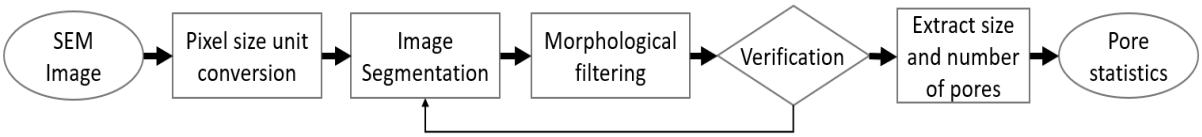

Figure 2-4: Schematic flowchart of the image-processing algorithm where the inputs are SEM images and output is the statistical data on pores, including size and distribution.

The main steps, after loading the SEM images into ImageJ FIJI, are described in detail below.

1) Image Scale conversions to set the size of pixels in the image to metric units

To convert the image sizes to micrometres (µm), perform the following sequence of steps:

- Click on 'Line Tool' (the curser will change to a cross)
- Click across the scale bar on the image so the bar is covered by a line
- Click Analyse > Set Scale, the distance in pixels will become the length of the scale bar in pixels
- Click on known distance and input the value of the original scale bar, e.g. 200, and then change units to scale units, e.g. µm as shown in Figure 2-5.

2) Segment images by apply thresholding to the SEM images

- Click on Image > Adjust > Threshold. The segmented regions represent the scaffold's pores.

Segmentation was performed using an automatic global (histogram-derived) thresholding technique described in (Gonzalez and Woods, 2008). The thresholding algorithm is integrated in the ImageJ plugin. Thresholding was used to segment the image into two categories, scaffold material and pores; carried out by analysis of the histogram of the image. The histogram of a scaffold image commonly has two distinct peaks representing the scaffold material (bright parts of image) and pores (dark parts of image) (Figure 2-5).

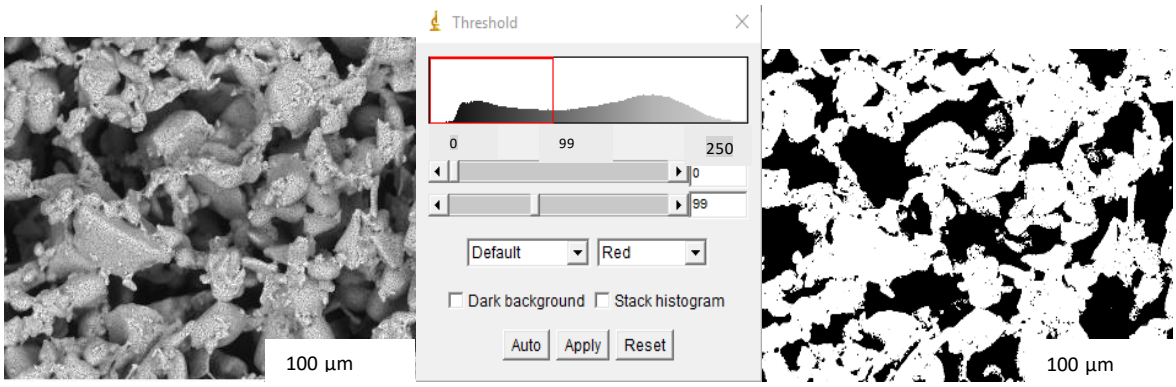

Figure 2-5: Original SEM Image (left), histogram and automatic threshold (middle), segmented image (right). Image sizes are 280x280 µm.

A sample SEM image, its relative histogram and segmented image are shown in Figure 2-5. Automatic thresholding offered a threshold at the lowest level in the histogram connecting the two peaks. The automatic threshold was normally suitable for this image processing application. However, it was possible to adjust the threshold manually to achieve a more accurate segmented image. The threshold was adjusted manually in images that lacked defined borders between the white areas (scaffold) and dark areas (the pores). These thresholds were chosen around the lowest point between the two peaks in the image histogram.

3) Change the segmented image to binary image

- Click on Process > Binary > Make Binary.

This conversion changes the intensity values for black and white parts of an image from 0 and 255 to 0 and 1, respectively. Conversion to the binary image is required for the next step.

4) <u>Disconnect pores from each other by applying morphological filters – Erosion and Dilation filters</u>

   - For Erosion, click on Process > Binary > Erode
   - For Dilation, click on Process > Binary > Dilate.

Erosion and dilation are two fundamental image-processing operations for morphological filters. For these morphological operations, a structure element of small size, usually a window size of 3 x 3 pixels, is scanned over the image and every point in the centre of structure element is replaced with one of the pixel values under the structure element based on this simple rule.

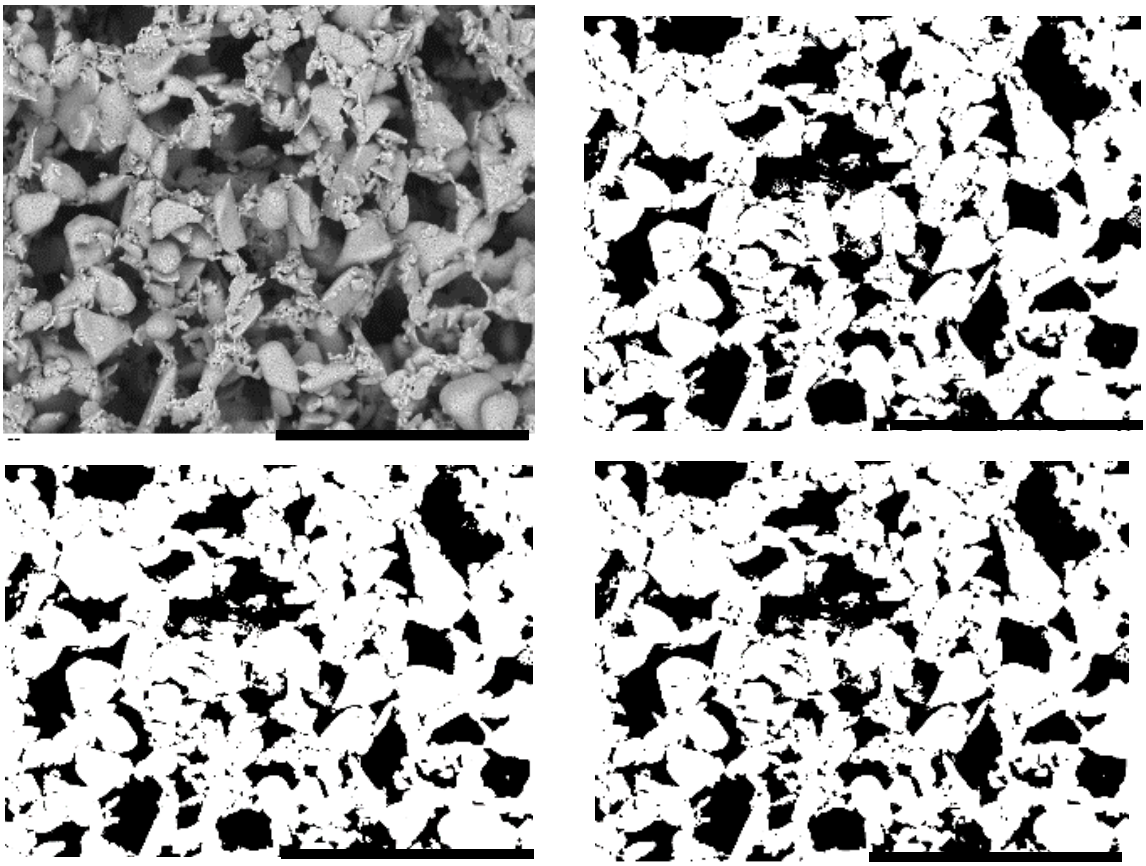

Figure 2-6: From left to right; (Top) Sample SEM image, original image after thresholding; (Bottom) After erosion, and final image after dilation. Pores are represented as black. AW material is represented as white. Image sizes are 430 µm x 430 µm. The scale bar represents 200 µm.

In erosion, if there is a white pixel under the structure element, the centre pixel will become white, otherwise it will be kept black. In dilation, if there is a black pixel under the structure element, the centre pixel will become black. Therefore, erosion disconnects black regions if the connection is smaller than the structure element and, also makes black regions smaller. Dilation will expand black region to recover the lost areas, however the connection between regions, which were disconnected in erosion will not be established again. The sequence of two processes allows separation of pores which are narrowly connected to each other while maintaining the size. Figure 2-6 shows a segmented SEM image following erosion and dilation. In both cases, a structure element of 3 x 3 pixels was used.

5) Pores sizes measurement by measuring areas in AW2 Scaffolds

These areas were the spaces (black) within the scaffold material (AW – white) representing pores sizes. The steps to extract and export pore sizes are below:

- Click on Analyse Particles > Show – Outlines (to see outlines)
- Click on Analyse the particles (to extract the area of each segmented region).

The results were analysed outside of ImageJ FIJI. The area of each pore with its index were saved in an excel sheet in metric units.

2.8.1 Histogram and Relative Frequency of pores

The pore size distribution has been presented as a histogram of the number of pores at specific size ranges, to further analyse the suitability of the scaffolds for bone cell growth. The relative frequency, Equation (1), of the pores can also be used to further study the distribution of pores within an acceptable range in greater detail. A bin is the range of values that divide the samples within a specific pore size range into a series of intervals. The bins are usually specified as consecutive, non-overlapping intervals, in this case referring to the pore size. Each bin includes the number of occurrences between *i* to *j*, where *i* is the first bin and *j* is the last bin the series.

The relative frequency can be calculated by normalising the number of pores with each size versus the total number of pores for the specific size range using the equation (1).

$$Relative\ Frequency\ = \frac{\text{Number of pores in each bin from } Bin\ i \text{ to } Bin\ j}{\sum_{Bin\ i}^{Bin j}(Number\ of\ pores\ at\ each\ bin)} \qquad (1)$$

Relative frequency is the number of values that fall into each bin (interval) divided by the total number of values or sum of values in all of the bins.

2.8.2 Evaluation Technique

Validation of image processing algorithm is necessary to establish the performance of the algorithm. The evaluation is performed qualitatively by comparing the output against the expected results by an expert or quantitatively by comparing the results of the algorithm on a known input and measuring the error in the outputs. The lower the error of the algorithm the better the accuracy. If the test is repeated and the error is stable, e.g., have lower standard deviation, the algorithm is considered to be more robust/reliable.

A reliable reference for evaluating the results of the algorithm is to use calibration samples of the SEM imaging instrument and comparing the results of the algorithm against the known size of the calibration circles. A calibration sample with six circles of different known sizes, 100, 200, 300, 500, 600 and 1000 µm, are used for this experiment, Figure 2-7.

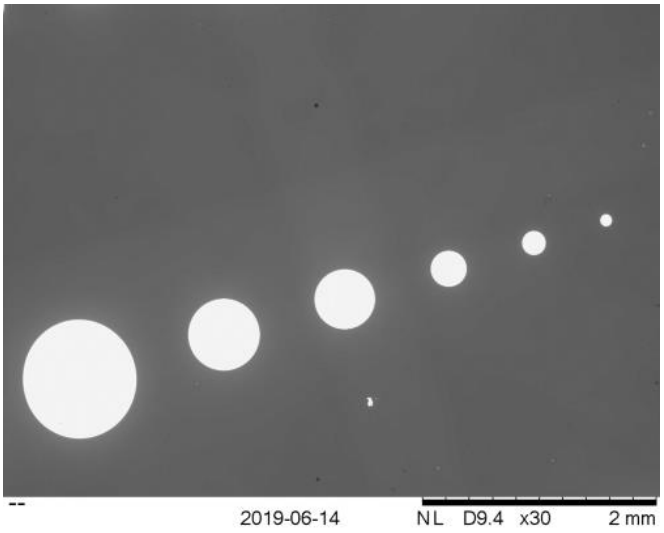

Figure 2-7: SEM image of calibration circles, scale bar represents 2mm

The error of algorithm (%) is measured by sum of errors for each of objects detected by algorithm against the real size given by the manufacturer, as shown in Equation (2).

$$Error\ (\%) = 100\ \frac{\sum_{i=1}^{N} \frac{(\text{size of } object\ i\ detected\ by\ algorithm - size\ of\ object\ i)}{\text{size of object i}}}{N} \quad (2)$$

The standard deviation of the error represents the robustness of the algorithm in measuring the size of calibration circles.

2.9 Archimedes' test for porosity measurement

Archimedes' principle uses an objects mass in air and in water to determine the density of the object; this can then be used in conjunction with other equations to determine the porosity of an object.

2.9.1 Archimedes' Protocol

The scaffolds mass (dry mass in grams) was measured on a density determining kit and precision balance (Kern ABT220-5D) prior to the Archimedes' analysis. The specialised piece of equipment, known as a density determinate kit, was used for these specific measurements. Figure 2-8 shows open and closed porosity in a schematic diagram of a scaffold. The mass (grams) of scaffolds submerged in a set volume (200 ml) of deionised water for a set duration of time (5 minutes) was then measured (submerged mass) on the precision balance. The scaffold was then removed from the water, left on absorbent material for 2 minutes (to remove excess liquid), and then the scaffold mass was measured again, this is known as the wet mass.

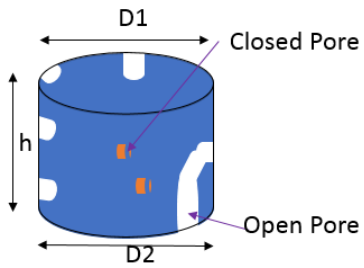

Figure 2-8 : Schematic diagram of a scaffold representing open and closed pores. Apparent volume is the combined volume of closed pores (orange) and scaffold material (blue).

2.9.2 Archimedes Calculations

The porosity of the scaffolds were measured based on Archimedes Principle as described in equations (3) to (9). The apparent volume is defined as the volume of material in the scaffold including the volume of closed pores, see Figure 2-8. This is calculated as the dry mass of the scaffold subtracted by the displaced water (submerged mass), which is then normalised by the density of water, (see equation (3)). Deionised water density is estimated to be 1 gcm^{-3}. This estimated water density value was used throughout in all calculations where water density was a factor.

$$Apparent\ Volume\ (cm^3) = \frac{\left(Dry\ mass\ (g) - Submerged\ mass\ (g)\right)}{water\ density\ (gcm^{-3})} \quad (3)$$

All scaffolds were a near cylindrical shape, and each one was considered as 'right circular conical frustum' or a 'truncated cone'. Digital callipers were used to take diameter measurements (*cm*) of the scaffolds at two end points of the scaffold, *D1* and *D2*. The average radius (*r)* was calculated using equation (4).

$$\boldsymbol{r} = \frac{D1 + D2}{4} \quad (4)$$

The volume of envelope (volume of cylinder) is defined as the volume of a scaffold including all of pores. It was calculated by taking the average radius (*r)* (equation (4)) and the height (h) of the dry scaffold in cm using callipers, these values were used in equation (5) to calculate the "envelope volume" of the dry scaffolds.

$$Envelope\ Volume\ (cm^3) = \pi r^2 h \quad (5)$$

The envelope volumes of the scaffolds (calculated volume of cylindrical scaffold) are particularly important for obtaining the bulk density of the scaffolds, which in turn aid in the calculation of the total percentage of pores within the scaffolds. Bulk density, or dry bulk

density, is defined as the material mass (AW2 powder) per volumetric unit. Equation (6) is used to compute bulk density.

$$Bulk\ Density\ (\ gcm^{-3}) = \frac{Dry\ mass\ (g)}{Envelope\ Volume\ (\ cm^3)} \quad (6)$$

In equation (6), the envelope volume includes the volume of material plus the volume of open and closed pores within the scaffold. The apparent density is defined as the density of the sample including the closed pores only. The apparent density of scaffolds can be computed using equation (7). AW2 powder density is given by the company [GTS] as 3.078 gcm^{-3}.

$$Apparent\ Density\ (gcm^{-3}) = \frac{Dry\ mass\ (g)}{Apparent\ Volume\ (cm^3)} \quad (7)$$

These calculations were exploited further to numerically estimate the total porosity of the scaffolds, equation (8), and estimate its open porosity using equation (9).

$$Estimated\ Total\ Porosity\ (\%) = \frac{(AW2\ Density - Bulk\ Density)}{AW\ Density}\ x\ 100 \quad (8)$$

$$Estimated\ Open\ Porosity\ (\%) = \frac{(AW2\ Density - Apparent\ Densiy)}{AW2\ Density}\ x\ 100 \quad (9)$$

2.10 Assessment of nutrients diffusion by 2-NBDG Glucose uptake test

The light sensitive glucose solution was prepared using 2-(N-(7-Nitrobenz-2-oxa-1,3-diazol-4-yl)Amino)-2-Deoxyglucose) (Fischer Scientific, UK), known as a 2-NBDG glucose uptake test, diluted in Phosphate Buffered Saline (PBS) to obtain a concentration of 0.06845 mg ml^{-1} (da Conceicao Ribeiro et al., 2018). To assess the uptake over time, the scaffold samples were placed into 24-well plates and labelled according to the time-points chosen (4-hours, 8-hours and 24-hours). As the scaffold samples chosen were approximately 8 mm in height, 1.5 ml of the 2-NBDG solution was added on top of each sample (to ensure that each scaffold was fully immersed in the yellow solution). The time it took the scaffolds to become yellow by solution

absorption was recorded (in seconds), the plates were then covered with foil and placed into the fridge until the set time-point was achieved. At each set time-point, the scaffolds were carefully removed from the yellow solution using precision tweezers, air dried for approximately 10 seconds to allow for any excess solution to drip off the sample. The sample was then placed into a new well that was pre-filled with 1.5 ml of PBS to release the absorbed 2-NBDG, this plate was also covered with foil and placed into the fridge. After 24-hours in the PBS solution, 100 µl (x3) of this solution was placed into 3 wells (of a 96-well plate). The plate containing the solution was analysed using fluorescence spectroscopy at an excitation emission of 465/540 nm using a Microplate reader (BMG Labtech, FLUOstar Omega). As a blank control, a scaffold was immersed in PBS solution for 24 hours, and its excitation was read.

A calibration curve is required to link fluorescence levels measured to relative glucose concentration. The curve is used as a reference to estimate glucose concentration in a sample (uptake or release) based on its fluorescence. To obtain this curve; 100 µl the 2-NBDG solution at 0.06845 mg ml^{-1} was placed into a well of a 96-well plate. A serial dilution was carried out and readings were taken at an excitation emission of 465/540 nm using the microplate reader. Again, as a blank control, wells containing only PBS were also read.

To obtain average fluorescence values, all samples were carried out in triplicate and each sample was analysed in triplicate to obtain an average reading. The values obtained from the PBS wells (blank) were subtracted from the values that included 2-NBDG solution. A mean was acquired from the values and the graphs plotted, using the relevant software a trendline was added, the R^2 value calculated, and the equation of the line also given. The calibration curve was used for reference to determine glucose concentration.

2.11 Compression test for mechanical properties evaluation

To understand the mechanical properties of the heat-treated scaffolds, a compression test was undertaken using a Shimadzu Compression Tester (Shimadzu Corporation, 2014 model AGS-X with 10kN load cell). Compressive strength and young modulus can be derived from the compression test. The scaffolds were subjected to minimal surface grinding to obtain parallel surfaces on the slightly conical frustum shaped scaffolds. The scaffold diameters were measured on both sides and the height was measured using a digital calliper. The parameters were a crosshead rate of 0.5 mm min^{-1}, with a load cell up to 10 kN for porous scaffolds

(scaffolds sintered < 1240°C). The scaffolds that were considered to be fully sintered 'dense' scaffolds were subjected to a load cell up to 100 kN. The experiment was performed with care and stopped immediately if a scaffold went under failure.

The average dimensions of the scaffolds were calculated using the average height and diameter. Equation (10) was used to calculate the average diameter (mm), D1 represents the smallest diameters recorded (the 'top' of the scaffold), and D2 represents the widest diameters (mm) of the scaffold (the 'bottom' of the scaffold). D1 and D2 were each measured at 5 points of the scaffold and the average used in equation (10).

$$D_{avg} = \frac{D_1 + D_2}{2} \qquad (10)$$

The average height (mm) was calculated by taking measurements across 5 different points of the scaffold and averaging them.

Stress and Strain are computed using Equations (11) and (12). The Δh refers to the change in the height of the scaffolds due to stress, and h0 is the initial height, strain is given as a percentage.

$$Stress\ (MPa) = \frac{Applied\ Force\ (N)}{Cross\ Sectional\ Area\ (mm^2)} \qquad (11)$$

$$Strain\ Percentage\ (\%) = \frac{\Delta h}{h0}\ x100 \qquad (12)$$

Young's modulus (equation (13)) is calculated from the initial linear slope (before the breaking point) of the graph at the early stage of compression (stress, strain) graph. The Young's modulus, E, is calculated as the slope of the curve before breaking point using equation (13):

$$E\ (MPa) = \frac{Stress\ (MPa)}{Strain}\ x100 \qquad (13)$$

2.12 Statistical analysis

All graphs show a mean of 3 samples unless stated otherwise. All error bars are ± standard deviations, unless stated otherwise. Using GraphPad Prism, SPSS software or Microsoft Excel, One-way ANOVA was used with a Tukey's post-hoc test, $p \leq 0.05$ was considered to be statistically significant correlating to * symbol, $p \leq 0.01$ is denoted by **, $p \leq 0.0001$ is denoted by ***.

3 Results

3.1 Cloud point

The cloud point temperature (°C) for different PLA concentrations (w:v) for a range of dioxane:water concentrations (v:v) was experimentally measured. The experimental result (n=1) is shown in Figure 3-1. The general trend of temperature for various PLA concentrations appears to correlate with increasing levels of water in the dioxane:water solution. However, there are some fluctuations in the values.

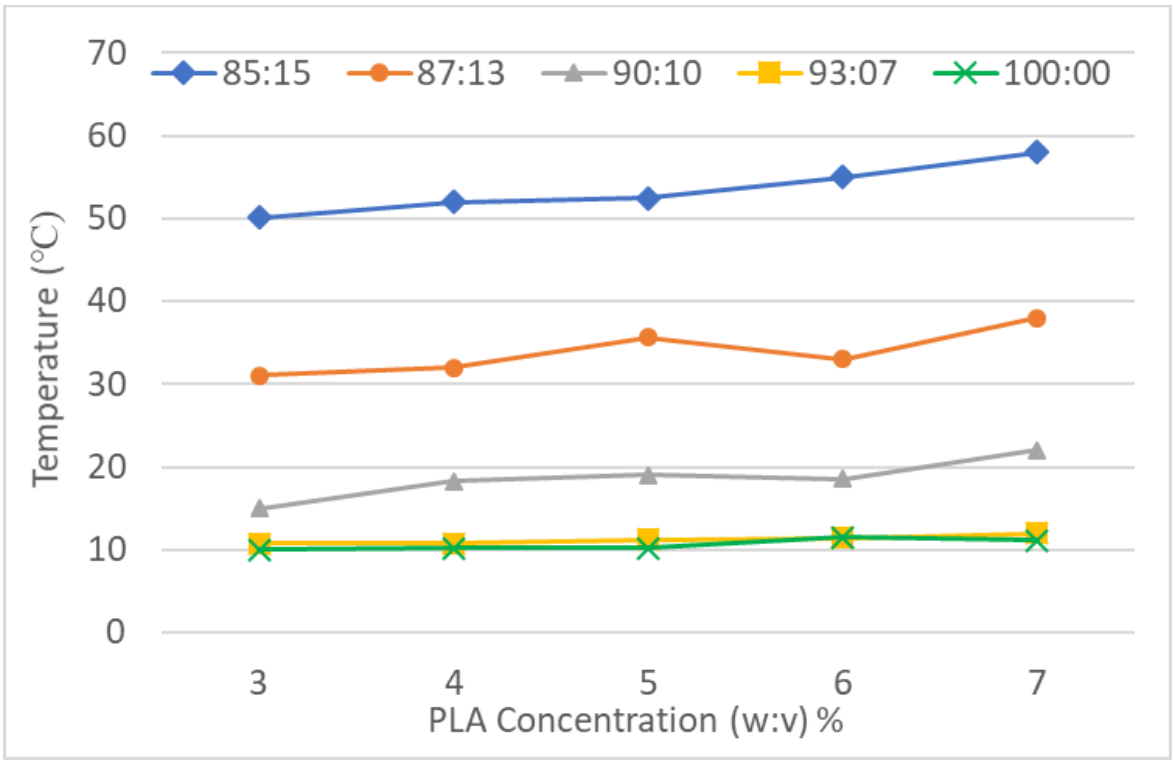

Figure 3-1: Temperature of cloud point with respect to different PLA concentrations and dioxane:water concentrations. N=1.

The degree of temperature change for dioxane:water in the following ratios: 90:10, 93:07 and 100:00 appears to be less evident. In 85:15 the temperature fluctuation (increase) is most evident at 7% PLA.

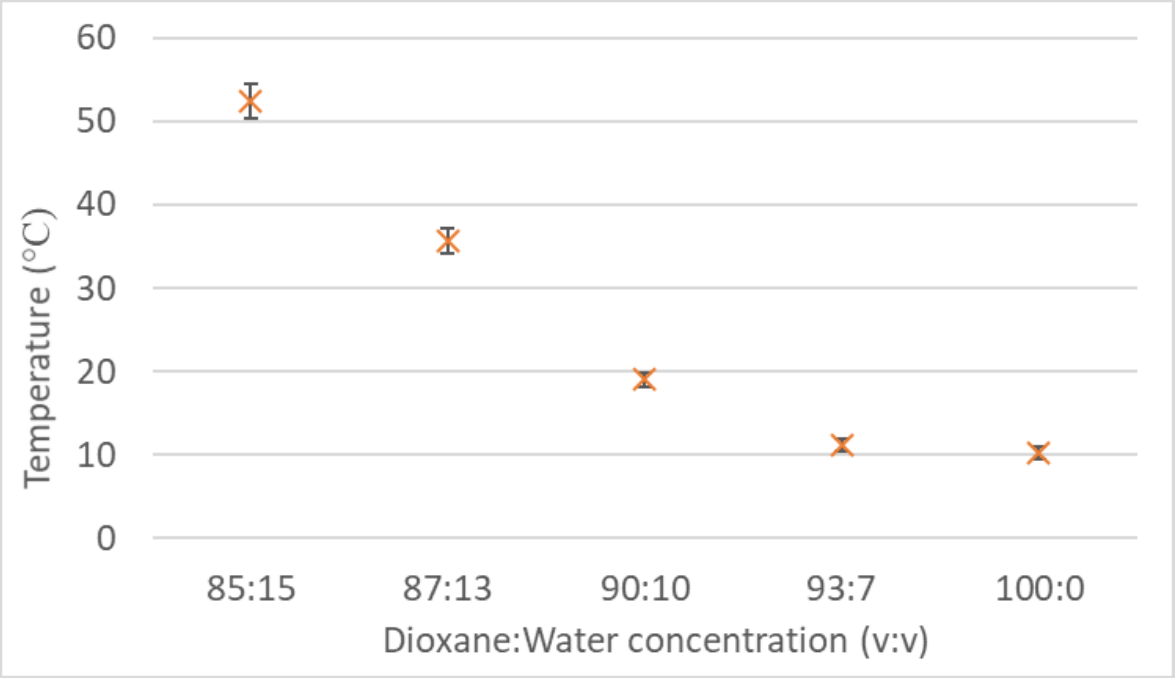

Figure 3-2: Graph of mean cloud point temperature versus Dioxane:Water (v:v) ratio with 5% PLA. Error bars represent standard deviations, N=5.

The concentration of 5% PLA was chosen in agreement with a comprehensive experiment reported in (Toumpaniari, 2016). The behaviour of 5% PLA in different dioxane:water concentrations to determine the cloud points is presented in Figure 3-2. The cloud point graph was used to optimise the manufacturing process for the AW2 scaffolds in this study. The results of the experiments, shown in Figure 3-2, identified a correlation between ratio of water to dioxane and cloud point. An increase in the water in dioxane:water resulted in a rise in the cloud point temperature. At 93:07 and 100:0, cloud point was reached at dioxane's freezing point temperature of between 10 - 12°C. There is a notable difference in the cloud point at dioxane:water 85:15 (52°C) and 100% dioxane (10°C), which indicates that the volume of water significantly effects the cloud point temperature.

3.2 Hot Stage Microscopy

The variations of AW2 glass ceramic shrinkage as a function of increasing temperature can be quantitatively evaluated by considering the sintering curve of AW2 powder particles with sizes between 20 – 53 µm, generated by temperature-controlled Hot Stage Microscopy (HSM). The sintering curves (Figure 3-3 and Figure 3-4) show the percentage change in area of the AW2 sample during thermal treatment.

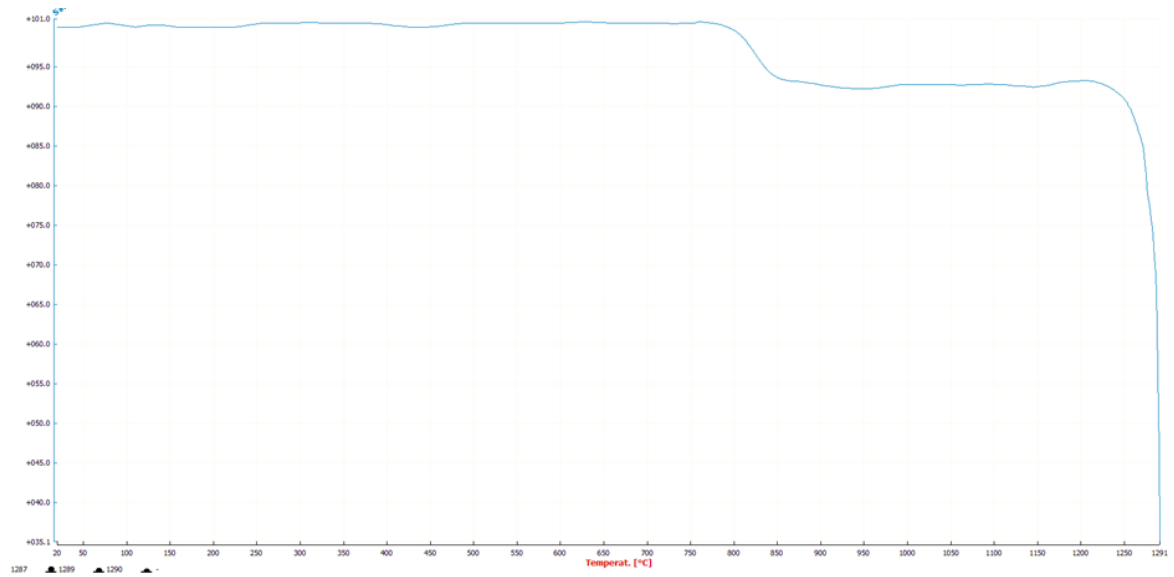

Figure 3-3: Graph shows sintering (%) of 20-53µm AW2 powder in relation to Temperature (°C) using Hot Stage Microscopy. This graph is from the Misura software and is a sample representative of 4 repeats. Standard deviations are not shown for visual simplicity.

The key thermal events representing the main behaviour of AW2 samples during the experiment include shrinkage temperature intervals (TS1 and TS2), the shrinkage amount (S1 and S2 at TS1 and TS2 respectively), and melting temperature interval (TM). These events are identified in the plotted curves of Figure 3-3 and Figure 3-4, and summarised in Table 3-1.

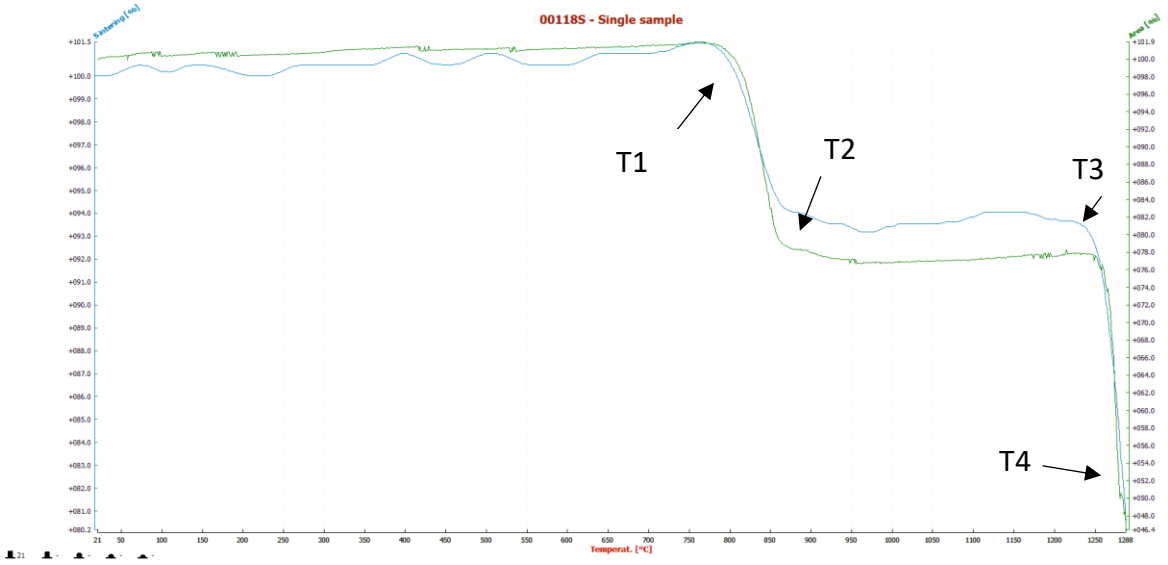

Figure 3-4: Hot Stage Microscopy Graph representing the sintering percentage (in blue) and percentage change of area (in green) of AW2 particles at 20-53µm versus temperature (°C).

Figure 3-4 shows the HSM curves for sintering (%) and the area (%) relative to temperature (°C). These curves were obtained using Misura software via the silhouettes of the AW2 powder samples as shown in Figure 3-5. This graph was also used to determine the significant temperature events reported in Table 3-1.

Generally, as the temperature increases, the sintering (%) and area of the AW2 sample (%) decrease. The HSM graph (Figure 3-4) represents the sintering percentage (in blue) and percentage change of area (in green) of AW2 particles with a size range of 20 – 53 µm versus temperature.

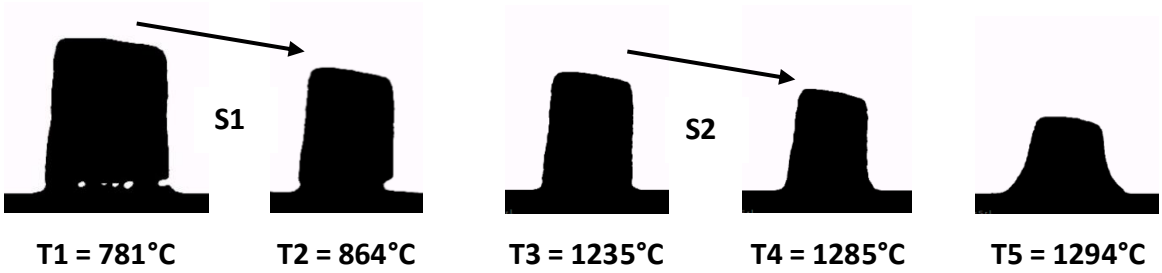

Figure 3-5: Hot Stage Microscopy images of cylindrical AW2 samples at different characteristic thermal events (represented as T1, T2, T3, T4, T4, T5). Arrows show sintering events.

Figure 3-5 shows the changes in the AW2 sample cylinder silhouettes from the HSM. The main thermal events are labelled, and changes are indicated with arrows. The silhouettes reduced in size between T1 to T2 (S1), and T3 to T4 (S2), the respective values with standard deviations are given in Table 3-1. The melting event is represented as T5 in Figure 3-5, and as TM in Table 3-1.

Samples	TS1 (°C)	S1 (%)	TS2 (°C)	S2 (%)	TM (°C)
AW2	780 ±9 - 864 ±14	5.8 ±1.3	1235 ±5 – 1285 ±2.5	11.7 ±1.7	1294 ±3.5

Table 3-1: Summary of thermal events derived from the Hot Stage Microscopy curves of AW2 powders. Values are averages with respective standard deviations. N=4.

The HSM results show the sintering behaviour in the AW2 sample, and can be explained in the following stages:

1) The rectangular silhouette as shown on the Misura program (Figure 3-5) retains its shape up until the first shrinkage temperature interval (T1) is reached (at approximately 781 ±9 °C).
2) The first shrinkage interval (shown as TS1 in Table 3-1) between 781 ±9 °C and 864 ±16°C (T2) results in a shrinkage (S1) of 5% as shown in Table 3-1.
3) A plateau was observed between T2-T3 (from 864 ±16 to 1235 ±5°C).
4) The second sintering event (TS2) onset was at 1235 ±5°C to 1285 ±2.5°C (T4) with a shrinkage (S2) of 11.7% ±1.6%.
5) The melting temperature (TM) could be seen by the rapid distortion of the sample silhouettes, at this point the experiment was stopped manually. The AW2 melting temperature was approximately 1294°C.

3.3 Sintering temperature optimisation

PLA (5%) was used in the production of the AW2 scaffolds (as described in methods section 2.3.4), which was burnt out during step 1 of the two-step heat treatment process, and thus a mass change of at least 5% was expected. The standard deviations in mass change were very low across all scaffolds. One-way ANOVA showed that there is high statistical significance between all of the scaffolds; the statistical significance was $p < 0.0001$ (***).

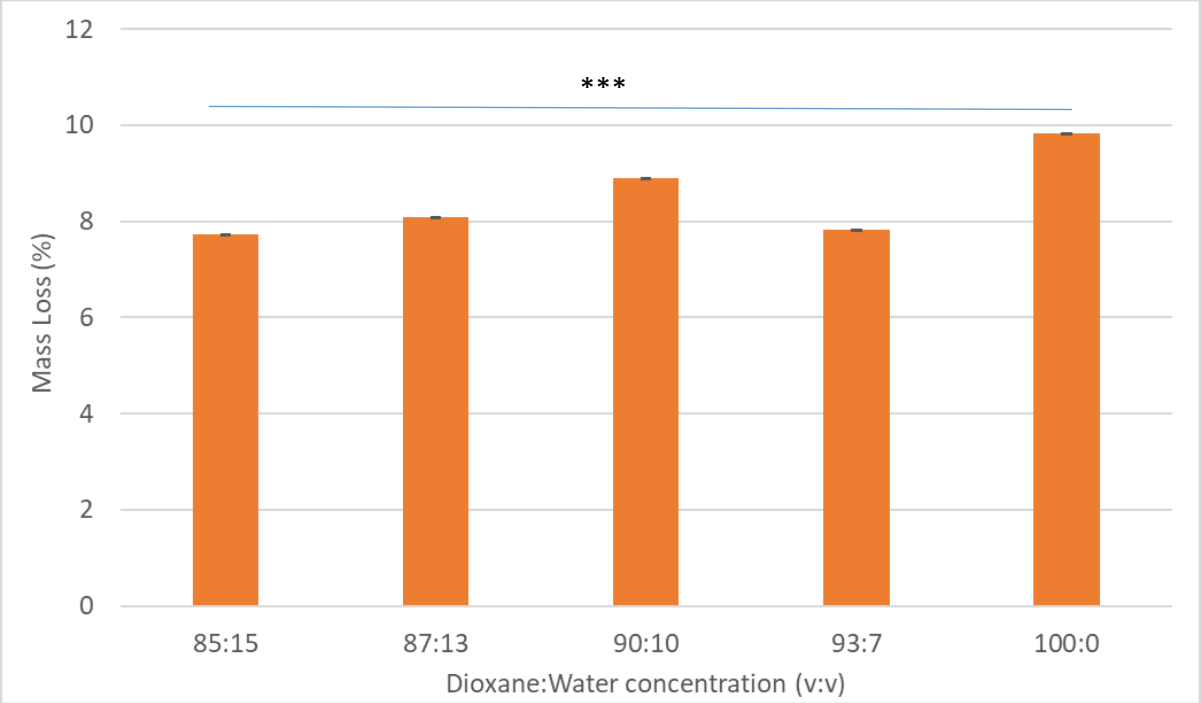

Figure 3-6: Mean mass loss after two-step heat treated scaffolds as a percentage (%). Error bars represent standard deviations. $p < 0.0001$ (***). N=5.

Figure 3-6 shows the percentage (%) of mass change for the scaffolds from a freeze-dried state, to after sintering (heat treatment), with a change identified between 7.7% to 9.8%, which is in line with the methodology. The highest loss of mass for scaffolds was at 90:10 and 100:00 dioxane:water concentrations.

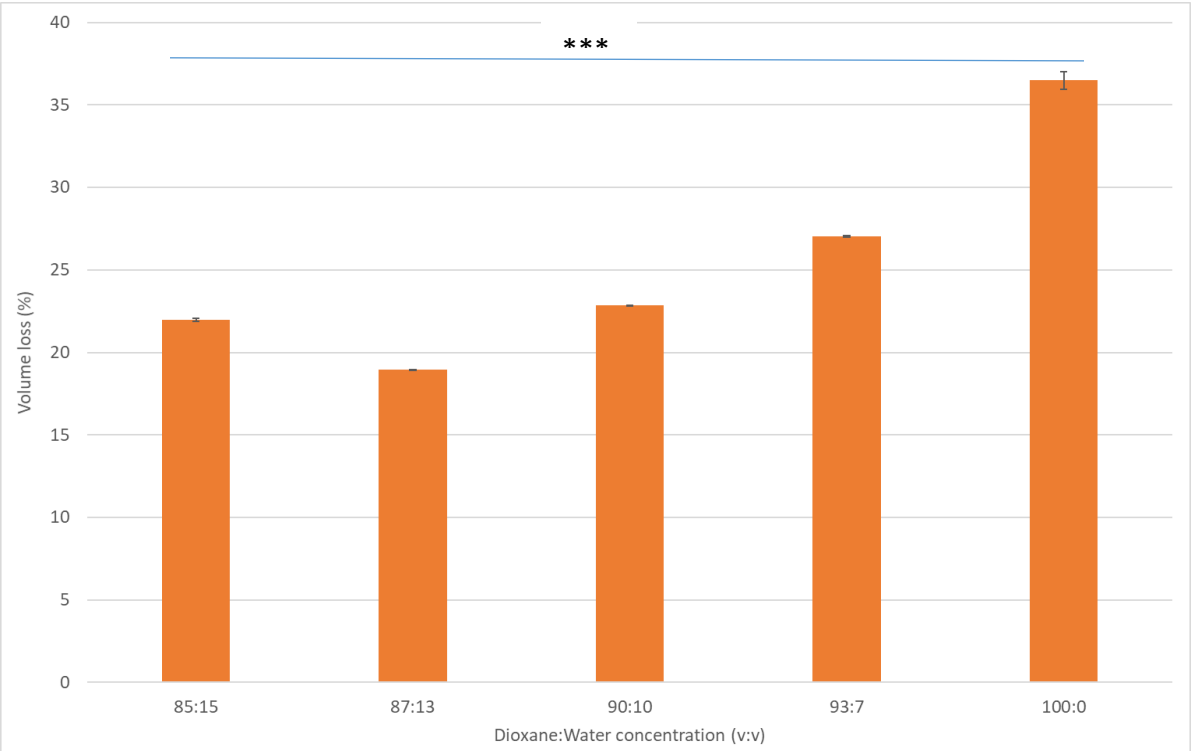

Figure 3-7: Mean volume loss of scaffolds after two-step heat treatment as a percentage (%). Error bars are standard deviations. $p < 0.0001$ (***). All scaffolds underwent the two-step heat treatment. N=5.

Figure 3-7 shows the volume shrinkage from freeze-dried scaffolds to post sintering, the most shrinkage was noted at 100:00, and the least shrinkage at 87:13 dioxane:water concentrations. The standard deviations are very small across all scaffolds with different dioxane:water concentrations. The results show that there is not an overall trend towards predicting volume shrinkage of scaffolds regarding dioxane:water ratios.

3.4 SEM Imaging of sintered scaffolds

The scaffolds were fabricated using the method described in Section 2.3.4, and SEM images were acquired for each of the scaffolds. Figure 3-8 shows sample SEM images of scaffolds (dioxane:water concentrations, 85:15, 87:13, 90:10, 93:07 and 100:00) fabricated with a two-step heat treatment, with 1235°C sintering temperature. There is necking visible between the particles at all the different concentrations. Pore size variations are noted as the dioxane:water concentrations differ.

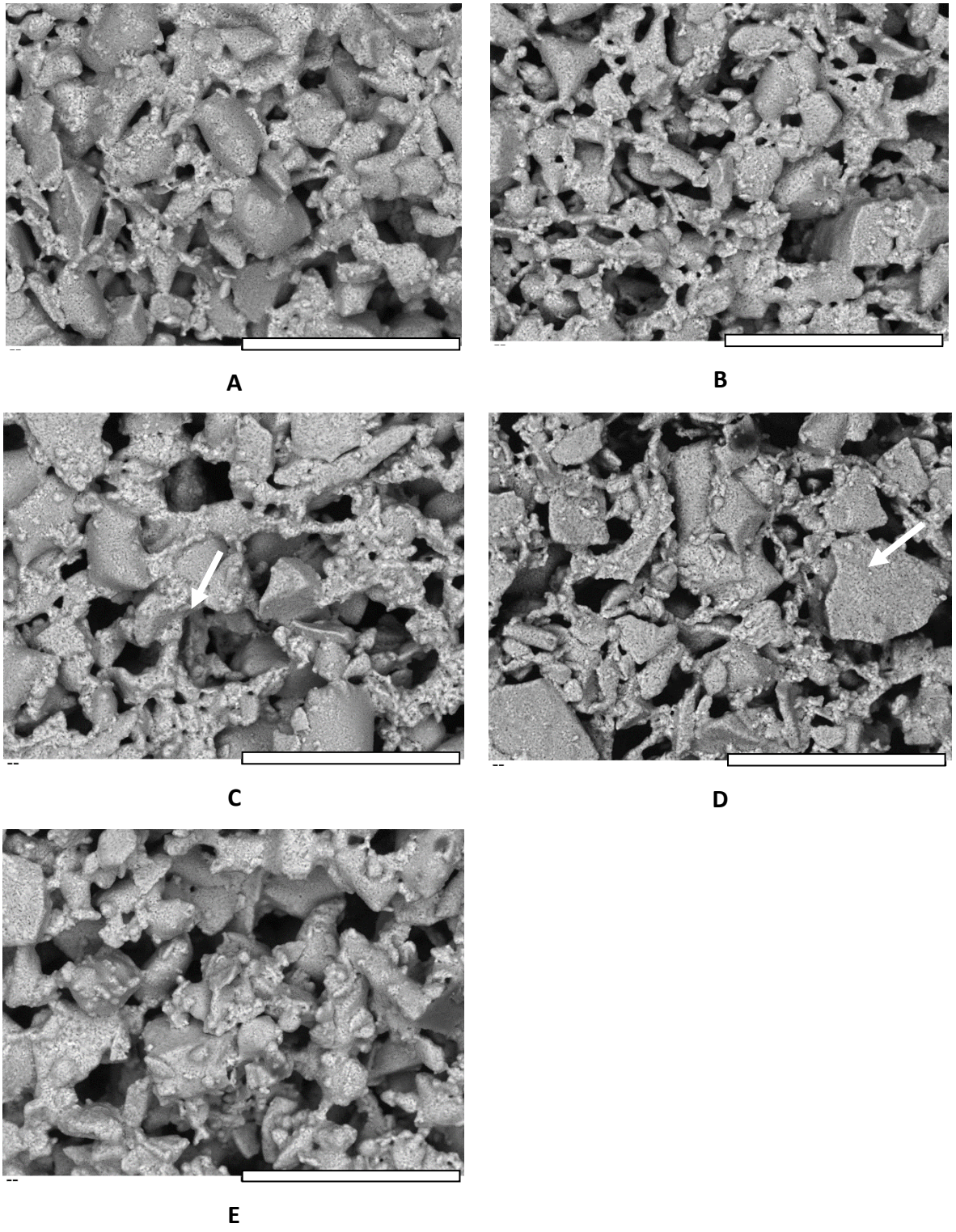

Figure 3-8: Scanning Electron Microscopy Image of scaffolds after two-step heat treatment, scale bars representative of 100µm. A) Dioxane: Water 85:15, large AW particles visible. B) Dioxane: Water 87:13 some porosity can be seen. C) Dioxane: Water 90:10 large pores visible and interconnections can be seen (arrow). D) Dioxane: Water 93:07 large AW particles can be seen (arrow). E) 100% Dioxane, pores are visible.

The scaffolds at 90:10 have the most open pores and larger in size. Handling stability was determined from 1220°C and above. Scaffolds at 1250°C were obtained, but they were attached to the platinum foil and had minimal porosity. This indicates that these temperatures are too high to obtain scaffolds of suitable pore sizes, a further problem was their stability and handling difficulties.

3.4.1 Evaluation of SEM Image Analysis Algorithm

SEM images of the standard calibration sample was used for evaluation of the image processing algorithm describes in Section 2.8. The algorithm was applied on the sample image which had circles of varying sizes and the results were analysed to represent the percentage (%) difference of the detected area against the real area of the circled supplied by the manufacturer. This process was repeated 5 times to generate the standard deviations of the error.

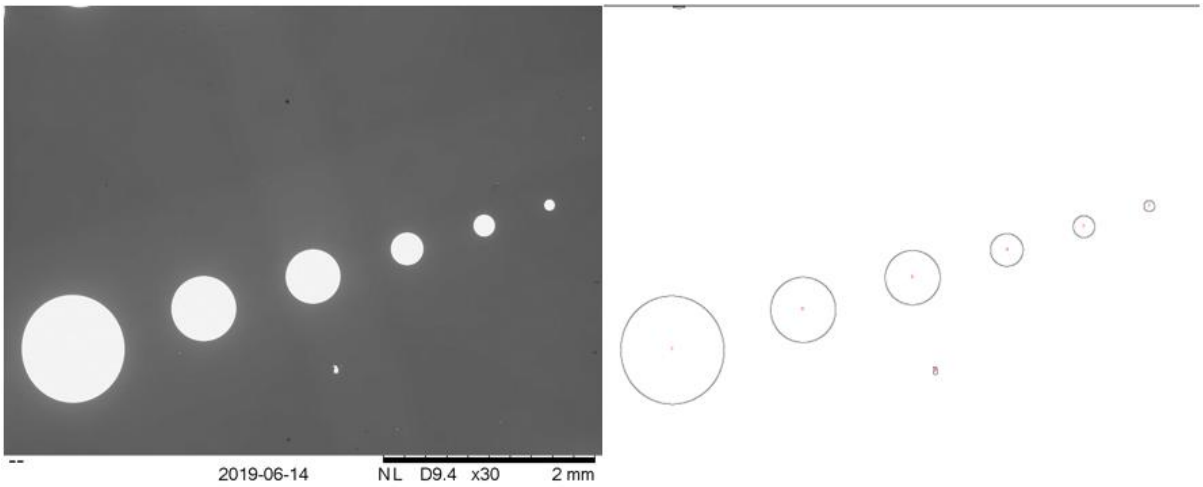

Figure 3-9: Calibration standard with 6 different circles of known dimensions. A) SEM image, B) Detected circles using the SEM image analysis algorithm.

Figure 3-9 shows the original SEM image of the standard calibration sample, and a sample result using the algorithm. Due to limited resolution of the SEM imaging, there will always be a slight error at the boundary of the image.

Figure 3-10. Magnified results of SEM image analysis for two of the circles.

The calibration circles shown in Figure 3-10 shows the different outcomes of the boundaries of the two circles. Circle number 3 has a symmetrical boundary as opposed to circle number 4 which shows an asymmetrical boundary. This represents that the size of circle number 3 is measured more accurately than circle number 4.

	Average	**Standard Deviation**
Percentage Error (%)	-1.36	2.29

Table 3-2: Percentage (%) Error of Image Analysis Algorithm applied on calibration standards image, N=5.

Table 3-2 shows the results of percentage (%) error of the detection algorithm against the true dimensions provided. The result is concluded over running the algorithm 5 times, and computing the average and standard deviation of the percentage (%) error using the equation (2). The results show that on average the size of the circles detected by the algorithm is 1.36% smaller than their real size. This represents that the algorithm the size reported by the algorithm are smaller than the real size. The standard deviation of 2.29% represents the variation of the detected circles which is partially due to the digitization effect and the resolution of the image which was 4.4 µm per pixel.

3.5 Porosity and Imaging Results

Archimedes' density calculations, as described in Section 2.9.2, was used to measure the Total porosity, Open porosity, and Closed porosity of the AW2 scaffolds.

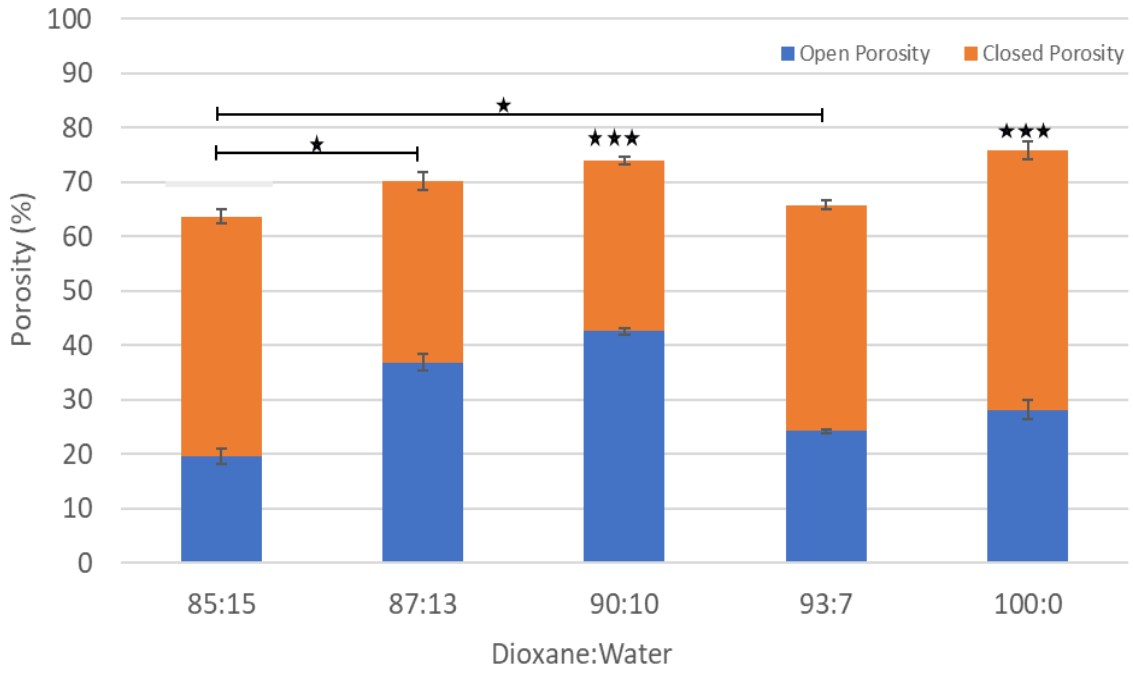

Figure 3-11: Graph of mean open porosity (%) and mean closed porosity (%) of scaffolds at different dioxane: water ratios. All scaffolds were sintered at 1235 °C. Open porosity is represented at the base of the graph in blue, the closed porosity is represented in the top section as orange. Statistical significance was determined at $p < 0.05$ (*) and $p < 0.0001$ (***) for open porosity. Mean values are shown with standard deviation, N=3.

Figure 3-11 shows that the total porosity for all of scaffolds were above 65%. Two groups of scaffolds (90:10 and 100:00) showed the highest total porosities of 74% and 75.8% respectively. Open porosity was the highest in scaffolds manufactured in 90:10 (dioxane: water), which also has one of the highest total porosities. High closed porosity was present in 100:00 (dioxane:water) scaffolds. Open porosity indicates interconnected pores within the scaffolds. Each of the scaffolds labelled with *** identify open porosity that is statistically significant with p-value <0.0001 against all the others. The other three scaffolds comprised of an open porosity with a statistical significance of $p < 0.05$ (*).

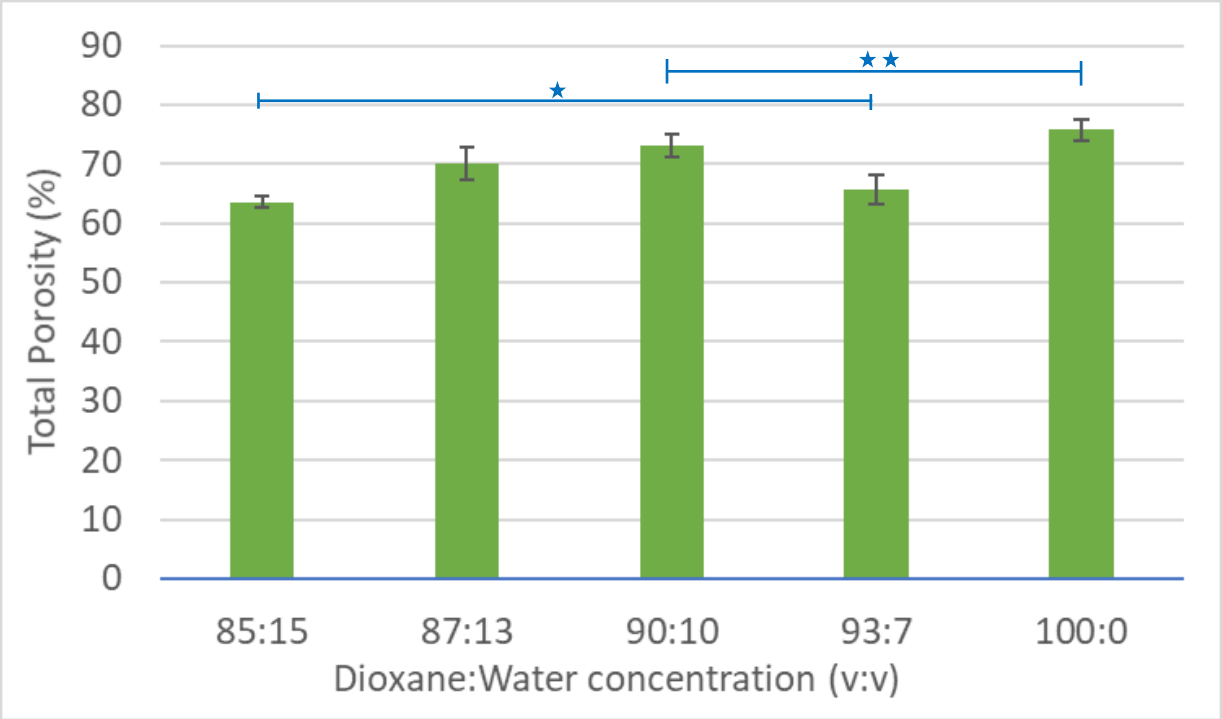

*Figure 3-12: Total porosity (%) within the scaffolds manufactured at different concentrations of dioxane:water. For all cases ($p<0.0001$, ***) apart from two cases shown on the figure with (*) or (**). Mean values are shown with standard deviation, N=3.*

Figure 3-12 demonstrates the total porosity calculated within scaffolds manufactured at different dioxane:water concentrations. All scaffolds are between 60% and 76% porous. One-way ANOVA indicated that dioxane:water concentration had a significant influence on the total porosity (%) of all the scaffolds, was a minimum significance of $p<0.05$ (*) to $p<0.0001$ (***). Cases with (*) or (**) are shown in the figure.

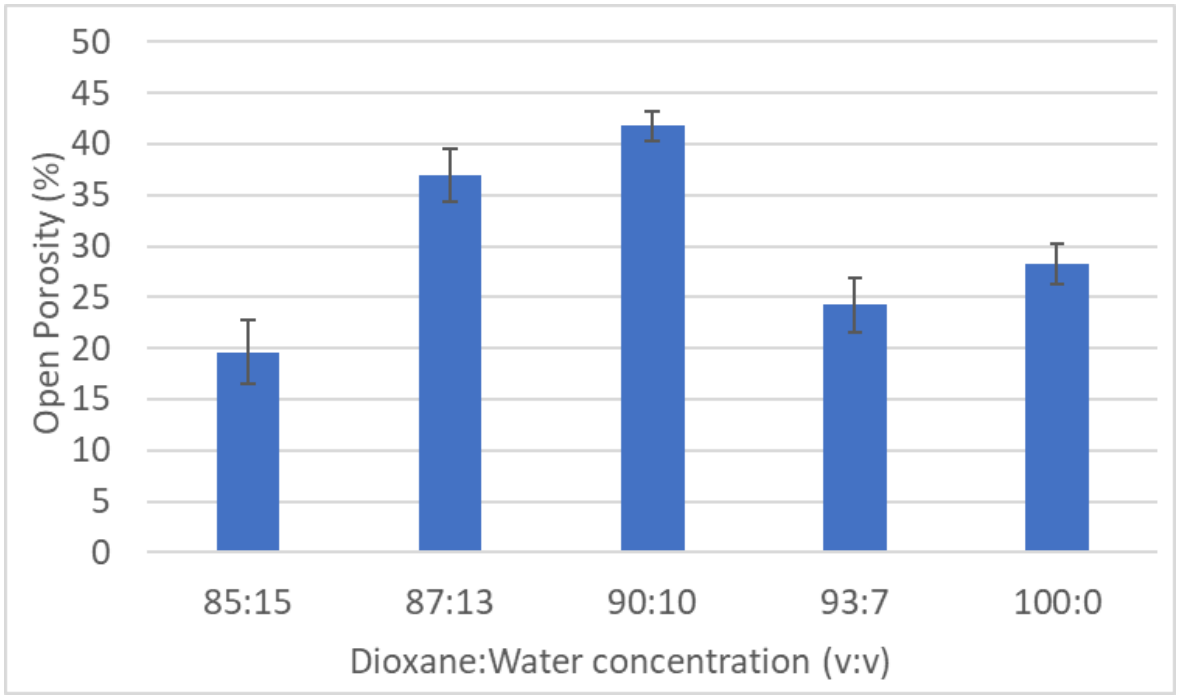

*Figure 3-13: Open porosity (%) within the scaffolds manufactured at different concentrations of dioxane:water. ($p<0.0001$, ***). Mean values are shown with standard deviation, N=3.*

Figure 3-13 demonstrates the open porosity of scaffolds manufactured at different dioxane:water concentrations. The open porosities vary from the lowest open porosity in 85:15 at 19.6% ±3.1% to the most open porosity in 90:10 at 41.8% ±1.43%.

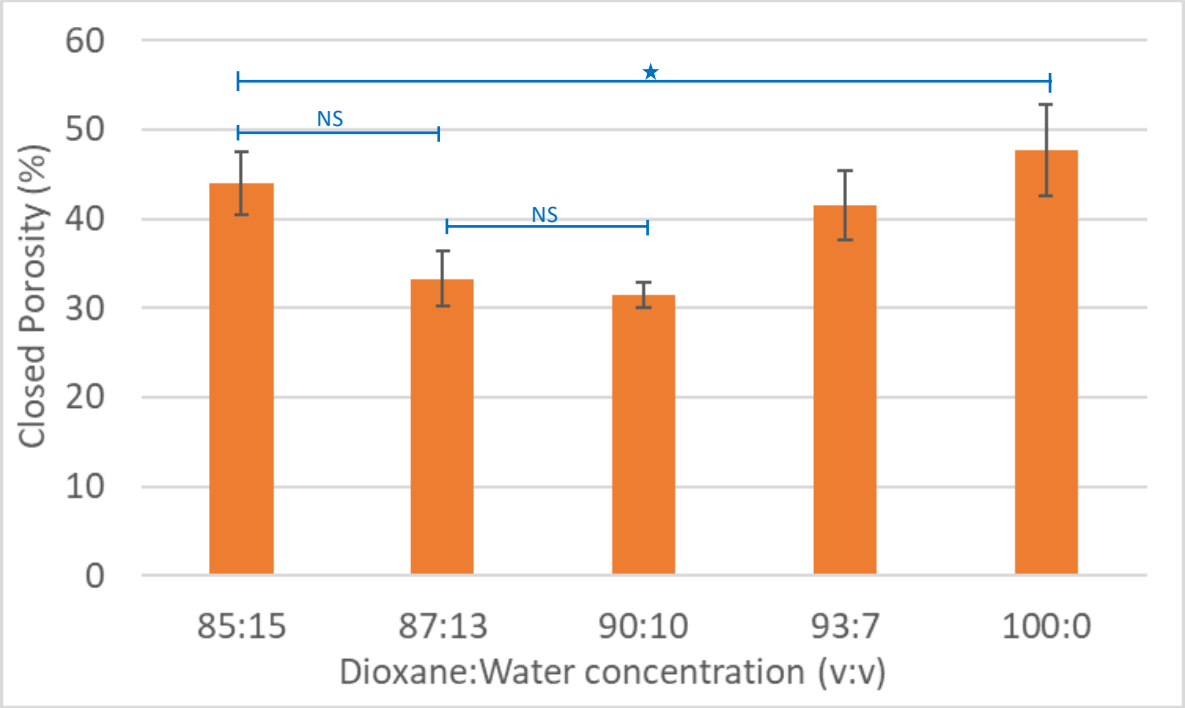

*Figure 3-14: Closed porosity (%) within the scaffolds manufactured at different concentrations of dioxane:water. For all cases ($p<0.0001$, ***) apart from the cases shown on the figure as not statistically significant (NS) or $p<0.05$ (*). Mean values are shown with standard deviation, N=3.*

Figure 3-14 demonstrates the closed porosities within the scaffolds manufactured at different dioxane:water concentrations, the scaffolds manufactured with 90:10 dioxane:water concentration had the lowest closed porosity at 31.4% ±0.7%, the scaffolds manufactured at 100:0 dioxane:water had the most closed porosity at 47.6% ±1.65%.

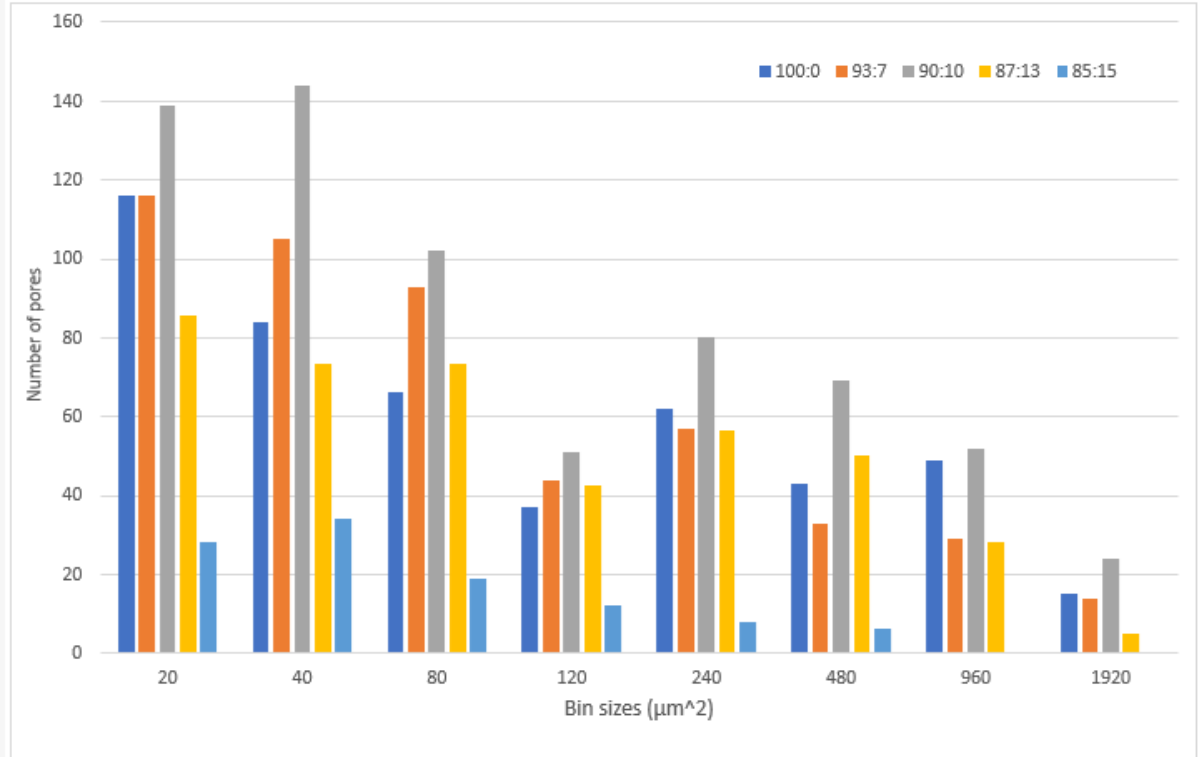

Figure 3-15: Distribution of pores for a different range of pore sizes, 10 - 1920 µm^2. Sizes below and above these ranges are excluded. All varieties of scaffolds and their bin ranges have significance against each other $p < 0.05$ (*). For readability, the ANOVA is not included on the graph. N=3.

Figure 3-15 shows the distribution of pores within different scaffolds manufactured using the two-step heating process with final temperatures in step 2 at 1235°C, for 1 hour. Scaffolds manufactured with 90:10 (dioxane: water) consistently have the highest number of pores at each bin size range. The lowest number of pores were found in scaffolds 85:15 (dioxane: water), which makes these scaffolds the most undesirable for cell growth. Pore sizes under 10 µm^2 are excluded from this graph, as they are not suitable for cell attachment, however, they play an important role for transport of nutrients and waste removal.

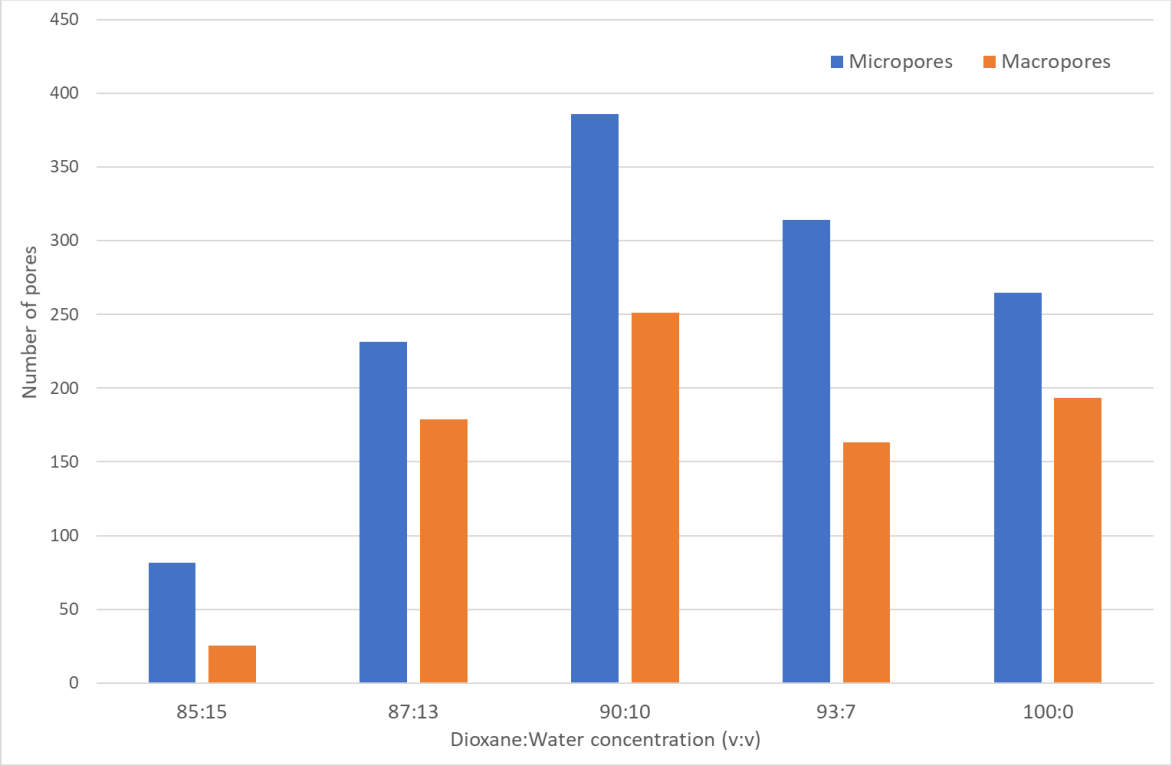

Figure 3-16: The average number of pores using SEM and image analysis technique. The micropores (blue) represent pores with sizes up to 80µm, the macropores (orange) represent pores of between 80 – 960 µm. N=3.

Figure 3-16 indicates the number of micropores (10 – 80 µm) and macropores (80 – 960 µm) within the scaffolds manufactured with different dioxane:water concentrations (v:v). The scaffolds manufactured with 90:10 (v:v) had the highest number of macropores and micropores amongst the group. The scaffolds manufactured with a ratio of 85:15 (dioxane:water) had the lowest number of micropores and macropores. All the scaffolds had higher numbers of micropores compared to macropores, therefore the number of smaller pores were more predominant in the scaffolds.

3.6 Nutrient Diffusion – 2NBDG

The calibration curve was used to determine the percentage of glucose released from the scaffolds. The values for 50% and 100% glucose have been omitted as they are not relevant to this study.

$$y = 14.48\,x \tag{14}$$

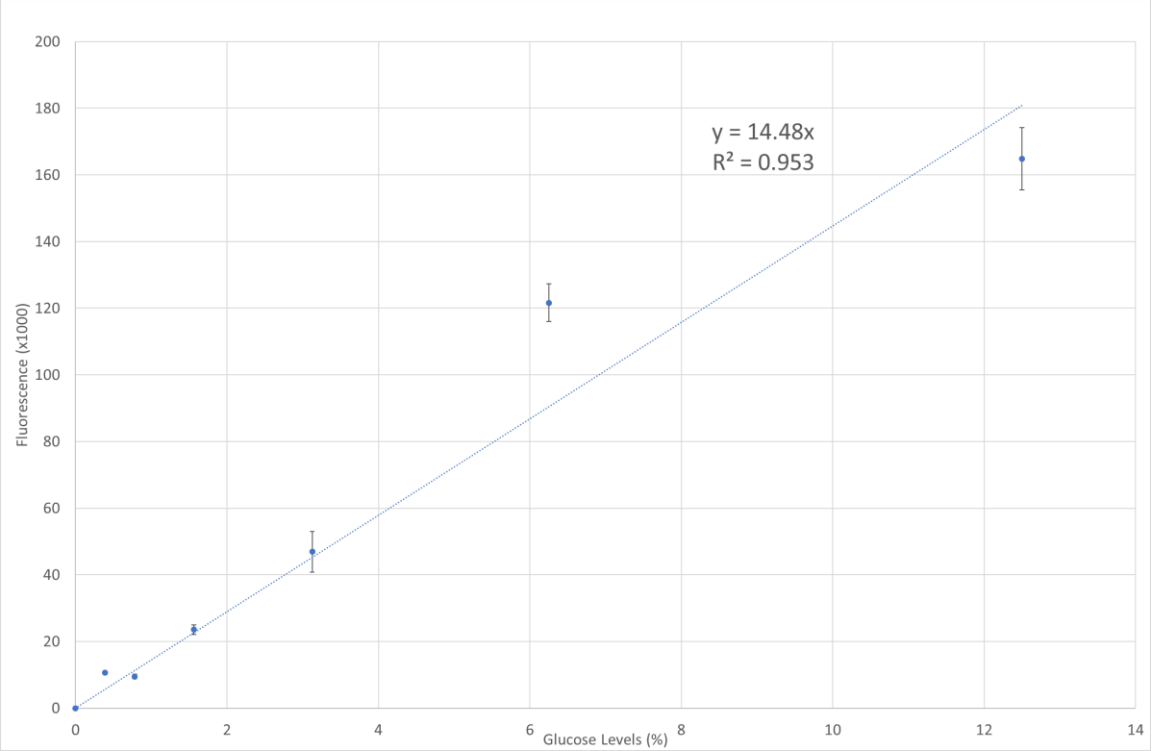

Figure 3-17: Calibration curve of 2-NBDG at different glucose concentrations. R^2 value is 0.95, mean values are shown with standard deviation, N=3.

The calibration curve (Figure 3-17) is considered to be linear, and equation (14) can be derived from the data. During experimentation the scaffolds became homogeneously yellow very fast (within seconds). After immersion in PBS for the set time, the scaffolds still remained yellow in hue, visually indicating slow release of the yellow 2-NBDG solution.

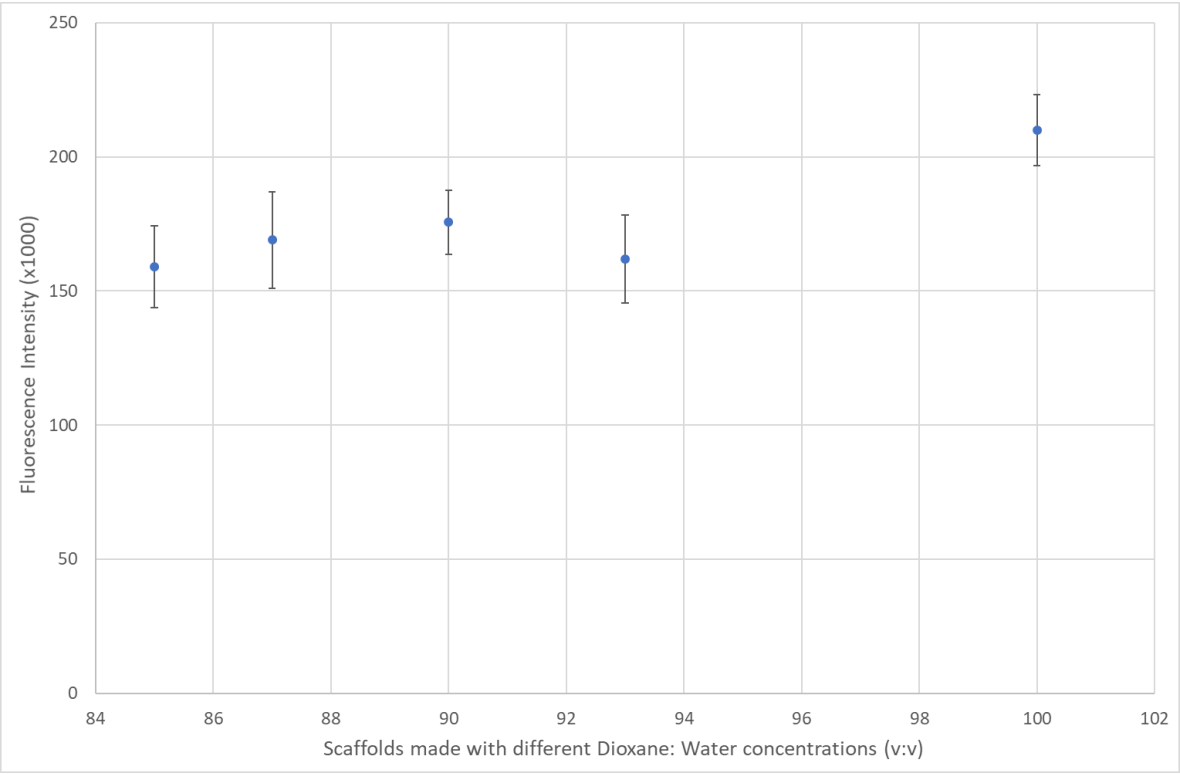

Figure 3-18: The fluorescence values obtained from the different scaffolds made with different dioxane:water concentrations, mean values are shown with standard deviation, N=3.

The fluorescence intensity (Figure 3-18) ranged from 159 to 210, and the calibration equation (14), was used to calculate the percentage of glucose released (Figure 3-19).

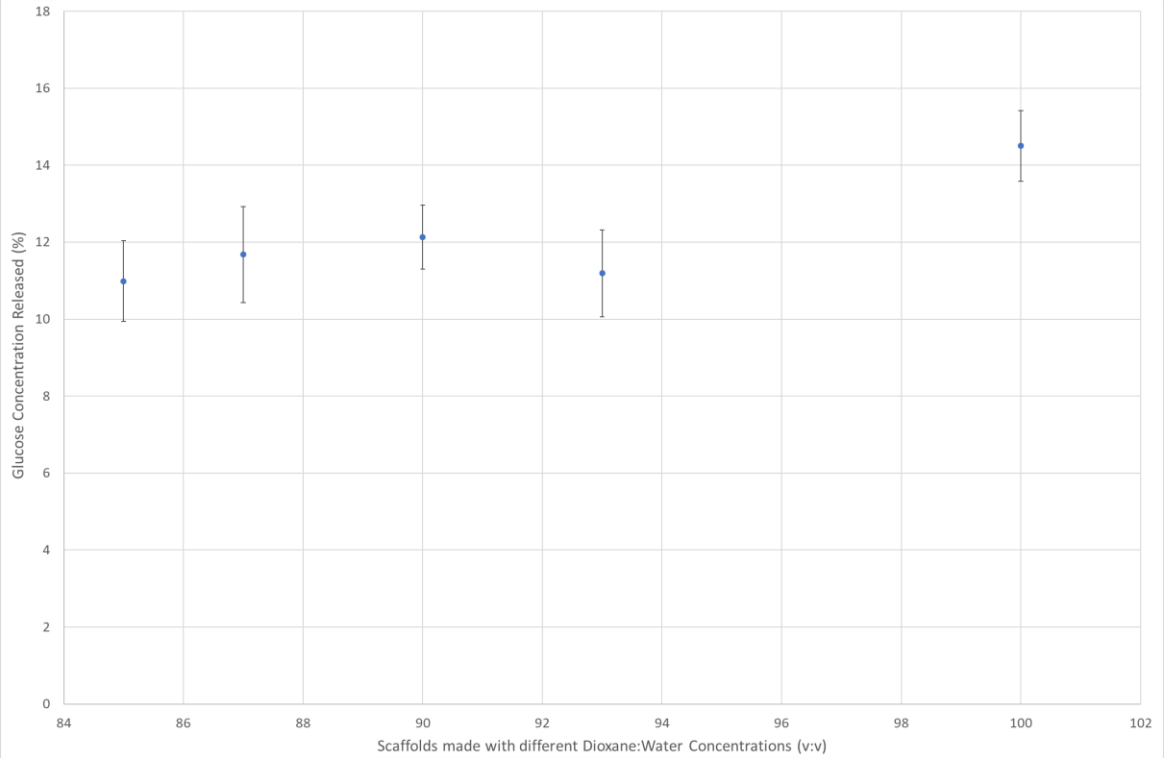

Figure 3-19: Graph of the Glucose released from the Scaffolds after 24-hours in PBS as a percentage (%), mean values are shown with standard deviation, N=3.

Figure 3-19 shows the calculated percentage of glucose released, the values fall between 11.0% – 14.5%. The scaffolds manufactured with 100% Dioxane, have the highest glucose release at 14.5% ±0.9 (STD).

3.7 Mechanical Properties – Compression

A sample stress against strain graph from a scaffold manufactured at 90:10 (dioxane: water) is shown in Figure 3-20.

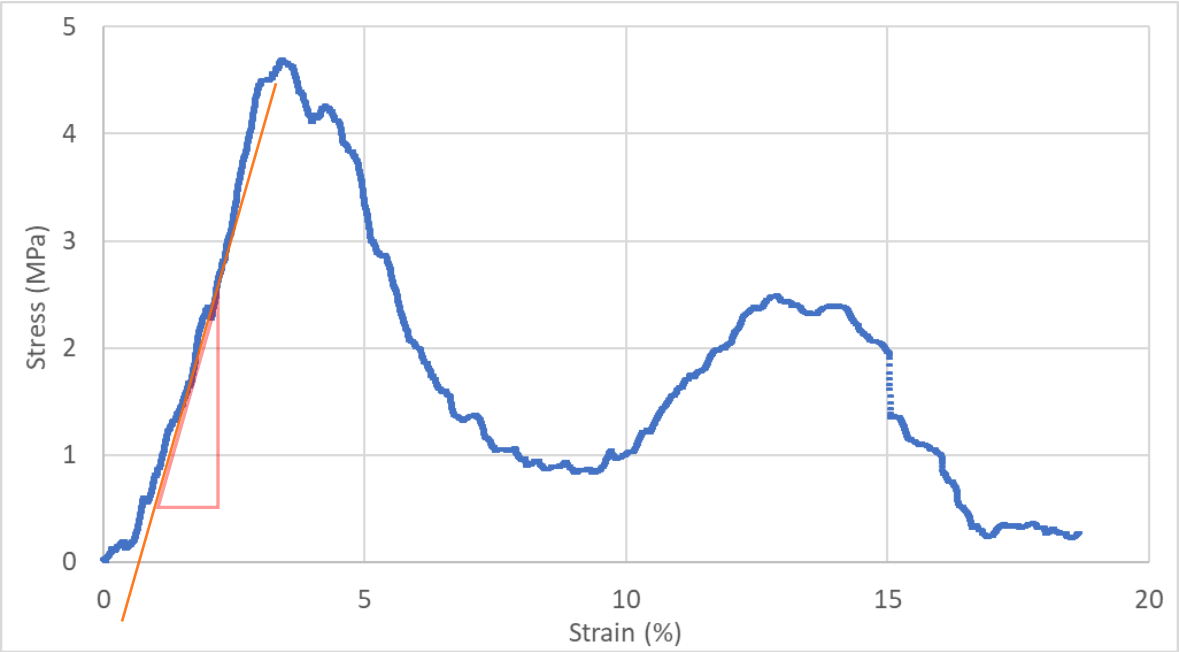

Figure 3-20: Stress-strain graph of a scaffold manufactured at Dioxane: Water 90:10 at 1235°C. The Youngs Modulus was calculated as the gradient of the linear region, in red.

In Figure 3-20, the stress starts to decrease around 3.75% strain and then increases around 9.3% strain. Young's modulus (E) is calculated as the slope around 2% strain, which is consistent with the range of strain for varieties of trabecular bones, spongy bones (Thurner et al., 2007).

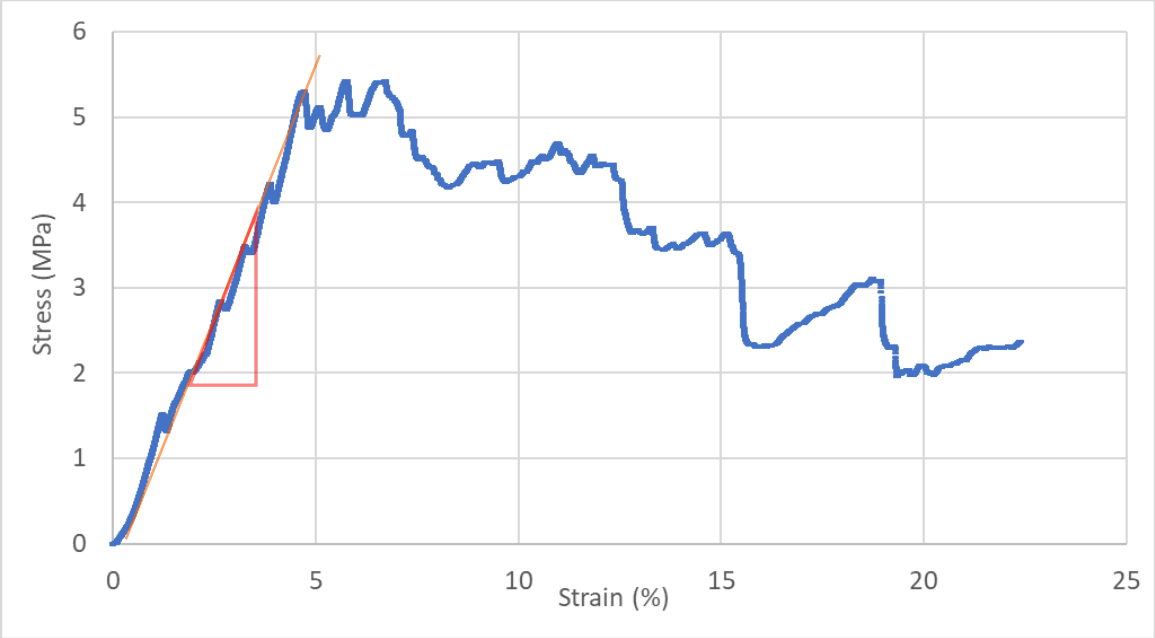

Figure 3-21: Stress-strain graph of a scaffold manufactured at dioxane: water (90:10) at 1235 °C. Modulus was calculated as the gradient of the linear region, in red.

Figure 3-21 shows the stress-strain graph for another scaffold manufactured at 90:10 (Dioxane: Water). This graph follows a different trend compared to the graph in Figure 3-20. It can be suggested that the pores within the scaffold in Figure 3-21 are more homogeneous, as the graph shows continuous regions of stress increase followed by fluctuations in stress levels with increasing strain and gradual failure in tolerating stress.

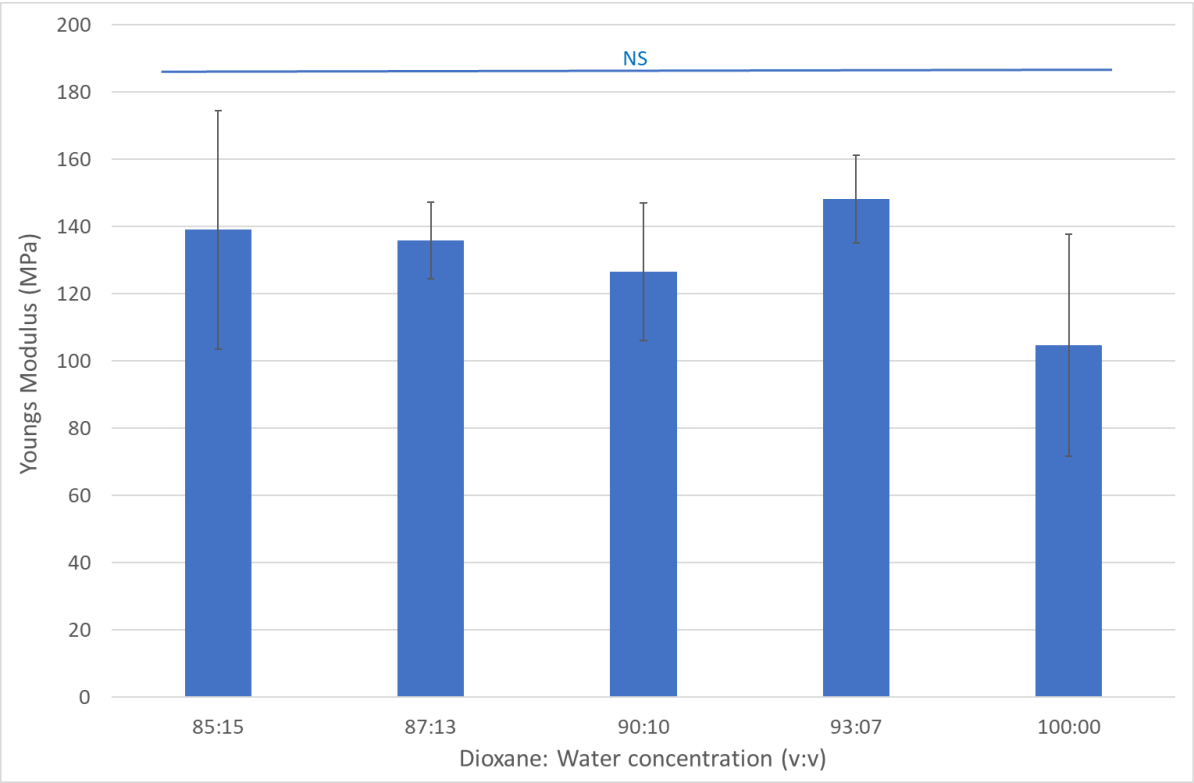

Figure 3-22:Young's Modulus (MPa) of the scaffolds in relation to manufacturing technique of scaffolds (different Dioxane concentrations) sintered at 1235°C. The Error bars represent standard deviations, N=3.

The average Young's modulus for different scaffolds was within 100 MPa to 140 MPa, as shown in Figure 3-22. Figure 3-22 shows that scaffolds manufactured with dioxane:water concentration 100:0 and 90:10 have the lowest tolerance for pressure with Young's modulus values of 110 MPa and 112 MPa, respectively. These scaffolds (100:00 and 90:10) have the most open porosity, and it is therefore reasonable that Young's modulus is generally the lowest. Scaffolds 90:10 have the lowest standard deviation. Standard deviation of 90:10 is very low in comparison to the other manufactured scaffolds; this represents greater repeatability within the manufacturing technique, producing scaffolds of similar compressive strengths. One-Way ANOVA with Tukey's multiple comparison test was carried out on the data presented in Figure 3-22, the test showed that there no statistical difference between the scaffolds exists; statistical significance was determined at $p < 0.05$.

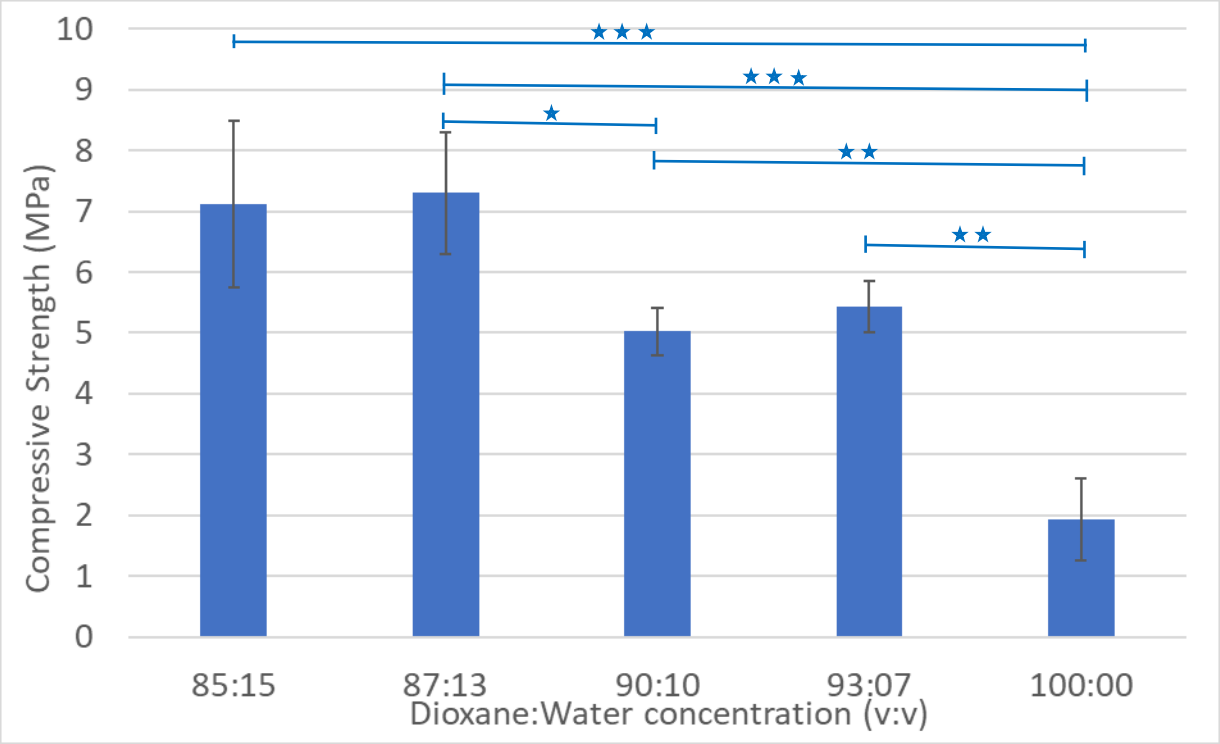

Figure 3-23: Compressive strength (MPa) of scaffolds manufactured with different concentrations of dioxane:water. Significance shown at p<0.01 (**) p<0.001 (***) p<0.05 (*). All other compressive strengths were not significantly different (NS).

Compressive strength of the scaffolds is shown in Figure 3-23. The peak compressive strength was calculated from the stress strain graphs, an example is shown in Figure 3-20.

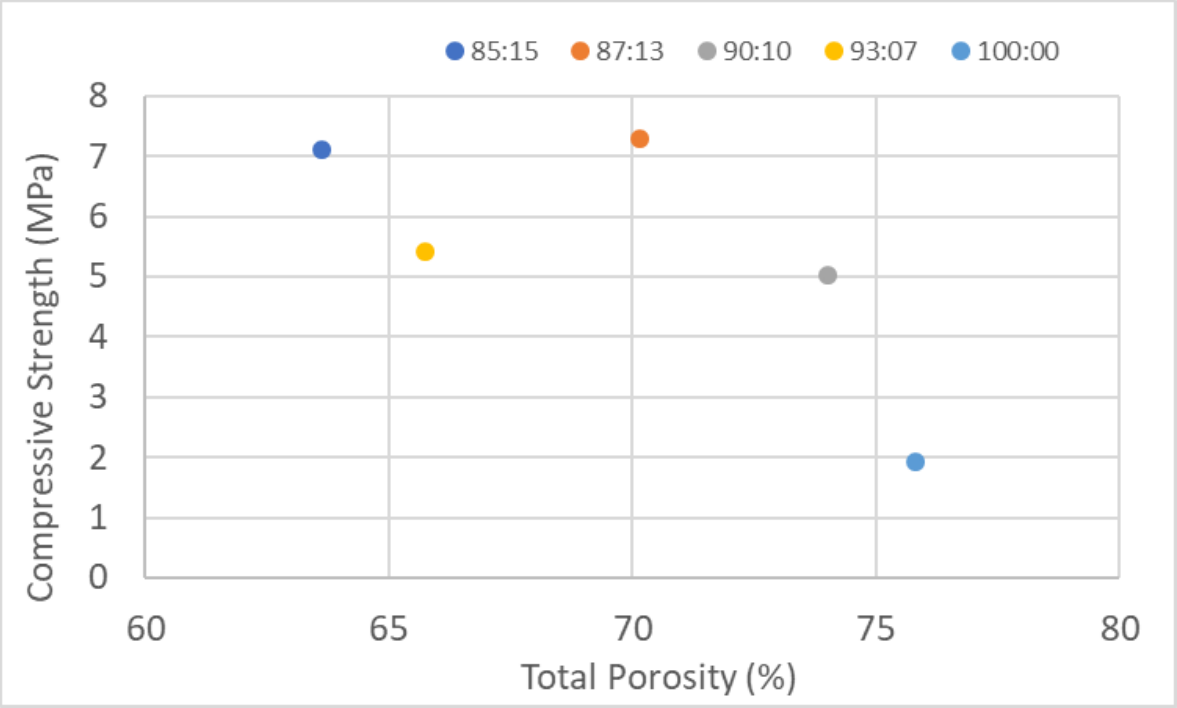

Figure 3-24: Graph demonstrating the relationship between the compressive strength (MPa) and the total porosity (%) of the scaffolds, N=3.

Figure 3-24 shows the total porosities of the scaffolds (%) in relation to the compressive strength (MPa). The figure suggest that compressive strength is inversely correlated to the total porosity.

3.8 Discussion

There are several factors that determine the suitability of scaffolds for cell testing. The main factors include the open porosity of the scaffolds, the total porosity, the size and number of pores, as well as the mechanical characteristics and handleability of the scaffolds (Rose et al., 2004, Will et al., 2008, Bose et al., 2012). Scaffold with great compressive strength may have minimal porosity, which would be disadvantageous with regards to cell tests. Scaffold's suitability is a balancing act of many factors, to logically select a repeatable scaffold manufacturing technique that will result in overall efficient scaffolds. These factors have been evaluated for each step of the manufacturing process, the results of which are presented in Chapter 3 – Scaffold Manufacturing Results. This section will focus on discussion of these results.

3.9 Hot Stage Microscope

Hot Stage Microscopy was used to study the sintering and shrinkage behaviour of the raw AW2 powder. The hot stage microscope enabled analysis of different particle fractions of the milled AW2 powder, which determined the temperature range for sintering and enabled observation of the shrinkage, which previously has been shown to be influenced by the shape of the raw AW powder (Toumpaniari, 2016, Rodrigues, 2018). The SEM images in this study showed a variety of particle shapes (cuboidal and elongated) present in the AW2 powder in the sintered scaffolds (Figure 3-8). These shapes have an effect with regarding to necking between particles during sintering, also on the pore shapes between the particles.

3.10 Cloud Point

The cloud point was vital for understanding the phase separation temperature and the effect of adding a non-solvent to the solubilisation of PLA. The point of turbidity was related to the water content used; higher water concentrations resulted in higher turbidity temperatures. It is important to note that there was only a 5% difference in water concentration between 85:15 and 90:10, but the cloud point temperature difference was around 30°C. In the 93:07 and 100:0 experiment, the cloud point temperature remained stable at around 10°C – 12°C, which is equal to the reported melting/freezing temperature of dioxane (Pohanish, 2017, Aldrich, 2020). This indicates that a water concentration of less than 7% has no noticeable effect on the cloud point temperature.

3.11 Pore sizes

Many architectonic characteristics of the scaffold influence the cells' ability to attach, proliferate and differentiate on scaffolds; the major factors include pore distribution, interconnectivity, pore size, and morphology. In relation to a biological point of view for cell tests, the porosity of scaffolds, both with regards to microporosity (10 µm – 80 µm] and macroporosity (80 µm – 960 µm] is vital for allowing penetration of nutrients and cells. Interconnectivity refers to a pore that enables connections between at least two other pores. Macroporosity and macro-interconnections enable cells to penetrate throughout the scaffolds and to remain within the pore boundaries. The microporosity and interconnectivity at this level allows nutrient and gas diffusion across the micropores and nanopores that permits waste disposal (Vacanti et al., 1988, Mikos et al., 1993, Woo et al., 2003) and enables a rough surface for the cells to attach to.

Figure 3-15 and Figure 3-16 show the distribution of pores across the different scaffolds, the graphs show that the scaffolds manufactured with a dioxane:water concentration of 90:10 have a higher number of micropores and macropores, indicating that these scaffolds are potentially more suitable for cell infiltration, attachment and differentiation.

Figure 3-8 shows that the surface of scaffolds and the pores have an overall rough morphology, which could potentially be appropriate for cell growth (Perez and Mestres, 2016). The large variations in pore sizes could offer a suitable environment for nutrient transfer, waste diffusion and cell attachment on the pores and surfaces, as seen in Figure 3-16, Figure 3-8, and Figure 3-15.

The pore areas measured using the image processing algorithm, are correct for any pore in the image which is not on the boundary of the image. However, parts of pores which touch the boundary of image are cut during imaging and such pores are imaged partially. This results in having smaller pore size for pores which are on the boundary of an image. Also, the statistics presented for pore sizes tend to exhibit the size of pores smaller than their true size. To rectify this error, one can add another step to the algorithm to find any pore which touches the boundary of image and exclude them from analysis. The area of image used to calculate the statistics will also need to be modified accordingly. This can be subject of future study.

3.12 SEM Images

Qualitatively, the connections between the AW2 particles (known as necking) were seen on the SEM images in Figure 3-8. Large particles (around 40 µm – 50 µm in size) can be observed in Figure 3-8A and D, both of which seem to show smaller pore sizes and less interconnections between the pores. This is in agreement with the results found from the Archimedes' calculations (Figure 3-11) as 85:15 and 93:07 scaffolds have the least amount of open porosity and the most closed porosities. A higher percentage of closed pores could be indicative of higher strength scaffolds, as the pores have AW2 particles on all sides and can provide stability.

In Figure 3-8D the white arrow indicates a large particle that is still similar in morphology to un-sintered AW2, although other particles in the SEM show necking. The scaffolds manufactured with dioxane:water concentrations of 93:07 appear to have relatively small pore sizes, and Figure 3-15 is in agreement as the pore size distributions show that 93:07

scaffolds have high numbers of micropores compared to the number of larger pores. The SEM images of the scaffolds identify high diversity in morphology of the pores among the different manufacturing techniques. In Figure 3-8C, there are clear large pores and interconnections can be seen on the 2D image, but in Figure 3-8A the pores look to be much smaller in size and more compact, this is supported by the findings shown in Figure 3-15.

Pore size bins in Figure 3-15 have been produced to show only pore sizes above 10 µm, this is in line with studies by (White and Shors, 1986, Lu et al., 1999) which showed that osteoblast cells successfully infiltrated a 10 µm – 50 µm porous interconnection in HA scaffolds. The osteoblast-like cell body (human osteosarcoma cell line SaOs-2) range from 5 µm to 50 µm in size, with a cell area ranging from 400 μm^2 to 800 μm^2, and the cell length varying from 40 µm to 90 µm (Baran et al., 2015). Osteoblast cells are usually thin and long (elongated) when in a suitable environment. Earlier research suggests that a pore size of 10 µm would allow ingrowth of osteoblast cells, while a 15 µm – 50 µm pore size would assure fibrous tissue formation, and the larger pore sizes would generally favour new bone formation (White and Shors, 1986, Lu et al., 1999). Recent studies suggest using scaffolds with large pore sizes of around 500 µm, however it contradicts with the biological nature of osteoblast cells which are usually 20 µm to 50 µm in diameter (Qiu et al., 2019) and the research by (Lee et al., 2010) which shows that scaffolds with pore sizes around 500 µm or more are not suitable for attachment of the pre-osteoblastic cells, M3T3-E1.

3.13 Porosity (Archimedes)

The porosity of the scaffolds were determined using the density kit and a liquid displacement method (Archimedes' analysis), Figure 3-11 shows that overall, the scaffolds had between 63% and 73% total porosity (sum of open and closed pores), which is considered to be a high overall porosity. The total porosity does not seem to follow a trend regarding the dioxane to water concentration, this is indicative that other factors in the manufacture and post-processing of freeze-dried scaffolds may be responsible for the greater variation in open porosities. Sintering temperature plays a vital role in the structural integrity and morphology of scaffolds, a high sintering temperature, close to or above the melting temperature can result in scaffolds with decreased microporosities (Bignon et al., 2002, Bignon et al., 2003, Habibovic et al., 2005). A lower sintering temperature can result in a higher number of micropores which aid in osteoblast adhesion (Bignon et al., 2003, Habibovic et al., 2005).

Porosity can decrease for high sintering temperatures, this can be due to shrinkage mechanisms (Bignon et al., 2002). The scaffolds have good interconnection, and good open porosity as indicated in the Archimedes' analysis (Figure 3-11) and the nutrient diffusion analysis (Figure 3-19).

It is very difficult to link the distribution of pores (Figure 3-16) to the porosity of the scaffolds (Figure 3-11), due to the fact that the measurement of internal pores is not possible using SEM images. Porosity measured using Archimedes' quantifies the porosity within the whole scaffold, while SEM only shows the pores on the outermost surface. Therefore, there can be discrepancies in relation to the distribution of pores on the surface and inside the scaffold, e.g. the surface of scaffold has micropores linked to many internal pores (open or closed pores) under the surface.

3.14 Glucose uptake – nutrient diffusion

The nutrient diffusion test suggests that the labelled glucose was up-taken by the scaffolds at a relatively similar rate across all scaffolds. The scaffolds showed a glucose release of around 11% to 14.5% within 24 hours in PBS, which suggests that the molecular porosity is adequate for nutrient diffusion and waste removal throughout the scaffolds, Figure 3-19. This microporosity is imperative for cell proliferation and differentiation. The time (4-hours, 6-hours and 24-hours) the scaffolds were in the glucose (2-nbdg) solution did not seem to have an effect on uptake or the release of the glucose. This indicates that for cell tests, the scaffolds can be pre-conditioned in the necessary media for as little as 4-hours prior to cell seeding, as duration did not significantly effect nutrient diffusion uptake. In the cell tests, the scaffolds may be preconditioned with media for less than 4-hours, other time points will be evaluated.

3.15 Mechanical Properties

The compression graphs of the scaffolds are particularly interesting as they show the porosity varies throughout the scaffolds, as shown in Figure 3-20, where the graph shows some failure around 4.0% with its lowest stress shown around a strain of 8% - 10%. From a strain of 10% onwards it appears that the scaffolds can tolerate stress again, this may be attributed to the pores breaking down under the compressive load, with the previously "empty pores" filling with AW2 powder particles and eventually resulting in a denser scaffold (Gervaso et al., 2016, Turnbull et al., 2018). The pores are increasingly filled with powder from the internal layers

and consequently are able to undertake a higher compressive load. This potentially suggest that porosity is available somewhat homogenously throughout the scaffold.

Comparing Young's modulus and compressive strength for different scaffolds as shown in Figure 3-22 and Figure 3-23, show that scaffolds in group 100:0 have the lowest value of Youngs modulus and compressive strength. Given that these scaffolds, 100:0, have the most total porosity (Figure 3-12), suggests that the percentage of porosity can be correlated with the scaffold's Young's Modulus and compressive strength, and consequently scaffolds structural stability.

Figure 3-22 shows that scaffolds manufactured from 100:0 dioxane:water concentration have the lowest Youngs Modulus at 104.6 MPa, with 90:10 having the second lowest tolerance at 126 MPa. These scaffolds (100:00 and 90:10) have the most open porosity and therefore it is reasonable that the calculated Young's modulus is generally lower than the other scaffolds, representing less tolerance to stress. The compressive strength of 100:0 is the lowest at 1.9MPa (Figure 3-23) which represents that this scaffolds manufacturing technique produces the weakest scaffolds for tolerating compressive loads. The scaffolds at 90:10 and 93:07 dioxane:water concentrations have the next small compressive strength of 5MPa and 5.4MPa respectively. The compressive strength appears to be inversely correlated with the total porosity, Figure 3-24 (Bignon et al., 2003). However, this relationship appears to be non-linear.

The change in stress/strain is almost linear initially up to around 4.5 MPa with some turbulence in (Figure 3-20), which is indicative of porous sections of the scaffolding starting to break. After the peak, at a maximum strain of around 4.5 MPa, the scaffold reaches breaking point. For this study the behaviour of scaffolds before the breaking point is most important. Figure 3-21 shows the stress/strain curve for a different scaffold. The behaviour before breaking point is similar to that observed in Figure 3-20, however, the behaviour after the breaking point varies in comparison. The behaviour of the scaffolds after the breaking point is reached, is not of interest for scaffold fabrication.

3.16 Evaluation Matrix

A set of tests were performed on three or more scaffolds from each category and the results were compared to find suitable scaffolds for bone tissue growth. An evaluation matrix was generated to combine these characteristics into one table (Table 3-3). This table shows the different levels of each parameter (from best to worst) for each group of scaffolds.

Dioxane: water ratio (v:v)	Mechanical properties (MPa)		Archimedes' analysis (Porosity)		Number of Pores in each range		Nutrient Diffusion
	Compressive Strength	Young Modulus	Open	Total	Micro 10 – 80 (µm)	Macro 80 – 960 (µm)	Glucose release
85:15	7.1 ±1.4	139.0 ±35.4	19.6 ±3.1	63.6 ±3.5	82	26	11.0 ±1.0
87:13	7.3 ±1.0	135.8 ±11.1	36.9 ±2.6	70.2 ±3.1	232	179	11.7 ±1.2
90:10	5.0 ±0.4	126.5 ±20.4	41.8 ±1.4	73.2 ±1.4	386	251	12.1 ±0.8
93:07	5.4 ±0.4	148.1 ±13.0	24.3 ±2.7	65.7 ±3.9	314	163	11.2 ±1.1
100:0	1.9 ±0.7	104.6 ±33.0	28.2 ±2.0	75.8 ±5.1	265	194	14.5 ±0.9

Table 3-3: Evaluation Matrix of the scaffolds represented from highest to lowest for each of the characteristics based on the experimental results. The dark brown/yellow represents the "best" in the characteristic's column. White or light yellow represents the "worst" characteristics.

To simply evaluate the effects of the dioxane:water concentration on the parameters a Likert scale with a weighting of 5 to 1 is used to represent the best to worst group of scaffolds for tissue regeneration. This allows for simple but comprehensive comparison between parameters respectively (see Table 3-4). The weights for comprehensive evaluation matrix are given for each of the parameters based on its effect on scaffolds' suitability in terms of mechanical strength, micro and macro pore sizes and the level of nutrition diffusion.

Scaffolds with higher compressive strength are more suitable for mimicking bone, therefore scaffolds manufactured with 87:13 and 85:15 dioxane:water concentration with high values of 7.3 MPa and 7.1 MPa are both given weighting 5, followed by 90:10 and 93:07 which are given equal weighting of 4. Scaffolds 100:0 is given the low weighting of 1 due to having a

much lower compressive strength of 1.9 MPa. The Youngs' modulus for all scaffolds are higher than 100 MPa, which all are suitable for bone regeneration and modelling, so they are given an equal weighting of 5. Given that higher porosity within scaffolds are more suitable for bone tissue growth, scaffolds with both higher open and total porosities are given higher weighting. Similarly, scaffolds with higher number of pores are given higher weightings and scaffolds with the lowest number of pores are given the lowest weight of 1. Scaffolds in group 100:0 have the higher level of glucose release so are given weighting of 5, and scaffolds 93:07 and 85:15 with closely similar glucose release levels of 11 and 11.2 are given the lowest weighting of 2 for that parameter.

Dioxane: water ratio (v:v)	**Mechanical properties (MPa)**		**Archimedes' analysis (Porosity)**		**Pore Sizes (µm)**		**Nut. Diff.**	**Total**
	Comp. Strength	Young Modulus	Open	Total	Micro 10 - 80	Macro 80 - 960	Glucose release	
85:15	5	5	1	3	1	1	2	18
87:13	5	5	4	5	3	4	3	29
90:10	4	5	5	5	5	5	4	33
93:07	4	5	2	4	4	3	2	24
100:0	1	5	3	5	3	4	5	26

Table 3-4: This table uses a Likert scale to rank the Best (5) and Worst (1) scaffold characteristics within each column. It is a numerical conversion of Table 3-3 above. The best scaffold is that manufacture from 90:10 (dioxane:water (v:v)) with the highest value of 33.

The sum of these weightings was computed for each of the five scaffold groups (dioxane:water concentrations), and then presented as a measure of scaffold suitability in Table 3-4. The results show that total scaffold suitability value is the highest for 90:10 dioxane:water concentration with a total weighting of 33; followed by scaffolds 87:13 with a weighting of 29; closely followed by 100:0 and 93:07 having closely similar weightings of 26 and 24, respectively. This analysis shows that the processing steps used to manufacture scaffolds with 90:10 dioxane:water (v:v) best represent human bone structure, consequently this manufacturing technique has been chosen for the next step of the study for tissue growth. The standard deviation of values in Table 3-3 shows that the scaffold group 90:10 has the lowest standard deviations in four out of five parameters, representing that the

manufacturing process for this group produces more predictable scaffolds with lowest variations, and therefore is most repeatable/reproducible.

3.17 Summary and Conclusion

An optimised manufacturing process for 3D porous Apatite-Wollastonite 2 scaffolds based on 90:10 dioxane:water Thermally Induced Phase Separation (TIPS) methods was presented here. Cloud point analysis for the TIPS process was used to determine the temperatures required for scaffold manufacturing. The manufacturing process produced repeatable scaffolds each time (over 140 scaffolds manufactured in different batches) with a porosity of 60-76% dependant on the dioxane:water concentration. Calculations based on Archimedes principal were utilised to obtain the open porosity, closed porosity and total porosity of the scaffolds, this was used to determine the best manufacturing method. An algorithm was designed to measure the pore sizes and distribution from Scanning Electron Microscopy (SEM) images of any given 3D scaffold surface. The algorithm was independent from the shape, size, and orientation of the pores. The accuracy was verified by applying the algorithm on SEM images of calibration kit with holes of varying standard sizes. The results on SEM images of the calibration kit showed an average error of ±1.2% and standard deviation of ±2.3% as validated against the sizes provided by the manufacturer of calibration kit. Mechanical tests were performed to determine the stability of the scaffolds for the intended purpose; to replicate bone as an *in-vitro* model. In conclusion the scaffold manufacturing process was repeatable and produced highly porous scaffolds, which will be further explored *in-vitro* in the next chapters.

4 Interconnectivity Improvement of AW2 Scaffolds

4.1 Abstract

In the Chapter 2 – Materials and Methods, an optimised process of manufacturing Thermally Induced Phase Separation (TIPS) AW2 scaffolds was presented. They will be referred to as AW2 scaffolds. To this end, the suitability of AW2 scaffolds in terms of porosity and interconnectivity due to sintering temperature and dioxane:water ratio were studied, and the manufacturing process optimised.

This chapter studies different potential approaches to further improve the interconnectivity of AW2 scaffolds. Improving interconnectivity is important as it can aid the progress of cell growth in scaffolds. This can be enhanced by either imposing interconnectivity during the scaffold manufacturing process or by modifying the manufactured scaffolds. The techniques include using a negative mould during scaffold manufacturing process to impose interconnectivity or generating interconnectivity by making holes (channels) and grooves on the scaffolds at some stage during the original manufacturing process. The potential techniques from each method are investigated and evaluated by comparing changes in the porosity and interconnectivity of scaffolds, performing the mechanical testing, and reproducibility of the scaffolds during the manufacturing process.

4.2 Introduction

Improving the interconnectivity of pores is known to help the progress of cell growth in scaffolds further (Lee et al., 2010, Turnbull et al., 2018). Interconnectivity is commonly improved by imposing interconnectivity during scaffold manufacturing process and/or by modifying manufactured scaffolds.

There has been great research on manufacturing scaffolds with controlled porosity and pore structures using 3D printed materials (Hutmacher, 2001, Bose et al., 2003, Hollister, 2005, Bose et al., 2013, Zhang et al., 2014, Barbeck et al., 2017, Pierantozzi et al., 2020, Camarero-Espinosa and Moroni, 2021). However, little attempts have been made to combine free-form scaffold manufacturing and controlled porosity manufactured scaffold (Hollister, 2005, Chaudhari et al., 2016, Toumpaniari, 2016). Toumpaniari, studied the method of improving interconnectivity by using 3D printed templates during manufacturing process. Toumpaniari

inserted AW powder into a 3D template followed by sintering, although this technique did not produce successful scaffolds as they were not uniform and unrepeatable. Others have used a single large channel in centre of the AW scaffold, and analysed the growth of Mesenchymal Stem Cells (MSCs) on such scaffold with *in-vivo* experiments on mice (Lee et al., 2015). The result was successful with the subcutaneous implantation in mice. This showed that improving interconnectivity can help with cell growth. However, having a single large channel may not be consistent with the structure of bone, it did show a promising result regarding cell growth on the scaffolds.

In this chapter (4), two groups of techniques based on different categories of interconnectivity improvements (during manufacturing and after manufacturing) were investigated. The first group focuses on enforcing interconnectivity by adding a 3D printed PLA scaffold during the manufacturing process, and the second group increases the interconnectivity by making holes and grooves into scaffold at later stages after manufacturing process. The next section describes (4.3) approaches used in each category of techniques in detail with methods of scaffold characterisation. The details of manufacturing process and results are presented in Section 4.4 which is followed by the concluding remarks on the evaluation of the achieved results for each of the techniques and the comparisons in Section 4.5.

4.3 Methods

Several different methods were explored to increase the interconnectivity (total porosity and open porosity) of AW2 scaffolds. In this section a Fused Filament Fabrication (FFF) 3D printer (Ultimaker 3) was used, which will be referred to as 3D printer.

4.3.1 Enforcing interconnectivity during manufacturing process

Three-dimensional porous Poly Lactic Acid (PLA) moulds with high interconnectivity have been designed, manufactured, and incorporated as negative moulds during scaffold manufacturing process. The negative moulds were printed using a Fused Filament Fabrication (FFF) 3D printer (Ultimaker 3) and used during casting stage of the process to produce scaffolds with large interconnectivity. The PLA size and the gap between PLA structure are critical factors in the design, and using the right printing parameters during 3D printing are essential to obtain stable reproducible results. The PLA structures are optimized to obtain stable reproducible results by carefully designing the PLA strut sizes, the gap between PLA

structure and modifying the printing parameters during 3D printing. In theory the negative PLA mould burns away during the sintering process, leaving behind an AW2 scaffold (inverse of the PLA negative mould).

The moulds were designed to have different gaps and different PLA strut sizes which represents the AW2 parts of scaffolds and the size of interconnectivity, respectively (Figure 4-1). The negative moulds were designed using AutoCAD software (Fusion 360 v2.0.10244), and manufactured using the 3D printer and PLA. The thickness and height of PLA, the gap between the layers for each of the designs, and the printing parameters (resolution, print speed, built plate temperature, and nozzle temperature) are major factors in the final product. These factors were optimised and altered to ensure reproducibility during the negative mould manufacturing. The printer setting, resolution = 100 µm, print speed = 60 mm per sec, build plate temperature = 60°C, and nozzle temperature = 200°C, were optimal values for printing 3D moulds used in experiments here. These parameters produced successful 3D printed moulds as in Figure 4-2 B .

A diverse range of cylindrical and cubical designs were initially investigated, with different void spaces and PLA thicknesses, and an initial evaluation on the manufactured scaffold was performed. Essentially, the initial evaluation aimed to establish whether the negative moulds are stable in terms of production during the casting process if the casting can be repeated with mechanically stable scaffolds produced. Four of the designs were chosen for detailed analysis, and are presented in Figure 4-1.

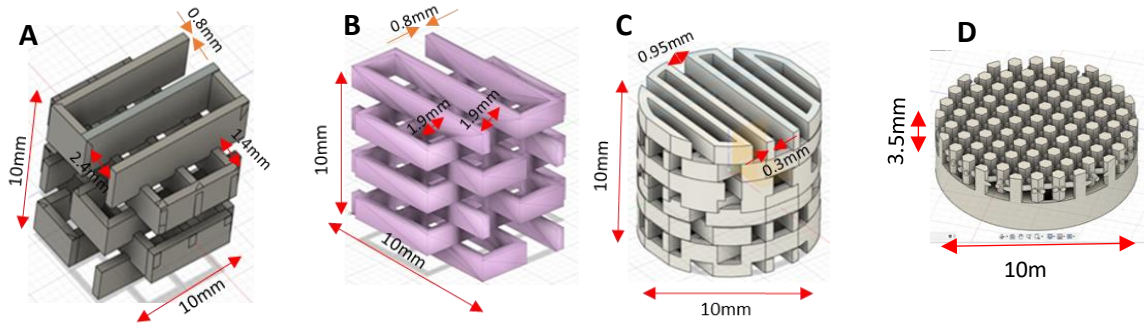

Figure 4-1: Four different CAD designs for 3D printed PLA to be used as negative mould (not to scale).

These designs where chosen as they would ideally permit interconnectivity in three dimensions, therefore allowing the media and cells to propagate within scaffold. The final evaluation of suitability of the scaffold in comparison to the original AW2 scaffold for cell seeding will be the subject of next chapter.

To allow the AW2 particles to easily fill the gaps in the negative PLA mould, large gaps of 950 µm to 2400 µm were left between the PLA filaments. Thus, the thickness of the negative PLA mould parts was chosen so that the AW2 scaffold gaps would be large enough for cell attachment (300 µm to 800 µm in width). Also, the design of moulds should ensure the continuity of movement of the printer head during printing is maintained. Any discontinuity in movement of printer head can cause unexpected results mainly at the start and end of PLA parts, where it is disconnected.

The designs in Figure 4-1 maintains continuity of printer head as best possible. In Figure 4-1, negative moulds A and B are square shaped with a width of 1 cm and negative moulds C and D are circular with diameter of 1 cm. Negative moulds A, B & C are 1 cm in height and negative mould D is 3.5 mm in height. For negative moulds A and B, the thickness of PLA pile is 800 µm. For negative mould A, the distance between PLA pile is 2400 µm with gap 1400 µm on each far side. For negative mould B the distance between PLA filaments is 1900 µm with same gap 1900 µm on each side. Negative mould C has PLA thickness of 300 µm with gap 950 µm between PLA pile horizontally. Negative mould D is hexagonal with each edge of hexagon being 288 µm, resulting in maximum distance between sides to be 500 µm. The distance between each hexagon with neighbouring hexagon is 500 µm and all neighbouring hexagons are inter-connected by a PLA tube of 500 µm in diameter.

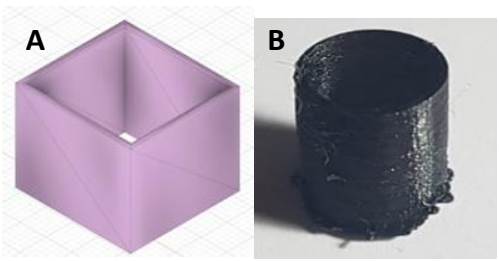

Figure 4-2: 3D printed PLA wall to fit around the 3D printed moulds. A) AutoCAD rendered wall design for square moulds. B) 3D printed wall for cylindrical moulds.

The wall counterpart for the moulds in Figure 4-1 are shown in Figure 4-2, with image A showing the Computer Aided Design (CAD) drawing for the square module, and the 3D printed wall for cylindrical mould. The mould inserts A and B (Figure 4-1) fits inside the square based wall printed using PLA material as shown in Figure 4-2 A. The mould inserts C and D fit the 3D printed PLA with circular base as shown in Figure 4-2 B. The printer setting for Ultimaker 3, resolution = 100 µm, print speed = 60 mm per sec, build plate temperature = 60°C and nozzle temperature = 200°C, were optimal values for printing 3D moulds used in experiments here.

A number of different methods to incorporate AW2 into the negative spaces of the 3D printed moulds was explored, that include 1) different sized AW2 powder particles (<20 µm,20-53 µm, 53-90 µm) in dry form, 2) AW2 powder mixed with deionised water in a paste form, 3) AW2 powder mixed with Ethanol in a paste form, and 4) AW2 slurry from the TIPS protocol as described in Chapter 2, Section 2.3.4, poured into the 3D moulds. To avoid the AW2 component from leaking out of the open spaces of the PLA structures, a number of different approaches were investigated: using aluminium foil as a wall around the structure, printing an incorporated PLA wall, using 3D printed PLA wall that was attached onto the structure post printing, and placing the PLA structures in the glass moulds. Removal of the walls could be performed at three different steps during scaffold manufacturing; 1) removing the wall after the initial freezing step, 2) removing the wall before freeze drying step, and 3) removing the wall after freeze drying.

The AW2 PLA dioxane:water (90:10) slurry was prepared using the steps described in the TIPS method in Chapter 2, Section 2.3.4. The wall was fitted around the scaffold to cover the border of scaffold properly. In all cases the base was fixed to the wall using superglue.

4.3.2 Two Step Heating Process (Sintering)

All 3D printed PLA incorporated AW2 scaffolds were placed on Pt foil on a refractory brick inside the furnace, and two-step heating process was based on the protocol described in Chapter 2, Methods section 2.6.

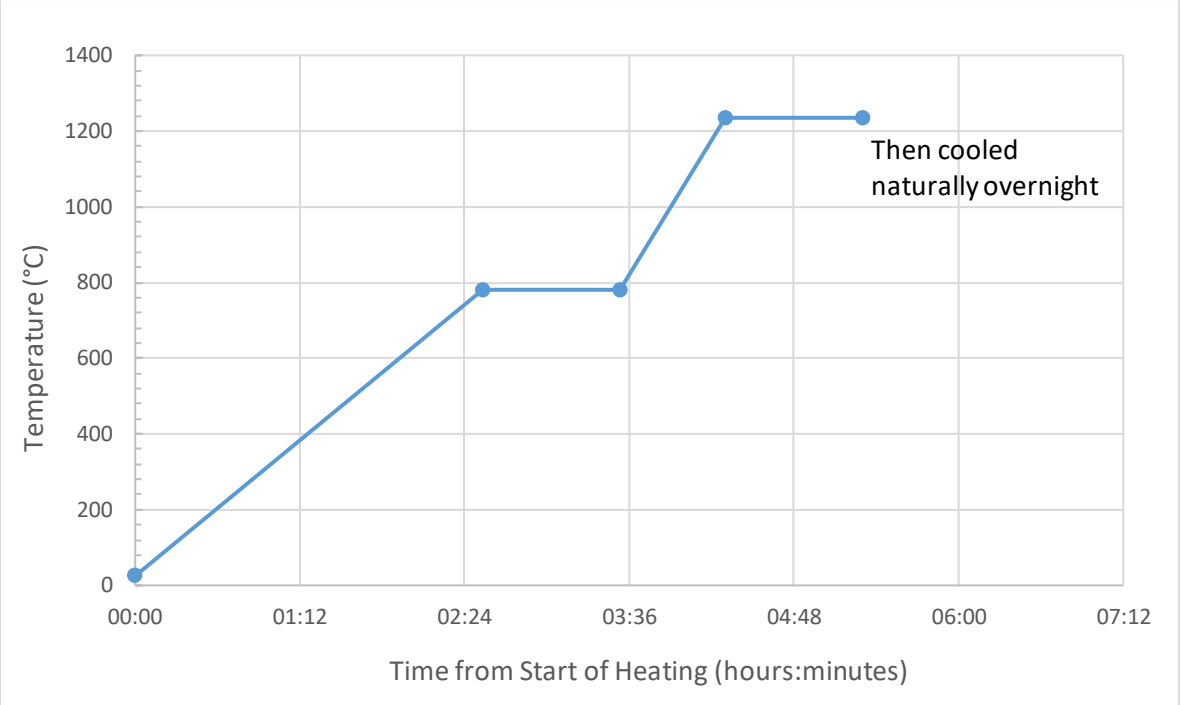

Figure 4-3: Plot showing temperature (°C) against time (hours:minutes) during the two-step heating process (cooling not shown). At 779°C there is a 1-hour dwelling, and at 1235°C there is also a 1-hour dwelling.

As shown in Figure 4-3, the furnace was heated from room temperature (approx. 20°C) to 779°C, using a heating rate of 5°C per minute, with one-hour dwelling time at 779°C, then heated to 1235°C at a rate of 10°C per minute, dwelling time at 1235°C for one-hour. The furnace was allowed to cool naturally overnight back to room temperature before removing the scaffolds, as demonstrated in Figure 4-3.

4.3.3 Scaffold modification prior to post-processing

After freeze-drying the same procedure reported in Section 2.6 was followed, the scaffolds were stored at room temperature (approximately 20°C) until the sintering stage (4.3.2 Two Step Heating Process (Sintering)). Prior to sintering, the scaffolds were carefully hand cut (to approximately 4 mm height) across the diameter using a double-edged metal razor blade. This resulted in relatively flat 3 – 4 mm thick disks of AW2 – PLA scaffolds, ready for sintering.

Figure 4-4: Porous AW2 scaffolds post sintering. A) Scaffolds cut to approximately 3-4 mm height. B) Scaffolds from a top view.

Photos of sintered scaffolds are shown in Figure 4-4, and were taken using a Samsung Galaxy Note9 Smartphone. The images are of original AW2 scaffolds on Pt foil post-sintering. The scaffolds show a slight conical frustum shape and are approximately 3 – 4 mm in height.

4.3.4 Singular channel formation using Glass tube

Two different pathways were explored for removing material by; either removing it after freeze-drying step (before sintering) or after sintering.

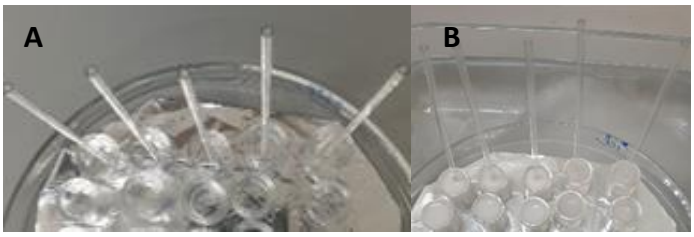

Figure 4-5: Process of slurry addition to glass tube/channel in glass moulds. A) Glass tubes are superglued to the middle of the glass moulds. B) slurry containing AW2 poured into glass moulds.

The addition of channels (a hole that connects the top to the bottom of the scaffold) at set diameters was investigated by using numerous techniques, such as; adding commercial glass tubes (2 mm external diameter supplied by RVI Newcastle, NHS UK) to the middle of the glass moulds and then pouring AW2 PLA dioxane:water slurry into the mould, allowing an overnight freeze, then removing the glass tubes, as can be seen in Figure 4-5.

4.3.5 Modified AW2 Scaffolds

Another technique was to make channels and grooves into the scaffolds at the freeze-dried state (prior to sintering) or after sintering. The channels allow for better circulation of media from the top to bottom of the scaffold, and also improves the interconnectivity of pores. The grooves allow for easier media movement at the bottom of the scaffold, as media can circulate along the channels and through the grooves. To ensure the channels are in the same position on each scaffold, a template with the channel positions was designed using AutoCAD, and the 3D printer was used to make the template guide. Two templates were designed to help with generating grooves and channels, one for adding the grooves and another one to make the channels by drilling. The addition of grooves and channels were carried out either before sintering (after freeze-dry step) and after sintering.

The templates were made with a range of different internal diameters (9 mm to 11 mm with an interval of 0.5 mm) to ensure each template will fit slightly varying range of diameters of the sintered AW2 scaffolds. The internal height of the templates was chosen to be 3 mm to ensure the scaffold is stable on top of the protective mat during the drilling and groove process. A sample template is shown in Figure 4-6 A to C.

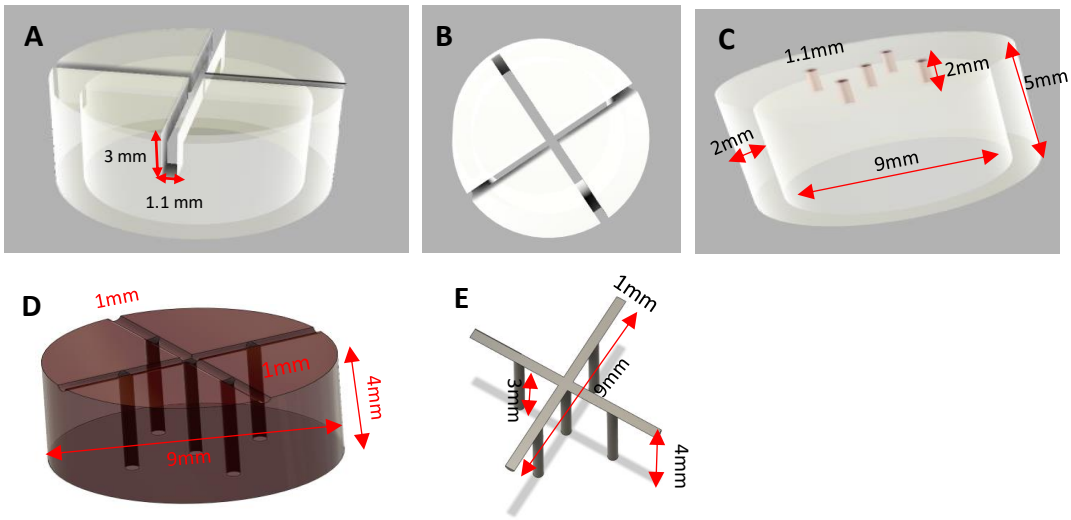

Figure 4-6: AutoCAD rendered designs. A & B) are the templates used for the grooves. C) Shows the template used for drilling the channels at set distances. D) Rendered representation of an upside-down scaffold with the grooves and channels. E) Represents the grooves and channels on a scaffold.

Set sized grooves in standard cross formation were added by using a rotating diamond saw with size 0.9 mm along the cut on template. Another set of templates were made and used

to guide the drilling process. Five holes are considered in the template, one in the centre and four in distance of 2.5 mm from the centre of template. Internal diameter of templates with holes has 5 different internal diameters (9 mm to 11 mm) similar to the template for grooves. Same diameter template with holes were used to drill the holes within in the middle of grooves.

Figure 4-6 A & B, a sample template for generating grooves is shown from two different angle of views. The width of the gap at the top of template is chosen to be 1.1 mm (Figure 4-6 A) and height of the cut is set to be 3 mm. This design allows, given the thickness at the top of template is 2 mm, grooves with depth of 1 mm and width of 1 mm to be made. This was carried out by putting the template on top of scaffold and cutting along the groove to make a 1 mm deep groove depth in the AW2 scaffold. Figure 4-6 D shows the schematic shape of the expected scaffold after grooves and drilling is completed and Figure 4-6 E shows the expected structure of added connectivity (channel and grooves) which represents the amount of material removed from the original AW2 scaffolds.

The successful technique for drilling the channels into sintered scaffolds was performed by a specially designed mould as shown in Figure 4-6. Manufacturing process for AW2 scaffolds is described in detail in Chapter 2.

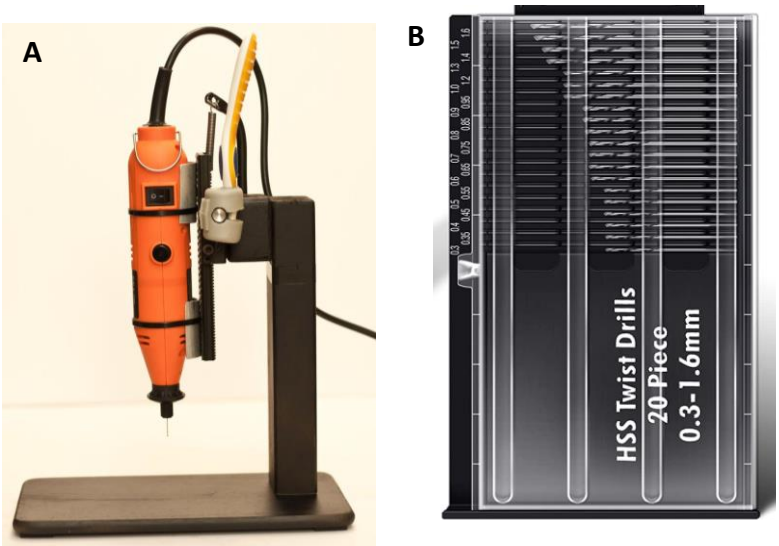

Figure 4-7: (A) Drill and stand used to perform drilling, (B) drill bit set with 0.6mm drill bit used to drill channels into AW2 Scaffolds.

The drill, shown in Figure 4-7, was purchased from Amazon.co.uk (Hi-Spec, 135W Multi-Purpose Rotary Combi tool Multi-tool, model number DT30304), with a 0.6 mm steel drill bit (21 piece drill bit set for jewellery, 0.3 – 1.6mm, Brand: Mudder, Amazon UK), on a stand (Multifunction jewellers benchtop drill stand with manual control, eBay). This technique of drilling channels post-sintering was promising for reproducibility and repeatability.

The mould enabled consistent holes to improve interconnectivity and allow circulation of media in the centre of scaffold as well as within the scaffold, and additional grooves were made for ease of media movement of media from the channels to the bottom of the scaffold. The sintered scaffolds had the channels drilled, with compressed air (Essential Electronics Compressed Air 5707) used to remove any AW2 particle debris.

This technique of drilling channels post-sintering was promising for reproducibility and repeatability. To ensure the channels are in the same position on each scaffold, a template with the channel positions was made on AutoCAD and the 3D printer used to make the template guide. The printer setting for Ultimaker 3, resolution = 100 µm, print speed = 60 mm per sec, build plate temperature = 60℃, and nozzle temperature = 200°C.

4.3.6 Scaffold Characterisation Methods

4.3.6.1 *Morphological Analysis*

A scanning electron microscope (SEM, Hitachi TM3030) was used to evaluate the surface morphology on the modified AW2 scaffolds on a microscopic scale. The scaffolds were placed upside-down (grooves facing upwards) on black carbon tape mounted on aluminium stubs and placed into the TM3030 (Hitachi) SEM chamber. Five areas of view were analysed specifically to include the modifications: channel (hole) and grooves. Images were captured at 15kV and saved as TIF or JPG format. The images were analysed using ImageJ FIJI software (fiji-java6-20170530, Released May 2017 (FIJI, 2021)) to measure the channel diameters and groove widths.

4.3.6.2 *Archimedes - Porosity measurements*

To evaluate the difference in porosity of AW2 before and after modification, density determination using Archimedes analysis was carried out. Firstly, after the two-step heat treatment process on AW2 scaffolds (outlined in Chapter 2, Section 2.6), these original AW2

scaffolds underwent the porosity measurement protocol in Chapter 2, Section 2.9. The scaffolds were then dried in a 50° oven overnight to remove any moisture. After modification (channels and grooves), the scaffolds dimensions were taken again, and the Archimedes protocol was followed again. The scaffolds were dried in a 50° oven overnight again and stored for other tests.

4.3.6.3 *Nutrient Diffusion*

To evaluate the differences between original AW2 scaffolds and modified AW2 scaffolds. A set of original AW2 scaffolds underwent a 2-NBDG glucose uptake test, using light sensitive glucose solution consisting of 2- (N- (7-Nitrobenz-2-oxa-1,3-diazol-4-yl) Amino) -2-Deoxyglucose) (Fischer Scientific, UK) over time. This test was carried out with the original AW2 scaffolds, and then the same scaffolds after they had been modified. Firstly, after the two-step heat treatment process of AW2 scaffolds, these original AW2 scaffolds here underwent the protocol mentioned in 4.3.6.1 and then 4.3.6.2 prior to being modified (channels and grooves). The scaffolds were then dried in a 50° oven overnight to remove any moisture. After modification (channels and grooves), the scaffolds dimensions were taken again, and the nutrient diffusion protocol was followed, as described in detail in the Chapter 2, Section 2.10.

4.3.7 Mechanical Properties

To understand the mechanical properties of the heat-treated scaffolds, compression tests were undertaken using a Shimadzu Compression Tester (Shimadzu Corporation, 2014 model AGS-X with 10kN load cell). Compressive strength and Young's modulus were calculated from the obtained stress-strain curves. The scaffold diameters were measured on both sides and the height was measured using a digital calliper. The average dimensions of the scaffolds were calculated using the average height and diameter, as previously explained in Chapter 2, section 2.11, using Equation (10). To start the stress test, made sure that the surface of load cell is on top of the scaffold and pressure is not negative, then started the experiment. This process ensures consistency in measurement, however there may not be any change in pattern (behaviour) of stress/strain graph. The parameters were a crosshead rate of 0.5 mm min^{-1}, with a load cell up to 10 kN for modified AW2 scaffolds and the experiment was stopped after the break of the scaffolds.

4.4 Results

4.4.1 Enforcing interconnectivity during manufacturing process

To produce good quality repeatable printed parts, the print settings of the 3D printer were modified for each of the designs (Figure 4-1) to optimize the printing resolution, nozzle temperature and also its printing speed. The printer setting for Ultimaker 3, resolution = 100 µm, print speed = 60 mm per sec, build plate temperature = 60°C, and nozzle temperature = 200°C.

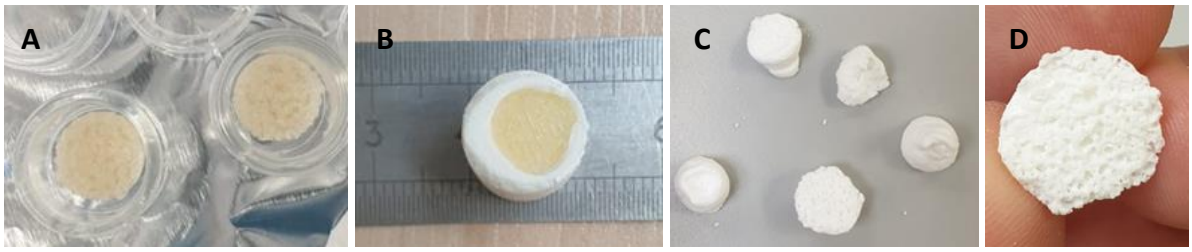

Figure 4-8: Stages of incorporating 3D printed hexagonal part (Figure 4-1 D) into AW2 TIPS. A) The 3D printed hexagonal pattern was placed at the bottom of the glass mould,, and then AW2 slurry poured on top. B) the bottom of freeze-dried TIPS AW2 PLA green part with the 3D printed part incorporated. C) multiple sintered AW2 scaffolds that had the hexagonal 3D printed part incorporated. D) magnified image of bottom of AW2 scaffold after sintering, showing the pores caused by the 3D printed part.

Figure 4-8 illustrates the multiple stages of incorporating the 3D printed hexagonal part (Figure 4-1 D) with the AW2 90:10 dioxane:water slurry from the TIPS protocol. In C) it can be clearly seen that the 3D printed part caused deformations to the sintered AW2 scaffold. This could be due to the PLA part having lower melting temperature and therefore causing movement of freeze-dried part and consequently collapse of the scaffold during sintering process. In rare occasions, reasonable scaffolds were generated like Figure 4-8 (D). A magnified image of the 3D printed incorporated section of the AW2 scaffold clearly shows large pores of size 400 µm to 600 µm. However, the scaffold itself was mechanically brittle and very inconsistent, Figure 4-8 (C). The scaffold could easily disintegrate during general handling or by small pressure between fingers. The results of many experiments using this particular technique showed that this process needs substantial refinement and more investigation to make the manufactured scaffold consistent and repeatable.

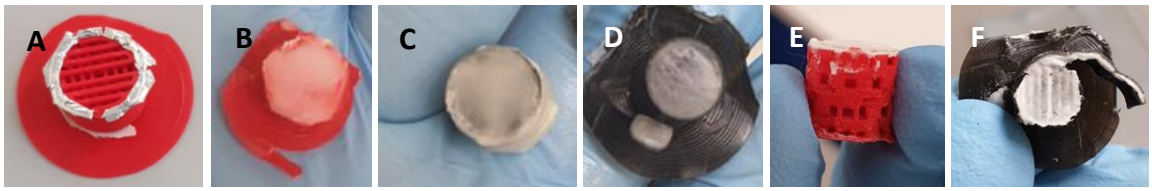

Figure 4-9: 3D printed PLA moulds (from Figure 4-1 C). A) 3D printed PLA mould with foil wall and 3D printed wall around it. B) 3D printed mould with AW2 slurry. C) 3D printed mould which has AW2 mixed with deionised water. D) 3D printed mould with AW2 mixed with ethanol. E) & F) are after freeze drying and show the viscosity of the AW2 slurry may have had a negative effect and did not fill all the gap layers within the PLA moulds.

Sample 3D printouts of groups of negative moulds with AW2 particles are shown in Figure 4-9 A to F. Pouring the AW2 PLA dioxane:water slurry proved difficult as the slurry would not fill all the space between the 3D PLA parts especially where the gap was very small. Manual shaking was found to aid the spreading of the slurry, and was required for the 3D negative PLA moulds with larger gaps. Figure 4-9 A shows a cylindrical 3D printed PLA design, with a foil wall, surrounded by PLA printed wall. Sample moulds with slurry after ethanol washes are shown in Figure 4-9 B. Therefore, any 3D negative PLA mould with a gap less than 1 mm was not successful, as shown in Figure 4-9 E & F.

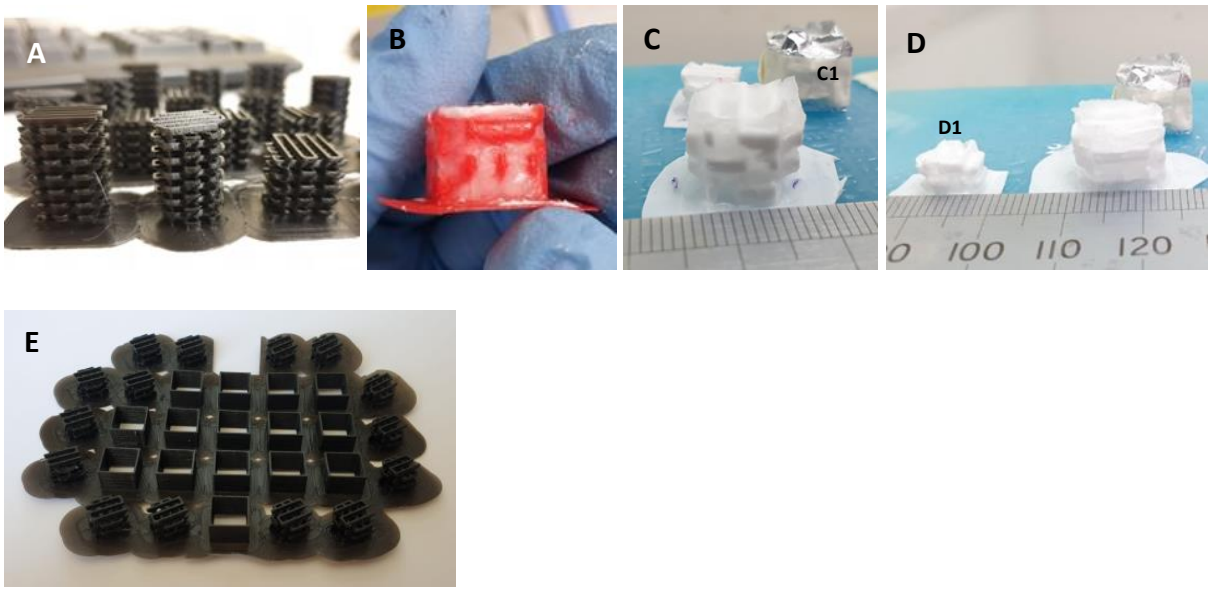

Figure 4-10: 3D printed PLA negative moulds, B – D) shows negative mould with AW2 slurry prior to freeze-drying. E) sample image of printed negative moulds and the walls.

Figure 4-10 shows 3D printed negative square moulds (CAD drawing shown in Figure 4-1, wall in Figure 4-2). 3D printed negative PLA square moulds with AW2 slurry after ethanol washes in shown in B to D. The moulds were covered with foil and masking tape as a wall to avoid spillage of the slurry, as shown in Figure 4-10 C1. Smaller sized mould was trialled, as shown in Figure 4-10 D1, but the AW2 slurry only covered the top surface of mould, similar to Figure 4-9 E & F, therefore these were excluded from the set and were not sintered. Other scaffolds were sintered but due to having small volume of AW2 particles and, in comparison, high PLA volume, there was very little AW2 left on the Pt foil as shown in Figure 4-11.

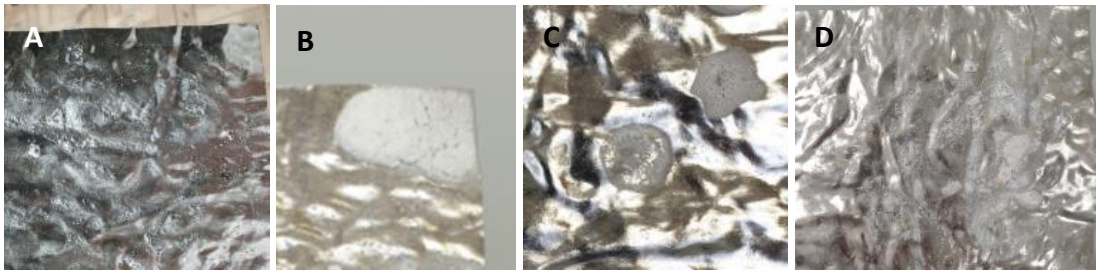

Figure 4-11: Sample Pt foil after two-step heat treatment with AW2 slurry in 3D printed negative PLA moulds. AW2 has collapsed and there is no structure available for further analysis.

Figure 4-11 (A – D) shows sample images of Pt foil with PLA negative moulds (Figure 4-9 and Figure 4-10) with AW2 slurry after heat treatment. It can be clearly seen that there has been a collapse of the material, and the AW2 particles were not stable to form a 3D structure (scaffold) of any sort. Therefore, using the negative moulds methods were considered as unsuccessful. Some AW2 fragments can be seen on the Pt foil (especially shown in B) but these techniques involving negative moulds did not produce scaffolds and were not repeatable in terms of sintering to form a scaffold.

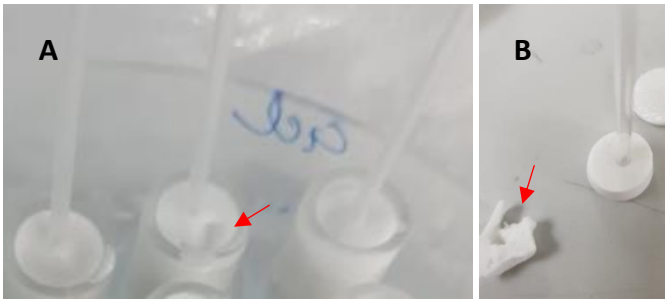

Figure 4-12: Results of slurry addition to glass tube/channel in glass moulds. A) after initial freeze, prior to ethanol washes, some deformities can be seen on surface (indicated by red arrow). B) After multiple ethanol washes, the glass tube was carefully removed, but cause considerable damage on the bottom left (indicated by red arrow).

Adding connectivity using commercial glass tubes and pouring slurry was tested with sample results shown in Figure 4-12. However, the process looked promising initially, removing the inner glass tube proved to be very difficult and damaging, as can be seen in Figure 4-12 B. The inner glass tube was very much integrated with the frozen AW2 mixture and caused damage to the scaffold. Therefore, this technique was not deemed successful.

4.4.2 Additional processing of scaffolds

The next technique explored was drilling the channels into sintered AW2 scaffolds, at this stage the scaffolds are porous, and mechanically stable as they consist of only AW2 material. The drilling was guided by a specially designed template, as detailed in Section 4.3.5. The template successfully enabled consistent drilling to be carried out and additional grooves to be made for ease of media movement from the channels to the bottom of the scaffold (as shown in Figure 4-13 taken using Samsung Galaxy Note 9 phone camera). The sintered scaffolds had the channels drilled using a guided template. High pressure gas was used to remove any AW2 particle debris formed during to drilling. The scaffolds channels were analysed using SEM to measure the diameter and the structure of channels and grooves.

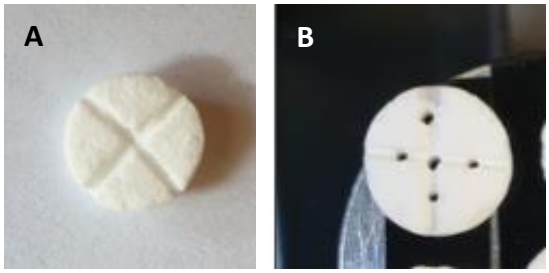

Figure 4-13: Sample photo of A) sintered AW2 scaffold after grooves addition. B) sample modified AW2 scaffold with grooves and channels.

Initially grooves in a cross shape was made at the bottom surface of scaffold (as shown in Figure 4-13). Then two designs were investigated; first design added vertical channels (top of scaffold to bottom) and the second design added horizontal channels (on the side of the scaffold) to the first design which would already have vertical channels. The second method proved to be too complicated for these AW2 scaffolds, and were not repeatable, therefore this technique was not explored further.

The general technique of drilling channels post-sintering was promising for reproducibility and repeatability. Templates are used to ensure that the channels are in the same position on each scaffold, a template with the channel positions was designed using AutoCAD, and the 3D printer was used to make the template guide. This first design method was applied on 10 samples with successful results (Figure 4-13 B) and mechanical test showed reasonable capabilities. Thus, this manufacturing method was considered as successful and repeatable, and was used for cell growth.

The same steps as the first method (channels from top to bottom surface and grooves on bottom surface) were performed on scaffolds at the freeze-dried state (prior to sintering), but due to the PLA content in the scaffold at this stage the scaffolds are very soft. Grooves were not added as this disintegrated the scaffolds every time, therefore it was not explored further with freeze-dried scaffolds.

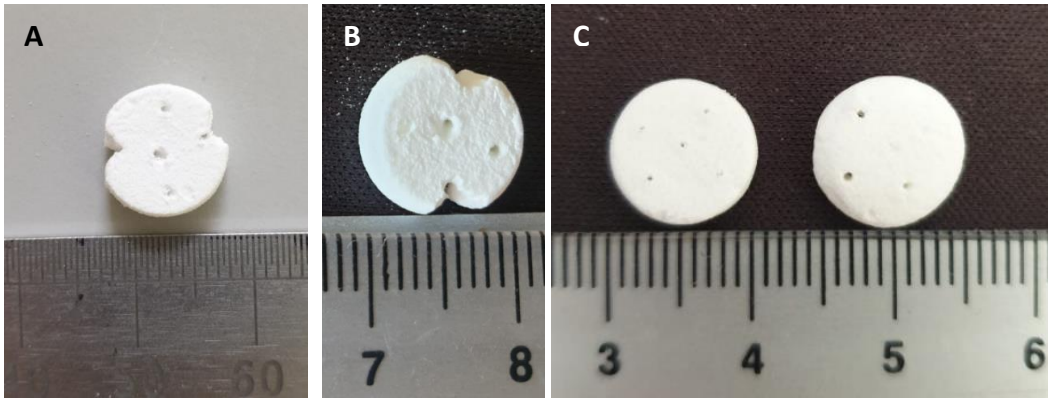

Figure 4-14: AW2 scaffolds that were modified (channels) after freeze-drying. A) Scaffold is damaged due to soft nature of freeze-dried state. B) the damaged scaffold from (A) post sintering. C) Channels were added to the freeze-dried Scaffolds, but some channels are now blocked post sintering. Scale bars are a ruler.

The channels were drilled into the freeze-dried scaffolds, but due to the polymeric nature of these scaffolds there was additional AW2/PLA material detaching from the freeze-dried scaffold, and in some cases due to softness and pressure from drill, the materials became denser around the holes causing the connective pores to become blocked with the AW2 PLA material and inevitably reducing porosity, Figure 4-14 C. This detachment of material and compressed material inside the channels resulted in a non-reproducible technique, Figure 4-14 A & B. Larger drill bits, up to 1000 µm in diameter had the same unsuccessful results with the freeze-dried scaffolds, as after sintering the channels became blocked. Also, upon sintering of the drilled freeze-dried scaffolds, the channels sintered in a non-uniform way, Figure 4-14, which again was not reproducible.

4.4.3 Morphology Analysis

In the modified AW2 scaffolds the channels were analysed morphologically and the diameters were measured using SEM as described in section 4.3.6.1. Figure 4-15 to Figure 4-17, show a sample of channels and grooves on AW2 scaffolds. The average channel diameter was 1mm ±100µm. The channels in the grooves (average width 1 mm ±50 µm) on the bottom of the scaffold, and larger AW2 particles can be seen in Figure 4-15 and Figure 4-16. Figure 4-17 shows the channels on the top surface of the scaffolds, where clear necking between particles is visible.

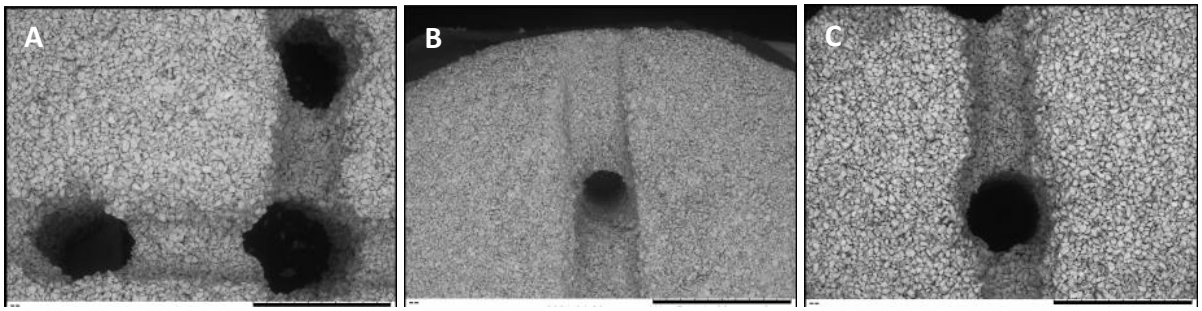

Figure 4-15: Modified AW2 scaffolds showing the grooves and channels (on underside of scaffold). Scale bars represent 2 mm.

Figure 4-15 shows the bottom side of the modified AW2 scaffolds with channels and grooves added post-sintering. The channels are relatively uniform in shape and distance to each other. The channels are primarily within the groove walls.

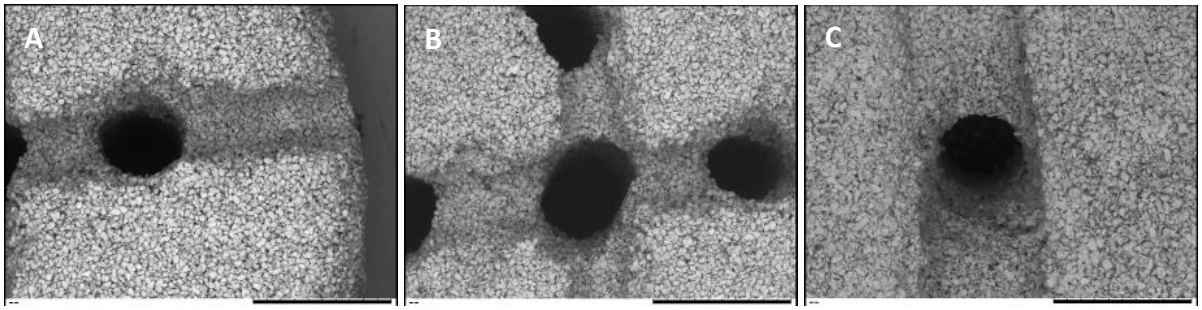

Figure 4-16: Sample SEM image of multiple modified AW2 scaffolds, scale bars represent 2 mm. Grooves and channels can be seen on the different scaffolds.

Figure 4-16 shows the bottom side of multiple modified AW2 scaffolds, with the grooves and channels clearly visible. The channels are relatively circular and uniform in size, and the grooves also appear to be uniform in width and depth. There are small diversions in shape of grooves and channels which are due to the crystalline nature of AW2 scaffolds and naturally uneven surface of scaffolds.

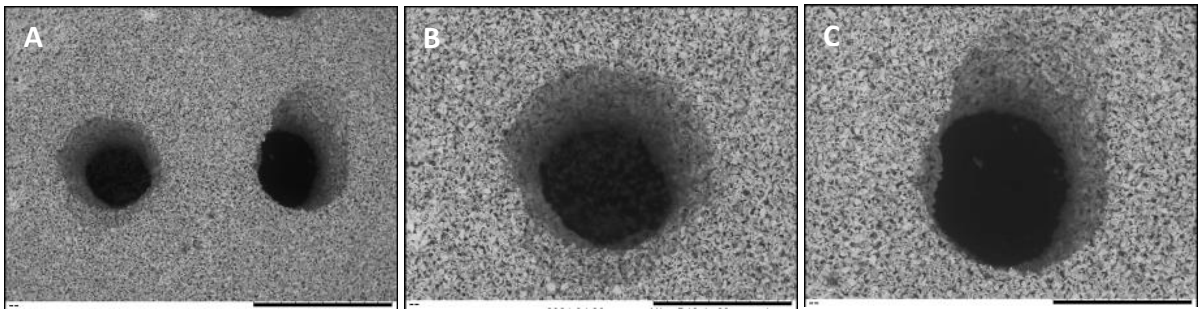

Figure 4-17: Sample SEM image of modified scaffolds, channels present on top side of scaffold. Scale bar represents 2 mm on A, on B & C scale is 1 mm.

Figure 4-17 shows modified AW2 scaffolds on the top side of the scaffold, the channels showing uniformity. The channels are circular in shape and the porosity of the AW2 scaffolds evident. The surface here shows more necking between particles at the top surface of the scaffold.

The results from the SEM analysis show uniform channels across scaffolds and uniform groove shapes and widths as well. The modification process was successfully repeatable, this method and result was utilized in the next chapter, and referred to as modified AW2 scaffolds, as the contain grooves and channels.

4.4.4 Porosity analysis

Porosity of scaffolds were evaluated using a density kit, based on Archimedes principal described in section 4.3.6.2. Figure 4-18 shows the total porosity (%) of the original AW2 scaffolds side by side with its modified AW2 counterpart. The scaffolds are labelled 1 to 4, for this porosity analysis four original AW2 scaffolds were tested first, and then they underwent modification, and were tested again. It is clear that modified AW2 scaffolds have more open porosity than the original scaffolds. The modified AW2 scaffolds have a significantly higher total porosity.

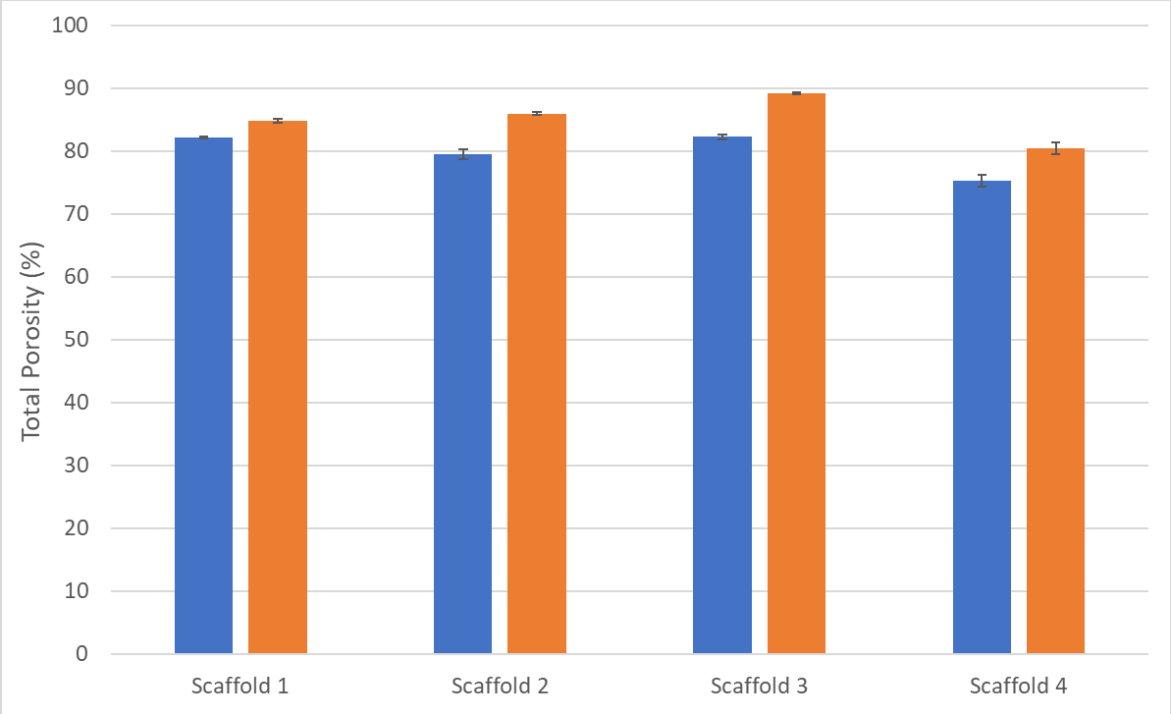

Figure 4-18: Total porosity (%) within AW2 scaffolds. Blue is original AW2 scaffold, orange is that same scaffold but modified with channels and grooves, N=3.

Figure 4-18 shows the original AW2 scaffold (blue) for total porosity (%) and then after modification with grooves and channels, it is shown in orange. The total porosity for all the scaffolds is between 75% and 88%. The total porosity significantly increased across all modified scaffolds compared to their original AW2 counterpart.

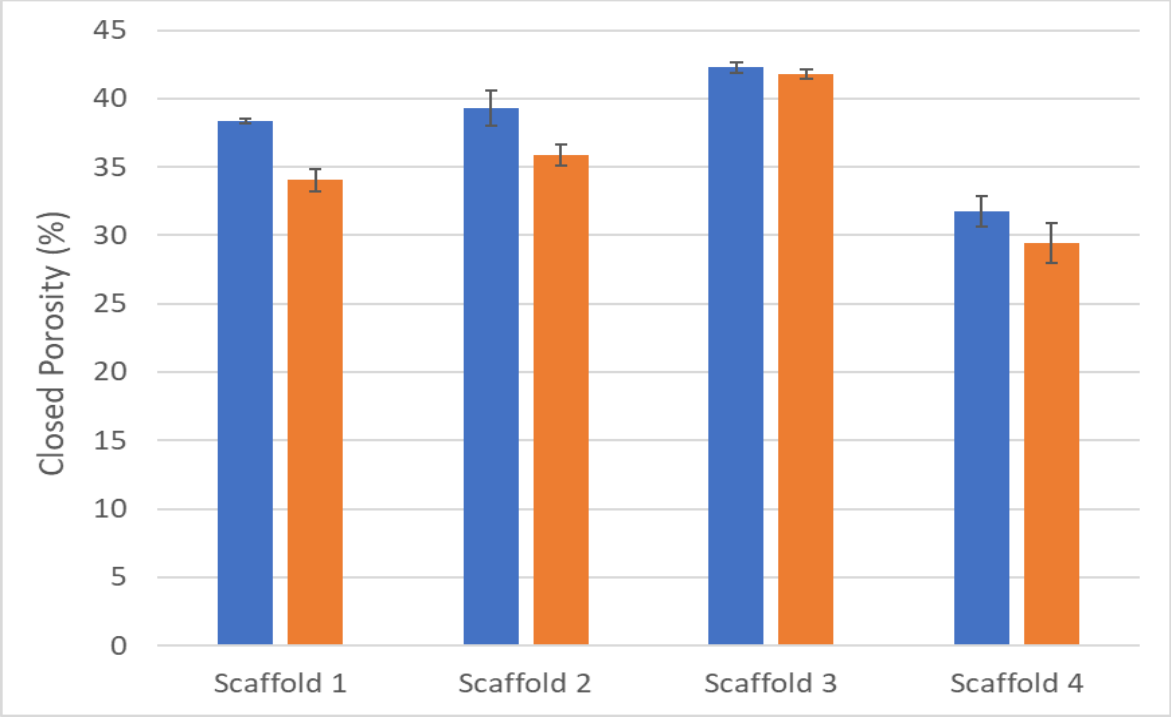

Figure 4-19: Close porosity (%) within both types of AW2 scaffolds. Blue is original AW2 scaffold, and orange bars are the same scaffold but modified with channels and grooves, N=3.

Figure 4-19 is a graph indicating the closed porosity (%) found in the AW2 scaffolds (blue) and its modified AW2 scaffold (orange). The modified AW2 scaffolds show less percentage of closed pores, compared to the original AW2 scaffolds. This indicates that the addition of the channels and grooves results in less closed pores in scaffolds.

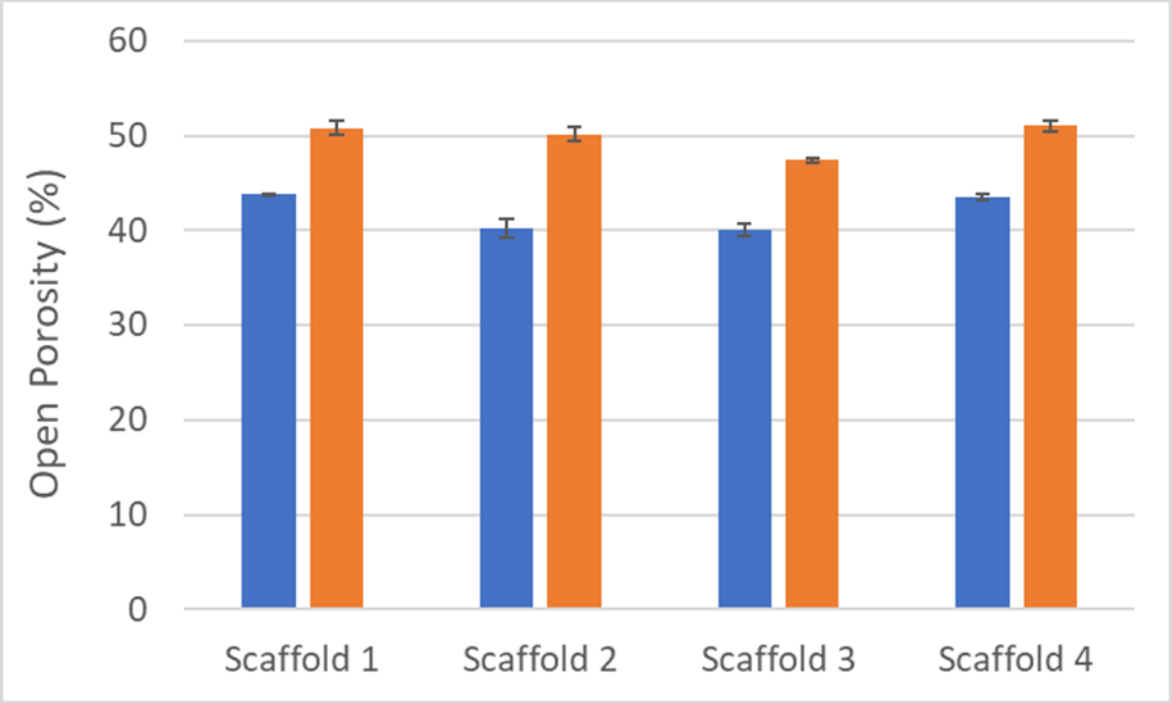

Figure 4-20: Open porosity (%) within the AW2 scaffolds (blue) and their modified counterparts (orange). Overall, the open porosity increases when the scaffolds have been modified, N=3.

Figure 4-20 shows the open porosity within the AW2 scaffolds (blue) and their modified counterparts (orange). The open porosity of the original AW2 scaffolds lies around 41 ±2 %, and when modified the open porosity increases to 49 ±2 %, this is almost a 20% increase in open porosity from the original value. This increase in open porosity might have an effect on the cells during the *in-vitro* tests. This will be investigated in the next chapter (Chapter 5). The modified scaffold has a significant increase in the open porosity, potentially indicating that some of the previously closed pores are now open due to the modifications (channels and grooves). Comparing Figure 4-19 and Figure 4-20, before and after post processing, it shows that the percentage of closed porosities are reduced, while the percentage of open porosities increase post modification, this can be interpreted that some of the closed pores are now open due to the modifications.

The results show that the modification on the original AW2 scaffolds resulted in an increase in over porosity (total porosity) and an increase in open porosity. This also consequently resulted in a decrease in closed porosity.

4.4.5 Nutrient Diffusion

The calibration curve (Figure 4-21) was used to determine the percentage of glucose released from the original AW2 scaffolds and the modified AW2 scaffolds. The curve is considered as a linear trendline ($R^2 = 0.987$), with the equation ($y = 7.37\ x$) used for the data analysis of the modified scaffolds. The values for glucose concentration above 25% have been omitted as they were not relevant to this study.

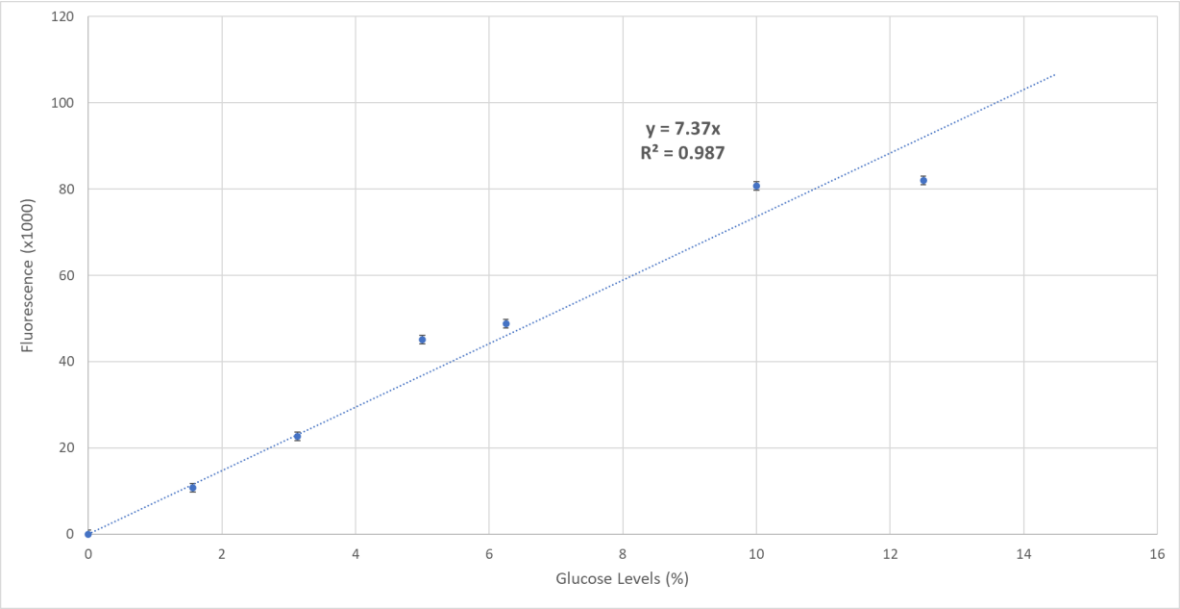

Figure 4-21: Calibration curve of 2-NBDG at different glucose concentrations for modified scaffold. R^2 value is 0.987 with $y=7.37x$. Error bars are standard deviations, $N=3$.

Figure 4-22 shows that the highest glucose released is from the modified AW2 scaffolds, which is due to the postprocessing modifications. One-Way ANOVA with Tukey's multiple comparison test was carried out on the data presented in Figure 4-22. The test showed that no statistical difference between the scaffolds exists; statistical significance was determined at $p < 0.05$.

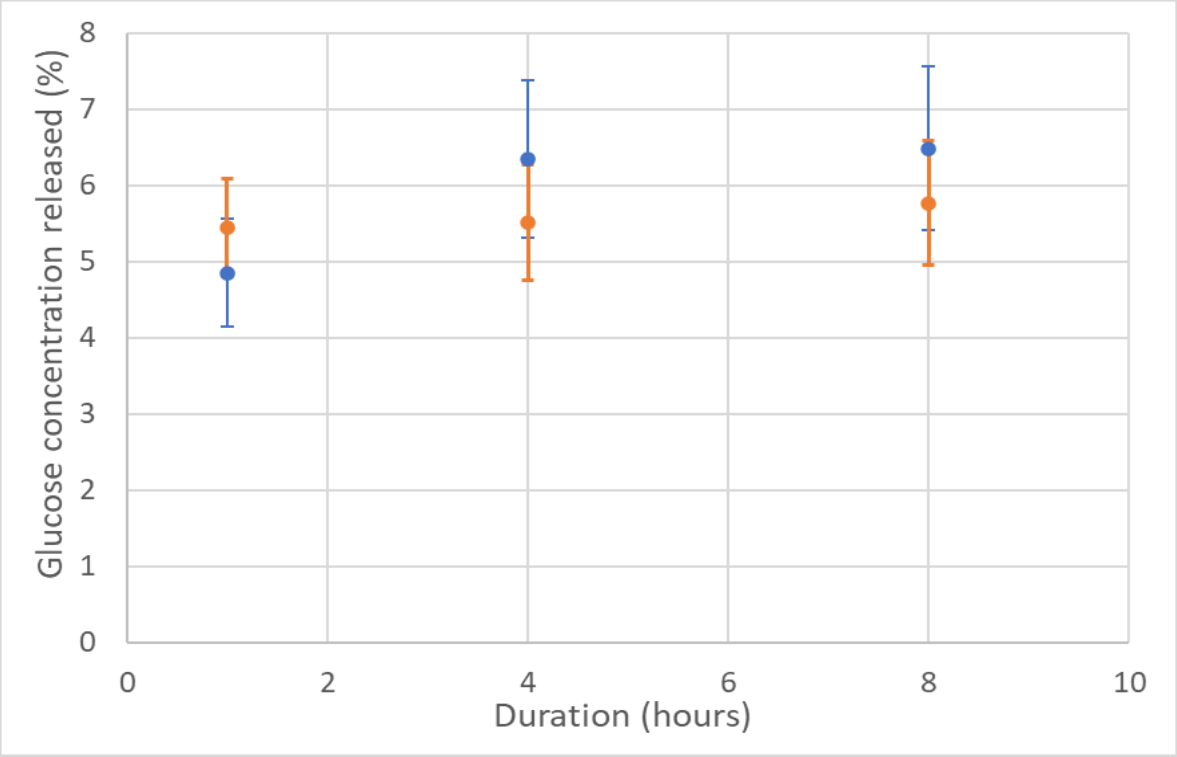

Figure 4-22: The glucose released after 24-hours in PBS. The original (blue) and modified (orange) scaffolds were kept in 2-nbdg solution for the duration (hours) and the Glucose released from these scaffolds after 24-hours in PBS are shown as a percentage (%). N=4, error bars represent standard deviations.

Figure 4-22 graph shows the glucose concentration released from scaffolds after 24-hours in PBS. The original AW2 scaffolds were tested first, and then they were post-processed (modified AW2 scaffolds), and the test repeated again. The duration in 2-nbdg solution is shown in hours, in relation to the glucose released after 24-hours in PBS. The modified scaffolds had released almost the same amount of Glucose across all durations, between 5.45% and 5.77%, therefore there are no significant differences. The original scaffolds have an increase in glucose released between 1-hour (4.85%) and 4-hours (6.35%) or 8-hours (6.5%), but there is no significant difference due to the standard deviations.

4.4.6 Mechanical Analysis

A sample stress against strain graph from modified AW2 scaffolds is shown in Figure 4-23. The stress starts to decrease at multiple points, but has a general increase until 3.6 MPa stress, when it then has a sharp decrease.

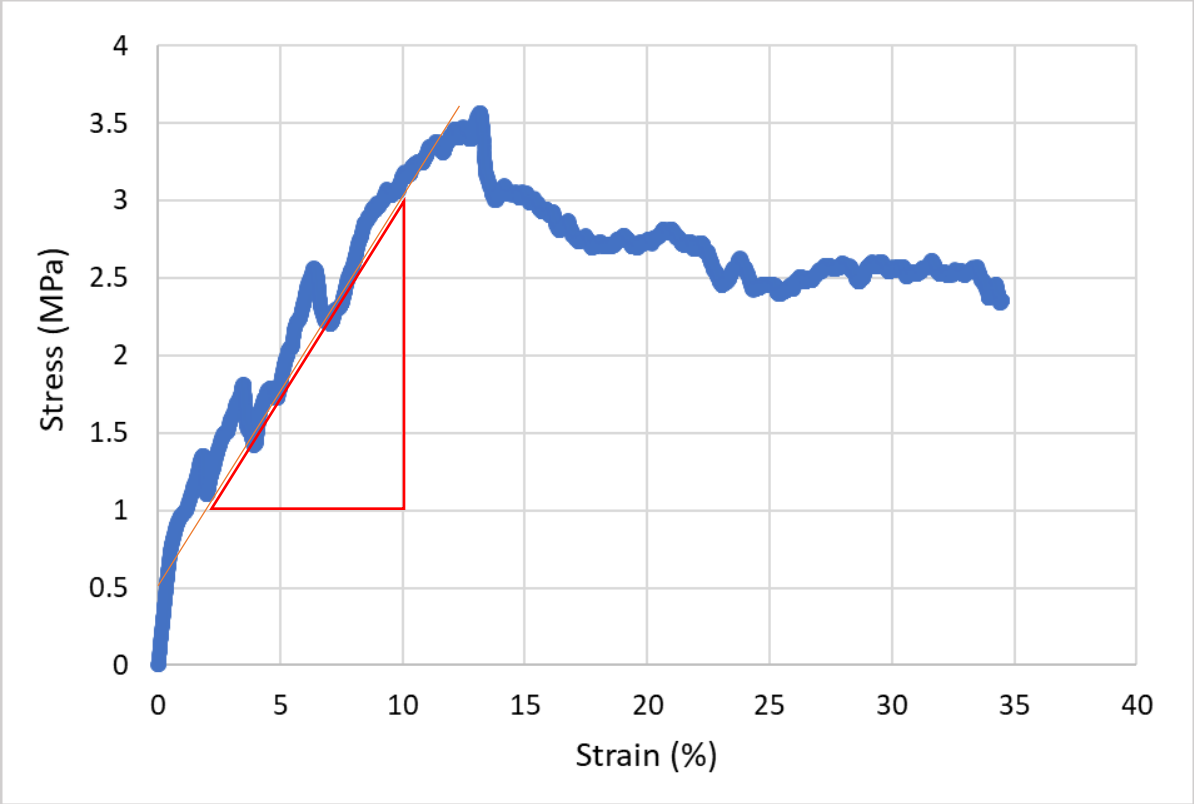

Figure 4-23: A stress- strain graph of a modified AW2 scaffold. The Youngs modulus was calculated at the gradient of the linear region, as shown in red.

The average Young's modulus for the modified AW2 scaffolds was 24 MPa to 27 MPa, as demonstrated in Figure 4-23. The figure shows that the modified AW2 scaffolds generally have a lower Young's modulus compared to the original AW2 scaffolds in Figure 3-21 (Chapter 3 – Scaffold Manufacturing Results, section 3.7).

4.5 Discussions

In this chapter multiple methods were explored to enhance the interconnectivity of the original AW2 scaffolds manufactured in previous Chapter 2, Methods section 2.3, made via the Thermally Induced Phase Separation (TIPS) method with 90:10 dioxane:water with 20 – 53 µm AW2 particle sizes. A series of methods, development and improvement eventually resulted in the successful modified AW2 scaffolds methods, which included drilled channels and grooves. Initially multiple other methods were trialled including various designs and manufacturing negative PLA mould using 3D printer. The void spaces in the negative moulds were increased in size during the method development, and AW2 trialled as a paste with

water and Ethanol, and AW2 TIPS slurry as well. Eventually AW2 slurry was the best method with the large negative moulds, as the slurry penetrated all the way through the negative mould, as shown in Figure 4-10 B & C. These AW2 slurry filled moulds underwent a two-step heat treatment (sintering process) and were unsuccessful, as shown in Figure 4-11. Clearly the material has collapsed and the AW2 that remained was not sufficient to have a 3D shape with the large interconnectivity that was designed originally. Although the results of the manufacturing process were not satisfactory using any negative moulds, the initial idea was valid, and further research is needed to acquire stable scaffolds. Further research should include using less 3D printed PLA, with larger voids (to ensure more AW2 penetration and material), which would in turn may give better stability to sintered scaffold. This development process was beneficial in the design development of scaffolds and inducing interconnectivity. The modified AW2 scaffolds (sintered AW2 scaffolds that had undergone groove additions and channel additions) were successful, and a repeatable process.

AW2 scaffolds were analysed using multiple different characterization techniques, the original AW2 scaffolds were characterised considerably before being modified and then characterised again in their modified state. The specific original scaffolds were modified to allow the results to be directly comparable. This was to ensure continuity and understanding of how the channels and grooves modifications affect the interconnectivity within the scaffolds. Understandably the same scaffolds could not be used for the mechanical tests, as this is a destructive technique, therefore the scaffolds were used in their modified form for this test. Non-destructive characterization methods were used to allow for comparison between the original and modified scaffolds.

Across multiple modified AW2 scaffolds, the channels diameters were consistent, however due to crystalline nature of the AW scaffolds, a slight diameter difference was evident. This could also be due to the particle size of the AW2 used in the original TIPS manufacturing process. The AW2 particle sized used to manufacture was 20 – 53 µm, therefore if 1 particle from each side of the drill bit was caught and drilled off, that can cause a larger opening around 116 µm. Also, during the drilling process there is the possibility of human error which occurs with user experience and practice. The channels' drilling process was practiced first on a sample of 3 scaffolds first, to ensure that repeatability could be obtained. It was discovered that 5 channels were a compromise between interconnectivity improvement

without compromising on the mechanical integrity of the scaffold. In the future, higher number of channels (e.g. 9) using a smaller drill bit (e.g. 200 µm) could be used, and an automated drilling process initiated.

The bottom surface of the scaffolds was rougher and more granular than the smoother top surface of the scaffolds. Therefore, on the top surface, the channels are more uniform and circular in shape, but on the bottom surface the channel diameters have slightly more variability and not always circular, as shown in Figure 4-16 B. The uniformity of the channels indicates a reproducible process. This slight variation in channel shape also corresponds to the crystalline composition of the AW2 material itself and the large particle sizes used, therefore, was expected.

In the density analysis the total porosity (Cheng et al., 2019) increased from original AW2 scaffolds compared to the modified AW2 scaffolds, Figure 4-18. The modification resulted in more open porosity (Lawrence and Jiang, 2017, Cheng et al., 2019), as shown with the density experiments. The increase in open porosity from the AW2 scaffolds to the modified scaffolds is evident in Figure 4-20. Increase in open porosity, suggests an increase in interconnectivity. Arguably interconnectivity is more important than pore size (Hutmacher, 2001), and the size of the interconnections should be of a large size, which is important regarding cell migration and proliferation (Hutmacher, 2001, LeGeros, 2002). The modified AW2 scaffolds therefore could increase the diffusion and exchange of nutrients, which could be beneficial to cell proliferation and tissue engineering applications.

Figure 4-22 indicates that the there is no significant difference in the release of glucose into PBS with relation to duration in 2-nbdg, the durations tested with 2-nbdg were 1-hour, 4-hours, and 8-hours. In the previous chapter, the scaffolds were tested up to 24 hours with 2-nbdg, but results showed that there was no significant different between 6 hours and 24-hours, therefore in these tests only up to 8 hours was tested. This test is important in determining the optimal durations for the scaffolds to be in media (scaffold preparation step) prior to cell seeding. This test showed that 1-hour is ideal for pre-soaking the scaffolds in media prior to seeding being carried out although, 1–4 hours is preferred due to potential variations (e.g., room temperature etc.). Although, soaking for just 1-hour would also be beneficial for the scaffolds and ultimately the cells. Therefore, a 1-hour soaking time of scaffolds prior to cell seeding was determined and will be utilised in the *in-vitro* tests.

The channel diameters are around 1 mm ±50 µm, it has been shown in literature that pore diameters over 300 µm are considered ideal for tissue growth (Bose et al., 2003, Karageorgiou and Kaplan, 2005, Murphy et al., 2010, Cheng et al., 2019), with pore diameters over 100 µm are considered necessary for cell attachment. In theory these additional channels should allow for tissue growth and aid in the media flow throughout the scaffold (Espanol et al., 2009). The increase in media flow will also aid in nutrient diffusion across the scaffold (Hollister, 2005, Gentile et al., 2012, Lawrence and Jiang, 2017).

4.6 Summary and Conclusions

Two groups of techniques were examined for interconnectivity improvement. The first group, enforcing connectivity during manufacturing using PLA scaffolds as negative mould, did not produce a stable outcome. The second group improved interconnectivity by adding channels and grooves to the scaffold as a postprocessing step. The postprocessed modifications on the original AW2 scaffolds resulted in better open porosity (interconnectivity) and total porosity. The interconnectivity parameters were characterised by density measurement, nutrient diffusion, SEM imaging, and mechanical tests. These tests helped determine the porosity differences between original scaffolds and modified scaffolds. Five channels and cross shaped groove was added to the scaffolds to encourage interconnectivity and porosity. The modified scaffolds had more open porosity and five larger pores than the original scaffolds. The biological benefits of the modifications and the original AW2 scaffolds will be investigated in the next chapter by *in-vitro* tests.

5 *In-vitro* tests with Scaffolds

5.1.1 Aims and Objectives

The overall aim of this chapter was to evaluate the possibility of using 90:10 TIPS AW2 3D porous scaffolds (as described in Chapter 2 – Materials and Methods) for tissue engineering applications. The AW2 scaffolds (original and modified) were evaluated under *in-vitro* conditions for 21 days.

To achieve this aim, the following objectives were identified:

1) To identify which cell type to use on the scaffolds;
2) To prepare the scaffolds for cell seeding;
3) To evaluate a suitable cell seeding density on the scaffolds;
4) To morphologically evaluate the cell seeded scaffolds;
5) To morphologically compare original scaffolds with the modified scaffolds.

5.2 Introduction

5.2.1 Cell Selection

Studies relating to osteoblast cell culture on porous scaffolds have mainly focused on comparing the suitability of different scaffolds against each other, evaluating the effect of different culture medias, and culture conditions. These three factors in addition to the initial number of cells seeded have been found to have a profound effect on cell proliferation and extracellular formation on scaffolds.

The effect of different cell lines was investigated by (Stevenson et al., 2016), where they used two different human osteoblast cell lines on porous titanium-surfaced scaffolds, surprisingly the commonly used MG63 human osteosarcoma cell line was found to behave differently to the scaffolds compared with primary human osteoblast cells (Cell Applications, 406-5a). Cells were seeded on cylindrical scaffolds (12 mm diameter and 9 mm depth) at 2.5 x10^4 cells per cm^2. At 24h the MG63 cells had an increase of 200% to 500% of metabolic activity (compared to the control) dependent on scaffold type. MG63 cells are tumour cells and therefore are expected to have fast doubling proliferation rates. In contrast human osteoblast cells (had a

decrease of 40% to 80% in metabolic activity. Metabolic activity was used as a representative of cell numbers. From 24 hours to 96 hours, MG63 cells had an associated decrease in metabolic activity on all of the different scaffolds. Primary human osteoblast cells showed an increase in metabolic activity on all but one of the scaffolds between 24h and 96 hours (Stevenson et al., 2016). In conclusion, it was found that primary human osteoblast cells elicit greater differences particularly in terms of cell survival/mortality as compared with MG63 osteoblast-like cell lines.

(Varley et al., 2017) used foetal-human osteoblast cells (Cell Applications, 406-05F) at a density of 6.5 $x10^4$ cells per cm^2 on 99% porous cylindrical collagen-glycosaminoglycan scaffolds (5 mm diameter, 4 mm depth) across different dynamic bioreactor conditions (using a 50 ml Falcon), which were compared to static conditions. It was found that 10 rpm and an 85% chamber fill was the optimum condition for cell proliferation on the scaffolds. The rotation of fluid improved mass transport into cells/scaffolds and consequently increased cell proliferation (Varley et al., 2017).

(Junkar et al., 2016) examined primary human osteoblast cells (Cell Applications, 406-05) at a seeding density of 1.0 $x10^4$ cells per cm^2 on different TiO_2 nanotube surface conditions for biomedical devices. Osteoblasts were used specifically as they are relevant for *in-vitro* models with the aim of studying biological compatibility of materials with the intention for bone implants (Junkar et al., 2016). It was found that after 7 days in culture, the cells had viability (MTT assay) of between 0.8 and 1.5 times compared to the control sample (plain Ti foil) (Junkar et al., 2016). From this study it was concluded that different surface properties can greatly affect the cytocompatibility *in-vitro*.

(Jones et al., 2007) used human osteoblast's isolated from the femoral head of patients; they used 8.0 $x10^4$ cells onto the scaffold surface (92% porosity, 10 x 10 x 5 mm bioactive glass 70S30C scaffold) with different cell culture medias (supplementations). The controls used here were Thermanox (TMX) discs, although it is more common to use tissue culture plastic or glass coverslips as a control. It was found that the use of these scaffolds supported osteoblast differentiation within the 21-day culture period, without the addition of supplements (Jones et al., 2007).

This chapter focuses on evaluating the suitability of the developed scaffolds for cell attachment and infiltration into the scaffold. To this end, different steps for experiments were designed and tested on small sample size (pilot study). Based on the initial experiment, the process was optimized for the main experiment which was performed on a large number of scaffolds for long term duration (21 days), with the original AW2 scaffold design and also the modified AW2 scaffolds. This chapter presents the design methodology (section 5.3) with materials used and essential preparation steps and considerations required before cell seeding. This section also covers various evaluation techniques including cell viability assays and morphological characterization (section 5.3.7) and methods employed to compare the results against each other. The result is presented in section 5.4, covering the pilot study which was used to estimate the optimum cell seeding density for the main experiment. It follows the results of experiments on AW2 scaffolds and modified postprocessed AW2 scaffolds. It also compares the number of viable cells measured using Presto Blue assay and Live/Dead analysis, mechanical strength of scaffolds after cell culture. In the investigations for the AW2 scaffolds, originally primary Adult human osteoblasts (Cell Applications, 405-5A) were planned to be used, due to great difficulty in obtaining the cells, primary foetal-human osteoblast cells were used (Cell Applications, 405-05F). Section 5.5 focuses on evaluating the results and performing comparative evaluation of the suitability of AW2 scaffold before and after postprocessing.

5.3 Materials and Methods

5.3.1 Materials

Unless otherwise mentioned, any water used was high quality deionised water from the Purite 300 water purification system (Purite, UK). During cell culture, Human Osteoblast Growth Medium (417-500, Cell Applications inc.) was used. Human Osteoblast Differentiating media (consisted of Human Osteoblast Growth media + 7.5 mM β-Glycerophosphate disodium salt hydrate (molecular weight 216.04 g/mol, Sigma Aldrich) + 200 nM Hydrocortisone (molecular weight 362.46 g/mol, Sigma Aldrich). For diluting supplements, Ethanol 200 proof purity, (Sigma Aldrich) and Sterile Filtered Water (molecular weight 18.02, Sigma Aldrich) were used. Dulbecco's Phosphate Buffered Saline (modified without calcium chloride and magnesium chloride, Sigma Aldrich) referred as PBS unless stated otherwise. Dimethyl sulfoxide (molecular weight 78.13 g/mol, Sigma Aldrich) referred to as DMSO.

Foetal Bovine Serum (FBS, Thermo Fisher Scientific). Apatite-Wollastonite 2 scaffolds (AW2 scaffolds) made according to section 2.3.4, with 90:10 Dioxane:Water were used for the *in-vitro* tests, for ease of reading these scaffolds will be referred to as AW2 scaffolds in this chapter. The AW2 scaffolds with post-sintering modifications will be referred to as modified AW2 scaffolds to ease reading.

5.3.2 Scaffold Sterilisation

Sterilisation of AW2 scaffolds and modified AW2 scaffolds was required prior to cell seeding. Hold scaffold using plastic tweezers and used pressurised gas (compressed air supply in lab) to remove any debris from each scaffold. In a Tissue Culture hood, each individual AW2 scaffold was put into a well of a sterile 24 – well plate. To each well add 1.5 ml of 100% Ethanol on each scaffold, then placed on an Orbital Shaker machine at 80 rpm for 10 mins, this is to ensure there were no loose debris in the scaffolds. Tweezer were used to carefully put each scaffold in a new well, added 1.5 ml of fresh 100% Ethanol to each well, placed plates under UV light lamp (UVP, UVLMS-38 EL series 3UV Lamp) at wavelength 254 nm for 30 mins in Tissue Culture hood, used tweezer to turn scaffolds upside down in ethanol, UV lamp was again for 30 mins. Used aspirator to aspirate ethanol from each well and scaffold. Wash each well twice with 1.5 ml PBS and aspirator, for the final wash place scaffolds with PBS under UV lamp for 30 mins. Aspirate PBS from wells and placed plates with lids off under UV lamp for 1–hour in Tissue Culture hood to allow for AW2 scaffolds to dry. Use parafilm around the plates to aid sterility until autoclave stage. Scaffolds were placed in an empty tip box and autoclaved on a "glass cycle" (glass cycle is defined at 121°C for 20 mins, Astell Classic AMB 430 Autoclave), once cycle was finished the scaffolds were put into 24–well plates in a Tissue Culture hood, under UV light for 20 – 30 mins prior to pre-cell treatment.

5.3.2.1 *Pre-cell treatment of Scaffolds*

After the UV light treatment, to pre-treat the scaffolds 1 ml of osteoblast growth media was added to each well for 5 mins in Tissue Culture hood. The media was aspirated, and then 1 ml of osteoblast growth media was added to each well again, place plates in incubator at 37°C for 1-hour. The AW2 scaffolds were considered as suitable for cell seeding.

5.3.3 Glass Coverslip Sterilisation

To sterilise the glass cover slips (which were used as a positive control), 13 mm diameter coverslips (VWR, thickness no1, borosilicate glass) were used. Empty 1000 µl tip boxes were

used as a flat surface, an excess of cover slips in a single layer were spread across two of these tip boxes in a Tissue Culture hood. Initially, the glass cover slips were washed in 70% Ethanol. The tip boxes were placed under the ultraviolet light in the tissue culture hood for 30 mins to ensure they were dry, the coverslips turned over and placed under UV light for a further 30 mins. These sterile coverslips were placed into the appropriate wells of 24–well plates. Prior to cell seeding, the coverslips were washed with 1 ml of osteoblast media for 1-hour in a 37°C incubator.

5.3.4 Cell Culture – Foetal Human Osteoblasts

The adherent primary cells used in this study were foetal Human Osteoblast Cells (HOb, 405-05F) obtained cryopreserved at passage 2, manufactured by Cell Applications Inc, supplied by Sigma Aldrich. The cells were expanded multiple times and placed in an incubator (with a humidified atmosphere of 5% CO_2 at 37°C) and used at passage 7 for seeding onto scaffolds.

5.3.4.1 *Cell thawing and Cryopreservation*

The cryopreserved osteoblasts were defrosted by suspending the cryogenic tube in a 37°C water bath until roughly 70% thawed. In a 15 ml falcon, 10 ml of room temperature osteoblast growth media was added. A 1000 µl tip and micropipette was used to transfer the thawed osteoblast cells into the falcon with growth media, invert falcon gently twice to ensure homogeneous mixing of cells and media, then centrifuge (Centrifuge 5702 – eppendorf) at 200 g for 5 mins at room temperature. Aspirate the supernatant and resuspend the cell pellet in 10 ml osteoblast growth media. The cells were counted (as described in 5.3.4.2) prior to seeding in a 25 cm^2 tissue culture treated flask.

To cryopreserve the osteoblast cells after expansion in 175 cm^2 flasks, cells were used at roughly 70% confluency. The adherent osteoblast cells were washed with room temperature PBS for 30 seconds and the PBS aspirated. Fridge temperature (4°C) Trypsin was used at a rate of 0.5 ml per 25 cm^2, and flask observed at room temperature under the light microscope for roughly 70 % of the cells to detach from the flask (roughly 2 to 3 mins). In the tissue culture hood, osteoblast growth media was added to the flask at twice the volume of trypsin used. An appropriately sized stripette was used to transfer the trypsin cell media solution to a falcon tube, 5 ml of fresh growth media was to the flask to detach and transfer any remaining cells and place into falcon tube. The falcon was centrifuged at 200 g for 5 mins. The supernatant was aspirated, and cell pellet resuspend in 5 ml of freezing solution (90 %

FBS + 10% DMSO), the cells were counted, and freezing solution added to equate roughly 1.0 x10^6 cells per 1 ml of solution. Place 1 ml of cell solution into each 1.8 ml internally threaded cryogenic vial (Corning), each vial placed into an 18–hole Nalgene Mr Frosty freezing container (Sigma Aldrich). The freezing container was stored in a -80°C freezer for 48–hours, then the vials transferred to liquid nitrogen storage (-196°C).

5.3.4.2 *Cell Counting*

To count viable cells, a Typan Blue Exclusion test was used after cell defrosting, cell expansion, cell cryopreservation and cell seeding onto scaffolds/plates/coverslips. Trypan blue dye (Trypan Blue Solution 0.4%, ThermoFisher Scientific) was used as it stains non-viable cells dark blue (visible under light microscopy), but viable cells do not take up this impermeable dye.

To count cells, an aliquot of 20 µl of media containing cells was mixed with 20 µl of trypan blue in a 0.2 ml tube. The number of unstained cells were counted using a 0.1 mm depth Neubauer chamber haemocytometer (Hawkley, UK) viewed under a light microscope with a phase contrast filter.

5.3.5 Cell Seeding - Density Assessment

A preliminary experiment was required to determine cell-seeding density of the foetal human osteoblast cells. To determine which cell seeding density to use in the main experiments (section 5.3.7), two cell densities were trialled: 2.5 x10^5 cells and 5.0 x10^5 cells. The cells were seeded as a 250 µl drop onto AW2 scaffolds and tissue culture plastic in 24–well plates incubated for 1–hour, then additional media added to obtain 1 ml total media volume. The scaffolds were kept in the same wells throughout the duration of the experiment (14 days).

5.3.5.1 *Pilot Study - Method*

The AW2 scaffolds were sterilised as described in section 5.3.2 and prepared for seeding as described in section 5.3.2.1. Only osteoblast growth media was used throughout the whole duration of the experiment. Presto Blue cell viability assay was carried out on days 1, 3, 5, 7, 10, and 14 as described in 5.3.8. After 14 days, the following tests were carried out on the scaffolds: Alizarin Red (section 5.3.10.1), Actin DAPI stain (section 5.3.11), and SEM imaging (section 5.3.10.2).

5.3.6 Main Experiment

Following the preliminary experiment, the results were used to determine the methods for the main experiment. The main experiment is described in this section. All scaffolds and controls were in triplicate and then repeated 2 weeks later, unless otherwise stated.

5.3.7 Optimized Cell Seeding onto Scaffolds

To obtain accurate number of cells seeded onto the scaffolds only and to allow for optimised imaging, the methods were altered for these main experiments.

After the pre-cell treatment of the AW2 scaffolds as previously described in 5.3.2.1, the osteoblast growth media was aspirated from each well using a vacuum aspirator. On top of each scaffold, 2.0×10^5 foetal osteoblast cells in 200 µl of media was gently added, as shown in Figure 5-1.

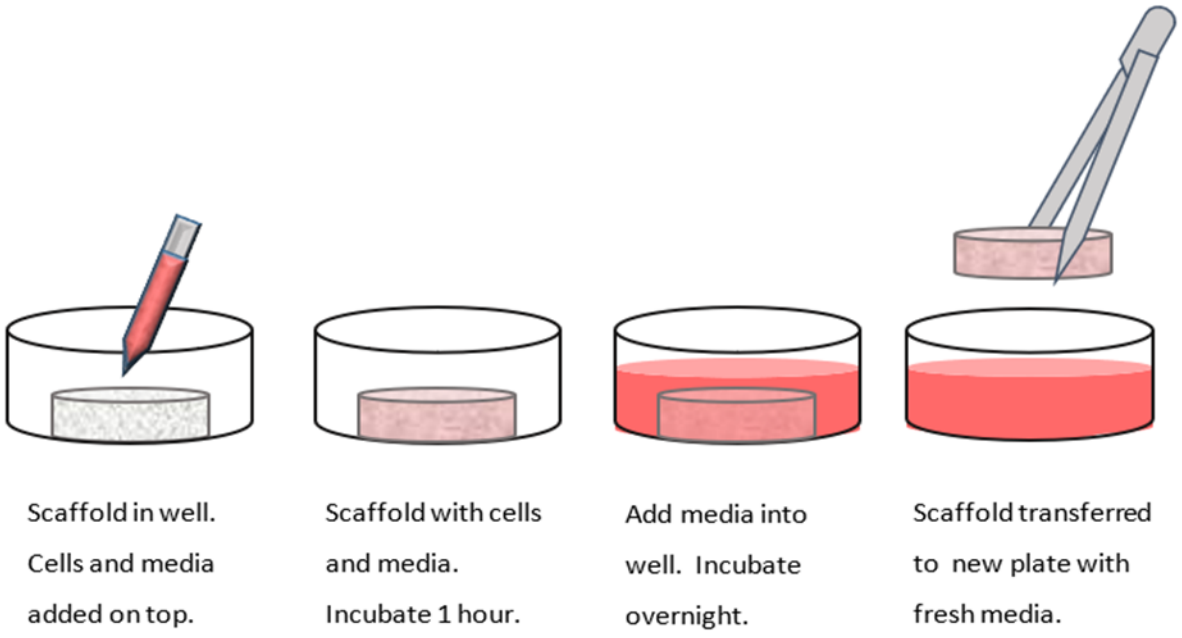

Figure 5-1: Illustration of cell seeding technique with AW2 scaffolds in a well of a 24–well plate.

The plates were placed in a 37°C incubator (Thermo Scientific, MIDI 40 CO_2 incubator) for 1–hour for cells to attach. After 1–hour in the incubator, 800 µl of osteoblast growth media was added to each well, then placed into 37°C incubator (5% CO_2 overnight). The following day (Day 1), using sterile metal tweezers the cell seeded scaffolds were carefully placed into a new 24–well plate with 1 ml of fresh media. The wells were refreshed with media every

second day with growth media, unless stated otherwise. To induce extracellular matrix formation of the osteoblast cells, on day 9 the media was changed to the differentiating media, and this was refreshed regularly until day 21 (final day of experiment).

5.3.8 Cell Viability and Growth

PrestoBlue Cell Viability Reagent (ThermoFisher Scientific) was used for obtaining cell viability and monitoring the growth of cells. It is a resazurin-based solution (resazurin is non-toxic) that is reduced to resorufin by viable living cells. This reduction is detected by a visible colour change (dark blue to red/pink colour) and is fluorescent detected by a microplate reader (BMG Labtech, FLUOstar Omega) using fluorescence (excitation/emission 544/590). PrestoBlue has a recommended incubation time between 10 mins and 4–hours depending on the number of cells and the sample type, and according to manufacturer's description can detect as few as 98–cells in a well. Calibration curves are required to help quantify the fluorescence readings from the microplate reader, and to determine the best incubation time due to the cell type used. Cell viability media consists of DMEM (no glucose, no glutamine, no phenol red, ThermoFisher Scientific), 1% GlutaMAX, 1% Penicillin Streptomycin (Sigma Aldrich) and 10% FBS inverted four times to ensure homogeneous distribution. Cell viability media was brought to room temperature prior to use.

5.3.8.1 *PrestoBlue Calibration Curve*

It is necessary to produce a calibration curve for every new batch/lot of PrestoBlue used and for each specific cell type. In this case, Foetal Human Osteoblast Cells were used at passage 7, then seeded onto 24–well plate at varying cell concentrations from 1 $x10^3$ cells up to 3.5 $x10^4$ cells, using the cell counting protocol in section 5.3.4.2, for an overnight incubation. An excess of cell viability media was prepared, and in a separate falcon prepare PrestoBlue mix consisting of, 10% PrestoBlue Cell Viability Reagent and 90% cell viability media. Media was aspirated from each well, add 1 ml of PrestoBlue mix to each well including a background well and incubate. At set time points 100 µl of the PrestoBlue mix from each well was put into a well of a 96–well plate, the plates were read on the microplate reader (FLUOstar Omega Microplate reader, BMG Labtech, Germany) and the gain equated at each time point. The time points were 30 mins, 1 h, 1.5 h, 2 h, 2.5 h, 3 h and 4 hours. The timepoints and calibration curves used here are for 2D cultures.

5.3.8.2 *Presto Blue Method on Cell Seeded Scaffolds*

Cell viability was carried out at set time points, on days 1, 3, 5, 7, 9, 14, and 21. In a tissue culture hood with the lights off, an excess of cell viability media was prepared. In an appropriate falcon, 10% PrestoBlue Cell Viability Reagent and 90% cell viability media was prepared, then inverted four times and covered with foil. Media was aspirated from all wells carefully, then 1 ml of PrestoBlue mix was added to each well and the cell plate was placed in a 37°C incubator. After the set time (1–hour) the cell plate was moved from the incubator into tissue culture hood, and, using a 200 µl micropipette and tip, 100 µl of solution from each 24–well was added into a 96–well clear flat-bottom plate (Corning). The cell plate was returned to the incubator for a further 30 mins. The fluorescence values of the 96–well plate was measured in the microplate reader using excitation and emission filter of 544 nm and 590 nm respectively, and set at the correct gain as calculated in initial calibration curve experiment. After 30 mins, the cell plate from incubator was placed into the tissue culture hood, and, using a 200 µl pipette, 100 µl of solution from each 24–well was added into a 96–well flat bottom plate, the fluorescence of the 96–well plate was then measured in the microplate reader. PrestoBlue mix was aspirated from each well, each well was washed once with cell viability media and aspirated, then 1 ml of osteoblast growth media (or osteoblast differentiating media depending on the day of experiment) was added to each well, before it was returned to the incubator.

5.3.9 Live/Dead Cell Viability Assay

ReadyProbes Cell Viability Imaging Kit Blue/Green (ThermoFisher Scientific) were used for morphologically determining the viability of cells. The AW2 scaffolds naturally fluoresce red and orange during confocal microscopy (Nikon A1 confocal microscope), therefore this specific kit was required. The NucBlue live stains the nuclei of live cells blue, and the NucGreen dead reagent stains the nuclei of the dead cells green. In a falcon, room temperature osteoblast media was prepared in excess, 2 drops of each NucBlue and NucGreen regent for millilitre of media was added and inverted four times to distribute evenly. The media was aspirated from each well of the 24–well plate without damaging cells. Added 1 ml of media containing regents to each well, and then incubated for 15 mins. The media containing the reagents was removed, and replaced with fresh media, then imaged immediately using confocal microscopy. NucBlue excitation/emission 360/460 nm, NucGreen

excitation/emission 504/523 nm. Live/Dead assay took place on day 1 and 3 of the main experiment.

5.3.10 Calcium Deposition Investigation

The osteoblast cells are expected to produce calcium deposits and mineralization when given differentiating media, which would indicate *in-vitro* bone formation. Alizarin Red Stain is an orange-red coloured stain used to identify calcium, usually in cultured cells *in-vitro*.

5.3.10.1 *Alizarin Red Staining*

Alizarin Red solution was prepared by dissolving 2 g of Alizarin Red Salt in 100 ml of water, agitated using benchtop vortex. The pH of the solution was adjusted to 4.1 – 4.3 using either Ammonium Hydroxide solution (NH_4OH, 1 molar, Sigma Aldrich) or Hydrochloric Acid (HCl 37%, Sigma Aldrich). The pH was checked prior to every use and adjusted to pH 4.1 – 4.3, the required volume was filtered through 0.22 µm syringe filter equipped with a PES membrane.

Remove plate from incubator, media is aspirated carefully, and washed with PBS twice. PBS was aspirated and 1.5 ml of 10 % neutral buffered formalin (Sigma Aldrich) was added to each well and placed on orbital shaker at 80 rpm for 60 mins at room temperature. The neutral buffered formalin was removed carefully, and cells washed with water before 1 ml of Alizarin Red Solution was added, plate was covered in foil and placed on orbital shaker at 80 rpm for 45 mins at room temperature. Aspirate the Alizarin Red solution, and wash wells four times with water for 5 mins at each wash. Aspirate the water and add 1.5 ml 2.5% Glutaraldehyde solution to each well. Samples were imaged using Leica Microscope (Leica M165 FC). Alizarin red staining was carried out on day 1, 14 and 21 of the main experiment.

5.3.10.2 *SEM Fixation and Imaging*

Samples from 5.3.10.1 were stored in an excess of 2.5% Glutaraldehyde solution, stored in the fridge (4°C) covered in aluminium foil. Prior to gold coating, a dehydration process was required. The Glutaraldehyde solution was aspirated, without disturbing cell layers, and washed three times with PBS. The dehydration process consisted of a series of 45–minute ethanol in deionised water washes (25:75, 50:50, 75:25, 90:10, 100:0) at room temperature. The samples in 100% ethanol were then taken to the Newcastle University SEM facility for gold coating using a Polaron Gold Coater (sputter time 40 seconds, 10 nm thickness, at 40

mA). Scanning electron microscopy imaging was carried out on two machines: Tescan Vega 3LMU and Hitachi TM3030.

5.3.10.3 *Alkaline Phosphatase activity*

The alkaline phosphatase (ALP) activity from each sample (cell seeded AW2 scaffolds and controls, and negative controls) was monitored using an Alkaline Phosphatase Assay Kit (Colorimetric) (Abcam, UK). In this kit p-nitrophenyl phosphate (pNPP) is used as a phosphate substrate which becomes yellow in colour when dephosphorylated by ALP, absorbance was measured on microplate reader at 405 nm. In brief, the culture media around the samples were analysed directly using the manufacturer's protocol. The culture media was collected before a media refresh, or prior to another analysis, therefore the culture media was in contact with the sample for at least an overnight incubation. The standards were prepared fresh every time the kit was used, according to manufacturer's protocol. Each sample was carried out in replicate and 80 µl of culture media used per well, incubation was at lab room temperature with the plate covered using foil for 60 mins, after which stop solution was added. The protocol on the microplate reader was set to shake for 30 seconds at 600 rpm linear before the plate was read at excitation 405 nm. Samples that produced signals higher than the highest standard were either analysed for bubbles (bubbles removed using a 10 µl tip) and read again, or were diluted in appropriate buffer and reanalysed – then the dilution factor was used in calculations.

5.3.10.3.1 ALP Standard curve calculations

The standard curve is required as the curve equation is used for calculating the amount of pNP in each sample well and, consequently, the ALP activity. Firstly, the corrected absorbance values were obtained by subtracting the mean absorbance value of standard 1 (blank) from all standard readings and sample readings. The duplicate readings for each standard were averaged and the readings plotted, e.g. using Microsoft Excel, to construct the standard curve. The linear trendline equation was generated and the R^2 value was obtained for the fitted trendline.

5.3.10.3.2 Calculations for ALP activity

The equation for standard curve was used to calculate the ALP activity for each of the samples, equation (15). The duplicate readings were averaged for each sample, which resulted in more accurate estimation of ALP activity. The background control wells' absorbance intensity was

used to correct each positive control well, the values for non-seeded scaffolds (negative controls) were used as a background in the AW samples. The equation for ALP activity in (µmol/min/ml) or (U/ml) is as follows:

$$ALP\ Activity = \left(\frac{B}{\Delta T * V}\right) * D \quad (15)$$

The amount of ρNP in a sample well, calculated from the standard curve (µmol), is "B". Reaction time (mins) is "ΔT", which is multiplied by the original sample volume (mL) added to the reaction wells "V". The sample dilution factor is denoted as "D".

5.3.11 Immunofluorescent Staining and Confocal Microscopy

ActinGreen 488 ReadyProbes reagent (ThermoFisher Scientific) to detect actin is visible as green in cells, and DAPI as blue nuclei in cells. First, media was aspirated from wells without damaging cell layers. Then 1 ml of room temperature Paraformaldehyde solution (4% in PBS) was added to each well, and incubated for 30 mins to fix cells. In an appropriate falcon, DAPI solution with PBS was made and kept covered with foil, after cells first 30 min in fume hood, these were washed once with PBS, and then added 1 ml of DAPI PBS solution to each well, incubated in dark for 30 mins. In an appropriate falcon, PBS with two drops of ActinGreen 488 reagent per millilitre of PBS was added and inverted four times to ensure even distribution, kept covered with foil. After the incubation with DAPI PBS, aspirated and washed with PBS three times. Added 1 ml of ActinGreen and PBS solution to each well, incubated in dark for 30 mins. After final incubation, aspirated the solution and washed three times with PBS, the cells were imaged as soon as possible. Stored with excess PBS, covered with foil and kept in 4°C fridge. Imaging was carried out using confocal microscopy (Nikon A1 microscope), ActinGreen 488 excitation/emission 495/518 nm FITC, for DAPI excitation/emission 360/460 nm.

5.3.12 Mechanical Test on Scaffolds

Compression analysis using a Shimadzu Compression Tester (Shimadzu Corporation, 2014 model AGS-X with 10kN load cell) was undertaken to evaluate the mechanical properties of the cell seeded scaffolds. Compressive strength and Young's modulus can be derived from the compression test, as described in Chapter 2, section 2.11 The cell seeded scaffolds and controls were used at their specific time points (day 1, 3, 7, 14 and 21), the scaffolds were

treated with paraformaldehyde for 30 minutes, then kept in sterile PBS until the day of the mechanical testing. The wet scaffolds diameters were measured on both sides and the height was measured using a digital calliper. The scaffold was placed into the PBS again for 1 min after the calliper measurements, and then this wet scaffold was placed on a single sheet paper of single ply tissue for 30 seconds before being placed into the machine.

The parameters were a crosshead rate of 0.5 mm min^{-1} with a load cell up to 10 kN for these wet scaffolds. The average dimensions of the scaffolds were used for calculations, as previously explained in Chapter 2, section 2.11, using Equation (10).

5.3.13 Statistical Analysis

All graphs show a mean of 3 samples unless stated otherwise. All error bars are ± standard deviations, unless stated otherwise. The software used was GraphPad Prism, SPSS software or Microsoft Excel. Unless stated otherwise, one-way ANOVA was used with a Tukey's post-hoc test, $p \leq 0.05$ was considered to be statistically significant correlating to * symbol, $p \leq 0.01$ is denoted by **, $p \leq 0.0001$ is denoted by ***.

5.4 Results

5.4.1 Preliminary Cell Experiment

The number of viable cells measured using PrestoBlue over a 14-day experiment are shown in Figure 5-2. Figure 5-2 shows the number of cells attached to AW2 scaffolds seeded with 2.5 x10^5 cells and AW2 scaffolds seeded with 5.0 x10^5 cells using PrestoBlue on days 1, 3, 5, 7, 10 and 13. The numbers of cells on both scaffolds follow a similar trend across the duration of the experiment, with the number of cells on the final day (day 14) being almost the same, with overlapping error bars. Both seeding densities reached a peak on day 7, with an evident decrease in the number of cells on day 10, following the same trend. Due to the similarities in behaviour, for the main experiments a cell seeding density of 2.0 x10^5 was used.

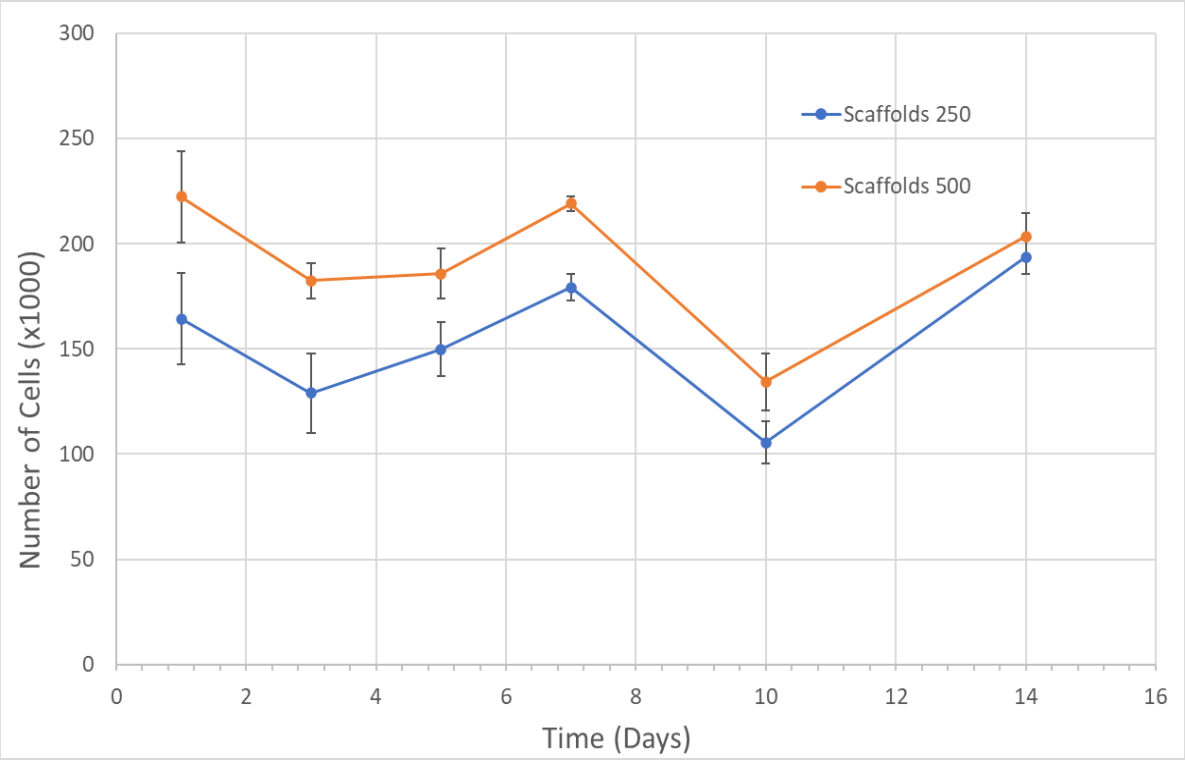

Figure 5-2: PrestoBlue viability assay for foetal human osteoblast cell seeded AW2 scaffolds across 14 days of culture with growth media. The orange values represent scaffolds seeded with 5.0 x10^5 cells, the blue represents scaffolds initially seeded with 2.5 x10^5 cells. Number of cells was calculated using a calibration curve, mean values are shown with standard error of mean, N=3.

To compare the cell proliferation between the cells seeded on tissue culture plastic (positive controls) and cells seeded on AW2 scaffolds, all conditions are shown on Figure 5-3. This allows for evaluation of trends across cell seeding densities (2.5 x10^5 and 5.0 x10^5) on scaffolds and 2D surface across 14 days in growth media, as shown in Figure 5-3. It can be noted that, regardless of culture method, the number of cells decrease from day 1 to day 3, and generally the numbers of cells steadily increase, except for tissue culture plastic seeded with 5.0 x10^5 cells where the decrease continues until day 5 but then increases until the peak at day 7. All conditions show a peak in number of cells at day 7 followed by a decrease in numbers.

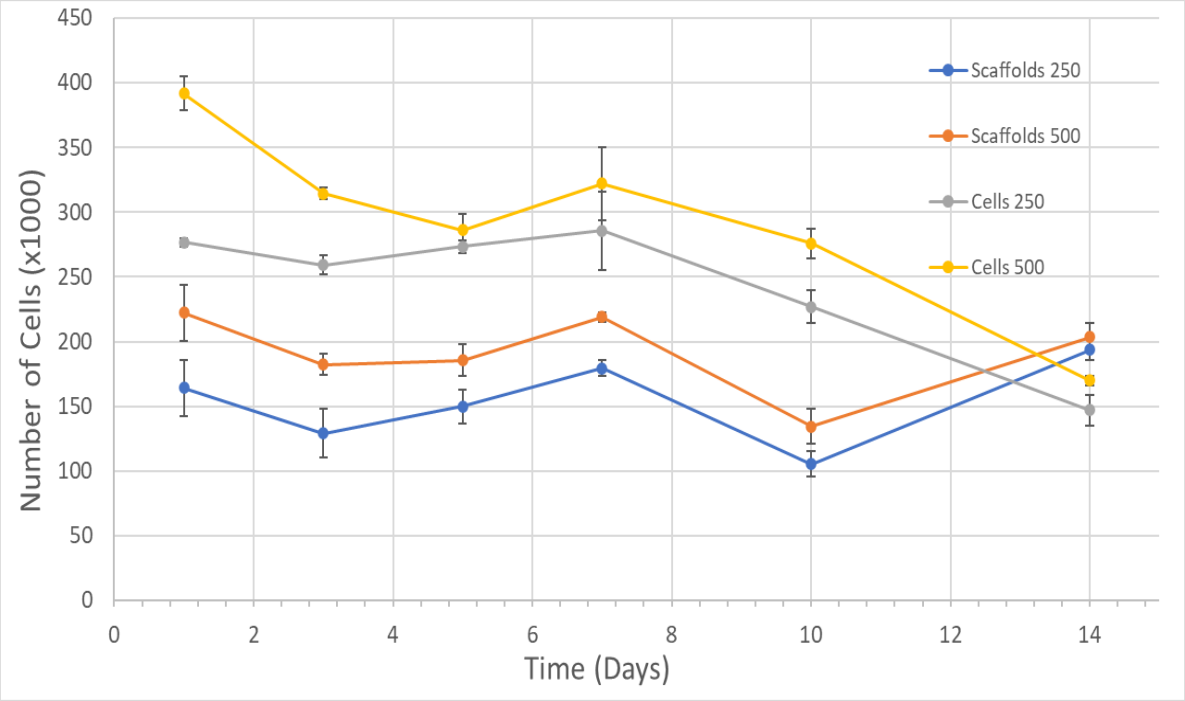

Figure 5-3: PrestoBlue viability assay for foetal human osteoblast cell seeded on tissue culture plastic (in legend as Cells) and AW2 scaffolds (in legend as Scaffolds), across 14 days of culture with growth media. The number in the legend 500 refers to seeding with 5.0 x10^5 cells, the number 250 refers to initially seeding of 2.5 x10^5 cells. Mean values are shown with standard error of mean, N=3.

Following the preliminary experiment, the number of cells were chosen as 2.0 x10^5 per scaffold, for the modified AW2 scaffolds and original AW2 scaffolds. The following results were achieved in the main experiment as outlined in Section 5.3.6.

5.4.2 Cell Viability and Growth

A PrestoBlue cell viability assay was carried out to determine the number of cells at specific time points. The calibration curve for PrestoBlue is shown in Figure 5-4, the R^2 value is 0.9894.

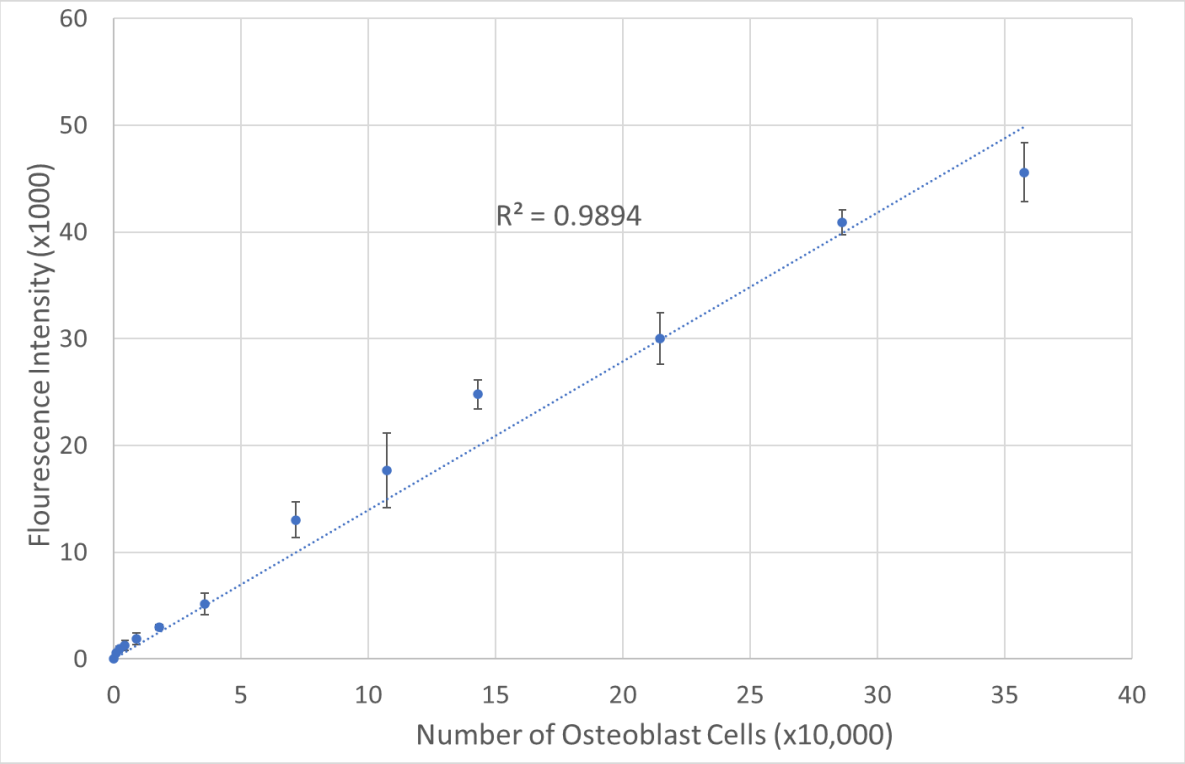

Figure 5-4: PrestoBlue calibration curve for foetal human osteoblast cells at passage 7. Shows linear relationship between number of cells (up to 360,000) and fluorescence, N=3.

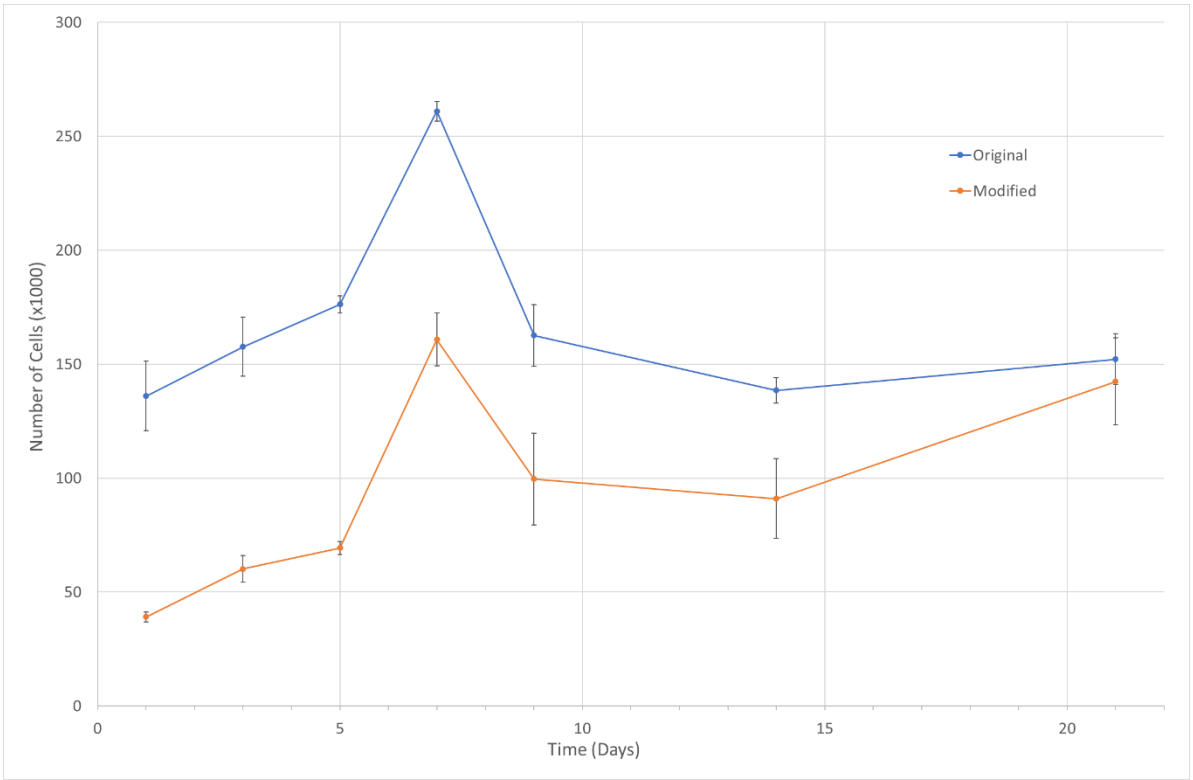

Figure 5-5: PrestoBlue viability assay for foetal human osteoblast cell seeded scaffolds (original and modified scaffolds) over a 21-day incubation period. Number of cells was calculated using the calibration curve, mean values are shown with standard error of mean, N=3.

The number of cells observed using PrestoBlue across multiple time points (day 1 to day 21) on cell seeded AW2 scaffolds is shown in Figure 5-5, initial seeding on day 0 was at 2.0 x10^5 cells per scaffold. Both scaffold types (original and modified) show a similar trend across the 21 days. The general trend shows a significant increase of cells (a peak) on day 7 for both scaffold types. There is a significant decrease in number of cells on day 9 for both scaffold types, and then differentiation media was added. On day 21 of the experiment, for both scaffolds, the number of cells is very similar (approximately 1.5 x10^5 cells), the error bars overlap on this final day.

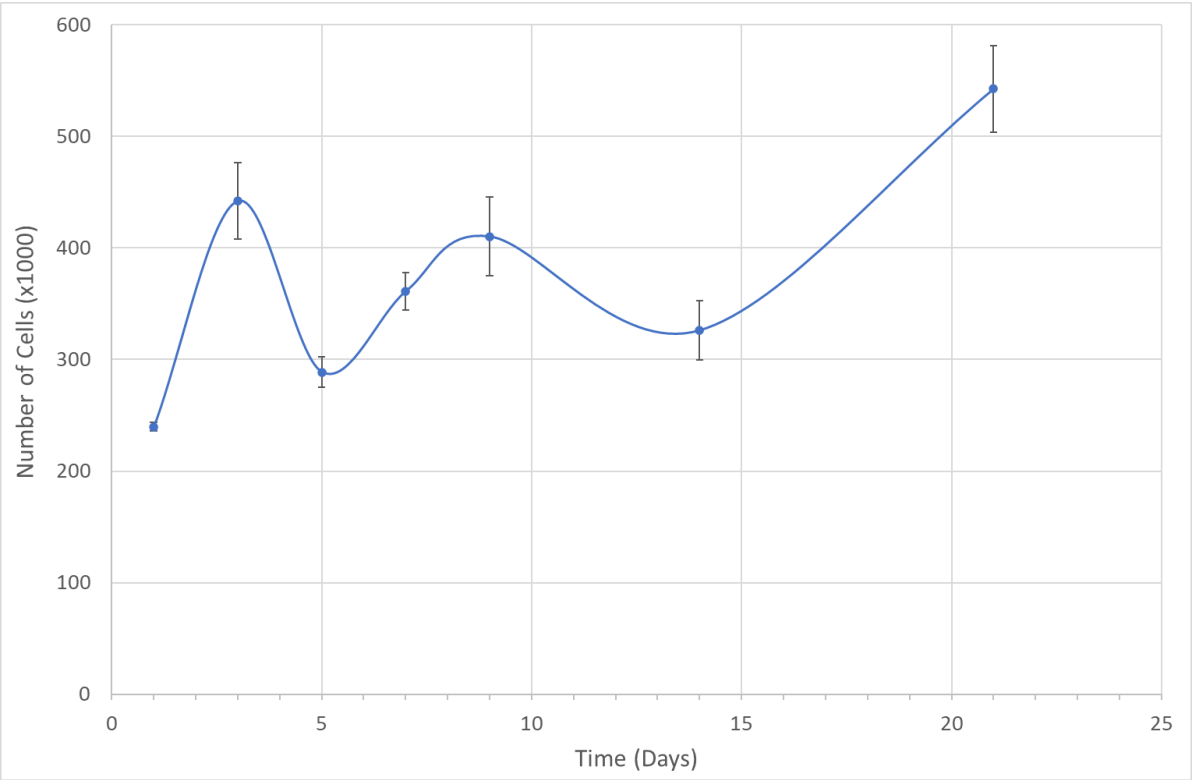

Figure 5-6: PrestoBlue viability assay for foetal human osteoblast cell glass coverslips (positive controls) over a 21-day incubation period. Number of cells was calculated using the calibration curve, mean values are shown with standard error of mean, N=6.

The positive controls for the main experiment were foetal osteoblast cells seeded on glass coverslips, the number of cells observed is shown in Figure 5-6, the initial seeding density on day 0 was at 2.0 x10^5 cells per scaffold, with the final day at day 21. At day 1, the cell number remained constant at 2.0 x10^5 cells, then showed a sharp increase to 4.5 x10^5 cells followed by a sharp decrease in cell numbers. There is an increase in cells until day 9, then a decline again until day 14, followed by the highest cell increase to 5.45 x10^5 cells at day 21, which also has the largest standard error of mean ±3.9 x10^4. The number of cells more than doubled from day 1 to day 21, with quite a non-consistent trend.

5.4.3 Live/Dead Cell Viability Assay

To evaluate the viability of the cells, a Live/Dead assay was performed on day 1 and 3 of the experiment. The blue colour seen in Figure 5-7 to Figure 5-9 represents the live cells (DAPI) and the green represents dead cells. This viability assay was carried out on modified scaffolds on day 1 only. A red and/or orange coloured assay were not used in any experiments, as the

scaffolds naturally fluoresce red as shown in Figure 5-8 below. The surface morphology of the scaffold can be imaged with a red filter, but this was only used very minimally. Therefore, almost all imaging from confocal microscopy was executed without the red and/or orange filters.

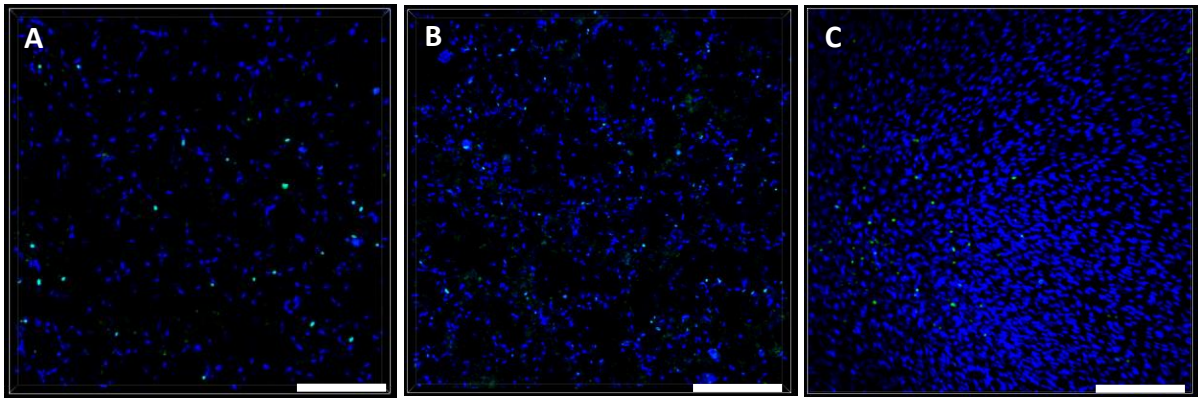

Figure 5-7: Live/Dead staining after 1 day of osteoblast culture, scale bar represents 300 µm. A) modified AW2 scaffold, z= 93.97µm, B) original AW2 Scaffold z=107.40µm, C) Positive control z=17.9µm

Figure 5-7 shows a sample image from Live/Dead assay of (A) modified scaffold, (B) AW2 scaffold, (C) positive control, after 1 day in culture with osteoblast cells. There are some dead cells visible as green fluorescence in all conditions. There appears to be around twice as many cells in the original scaffold compared to the modified scaffold (A), this correlates with the PrestoBlue results for day 1 of culture.

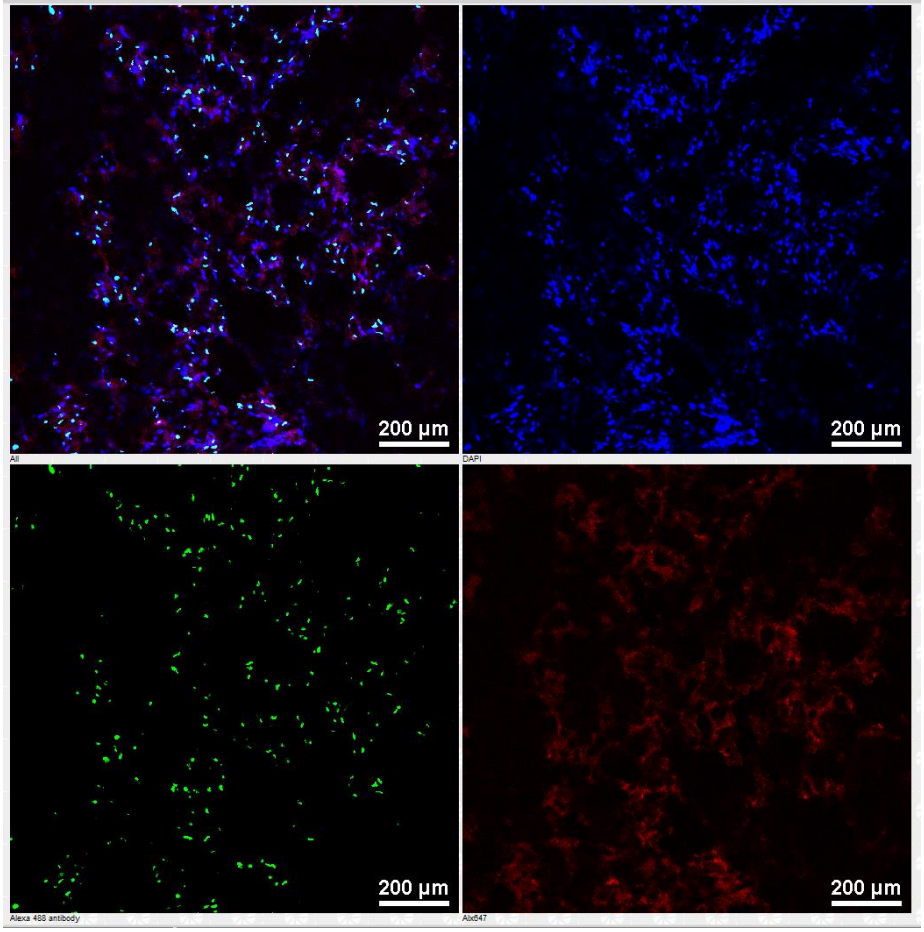

Figure 5-8: AW2 scaffold cultured with osteoblast cells for 3 days, with three-colour merged image of blue (live cells), green (dead cells), and red (natural scaffold fluorescence).

Figure 5-8 shows Live/Dead assay on AW2 scaffolds cultured in osteoblast cells for 3 days, three different filters on the confocal microscope were used for this imaging. Filters shown are DAPI (blue), Alexa 488 (green) and ALX847 (red), and the merged image. The scaffolds naturally fluoresce red; therefore this filter was deactivated during almost all confocal imaging as it interferes with the image analysis.

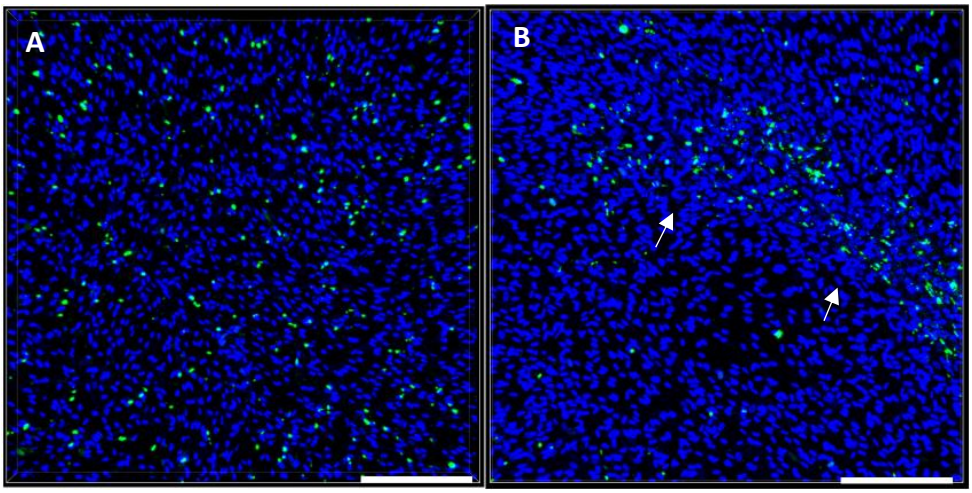

Figure 5-9: Live/Dead staining after 3 days of culture with Osteoblast cells, scale bar represents 300 µm. A) a small proportion of evenly spread dead cells (green) across the AW2 scaffold, z-depth: 148 µm. B) live/dead on glass coverslips shows that the dead cells are primarily in the top right corner where there is also high concentration of live cells, z-depth: 31 µm.

Figure 5-9 is a sample image from confocal imagining of osteoblast cells cultured on AW2 Scaffolds (A) and Glass coverslips (B) after 3 days. The live cells are indicated by blue (DAPI) and green indicates dead cells. On AW2 scaffolds (A) the general confluency of the cells is relatively even across the surface imaged, on the glass coverslips (B) there are areas of minimal cells (black patches) and areas of high cell density as indicated by the high blue signal. On the high concentration of cells (indicated by white arrow), there also is a high number of dead cells.

5.4.4 Alizarin Red Stain

Alizarin Red staining was carried out on AW2 scaffolds and their controls at specific time points (days: 1, 14 and 21).

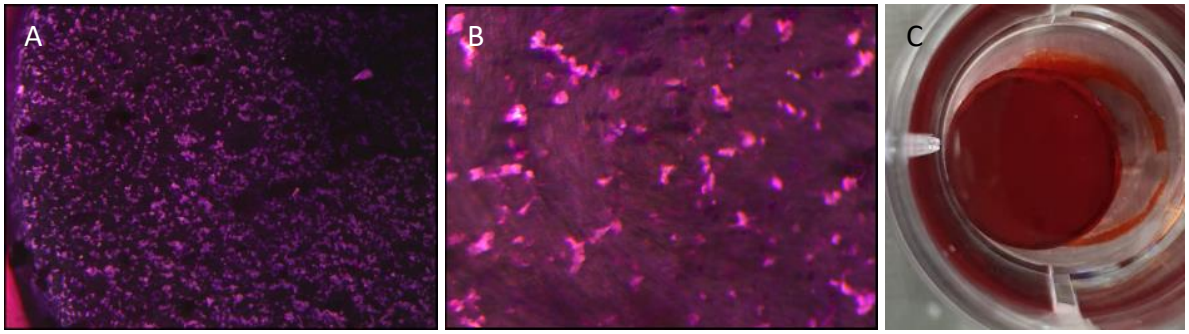

Figure 5-10: Sample images from Alizarin Red stain shown here. A and B) are osteoblast seeded original AW2 scaffolds using stereomicroscopy, scaffold surface morphology can be visualised to some extent, but calcium deposits in cells are not easily identifiable. C) is an original AW2 scaffold seeded with osteoblast cells for 14 days. There is no orange/red colour differentiation across the scaffold.

Due to the nature of the AW2 material (calcium content), the alizarin red colour under the Leica microscope appeared the same red colour across all the scaffolds including the negative controls, as shown in samples images in Figure 5-10. The results were inconclusive and have therefore not been included.

5.4.5 Alkaline Phosphatase

A standard curve was carried out for each experiment using the manufacturer's protocols, as described in section 5.3.10.3.

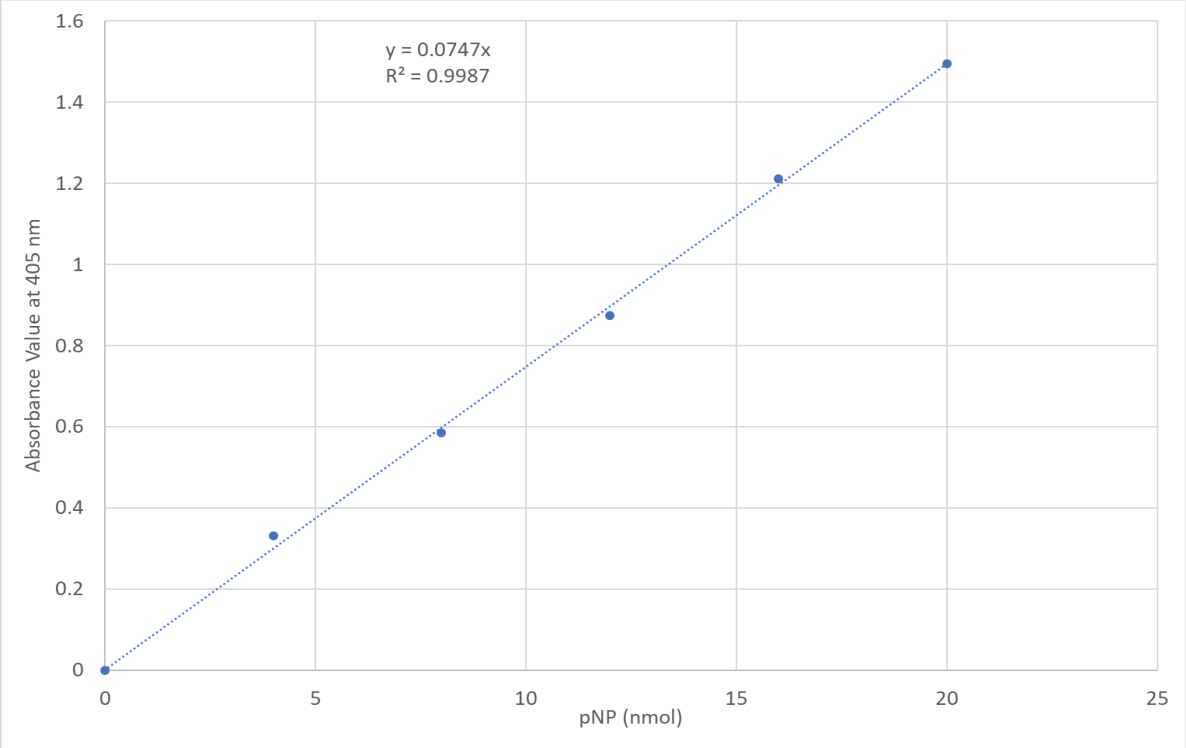

Figure 5-11: A ρNP (p-Nitrophenol) standard calibration curve for Alkaline Phosphatase (ALP). Linear relationship is shown between ρNP values and absorbance, N=3.

A sample standard curve (Figure 5-11) used in an experiment is below for demonstration purposes, with an R^2 value of 0.9987.

.

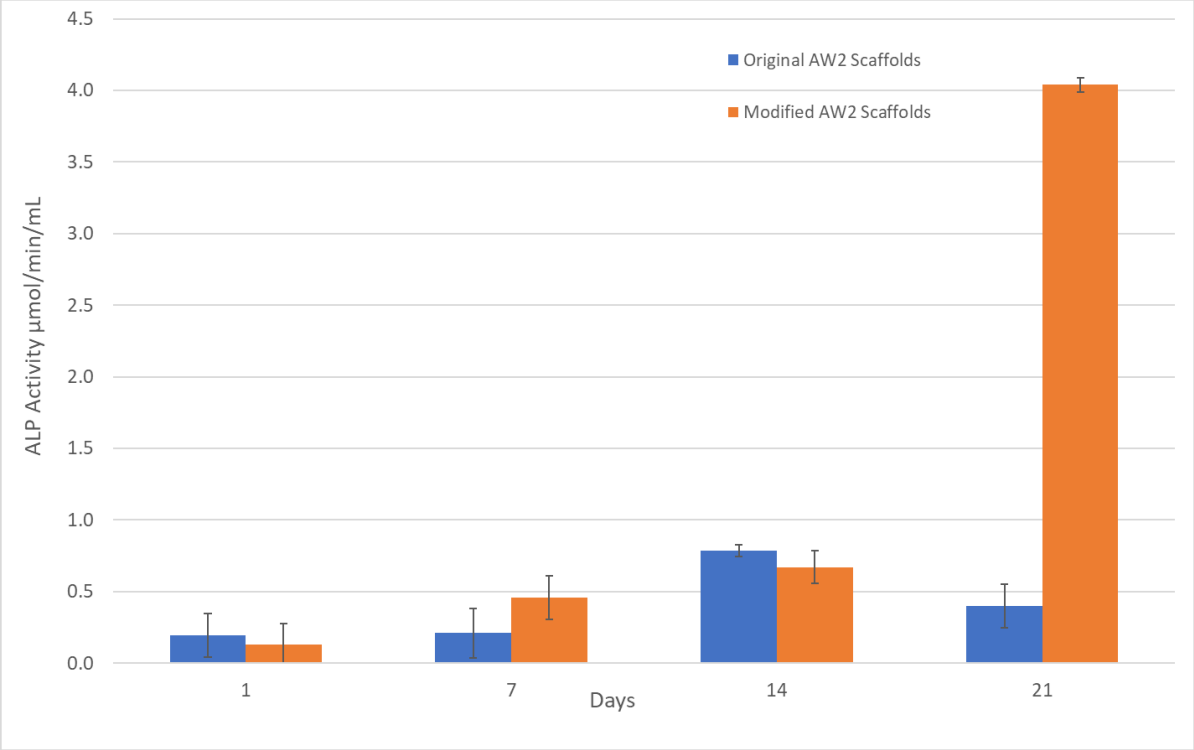

Figure 5-12: Normalised Alkaline Phosphatase levels on cell seeded scaffolds up to 21 days in culture. Original AW2 scaffolds are shown in blue, and modified AW2 scaffolds are shown in orange. Differentiation media was added from day 9 of culture. Error bars represent standard deviations, N=3.

Figure 5-12 shows normalised ALP levels, the negative controls (scaffolds without cells) were used for normalising the data. The ALP levels on day 1 of the experiment are very similar, with overlapping error bars, no significant difference was reported. The ALP levels gradually increased for both scaffold types up to day 14, with a sharp increase between day 7 and day 14. It is important to note that differentiation media (which includes the steroid Hydrocortisone) was used from day 9 of the experiment, and refreshed every other day where possible. The modified scaffolds had a 7-fold increase in ALP levels between day 14 and day 21. The original AW2 scaffolds experienced a decrease in ALP levels between day 14 and day 21. It appears that the differentiating media had an effect on the ALP levels in the cell seeded scaffolds as well as the positive controls Figure 5-13, which was to be expected (Liu et al., 1999, Fromigué et al., 1998, Radin et al., 2005, Hoemann et al., 2009, Lin et al., 2012, Nasello et al., 2020).

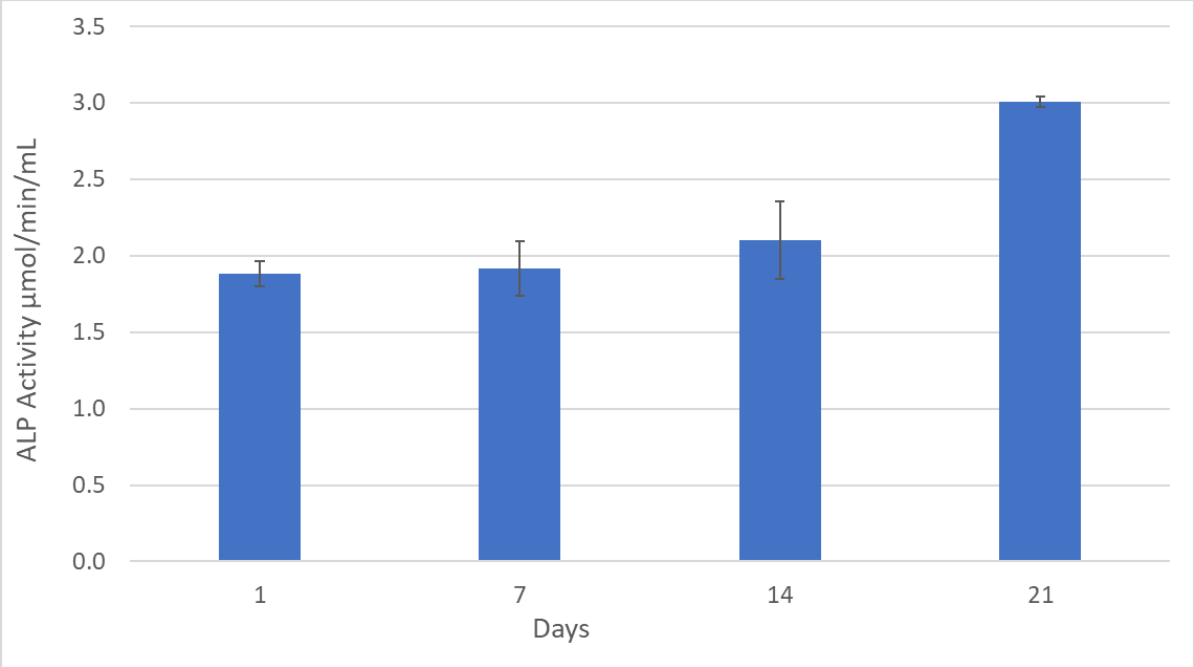

Figure 5-13: Alkaline Phosphatase levels shown on positive controls (Cells on coverslips) up to 21 days in culture. Differentiation media was added on day 9. Error bars represent standard deviations, N=3.

Alkaline Phosphatase levels in the control wells, cells seeded on coverslips for up to 21 days, are shown in Figure 5-13. The trend shows a gradual increase from day 1 to day 14, and then a sharp increase between day 14 and day 21. From day 14 to 21 there is a nearly a 50% increase in ALP levels.

5.4.6 Actin/DAPI stain – Confocal Microscopy

ActinGreen 488 ReadyProbes reagent was used to detect F-actin as green in cells, and DAPI was used to detect nuclei of cells as blue. This staining was carried out on AW2 scaffolds on days 1, 7, 14 and 21. The images were obtained using confocal microscopy with differing Z-depths stated in the captions. The images will be organised as cell seeded scaffolds (images A, B and C), and the positive controls (D, E and F). Unless stated otherwise due to confocal program limitation, images A & D have a width and height of 1272 µm, image B & E has a width and height of 636 µm, and image C & F has a width and height of 318.2 µm.

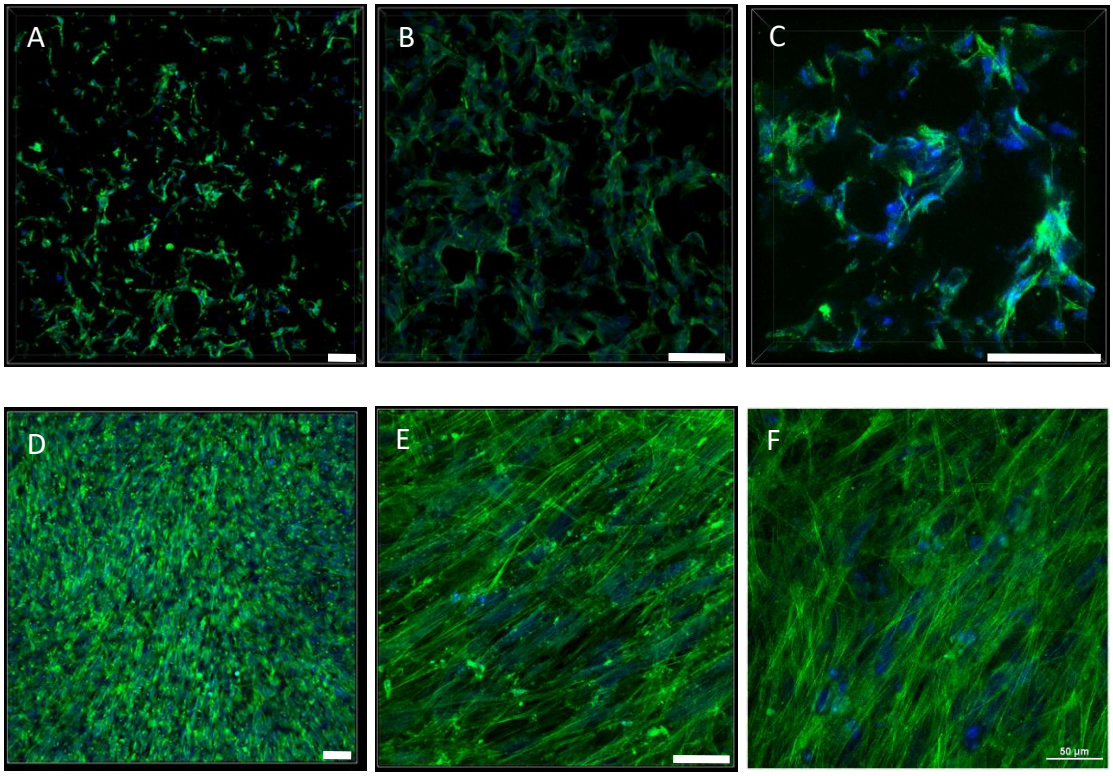

Figure 5-14: Confocal images at day 1 of experiment, z-depth (µm) is as follows A: 161.1, B: 143.2, C: 102.0, and D: 53.7. On E & F, the height and width is 318.2 µm with a z-depth of E: 10.5 and F:0.0 µm. Scale bar represents 100 µm unless stated otherwise. Osteoblasts on Scaffolds are not fully covering the scaffolds, but do show signs of integrating into pores. The cells have a spread-out morphology on the scaffolds, yet on the glass cover slip appear to be spindle shaped.

Figure 5-14 shows the morphology of the Osteoblast cells on AW2 scaffolds and glass coverslips after culturing for 1 day. The cells do not fully cover the AW2 scaffold surface, there are black background areas visible, which indicates no staining. An area that has no staining, indicates that it is the AW2 material with no cell coverage.

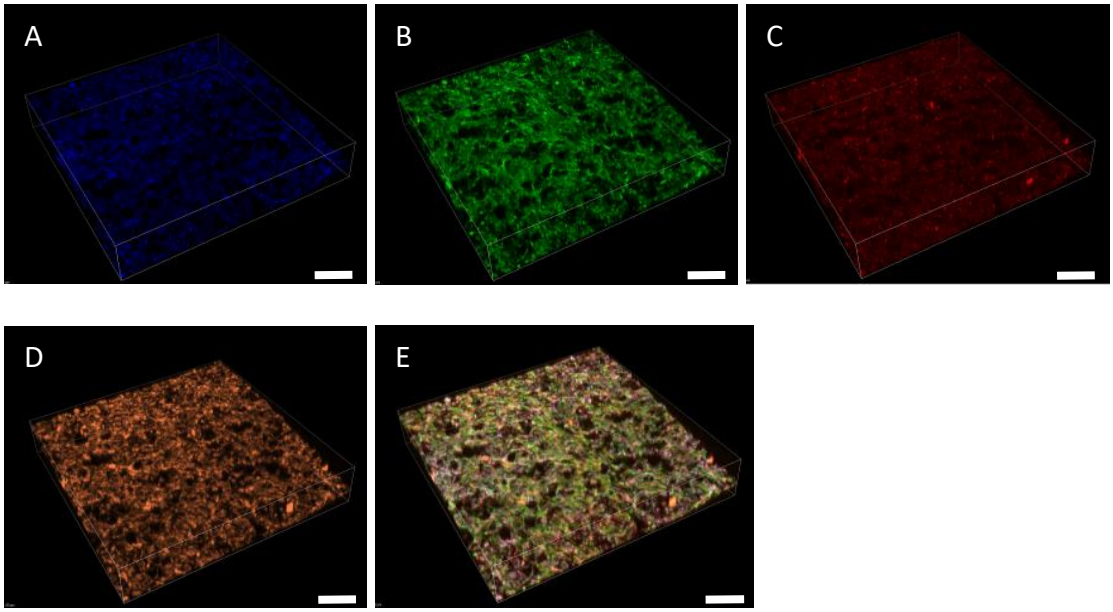

Figure 5-15: Confocal microscopy image of AW2 scaffolds cultured with Osteoblast cells for 1 day, height 1272.0 µm, width 1272.0 µm, z-depth 224.0 µm. Scale bar represents 200 µm. A) the blue represents the nucleus of the cells stained with DAPI. B) Actin filaments are stained green. C) the sintered AW2 particles fluoresce red with a red filter. D) the sintered AW2 particles also naturally fluoresce orange when viewed using an orange filter. The scaffold surface can be seen readily with the orange filter showing the pores as black. E) Osteoblast seeded AW2 scaffold surface is shown with all filters 'on' during the imaging process.

AW2 scaffolds cultured with Osteoblast cells for 1 day are shown in Figure 5-15, with a height and depth of 1272 µm, and a z-depth of 224.0 µm. All filters were used in the imaging to show the effects of the scaffold's natural immunofluorescence and the negative consequence it would have on imaging. Regarding the orange filter, Figure 5-15-D, the scaffold morphology and pores can be seen quite easily. The final merged image (Figure 5-15-E) is not comprehensible to draw conclusions from due inability to differentiate between the multiple colours.

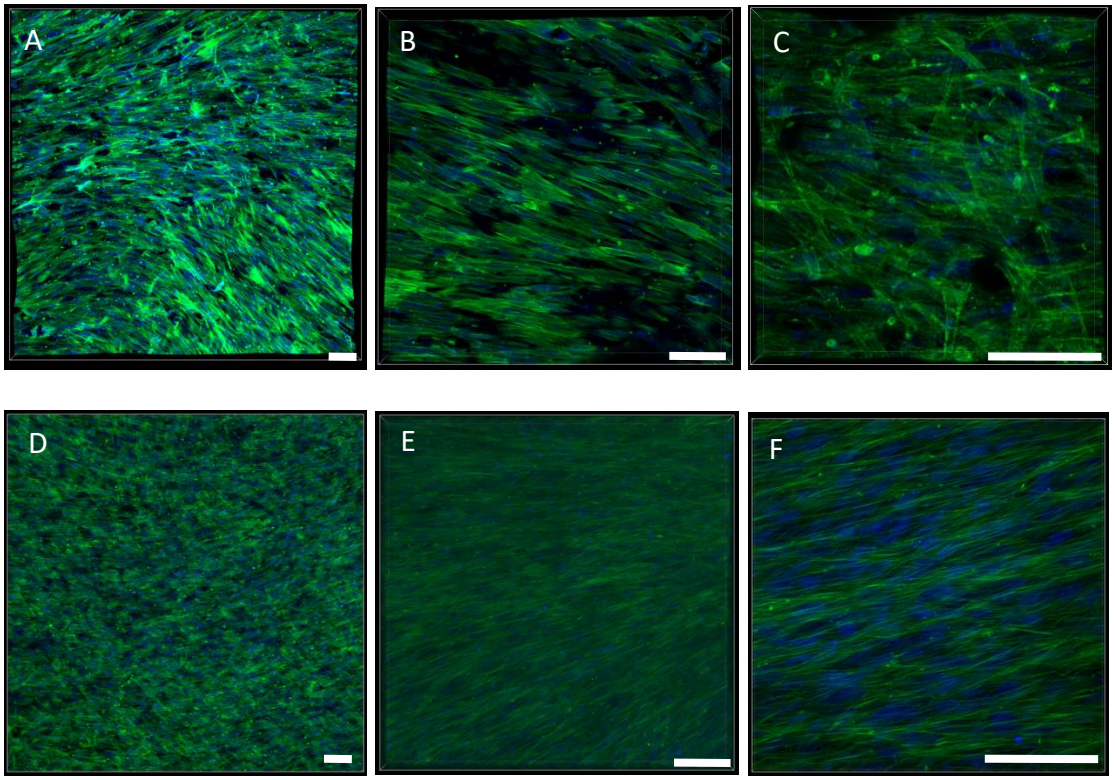

Figure 5-16: AW2 scaffolds and glass coverslips cultured with Osteoblast cells for 7 days. A: 197.95, B: 102.0, C: 58.28, D: 32.32, E, 75.0, F:11.55 µm. A) a pattern can be seen forming with most of the actin filaments going towards similar directions. B) actin filaments are towards the same direction, some dark gaps visible indicating not all of the surface is covered in cells. C) upon magnification mixed directions of actin filaments visible, and brighter points suggesting nucleation points.

Figure 5-16 shows the morphology of the Osteoblast cells on AW2 scaffolds and glass coverslips after culturing for 7 days. The cells appear to cover most of the surface of the scaffold, with some areas still not fully covered. In C) it can be seen that the actin filaments are spread out, suggesting stress filaments as it is multidirectional, the nuclei are visible but appear to be deeper in the z-layer than the actin filaments. In F) the filaments appear to be mostly in the same direction, with the nuclei visible.

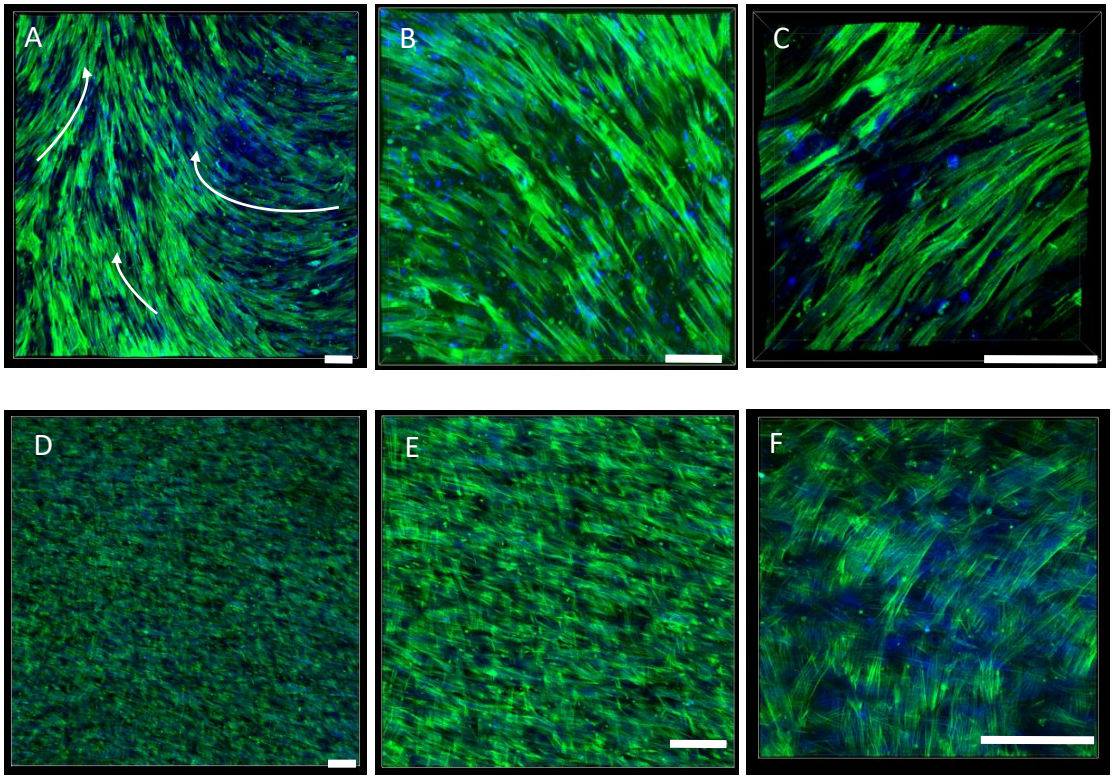

Figure 5-17: Actin (green) and DAPI (blue) staining illustrating morphology after 14 days of Osteoblast cell culture with AW2 scaffolds and glass coverslips. Z-depth µm are as follows; A: 80.55, B: 81.0, C: 100.5, D: 26.85, E: 20.8, F: 16.0. Scale bars represent 100 µm.

The morphology of Osteoblast cells cultured for 14 days with AW2 scaffolds (A, B, C) and glass coverslips (D, E, F) is shown in Figure 5-17. On AW2 scaffolds, the alignment of the actin (green) appears to follow a pattern (arrows to show pattern direction) and is visible on the scaffolds, with some areas showing increased actin florescence. The alignment profile of actin on glass scaffolds are in a similar orientation to each other, but upon magnification the cell orientations appear to vary in different directions.

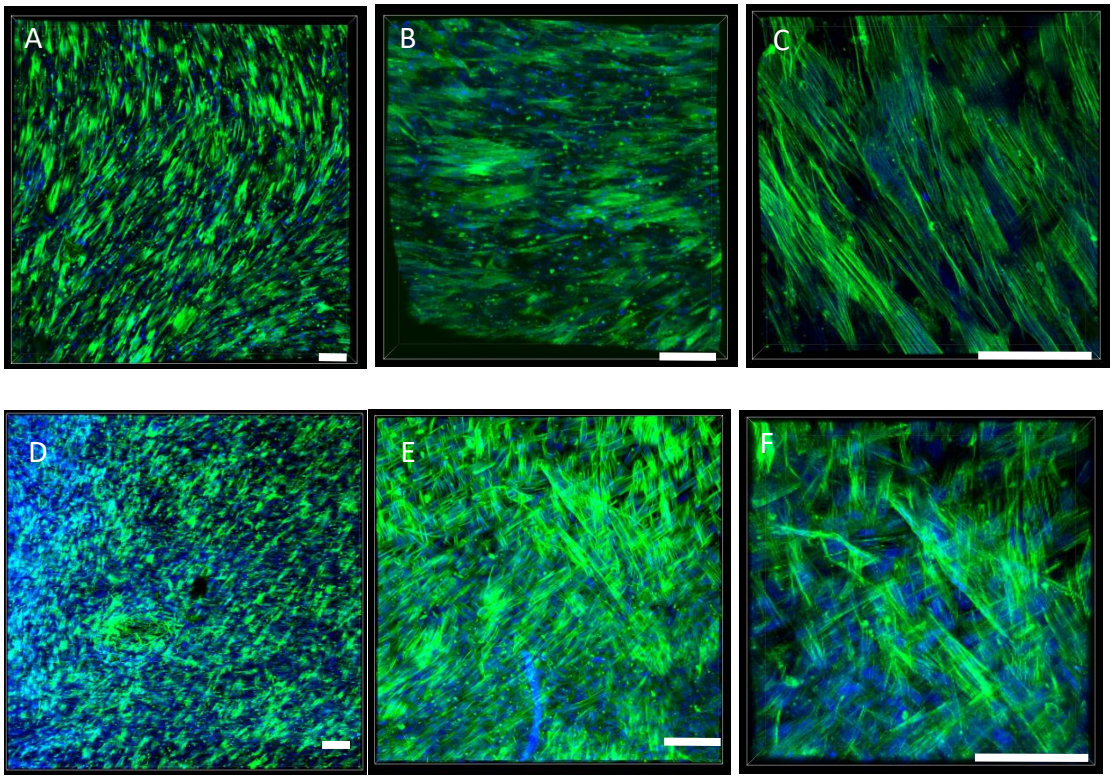

Figure 5-18: Actin (green) and DAPI (blue) staining illustrating morphology after 21 days of Osteoblast cell culture with AW2 scaffolds and glass coverslips. Z-depth µm are as follows; A: 183.47, B: 148.20, C: 70.2, D: 53.7, E: 42, F: 90.0. Scale bars represent 100 µm.

Figure 5-18 shows osteoblast cells on AW2 Scaffolds and on glass cover slips after 21 days of culture. The actin filaments on the scaffolds are unidirectional as seen in A) and B). The actin fibres on the glass cover slips don't appear to follow a pattern or direction, and the cells appear to be spread out in nature as shown in F).

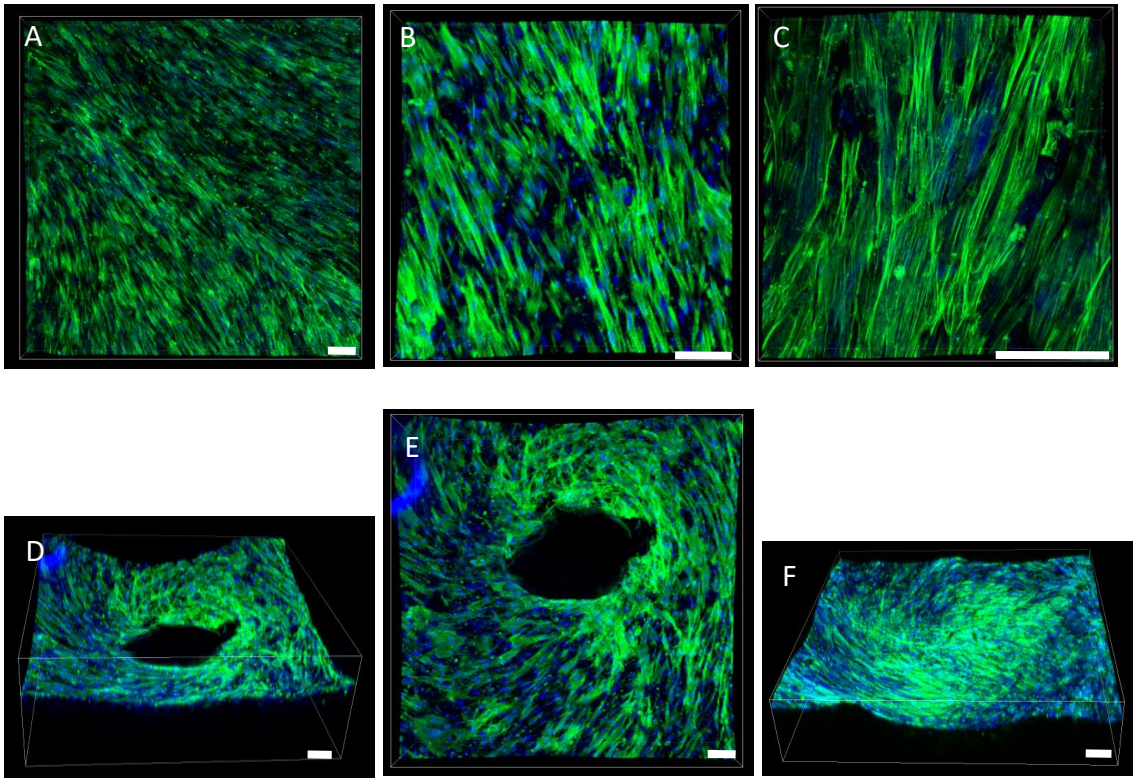

Figure 5-19: Modified AW2 Scaffolds are 21 days in culture with Osteoblast cells. Z-depth µm are as follow; A: 152.15, B: 130.0, C: 57.0. Images D – F) are of a width and height of 1272 µm, with a depth of D: 480.0, E: 480.0 and F: 286.4, respectively. Scale bar represents 100 µm.

Figure 5-19 shows modified AW2 scaffolds after 21 days in culture with osteoblast cells. In figures A – C it is from the flat region of the modified AW2 scaffolds, which shows unidirectional actin fibres. In figures D) and E) the same channel is shown with two different image views, the cells appear to have penetrated the channel, and fully covered the channel as shown on F).

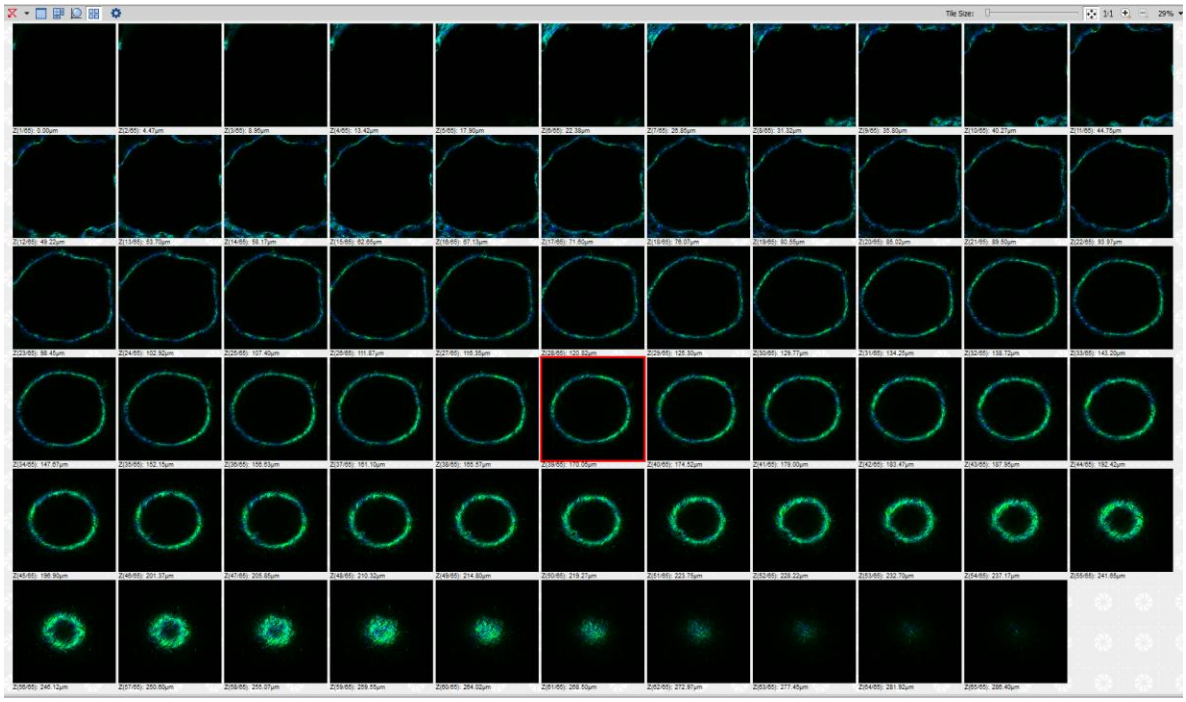

Figure 5-20: Osteoblasts cells cultured on modified AW2 scaffolds for 21 days, 65 slices of the z-stack are shown on one channel.

Figure 5-20 shows 65 slices of the full z-stack shown in Figure 5-19 F, the cell coverage across the channel (modification) can be seen across the different z-depths, each image square is 1272 µm by 1272 µm. The cell coverage can be clearly visualised in each individual layer of the z-stack from the edge of the channel to the centre.

5.4.7 Scanning Electron Microscopy

The adhesion and morphology of Osteoblast cells on different surfaces (glass cover slip, AW2 scaffolds and modified AW2 scaffolds), also unseeded AW2 scaffolds at set time points in culture (days 1, 3, 7, 14 and 21) are shown in this section. Cells seeded on glass coverslips are positive controls, and unseeded AW2 scaffolds are negative controls, cell seeded modified scaffolds are also imaged. In the cell seeded AW2 scaffolds the cells are attached to the AW2 surface, across the pores and penetrated inside the pores, Figure 5-21 to Figure 5-23. The Osteoblast cells attached readily to the AW2 surfaces, as shown in day 1, increasing in cell penetration throughout the pores, cell coverage and multilayering at each increasing time point. The morphology of the cells especially changed from day 7 (Figure 5-22) to increasingly include cell-sheet patterning, dense multilayering of cells, mineralisations, rounded particles, rough particle formations and particle formations engulfed by cells. These particles and cell

sheets were analysed further by Energy-dispersive X-ray spectroscopy (EDS) for elemental analysis.

After 7 days in culture, a layer of cells covering the scaffolds can be observed in the overview images, Figure 5-22. After 21 days the osteoblast cells have covered the channels of the modified scaffolds, forming an almost uniform layer as shown by SEM imaging in Figure 5-25. Upon close inspection of the cells at the channel openings, the cell can be clearly seen with fibre-like attachments to different AW2 particles and have penetrated into the channel. They morphologically represent like osteocytes and indicate cauliflower-like projections on some cells (Magallanes-Perdomo et al., 2011, Zhang et al., 2014).

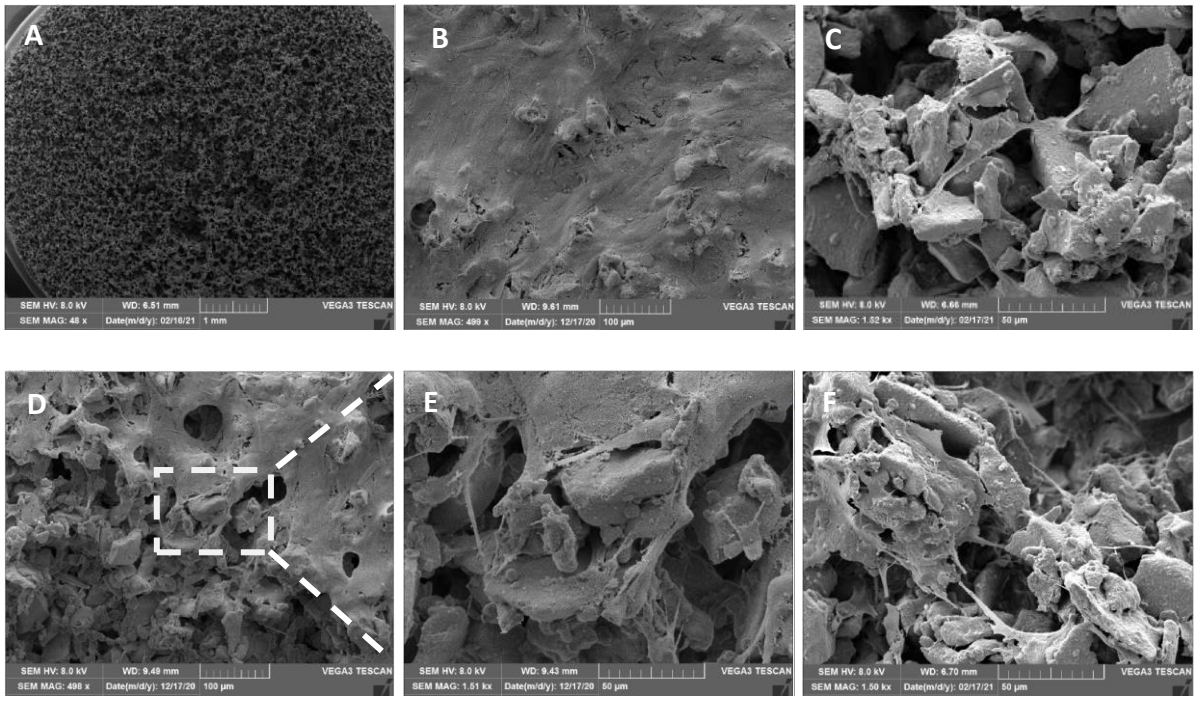

Figure 5-21: SEM of Osteoblast cells cultured on AW2 scaffolds cultured for 1 day. A) Overview image of scaffold surface, high porosity visible and cell coverage on AW2 material. B) densely populated area on scaffold with Osteoblast cells, areas are not homogeneously covered. C) Cell attachment sites onto AW2 particles and across pores. D) Sample of scaffold and larger pores with non-homogenous Osteoblast cell coverage. E) Magnified image of area shown as white dash-line box on (D), cell attachment to AW2 particles is visible. F) Cells attached to particles across pores.

Figure 5-21 shows sample images from day 1 cell cultured scaffolds, the morphology of the cells appears to be flat and spread out on the AW2 surface, but does not appear to cover pores completely, individual cells are not visible unless magnified as shown in C, E and F.

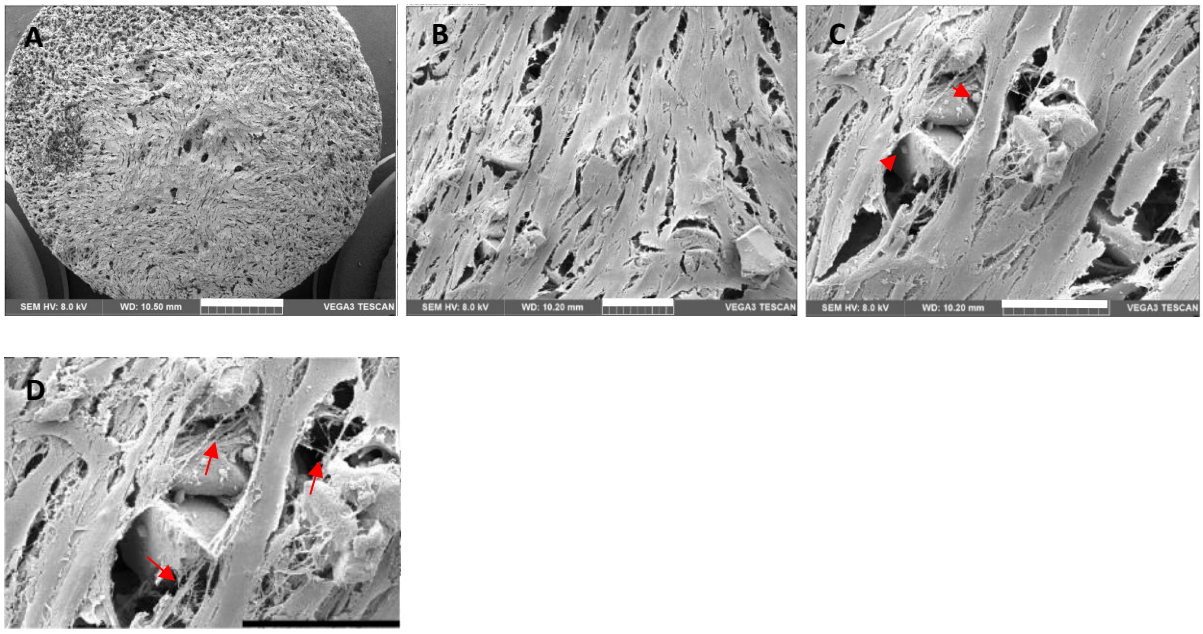

Figure 5-22: SEM of Osteoblast cells cultured on AW2 scaffolds for 7 days. A) Scale bar represents 2mm, overview of the top surface of the scaffold. B) Scale bar represents 100µm, improved cell coverage of scaffold surface, cells appear to be in more than one layer. C) Scale bar represents 50µm, appears to be mineralisation on the cell surface as directed by red arrow heads. D) is a zoomed in image of C in the area between the red arrow heads. Cell attachments and multiple layers of cells under the outermost layer, as shown by red arrows.

AW2 scaffolds cultured with Osteoblast cells for 7 days are shown in Figure 5-22, in the magnified images (B and C), there is clearly a multilayer of elongated cells covering the scaffold surface, the outermost layer of cells appearing elongated and striated. In A) a thicker multilayer of cells appears in the centre of the scaffold and a cell pattern appears to be forming. Relatively confluent coverage of cells is shown, although some pores are still visible especially at the top of the image. Cell fibres can be seen under the spaces between cells on the outermost layer as indicated by red arrows.

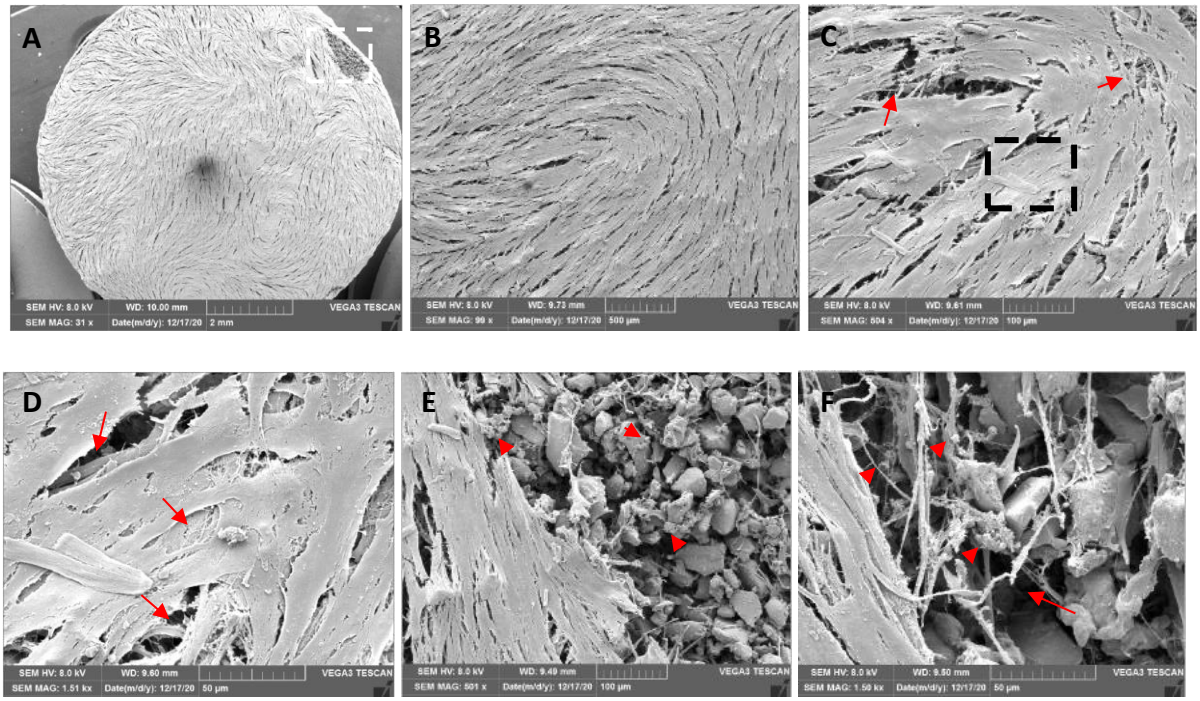

Figure 5-23: SEM of AW2 scaffolds cultured for 14 days with Osteoblast cells. The red arrows indicate multiple cell layers. Red arrowhead indicates mineral formations on cells. A) Overview image of the cell covered scaffold. All top surface of the scaffold is covered evenly in Osteoblasts, a patterning of cell direction can be seen. Images E and F represent higher magnification images taken from the white box area. B) The Osteoblast cells appear to follow a curved pattern in an elongated format. More than one layer of cells is visible as demonstrated in C) where additional layers of cells into pores can be seen, the black box is magnified in D) where multiple cell layers are seen on the surface of the cells as well as the areas of slight cell lifting. E & F) show clear cell infiltration, attachment, and elongation into the pores of the scaffolds.

Sample SEM images of scaffolds cultured with Osteoblasts for 14 days is shown in Figure 5-23, media was changed to differentiating media for 5 days. The scaffold surface is homogenously covered with a dense multilayer Osteoblast cell sheet, and a cell pattern appears to have formed. The area marked with a white box is due to some damage from tweezers upon handling. This damaged area allows for further investigation into the scaffold surface as it exposed layers of cells and pores under the outermost cell layer. The patterning of cells can be seen clearly in (B) and slight lifting of cells from each other was investigated further in C and D. Which shows multiple layers of cells and potential mineral formation on the cell surface.

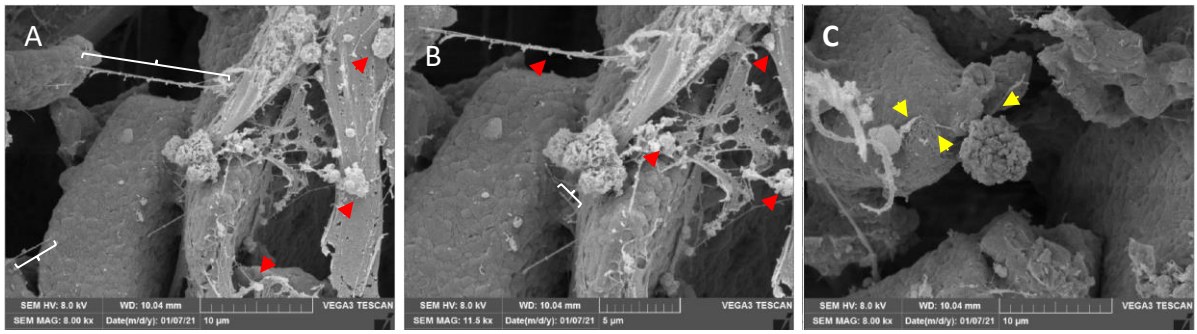

Figure 5-24: Mineralisation formations on AW2 scaffolds cultured for 14 days with Osteoblast cells. A) multiple mineralisation formations apparent on the cell structure (red arrow heads). B) is a magnified image of A, to show cauliflower formations more clearly and cell attachment across particles at small distances (2 µm). C) Large cauliflower formation and smooth mineral formation, cell attachment fragments visible as indicated by yellow arrowheads.

Figure 5-24 shows AW2 scaffolds cultured with Osteoblast cells after 14 days, with 5 days in differentiating media. The images were taken of sections where the cell carpet has lifted slightly and shows the cells and scaffold surface underneath. A and B show mineralisation formed on Osteoblast cells at multiple points. Multiple cauliflower-like shaped formations are visible on the cells as shown by red arrowheads. There are multiple cell fibres visible that have attached across different AW2 particles from 15 µm to 2 µm as shown by white brackets. C) shows a large cauliflower-like projection at the end of an AW2 particle where cell attachment fibres appear around it. A smaller smoother mineralised projection is visible on the left side with cell fragments visible.

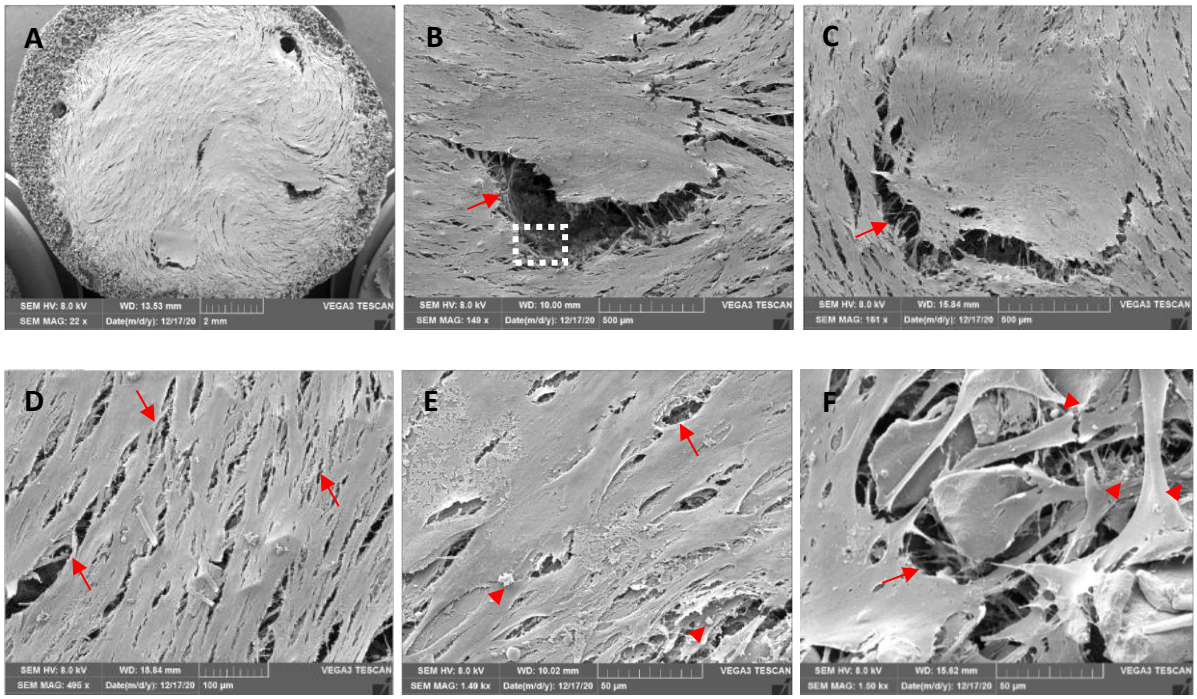

Figure 5-25: Modified AW2 scaffolds cultured with Osteoblast cells for 21 days. A) Three channels are completely covered by cells, a cell patterning appears on the scaffold surface. B & C) magnified image of cell covered channels, some lifting of cells visible on edge, multiple cell layers visible. D) magnification of cell patterning, multiple elongated cell layers visible. E) Magnification of cell pattern shows multiple layers, some cauliflower-like mineralisation on the cells. F) magnification of channel edge lifting shows as white box in B, indicating multiple cell attachment and layers within the channel and surrounding pores. Mineralisation visible along cell fibres.

Sample SEM images from modified AW2 scaffolds cultured with Osteoblast cells for 21 days, cultured in differentiating media for 12 days, are shown in Figure 5-25. The majority of channels are fully covered by cells, there is some cell lifting visible along the edge of some channels. Also shown is a sample image inside a cell covered channel (white box in image B) due to the cell lifting and magnified (F), showing mineral formations along cell fibres. Multiple layers of cells are visible penetrating pores and channels, also seen in actin/DAPI confocal imaging.

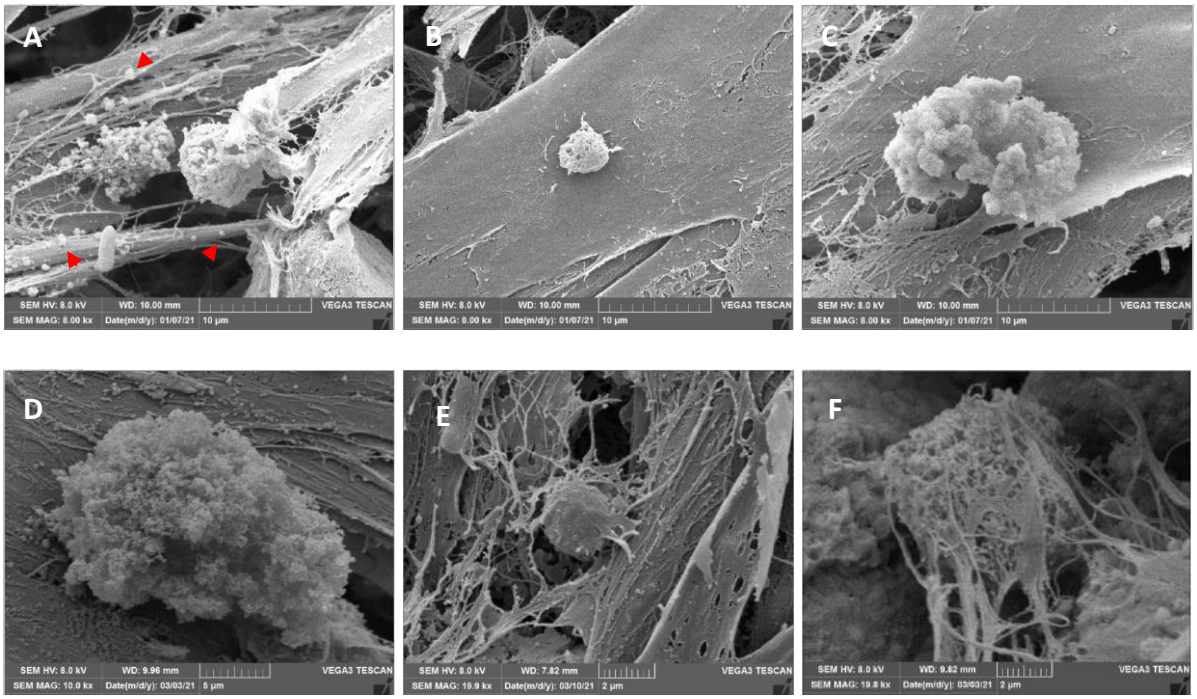

Figure 5-26: Mineralisation nodules on cells forming cauliflower shapes, modified AW2 scaffolds cultured with Osteoblast cells for 21 days. A) Mineralisation formations on cell fibres, larger cauliflower shaped formation on different cells. B) smooth rounded particle on a cell, multiple cell layers visible. C & D) large rough cauliflower formations on top of cells. E & F) smooth and rough particle formation engulfed by cells.

Further investigation occurred on the surfaces and cell edge liftings of the modified AW2 scaffolds cultured in Osteoblast cells with additional SEM magnifications, Figure 5-26. The images show mineralisation formations on cells, with different morphologies: smooth rounded, rough cauliflower, rough and smooth particles engulfed by cells. The formations occur on the cell surfaces, not on the AW2 particle, this is indicative of Calcium Phosphate-like particles, and is in agreement with EDS analysis. Due to gold coating overlapping with the Phosphorous peak, deeper considerations are not possible. Fibrous network is visible, and assumed to be new Collagen formation.

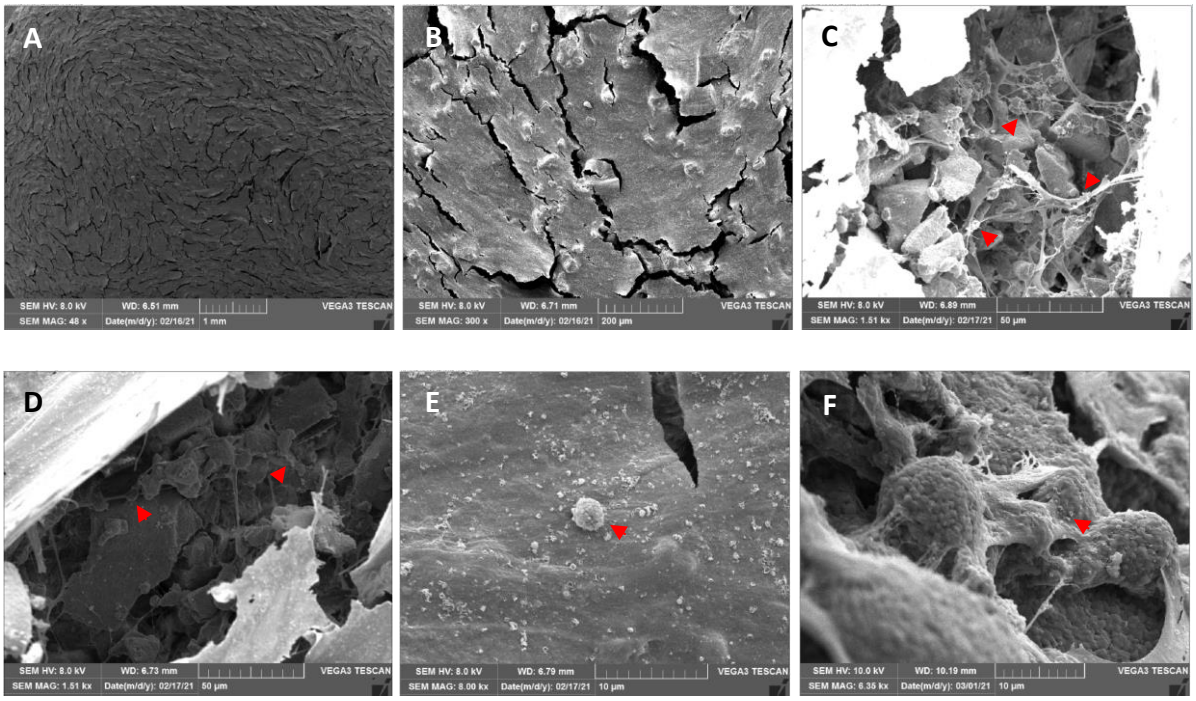

Figure 5-27: AW2 scaffold cultured with Osteoblast cells for 21 days. A & B) dense multilayer cell sheet on surface visible. Cracks in the cell sheet, pattern not immediately visible. C & D) multilayer of cells visible in crack of cell sheet, red arrow heads represent mineral formations on cells. E & F) cauliflower formations and mineral particles visible on cells. Cells have attached and formed around AW2 particles and pores.

AW2 scaffolds cultured with Osteoblast cells for 21 days are shown in Figure 5-27. Dense cell sheet layers are visible, as well as cracking in the cell sheet layer. Mineral formations representing smooth round particles and rough cauliflower formations are visible on the surface layer and in the layers between the cracks. Cells have covered the AW2 particles to form a cell sheet layer, the AW2 particles appear smooth in appearance, as shown in F.

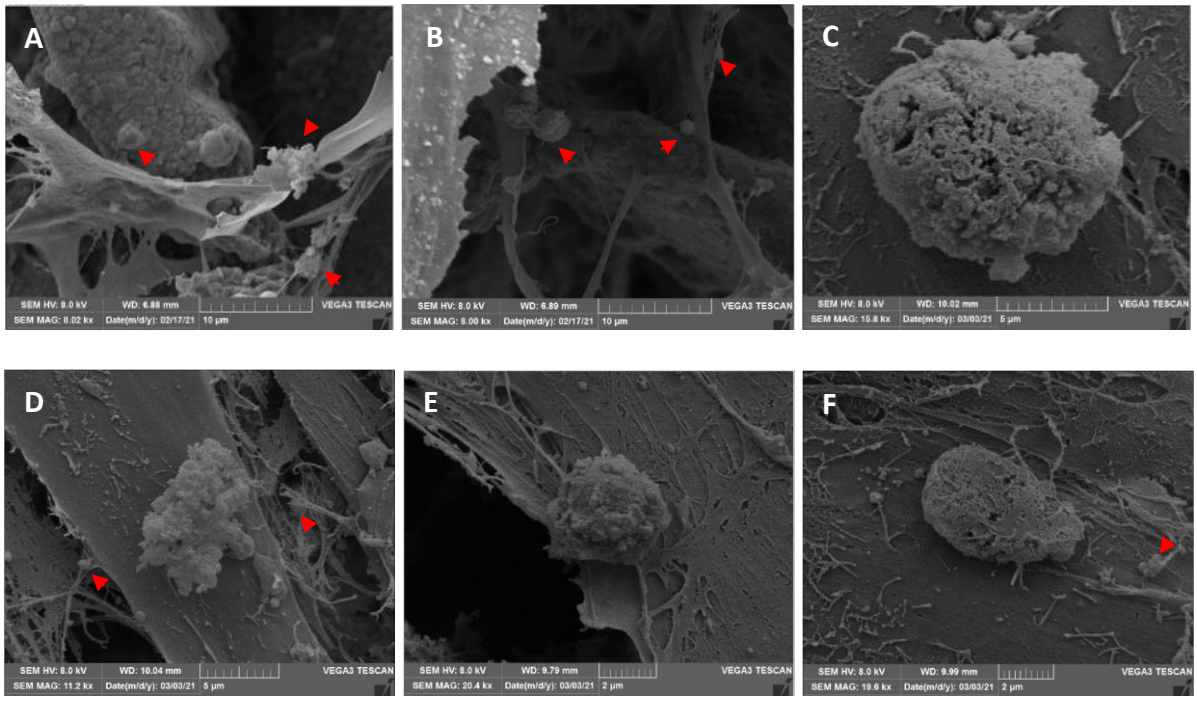

Figure 5-28: Magnified images of Osteoblast cells cultured on AW2 scaffold for 21 days. Different mineral formations are visible on top of the cell surface, as indicated by red arrow heads.

Figure 5-28 shows magnified SEM images of cell seeded AW2 scaffolds cultured for 21 days. Red arrow heads indicate some mineral formation on cells. Multiple cauliflower formations can be seen on cells which have attached across pores and on AW2 particles (A & B). Rough exterior cauliflower formations visible on top of cell layers (C, D & E). Cells appear to have attached to the mineral formations on C and F, a thin (nanometre scale) layer of cellular material is visible on the mineral surface.

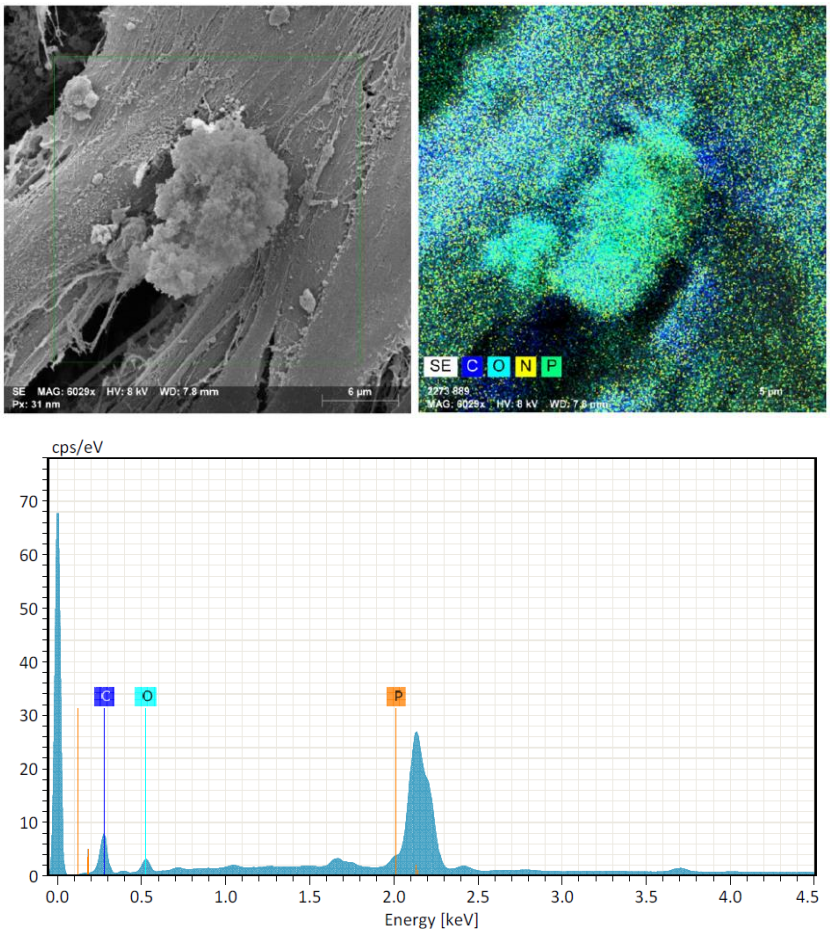

Figure 5-29: Sample of EDS spectra from a cauliflower formation, original AW2 scaffold seeded with osteoblast cells after 14 days in culture.

Figure 5-29 shown as SEM image of a cauliflower formation on the cell layer of an original aW2 scaffold after 14 days in culture. The EDS spectra is also shown below for reference, the Phosphorus (P) peak overlaps with the peak for Gold (Au) as seen in the spectra.

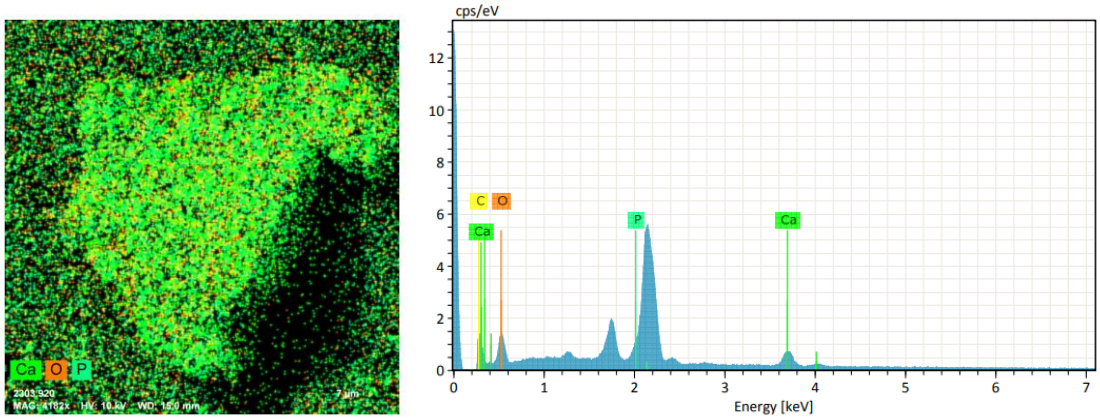

Figure 5-30: Sample EDS from a smooth particle formation on the top surface of the modified AW2 scaffold after 21 days in culture. High Calcium and Phosphorous formations, indicating mineralisation.

Figure 5-30 is a sample of a smooth particle formation on the top cell surface of a modified AW2 scaffold seeded with osteoblasts 21 days in culture. There are high levels of Calcium visible and Phosphorous which indicate mineralisation on the top surface of cells. This can be due to the cell activity producing a new mineral phase.

5.4.8 Mechanical Analysis

A sample stress-strain graph from an AW2 scaffold cultured for 7 days with osteoblast cells is shown in Figure 5-31.

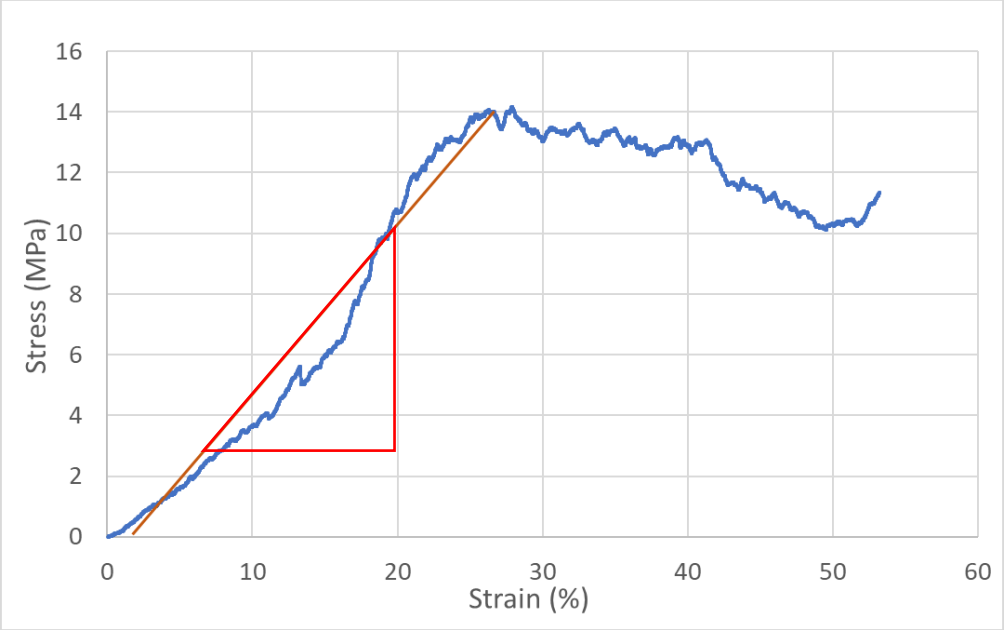

Figure 5-31: A stress - strain graph of a 90:10 AW2 scaffold seeded with osteoblast cells for 7 days.

In Figure 5-31, the stress increases up to a maximum of 14 MPa at 26% strain, then falls smoothly to 10 MPa (approx 48 % strain) before showing an increase in stress again. The experiment was stopped at this point as full failure had occurred. The average Young's modulus was between 50-55 MPa for cell seeded scaffolds after 7 days, for this sample the Young's modulus was 53 MPa. The Young's modulus at day 7 is around half the value of the original dry 90:10 AW2 scaffolds (Figure 3-22), this shows that there is a reduction in compresive stress of the scaffolds after 7 days seeded with osteoblast cells and in media.

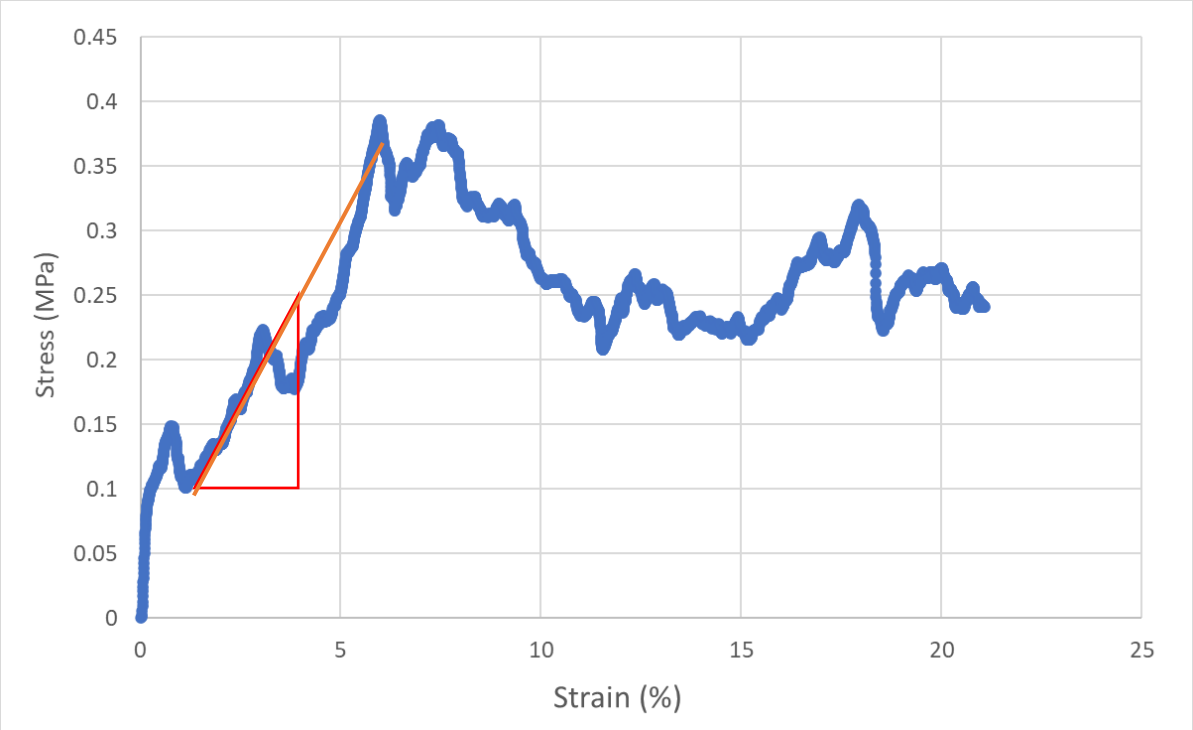

Figure 5-32: A stress - strain graph of a modified AW2 scaffold seeded with osteoblast cells for 21 days.

Figure 5-32 shows modified AW2 scaffolds after 21 days in culture with osteoblast cells, this graph shows a Youngs modulus 5.55 MPa. The modified scaffolds have grooves on the bottom and 5 channels, all of which reduce the mechanical stability of the scaffolds, as shown in Figure 5-32.

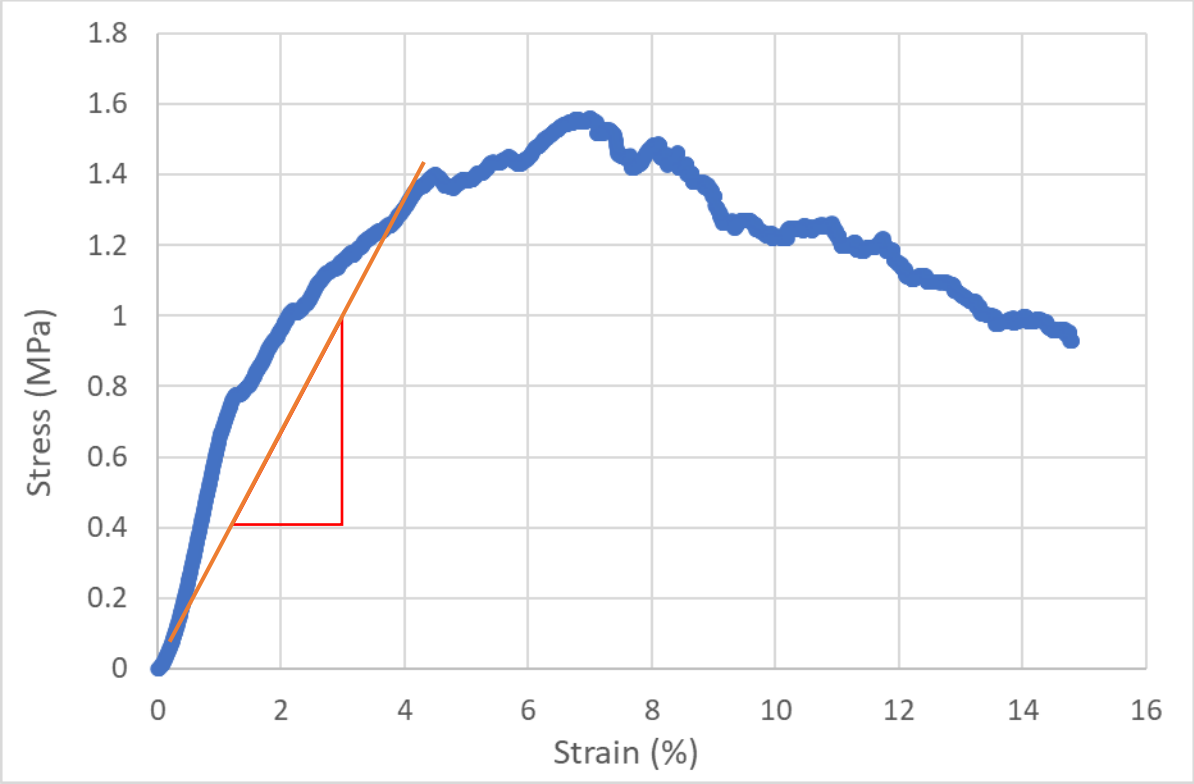

Figure 5-33: A stress - strain graph of a 90:10 AW2 scaffold seeded with osteoblast cells for 21 days in culture.

Figure 5-33 shows the sample graph from original AW2 scaffold after 21 days in culture with osteoblast cells, this graph shows the Youngs modulus of 20 MPa. The break pattern shown on the original AW2 scaffolds are more even compared to the modified scaffolds which show multiple break points.

5.5 Discussion

The suitability of scaffolds manufactured with AW2 using the TIPS process and dioxane:water 90:10 (Chapter 2, section 2.3.4) was investigated in this chapter. The main aims were to determine the suitability of these scaffolds *in-vitro* using foetal osteoblast cells, these were cultured together for 21 days. The ability for these scaffolds to initiate and aid mineralisation of the osteoblast cells was paramount to this research. This section discusses the findings found in the results section.

In red/blue/green images of live/dead cell seeded scaffolds shown in Figure 5-8, focussing on the red filter image some areas of the scaffold do not show as red, this is highly likely to be

where there are large open pores present (over 100 µm diameter). Also, when comparing to the blue filter and green filter images they both lack cells in the same black area of the red image. There is a high number of green/dead cells visible in this particular merged image, this is in comparison to other examples of Live/Dead carried out. The high number of dead cells in Figure 5-8, could be explained by the fact that this merged image was taken after a few hours of confocal imaging, this would have influenced the cells and fluorescence, as imaging of Live/Dead cells is recommended within 2 hours of the assay.

Figure 5-7 compares Live/Dead between modified scaffolds, original scaffolds and positive control, it is clear that the positive control has the greatest number of cells as there is the highest density of fluorescence compared to the background (black). The modified scaffolds have the least fluorescence compared to the background, and it can be estimated that it has roughly two to three times less blue fluorescence compared to the original AW2 scaffold, (B). This is in agreement with the PrestoBlue findings, Figure 5-5 & Figure 5-6, at day 1 of culture the original scaffolds found 1.35 $x10^5$ metabolically active cells, which is around triple the number of cells in the modified scaffolds (4.0 $x10^4$ cells). The positive controls found 2.2 $x10^5$ cells from the PrestoBlue assay, which is nearly double the number of cells of the original scaffolds, and these findings are also seen in the Live/Dead images, Figure 5-7. The actin/DAPI staining for day 1 was carried out on original AW2 scaffolds and positive controls, as shown in Figure 5-14 A & D, the relationship with the green fluorescence coverage follows the same relationship with the PrestoBlue assay at day 1 and the Live/Dead assay at day 1.

In Figure 5-9, the number of green (dead cells) is higher than anticipated at day 3, but there is a high number of blue (live cells), this high number of live cells does coincide with the increase in number of cells shown in the PrestoBlue assay (Figure 5-5 & Figure 5-6). In Figure 5-9 B, the arrows show the area with a high concentration of live cells and the highest concentration of dead cells, the cells form multilayers on the glass coverslips, and this may be the cause of the high number of dead cells. When cells form multilayers on glass (2D substrate), there is difficulty for the attached layers (deepest layer of cells) to be in contact with fresh media, this could consequently result in cell death and detachment from the substrate. On this three-dimensional substrate (AW2 scaffolds) with open porosity, there are different avenues for fresh media to be in contact with cells. The modified scaffolds were purposefully manufactured with large channels and grooves on the bottom of the scaffold,

this was to increase open porosity in the scaffolds to enable improved media flow and consequently waste transfer.

The literature varied quite considerably with regards to number of cells required for cell seeding with human osteoblasts, osteosarcoma cells (MG63) and mesenchymal stem cells (MSC), therefore the preliminary experiment was required in order to determine the optimum number of cells for seeding in the main experiment. The number of metabolically active (live) cells attached to the scaffolds increased more than three-fold from day 1 to day 7 in the modified scaffolds, Figure 5-5, in the original AW2 scaffolds the live cells increased by almost double. This dramatic increase in metabolically active cells was witnessed in both scaffold types (Figure 5-5), they follow a similar trend to each other from day 1 until day 21, the final number of cells on day 21 is very similar. The number of cells seeded was the same for both scaffold types (2.5 $x10^5$ cells), but initial number of cells attached onto the two different scaffold types was very different: the modified scaffold had around 4.0 $x10^4$ cells whilst the original scaffold had around 1.35 $x10^5$ cells. This resulted in very similar numbers of cells after 21 days in culture, Figure 5-5, approximately 1.5 $x10^5$ cells. This suggests that the cells were proliferating more actively on the modified scaffolds, compared to the original scaffolds, as the initial cell attachment was lower, yet the final cell numbers after 21 days were very similar. In the PrestoBlue preliminary study, Figure 5-3, the scaffolds and positive controls were seeded with either 2.5 $x10^5$ or 5.0 $x10^5$ cells, by the end of the study (day 14) the cell numbers for scaffolds were almost the same (2.0 $x10^5$) and the cell numbers for positive controls were very similar (1.5 $x10^5$ and 1.6 $x10^5$). It would have been interesting to continue the preliminary study until day 21, the same length as the main experiment, but due to time constraints this did not arise. In Figure 5-2, the preliminary experiment, there was an initial decrease in the number of cells attached onto the scaffolds, this could be due some of the cells filling the closed pores and consequently cell death. They could also close the pores, and consequently detach from the scaffolds therefore causing a decrease in cell number. After day 3 there is an increase in number of cells, until a peak at day 7 for both seeding densities. Between day 7 and day 10 there was a decline in number of cells noted, Figure 5-2. Osteoblast cells naturally agglomerate, this was clearly visible in the positive controls where the cell agglomerates were easily visible by eye. These multilayering agglomerations also

resulted in some of these cells detaching from the surface, and even floating in the media whilst some cells remained attached to the substrate.

The preliminary experiment used growth media for the full 14 days of the experiment, but in the main experiment the culture media was changed to differentiation media at day 9 until day 21, section 5.3.7. The differences in the media used (growth vs differentiation) influenced the proliferation of the cells: on day 9 of the main experiment the cells were 1.0 x10^5 cells and 1.6 x10^5 cells (Figure 5-5), whereas in the preliminary experiment at day 10 there was 1.0 x10^5 cells and 1.4 x10^5 cells (Figure 5-2). The original scaffolds in the main experiment had a 35% decrease in cell numbers between day 7 and 9, compared to the 250 scaffolds in the preliminary experiment which had a 41% decrease in cell numbers between day 7 and day 10. This decrease in cell numbers for both experiments is a significant decrease, but arguably a similar percentage decease (35% and 41%) after 48-72 hours, the cells have a decline in cell number after the day 7 peak regardless of initial seeding density and scaffold type. This decline of cell numbers in the preliminary experiment was a determining factor in the decision to change the growth media to differentiation media, section 5.3.7. The positive controls for the preliminary experiment followed a similar trend to the seeded scaffolds, but the positive control continued to decrease in number after day 10, with the final number of cells after 14 days being considerably lower than day 1. In the main experiment, the number of cells in the positive controls more than doubled between day 1 and day 21, but the trend is an increase in cell number then a sharp decrease in cells followed by an increase again, Figure 5-6. On day 21 the positive controls have 5.42 x10^5 ±3.89 x10^4 cells, these high number of cells were not observed under the light microscope, and actin staining and SEM imaging, but can be explained by the fact that there were areas of dense multi-layered cells on the coverslip, as well as some of the cell sheet had detached from one side and was therefore floating in the media. As some of the cell sheet was attached to the coverslip, but the other parts were floating, this enabled the floating cells to receive more media on more cell surface area, this could have caused the very high cell numbers. The PrestoBlue assay would also be in contact with more cell surface area, therefore these floating sheets may have been the cause for the very increased metabolic activity. The main experiment positive controls do not have the same trends as observed in the AW2 or modified scaffolds.

The adhesion and morphology of the Osteoblast cells on the top surface of AW2 scaffolds were characterised by SEM observations. After 1 day in culture, the cells on the scaffolds had attached to AW2 particles, these osteoblast cells were quite spread out in morphology, and starting to attach across and into pores (Zhang et al., 2014). Cell extensions and projections were visible between pores and on the AW2 particles. The EDS analysis was performed on particles found on top of cell layers; this was to avoid the AW2 particles being analysed. The modulation and mineralisation on the cell surface could be observed more readily with increased duration in culture (Kaur et al., 2019). There were no mineralised particles visible on samples on day 1. After 1-week in growth media, the AW2 samples show modulation in their morphology and mineralisation as shown in Figure 5-22 C & D. After 14 days in culture, crystal like structures, cauliflower shaped particles and mineralised deposits are clearly seen in Figure 5-23 and more in depth in Figure 5-24 (Kaur et al., 2019, Camarero-Espinosa and Moroni, 2021).

Osteoblast cells formed elongated multilayers (Schmidt et al., 2002, Venugopal et al., 2008, Yuste et al., 2021), and visible observations of mineral particles on the surface of the osteoblast cells after 7 days in culture, Figure 5-22. The cells appear to grow in multilayers at 14 days in culture, are elongated in morphology and show multiple preference directions, which has formed a fingerprint like pattern as shown in Figure 5-23 A & B, (Schmidt et al., 2002, Walsh et al., 2016). The cell pattern in Figure 5-23 A, B & D appears to be similar to a loop fingerprint pattern and whorl pattern in some places (Walsh et al., 2016), although the significance of these particular patterns is still unknown in literature.

The cell orientations on actin stained AW2 scaffolds appear to be very similar from day 7 to 14, as shown in A of Figure 5-15 and Figure 5-16 (Yao and Wong, 2015). The alignment of the actin filaments on AW2 scaffolds are elongated and follow similar directional patterns to each other (Mullen et al., 2013, Westhauser et al., 2020). On the positive control, after 14 days of culture, the actin filaments appear to be spread out in morphology and multidirectional, which is especially visible in Figure 5-17 E & F, although on day 7 the actin filaments were aligned as seen in Figure 5-16 E & F. This change in morphology was visible after 21 days in culture on cover slips, the cell morphology appears multidirectional and spread out, also there was a multilayer of cells. Although, it should be noted that on the glass coverslips there was some cell sheets that had agglomerated and then detached from the glass surface on

occasion, some cell areas would detach fully, whereas usually an area would detach from the glass, but some remained attached to the cells that were on the glass, therefore floating slightly in the media. These floating cells have more access to media, than if they were attached to the glass substrate.

The extracellular matrix, often referred to as the ECM, is a three-dimensional non-cellular structure that is secreted by cells (Lin et al., 2020). The ECM of different tissue types have their own specialised composition and topology, which also adapts to the surrounding environmental stresses for example: growth factors, pH, and mechanical stresses (Frantz et al., 2010, Mouw et al., 2014, Bonnans et al., 2014, Lin et al., 2020). It has been shown previously, (Polak et al., 2013), that a dry scaffold can aid in drawing cells into the microporous network of rigid porous scaffolds due to capillary forces. The AW2 scaffolds were prepared for cell seeding by soaking in osteoblast growth media for 1-hour in an incubator, but to aid in cell infiltration in pores the media was aspirated using a vacuum aspirator, section 5.3.2.1 and 5.3.7. The vacuum aspirator has a higher vacuum function to remove media compared to a micropipette and microtip attachment. Therefore, to try and mimic the dry scaffolds technique, the vacuum aspirator was used to try to remove as much media as possible from the scaffold and the well plate. Understandably, the AW2 scaffolds were not completely "dry", but effort was made to ensure the pores were not flooded with media. It would be interesting to investigate the differences in cell attachment and depth of penetration within the pores with AW2 scaffolds prepared in different methods for cell seeding, for example, completely dry scaffolds, aspiration from media treated scaffolds, scaffolds with 1 ml media in the well, and the use of suspension plates compared to standard tissue culture treated plates.

ALP is expressed by Osteoblast cells to provide phosphate ions and initiate the mineralisation process (Chai et al., 2012, Nasello et al., 2020). To promote mineralisation by providing phosphate ions, ALP hydrolyses a mineralisation inhibitor (pyrophosphates) (Chai et al., 2012). It has been reported in literature that higher cell densities were in favour of promoting morphological transformation, dendrite formation, and mineralisation of osteoblastic cells (Nasello et al., 2020, Mc Garrigle et al., 2016, Chang and Liu, 2021), although (Mullen et al., 2013) reported the opposite results. It should be noted that the cell densities used in this research and culture environments were not the same as those used within the

aforementioned studies, therefore a comprehensive comparison is not appropriate. There is debate regarding cell density and its biophysical role in osteocyte differentiation (Chang and Liu, 2021). The results from the pilot study indicate that after 14 days of culture, the final cell numbers were almost the same regardless of the initial scaffold cell seeding density being high or low, Figure 5-2.

5.6 Summary and Conclusions

In this chapter, original and modified 3D porous Apatite-Wollastonite2 (AW2) scaffolds were explored in an *in-vitro* environment using human foetal osteoblast cells. Their suitability was characterised based on cell proliferation and maturation. Concerning the biological performance on the two groups of scaffolds, the results showed that both groups of scaffolds positively enabled cell seeding, cell integration and attachment, proliferation, and maturation without interfering with cellular viability over a long-time period (21 days in culture).

Viability and proliferation of cells were monitored using two different methods: Live/Dead assay with confocal microscopy, and resazurin based assay (PrestoBlue). The results show overall good cell growth on both categories of scaffolds; however the modified scaffold showed a greater rate of cell growth. The chemical properties of the cell environment were analysed using EDS, and mineralisation of the osteoblast cells was confirmed via SEM and EDS. The morphology of the cells was observed using SEM, and its cytoskeleton organisation extensively analysed by confocal microscopy using Actin/DAPI stain. In terms of morphology, there was no significant difference between the two categories of scaffolds, both with satisfactory positive outcomes.

In conclusion, both groups of AW2 scaffolds supported cell adhesion, induced cell proliferation and encourage mineralisation from the osteoblasts and its extracellular matrix. The results appear very consistent over the pilot study and the main study, both supporting that the 3D porous scaffolds manufactured by the 90:10 TIPS process with AW2 provided the necessary porous environment for good biological performance and development *in-vitro*. This study also supports that modified scaffolds perform better overall than original scaffolds, in terms of biological performance. This can be due to the improved interconnectivity, attributable to the additional large channels and grooves, which potentially could improve

media circulation, waste removal, and mass transfer of media components. In brief, this study can be used as a basis for further *in-vitro* studies, and potentially performing *in-vivo* animal studies to confirm the suitability of the designed AW2 scaffolds for *in-vivo* applications.

Chapter 6 – Final Remarks

6 Outcomes and Novelty

This thesis presented an optimised Thermally Induced Phase Separation (TIPS) technique using glass-ceramic Apatite-Wollastonite 2 (AW2) for manufacturing porous AW2 structures (scaffolds) that closely mimics the complex bone-tissue architecture. Each step of the manufacturing process was optimised, and a high number of scaffolds were fabricated and tested *in-vitro* for cell growth and the results represents the repeatability of this technique. It was shown that the structure and morphology (average pore size and distribution), interconnectivity and mechanical properties depend upon the combination and operating conditions adopted for the process, including polymer concentration, solvent/non-solvent ration, cloud temperature and duration (La Carrubba et al., 2008). It was also demonstrated that modifying the scaffolds to allow for additional interconnectivity, produced more overall cell growth whilst still maintaining the structural stability scaffolds.

6.1 Novel Scaffolds using AW2 to Replicate Bone Structure

This study started by attempting to replicate the Toumpaniari's technique (Toumpaniari, 2016), for fabricating scaffolds, and despite many attempts this was not deemed successful. The lack of success in reproducing the results could be due to using a different AW and/or having limited details of the methodology described in (Toumpaniari, 2016) which left room for errors and interpretation. Toumpaniari used glass ceramic AW1 with composition of 4.6% MgO, 44.7% CaO, 34% SiO_2, 16.2% P_2O_5, 0.5% CaF_2 (Toumpaniari, 2016) which was not available or used for this study. In this study AW2 with composition of 3.68% MgO, 44.81% CaO, 35.49% SiO_2, 15.47% P_2O_5, 0.19% CaF_2, 0.02% SrO, 0.09% Fe_2O_3, 0.14% Al_2O_3 was utilised (Rodrigues, 2018). The glass ceramics (AW2) behaved differently during sintering and the manufacturing process, and required a great deal of optimization to produce repeatable scaffolds.

Apatite-Wollastonite (AW) has been used by many other researchers (Kokubo et al., 1982, Kokubo, 1991, Sautier et al., 1994, Yamada et al., 1994, Fujita et al., 2000, Rea et al., 2004, Teramoto et al., 2005, Dyson et al., 2007, Zhang et al., 2009, Lee et al., 2015, Toumpaniari, 2016, Mancuso, 2016, Dziadek et al., 2017, Tcacencu et al., 2018, Fernandes et al., 2018, Rodrigues, 2018, Turnbull et al., 2018, Melo et al., 2019), some of which used AW1 with

promising results (Lee et al., 2015, Toumpaniari, 2016, Rodrigues, 2018). However there is only one report of using AW1 with TIPS for scaffold manufacturing which was tested *in-vitro* (Toumpaniari, 2016), the TIPS process used 100% Dioxane mixed at 40°C. A review of literature using AW in scaffolds has been presented in Chapter 1 – Project Aims and Literature Review.

This thesis optimised scaffold manufacturing process based on TIPS using different concentrations of Dioxane with water and AW2. Alterations and optimisations were made to the methods produced repeatable AW2 scaffolds, further modifications were carried out post-sintering to improve interconnectivity which produced modified AW2 scaffolds.

It is well established that TIPS process is very sensitive to the experimental procedure; polymer solution, concentrations of solvent/non-solvent, starting composition, durations and temperature all highly influence the final porous structure. In this thesis, the cloud point for different PLA dioxane:water concentrations were measured and used as one of the critical factors in the manufacturing process. The correlation between measured cloud points against concentration were consistent with the literature (Hua et al., 2002, La Carrubba et al., 2008).

6.2 Novel Open Porosity Measurement Method

Total porosity is commonly used for analysis of scaffolds with few literatures reporting open porosity as more important factor. The literature on open porosity was primarily calculated for 3D printed scaffolds where the design is clearly known and mainly using wet, submerged, and dry mass measurements. Such measurement methods are user dependent. This thesis presents a novel method of measuring open porosity based on Archimedes' and described in Section 2.9 of the thesis.

6.3 Novel Image Processing

A novel image processing algorithm is designed and used to measure pore sizes and their distribution on the AW2 scaffold surface. The algorithm was implemented using ImageJ and its accuracy was validated by applying on SEM image of calibration circles of various known sizes (company standards). The algorithm provides a systematic technique for measuring pore sizes and distribution against manual measurement, which are time consuming, exhaustive, and subject to user errors and more importantly fatigue. Pore sizes and distribution of pores were measured using this technique and used for optimising the

manufacturing process. A research paper based on this technique has been submitted to a journal.

Due to boundary conditions, the statistics presented for pore sizes tend to exhibit the size of pores smaller than their true size. This can be resolved by adding another step to the algorithm to find any pores which touch the boundary of image and exclude them from analysis. The area of image used to calculate the statistics will also need to be modified accordingly. This can be subject of future study.

6.4 Evaluation of Compression Test, and its relationship with Porosity

Compression test has been widely reported as a feature of suitability of scaffold manufactured to replicate bone. In this research, compressive strength and Young's modulus was studied to establish the suitability of scaffolds to replicate bone as an *in-vitro* model. It is also shown that the compressive strength of scaffolds are inversely correlated with the total porosity. This is the first such study presenting compressive strength of AW2 scaffold using TIPS manufacturing process. The compressive strength of the AW2 scaffolds before and after cell seeding were tested for AWs scaffolds and the modified version. The results showed that both groups of scaffolds have appropriate level of mechanical strength for an *in-vitro* model.

6.5 Nutrition Diffusion Analysis

Interconnectivity and nutrient diffusion of the scaffolds were determined using light sensitive glucose solution. Nutrition diffusion is an important factor which represents the suitability of scaffolds for cell growth and nutrient dispersion. This study showed that the scaffolds allow for nutrition diffusion and are suitable for cell culture as validated by *in-vitro* test results.

6.6 Repeatability and Reproducibility of the Scaffold Manufacturing Method

The optimization process was successful as large number of scaffolds (at least 140) were manufactured successfully (sample shown in Figure 4-4) and tested for mechanical, porosity, and cell seeding. Producing large number of scaffolds shows that the technique presented in this report is repeatable and can potentially be used for large scale production. A new method of evaluating the quality of manufactured scaffolds was presented in a form of the Evaluation Matrix. The evaluation matrix combined all important features that scaffolds may possess, each of which represents an important metric for suitability of scaffold to replicate bone

structure. This is the first TIPS method of AW2 scaffold manufacturing technique which produces repeatable scaffolds suitable for cell seeding.

6.7 Interconnectivity Improvement

The interconnectivity and open porosity of the AW2 scaffolds were suitable for cell seeding, attachment and proliferation. This was further improved by the addition of five channels and two grooves on the bottom surface of the post-sintered scaffolds. This technique was found to be repeatable and improved the open porosity of the scaffolds. The modified AW2 scaffolds were also used in the *in-vitro* studies for comparison with the original AW2 scaffolds.

6.8 *In-Vitro* Studies

The original AW2 scaffolds and the modified AW2 scaffolds were both involved in the *in-vitro* studies for 21 days and compared against controls and also each other. Both groups of scaffolds successfully facilitated attachment of Osteoblast cells, proliferation of the cells and extracellular matrix formation with Calcium Phosphate structures formed. Multiple validation techniques were explored, such as Live/Dead, Presto Blue, Actin/DAPI fluorescence using confocal microscopy, scanning electron microscopy, alizarin red, Energy-dispersive X-ray spectroscopy and mechanical tests. In conclusion these scaffolds are an option for replicating bone structure *in-vitro* for future use. Due to Covid-19 pandemic, additional investigations using X-ray Photoelectron Spectroscopy (XPS) were not possible, and this would be a good method for probing the composition and electronic structure of the cell seeded scaffold surface in the future. For future work, further investigations into the fibrous network formation on the scaffolds with fluorescence staining of Collagen Type I and gene expression using Quantitative Polymerase Chain Reaction (qPCR) would provide more detailed information. Also, addition EDS on non-gold coated samples would provide further deeper considerations regarding the cell layers on the scaffolds.

6.9 Conclusion

This thesis explored methods to reliably incorporate AW2 into manufacturing of a 3D porous scaffolds to replicate bone structure. Adjustments, and improvements were made to optimize the scaffold manufacturing process to repeatably procedure porous AW2 scaffolds with consistent results over large number of tests. These AW2 scaffolds were additionally modified to encourage further interconnectivity, increase media flow and increase open porosity. Evaluating the two scaffold types in an *in-vitro* environment enabled understanding

of the effects of large channels and modification on cells. More tests would help to further compare the two scaffold types in more details. Due to COVID19 pandemic and restrictions worldwide, there was an absence of time to expand this research further detail. In conclusion both the original AW2 scaffolds and modified AW2 scaffolds are considered to be suitable structures to replicate bone for an *in-vitro* model.

References

ABBASI, N., HAMLET, S., LOVE, R. M. & NGUYEN, N.-T. 2020. Porous scaffolds for bone regeneration. *Journal of Science: Advanced Materials and Devices,* 5**,** 1-9.

AKAY, G., BIRCH, M. A. & BOKHARI, M. A. 2004. Microcellular polyHIPE polymer supports osteoblast growth and bone formation in vitro. *Biomaterials,* 25**,** 3991-4000.

ALDRICH, S.-. 2020. *Dioxane Safety Data sheet* [Online]. Sigma Aldrich. [Accessed 02/04/2020 2020].

ALHARBI, N. H. J. 2016. *Indirect three dimensional printing of apatite-wollastonite structures for biomedical applications.* Newcastle University.

AMZIANE, S., COLLET, F., AL, E. & NIYIGENA, C. 2017. *Bio-aggregates Based Building Materials: State-of-the-Art Report of the RILEM Technical Committee 236-BBM*.

ASHMAN, O. & PHILLIPS, A. M. 2013. Treatment of non-unions with bone defects: Which option and why? *Injury,* 44**,** S43-S45.

ATKINSON, D. & MCMILLAN, P. 1977. Glass-ceramics with random and oriented microstructures. *Journal of Materials Science,* 12**,** 443-450.

BAE, Y. C., LAMBERT, S. M., SOANE, D. S. & PRAUSNITZ, J. M. 1991. Cloud-point curves of polymer solutions from thermooptical measurements. *Macromolecules,* 24**,** 4403-4407.

BARAN, E. T., PIRRACO, R. P., CERQUEIRA, M. T., MARQUES, A. P., RETOLAZA, A., MERINO, S., NEVES, N. M. & REIS, R. L. 2015. Depth (Z-axis) control of cell morphologies on micropatterned surfaces. *Journal of Bioactive and Compatible Polymers,* 30**,** 555-567.

BARBECK, M., SERRA, T., BOOMS, P., STOJANOVIC, S., NAJMAN, S., ENGEL, E., SADER, R., KIRKPATRICK, C. J., NAVARRO, M. & GHANAATI, S. 2017. Analysis of the in vitro degradation and the in vivo tissue response to bi-layered 3D-printed scaffolds combining PLA and biphasic PLA/bioglass components - Guidance of the inflammatory response as basis for osteochondral regeneration. *Bioact Mater,* 2**,** 208-223.

BARRÈRE, F., MAHMOOD, T. A., DE GROOT, K. & VAN BLITTERSWIJK, C. A. 2008. Advanced biomaterials for skeletal tissue regeneration: Instructive and smart functions. *Materials Science and Engineering: R: Reports,* 59**,** 38-71.

BARTOŠ, M., SUCHÝ, T. & FOLTÁN, R. 2018. Note on the use of different approaches to determine the pore sizes of tissue engineering scaffolds: what do we measure? *BioMedical Engineering OnLine,* 17**,** 110.

BERNSTEIN, A., NIEMEYER, P., SALZMANN, G., SÜDKAMP, N. P., HUBE, R., KLEHM, J., MENZEL, M., VON EISENHART-ROTHE, R., BOHNER, M., GÖRZ, L. & MAYR, H. O. 2013. Microporous calcium phosphate ceramics as tissue engineering scaffolds for the repair of osteochondral defects: Histological results. *Acta Biomateriala,* 9**,** 7490-7505.

BIGNON, A., CHEVALIER, J. & FANTOZZI, G. 2002. Effect of ball milling on the processing of bone substitutes with calcium phosphate powders. *Journal of Biomedical Materials Research,* 63**,** 619-626.

BIGNON, A., CHOUTEAU, J., CHEVALIER, J., FANTOZZI, G., CARRET, J. P., CHAVASSIEUX, P., BOIVIN, G., MELIN, M. & HARTMANN, D. 2003. Effect of micro- and macroporosity of bone substitutes on their mechanical properties and cellular response. *Journal of Materials Science: Materials in Medicine,* 14**,** 1089-1097.

BLAKER, J. J., MAQUET, V., JÉRÔME, R., BOCCACCINI, A. R. & NAZHAT, S. N. 2005. Mechanical properties of highly porous PDLLA/Bioglass® composite foams as scaffolds for bone tissue engineering. *Acta Biomaterialia,* 1**,** 643-652.

BOHNER, M., LOOSLI, Y., BAROUD, G. & LACROIX, D. 2011. Commentary: Deciphering the link between architecture and biological response of a bone graft substitute. *Acta Biomaterialia,* 7**,** 478-484.

BONNANS, C., CHOU, J. & WERB, Z. 2014. Remodelling the extracellular matrix in development and disease. *Nature Reviews Molecular Cell Biology,* 15**,** 786-801.

BOSE, S., DARSELL, J., KINTNER, M., HOSICK, H. & BANDYOPADHYAY, A. 2003. Pore size and pore volume effects on alumina and TCP ceramic scaffolds. *Materials Science and Engineering: C,* 23**,** 479-486.

BOSE, S., ROY, M. & BANDYOPADHYAY, A. 2012. Recent advances in bone tissue engineering scaffolds. *Trends Biotechnol,* 30**,** 546-54.

BOSE, S., VAHABZADEH, S. & BANDYOPADHYAY, A. 2013. Bone tissue engineering using 3D printing. *Materials today,* 16**,** 496-504.

BOSKEY, A. L. 2013. Bone composition: relationship to bone fragility and antiosteoporotic drug effects. *BoneKEy reports,* 2.

BOYDE, A. 1972. Scanning electron microscope studies of bone. *The biochemistry and physiology of bone,* 1**,** 259-310.

BRYDONE, A., MEEK, D. & MACLAINE, S. 2010. Bone grafting, orthopaedic biomaterials, and the clinical need for bone engineering. *Proceedings of the Institution of Mechanical Engineers, Part H: Journal of Engineering in Medicine,* 224**,** 1329-1343.

BURG, K. J., PORTER, S. & KELLAM, J. F. 2000. Biomaterial developments for bone tissue engineering. *Biomaterials,* 21**,** 2347-2359.

BURTON, T. P. & CALLANAN, A. 2018. A Non-woven Path: Electrospun Poly(lactic acid) Scaffolds for Kidney Tissue Engineering. *Tissue Engineering and Regenerative Medicine*.

CALLISTER, W. D. & RETHWISCH, D. G. 2018. *Materials science and engineering: an introduction*, Wiley New York.

CAMARERO-ESPINOSA, S. & MORONI, L. 2021. Janus 3D printed dynamic scaffolds for nanovibration-driven bone regeneration. *Nat Commun,* 12**,** 1031.

CAROTHERS, W. H., DOROUGH, G. L. & NATTA, F. J. V. 1932. STUDIES OF POLYMERIZATION AND RING FORMATION. X. THE REVERSIBLE POLYMERIZATION OF SIX-MEMBERED CYCLIC ESTERS. *Journal of the American Chemical Society,* 54**,** 761-772.

CHAI, Y. C., CARLIER, A., BOLANDER, J., ROBERTS, S. J., GERIS, L., SCHROOTEN, J., VAN OOSTERWYCK, H. & LUYTEN, F. P. 2012. Current views on calcium phosphate osteogenicity and the translation into effective bone regeneration strategies. *Acta Biomater,* 8**,** 3876-87.

CHANG, B. & LIU, X. 2021. Osteon: Structure, Turnover, and Regeneration. *Tissue Eng Part B Rev*.

CHARLESHARRIS, M., DELVALLE, S., HENTGES, E., BLEUET, P., LACROIX, D. & PLANELL, J. 2007. Mechanical and structural characterisation of completely degradable polylactic acid/calcium phosphate glass scaffolds. *Biomaterials,* 28**,** 4429-4438.

CHAUDHARI, A. A., VIG, K., BAGANIZI, D. R., SAHU, R., DIXIT, S., DENNIS, V., SINGH, S. R. & PILLAI, S. R. 2016. Future Prospects for Scaffolding Methods and Biomaterials in Skin Tissue Engineering: A Review. *Int J Mol Sci,* 17.

CHEN, J.-S., TU, S.-L. & TSAY, R.-Y. 2010. A morphological study of porous polylactide scaffolds prepared by thermally induced phase separation. *Journal of the Taiwan Institute of Chemical Engineers,* 41**,** 229-238.

CHENG, A., SCHWARTZ, Z., KAHN, A., LI, X., SHAO, Z., SUN, M., AO, Y., BOYAN, B. D. & CHEN, H. 2019. Advances in Porous Scaffold Design for Bone and Cartilage Tissue Engineering and Regeneration. *Tissue Eng Part B Rev,* 25**,** 14-29.

CHOU, C. C., FENG, K. C., RAEVSKI, I. P., CHEN, H., TSAO, C.-Y., CHEN, P.-Y., CHEN, C.-S., LU, C.-A. & TU, C.-S. 2017. Part I: Effects of two-stage heat treatment on densification, microstructural features and dielectric properties of CaO–MgO–SiO2 glass-ceramics with ZrO2 nucleating agents. *Materials Research Bulletin,* 96**,** 66-70.

CLAFSHENKEL, W. P., RUTKOWSKI, J. L., PALCHESKO, R. N., ROMEO, J. D., MCGOWAN, K. A., GAWALT, E. S. & WITT-ENDERBY, P. A. 2012. A novel calcium aluminate-melatonin scaffold enhances bone regeneration within a calvarial defect. *Journal of pineal research,* 53**,** 206-218.

CONOSCENTI, G., CARRUBBA, V. L. & BRUCATO, V. 2017. A Versatile Technique to Produce Porous Polymeric Scaffolds: The Thermally Induced Phase Separation (TIPS) Method. *Archives in Chemical Research,* 01.

DEUBENER, J. & HÖLAND, W. 2017. Editorial: Nucleation and Crystallization of Glasses and Glass-Ceramics. *Frontiers in Materials,* 4.

DHANDAYUTHAPANI, B., YOSHIDA, Y., MAEKAWA, T. & KUMAR, D. S. 2011. Polymeric scaffolds in tissue engineering application: a review. *International journal of polymer science,* 2011.

DIVIETO, C. & SASSI, M. P. 2015. A first approach to evaluate the cell dose in highly porous scaffolds by using a nondestructive metabolic method. *Future science OA,* 1**,** FSO58-FSO58.

DOI, K., OUE, H., MORITA, K., KAJIHARA, S., KUBO, T., KORETAKE, K., PERROTTI, V., IEZZI, G., PIATTELLI, A. & AKAGAWA, Y. 2012. Development of implant/interconnected porous hydroxyapatite complex as new concept graft material. *PLoS One,* 7**,** e49051.

DONG, Z., LI, Y. & ZOU, Q. 2009. Degradation and biocompatibility of porous nano-hydroxyapatite/polyurethane composite scaffold for bone tissue engineering. *Applied Surface Science,* 255**,** 6087-6091.

DYSON, J. A., GENEVER, P. G., DALGARNO, K. W. & WOOD, D. J. 2007. Development of custom-built bone scaffolds using mesenchymal stem cells and apatite-wollastonite glass-ceramics. *Tissue Eng,* 13**,** 2891-901.

DZIADEK, M., STODOLAK-ZYCH, E. & CHOLEWA-KOWALSKA, K. 2017. Biodegradable ceramic-polymer composites for biomedical applications: A review. *Mater Sci Eng C Mater Biol Appl,* 71**,** 1175-1191.

EDALAT, F., BAE, H., MANOUCHERI, S., CHA, J. M. & KHADEMHOSSEINI, A. 2012. Engineering approaches toward deconstructing and controlling the stem cell environment. *Annals of biomedical engineering,* 40**,** 1301-1315.

ELHADIDY, A. M., PELDSZUS, S. & VAN DYKE, M. I. 2013. Development of a pore construction data analysis technique for investigating pore size distribution of ultrafiltration membranes by atomic force microscopy. *Journal of Membrane Science,* 429**,** 373-383.

ESPANOL, M., PEREZ, R. A., MONTUFAR, E. B., MARICHAL, C., SACCO, A. & GINEBRA, M. P. 2009. Intrinsic porosity of calcium phosphate cements and its significance for drug delivery and tissue engineering applications. *Acta Biomaterialia,* 5**,** 2752-2762.

FERNANDES, H. R., GADDAM, A., REBELO, A., BRAZETE, D., STAN, G. E. & FERREIRA, J. M. F. 2018. Bioactive Glasses and Glass-Ceramics for Healthcare Applications in Bone Regeneration and Tissue Engineering. *Materials (Basel, Switzerland),* 11**,** 2530.

FERNANDEZ-MARTIN, C., BRUNO, G., CROCHET, A., OVONO OVONO, D., COMTE, M. & HENNET, L. 2012. Nucleation and Growth of Nanocrystals in Glass-Ceramics: An In Situ SANS Perspective. *Journal of the American Ceramic Society,* 95**,** 1304-1312.

FIJI. 2021. *Fiji Downloads* [Online]. Available: https://imagej.net/software/fiji/downloads [Accessed 11/07/2021 2021].

FLYNT, J. 2017. *Polylactic Acid (PLA): The Environment-friendly Plastic* [Online]. 3D Insider Available: https://3dinsider.com/what-is-pla/ [Accessed 26/04/2020 2020].

FRANCO, J., HUNGER, P., LAUNEY, M. E., TOMSIA, A. P. & SAIZ, E. 2010. Direct write assembly of calcium phosphate scaffolds using a water-based hydrogel. *Acta Biomater,* 6**,** 218-28.

FRANTZ, C., STEWART, K. M. & WEAVER, V. M. 2010. The extracellular matrix at a glance. *Journal of Cell Science,* 123**,** 4195-4200.

FROHLICH, M., GRAYSON, W. L., WAN, L. Q., MAROLT, D., DROBNIC, M. & VUNJAK-NOVAKOVIC, G. 2008. Tissue engineered bone grafts: biological requirements, tissue culture and clinical relevance. *Current stem cell research & therapy,* 3**,** 254-264.

FROMIGUÉ, O., MARIE, P. J. & LOMRI, A. 1998. Bone morphogenetic protein-2 and transforming growth factor-β2 interact to modulate human bone marrow stromal cell proliferation and differentiation. *Journal of Cellular Biochemistry,* 68**,** 411-426.

FU, L., ENGQVIST, H. & XIA, W. 2020. Glass–Ceramics in Dentistry: A Review. *Materials,* 13**,** 1049.

FUJITA, H., IIDA, H., IDO, K., MATSUDA, Y., OKA, M. & NAKAMURA, T. 2000. Porous apatite-wollastonite glass-ceramic as an intramedullary plug. *The Journal of bone and joint surgery. British volume,* 82**,** 614-618.

GAO, C., DENG, Y., FENG, P., MAO, Z., LI, P., YANG, B., DENG, J., CAO, Y., SHUAI, C. & PENG, S. 2014. Current progress in bioactive ceramic scaffolds for bone repair and regeneration. *International journal of molecular sciences,* 15**,** 4714-4732.

GARGIULO, C., THAO, H. D., TUAN, H. M., THUY, T. T. T., VAN, P. H., FILGUEIRA, L. & TOAI, T. C. In Vitro Culture and Differentiation of Osteoblasts on Coral Scaffold from Human Bone Marrow Mesenchymal Stem Cells. 2010 Berlin, Heidelberg. Springer Berlin Heidelberg, 211-215.

GARIBOLDI, M. I. & BEST, S. M. 2015. Effect of ceramic scaffold architectural parameters on biological response. *Frontiers in bioengineering and biotechnology,* 3**,** 151.

GENTILE, P., CHIONO, V., CARMAGNOLA, I. & HATTON, P. 2014. An Overview of Poly(lactic-co-glycolic) Acid (PLGA)-Based Biomaterials for Bone Tissue Engineering. *International Journal of Molecular Sciences,* 15**,** 3640-3659.

GENTILE, P., MATTIOLI-BELMONTE, M., CHIONO, V., FERRETTI, C., BAINO, F., TONDA-TURO, C., VITALE-BROVARONE, C., PASHKULEVA, I., REIS, R. L. & CIARDELLI, G. 2012. Bioactive glass/polymer composite scaffolds mimicking bone tissue. *Journal of Biomedical Materials Research Part A,* 100**,** 2654-2667.

GERVASO, F., PADMANABHAN, S. K., SCALERA, F., SANNINO, A. & LICCIULLI, A. 2016. Mechanical stability of highly porous hydroxyapatite scaffolds during different stages of in vitro studies. *Materials Letters,* 185**,** 239-242.

GHASEMI-MOBARAKEH, L., SEMNANI, D. & MORSHED, M. 2007. A novel method for porosity measurement of various surface layers of nanofibers mat using image analysis for tissue engineering applications. *Journal of Applied Polymer Science,* 106**,** 2536-2542.

GHERSI, G., CARFI'PAVIA, F., CONOSCENTI, G., MANNELLA, G., GRECO, S., RIGOGLIUSO, S., LA, C. V. & BRUCATO, V. 2016. PLLA scaffold via TIPS for bone tissue engineering. *Chemical Engineering Transactions,* 49**,** 301-306.

GLEESON, J., PLUNKETT, N. & O'BRIEN, F. 2010. Addition of hydroxyapatite improves stiffness, interconnectivity and osteogenic potential of a highly porous collagen-based scaffold for bone tissue regeneration. *Eur Cell Mater,* 20**,** 30.

GOGOLEWVKI, S. 1992. Resorbable polymers for internal fixation. *Clinical Materials,* 10**,** 13-20.

GONZALEZ, R. C. & WOODS, R. E. 2008. *Digital Image Processing*, Pearson/Prentice Hall.

GOONOO, N., BHAW-LUXIMON, A. & JHURRY, D. 2014. In vitro and in vivo cytocompatibility of electrospun nanofiber scaffolds for tissue engineering applications. *RSC Advances,* 4.

GRAFAHREND, D., HEFFELS, K.-H., BEER, M. V., GASTEIER, P., MÖLLER, M., BOEHM, G., DALTON, P. D. & GROLL, J. 2011. Degradable polyester scaffolds with controlled surface chemistry combining minimal protein adsorption with specific bioactivation. *Nature materials,* 10**,** 67-73.

GREENWALD, A. S., BODEN, S. D., GOLDBERG, V. M., KHAN, Y., LAURENCIN, C. T. & ROSIER, R. N. 2001. Bone-graft substitutes: facts, fictions, and applications. *JBJS,* 83**,** S98-103.

GRIFFON, D. J., SEDIGHI, M. R., SCHAEFFER, D. V., EURELL, J. A. & JOHNSON, A. L. 2006. Chitosan scaffolds: interconnective pore size and cartilage engineering. *Acta Biomater,* 2**,** 313-20.

GUARINO, V. & AMBROSIO, L. 2010. Temperature-driven processing techniques for manufacturing fully interconnected porous scaffolds in bone tissue engineering. *Proc Inst Mech Eng H,* 224**,** 1389-400.

GUARINO, V., CAUSA, F., TADDEI, P., DI FOGGIA, M., CIAPETTI, G., MARTINI, D., FAGNANO, C., BALDINI, N. & AMBROSIO, L. 2008. Polylactic acid fibre-reinforced polycaprolactone scaffolds for bone tissue engineering. *Biomaterials,* 29**,** 3662-3670.

GUDA, T., APPLEFORD, M., OH, S. & ONG, J. L. 2008. A Cellular Perspective to Bioceramic Scaffolds for Bone Tissue Engineering: the State of the Art. *Current Topics in Medicinal Chemistry,* 8**,** 290-299.

GUNATILLAKE, P. A. & ADHIKARI, R. 2003. Biodegradable synthetic polymers for tissue engineering. *European Cells and Materials*.

HABIBOVIC, P., YUAN, H., VAN DER VALK, C. M., MEIJER, G., VAN BLITTERSWIJK, C. A. & DE GROOT, K. 2005. 3D microenvironment as essential element for osteoinduction by biomaterials. *Biomaterials,* 26**,** 3565-3575.

HAJIALI, F., TAJBAKHSH, S. & SHOJAEI, A. 2018. Fabrication and Properties of Polycaprolactone Composites Containing Calcium Phosphate-Based Ceramics and Bioactive Glasses in Bone Tissue Engineering: A Review. *Polymer Reviews,* 58**,** 164-207.

HANNAH, K. M., THOMAS, C. D. L., CLEMENT, J. G., DE CARLO, F. & PEELE, A. G. 2010. Bimodal distribution of osteocyte lacunar size in the human femoral cortex as revealed by micro-CT. *Bone,* 47**,** 866-871.

HARLEY, B. A., LEUNG, J. H., SILVA, E. C. & GIBSON, L. J. 2007. Mechanical characterization of collagen–glycosaminoglycan scaffolds. *Acta biomaterialia,* 3**,** 463-474.

HARRIS, L. D., KIM, B. S. & MOONEY, D. J. 1998. Open pore biodegradable matrices formed with gas foaming. *J Biomed Mater Res,* 42**,** 396-402.

HE, L., ZHANG, Y., ZENG, X., QUAN, D., LIAO, S., ZENG, Y., LU, J. & RAMAKRISHNA, S. 2009. Fabrication and characterization of poly(l-lactic acid) 3D nanofibrous scaffolds with controlled architecture by liquid–liquid phase separation from a ternary polymer–solvent system. *Polymer,* 50**,** 4128-4138.

HE, W., MA, Z., YONG, T., TEO, W. E. & RAMAKRISHNA, S. 2005. Fabrication of collagen-coated biodegradable polymer nanofiber mesh and its potential for endothelial cells growth. *Biomaterials,* 26**,** 7606-7615.

HENKEL, J., WOODRUFF, M. A., EPARI, D. R., STECK, R., GLATT, V., DICKINSON, I. C., CHOONG, P. F., SCHUETZ, M. A. & HUTMACHER, D. W. 2013. Bone regeneration based on tissue engineering conceptions—a 21st century perspective. *Bone research,* 1**,** 216.

HING, K. A., ANNAZ, B., SAEED, S., REVELL, P. A. & BUCKLAND, T. 2005. Microporosity enhances bioactivity of synthetic bone graft substitutes. *Journal of Materials Science: Materials in Medicine,* 16**,** 467-475.

HING, K. A., BEST, S. M., TANNER, K. E., BONFIELD, W. & REVELL, P. A. 2004. Mediation of bone ingrowth in porous hydroxyapatite bone graft substitutes. *Journal of Biomedical Materials Research Part A: An Official Journal of The Society for Biomaterials, The Japanese Society for Biomaterials, and The Australian Society for Biomaterials and the Korean Society for Biomaterials,* 68**,** 187-200.

HO, S. T. & HUTMACHER, D. W. 2006. A comparison of micro CT with other techniques used in the characterization of scaffolds. *Biomaterials,* 27**,** 1362-1376.

HOEMANN, C. D., EL-GABALAWY, H. & MCKEE, M. D. 2009. In vitro osteogenesis assays: influence of the primary cell source on alkaline phosphatase activity and mineralization. *Pathol Biol (Paris),* 57**,** 318-23.

HOLLAND W., B. G. 2004. Glass-ceramic technology,"The American Ceramic Society", Westerville, OH, USA, 2002, pp. 372. *Science of Sintering,* 36**,** 215-216.

HOLLISTER, S., LIN, C., SAITO, E., LIN, C., SCHEK, R., TABOAS, J., WILLIAMS, J., PARTEE, B., FLANAGAN, C., DIGGS, A., WILKE, E., VAN LENTHE, G., MÜLLER, R., WIRTZ, T., DAS, S., FEINBERG, S. & KREBSBACH, P. 2005. Engineering craniofacial scaffolds. *Orthodontics & Craniofacial Research,* 8**,** 162-173.

HOLLISTER, S. J. 2005. Porous scaffold design for tissue engineering. *Nature Materials,* 4**,** 518-524.

HU, Y., GRAINGER, D. W., WINN, S. R. & HOLLINGER, J. O. 2002. Fabrication of poly (α-hydroxy acid) foam scaffolds using multiple solvent systems. *Journal of Biomedical Materials Research: An Official Journal of The Society for Biomaterials, The Japanese Society for Biomaterials, and The Australian Society for Biomaterials and the Korean Society for Biomaterials,* 59**,** 563-572.

HUA, F. J., KIM, G. E., LEE, J. D., SON, Y. K. & LEE, D. S. 2002. Macroporous poly(L-lactide) scaffold 1. Preparation of a macroporous scaffold by liquid-liquid phase separation of a PLLA-dioxane-water system. *Journal of Biomedical Materials Research,* 63**,** 161-167.

HULBERT, S. F., YOUNG, F. A., MATHEWS, R. S., KLAWITTER, J. J., TALBERT, C. D. & STELLING, F. H. 1970. Potential of ceramic materials as permanently implantable skeletal prostheses. *Journal of Biomedical Materials Research,* 4**,** 433-456.

HUTMACHER, D. W. 2001. Scaffold design and fabrication technologies for engineering tissues — state of the art and future perspectives. *Journal of Biomaterials Science, Polymer Edition,* 12**,** 107-124.

ISHIGAMI, T., NII, Y., OHMUKAI, Y., RAJABZADEH, S. & MATSUYAMA, H. 2014. Solidification Behavior of Polymer Solution during Membrane Preparation by Thermally Induced Phase Separation. *Membranes,* 4**,** 113-122.

IVANCHENKO, L. A. & PINCHUK, N. D. 2003. Making Calcium Phosphate Biomaterials. *Powder Metallurgy and Metal Ceramics,* 42**,** 357-371.

JAMES, P. F. 1995. Glass ceramics: new compositions and uses. *Journal of Non-Crystalline Solids,* 181**,** 1-15.

JODATI, H., YıLMAZ, B. & EVIS, Z. 2020. A review of bioceramic porous scaffolds for hard tissue applications: Effects of structural features. *Ceramics International*.

JONES, J. R., TSIGKOU, O., COATES, E. E., STEVENS, M. M., POLAK, J. M. & HENCH, L. L. 2007. Extracellular matrix formation and mineralization on a phosphate-free porous bioactive glass scaffold using primary human osteoblast (HOB) cells. *Biomaterials,* 28**,** 1653-1663.

JUN, I.-K., SONG, J.-H., CHOI, W.-Y., KOH, Y.-H., KIM, H.-E. & KIM, H.-W. 2007. Porous Hydroxyapatite Scaffolds Coated With Bioactive Apatite?Wollastonite Glass?Ceramics. *Journal of American Ceramic Society* 90**,** 2703-2708.

JUNKAR, I., KULKARNI, M., DRAŠLER, B., RUGELJ, N., MAZARE, A., FLAŠKER, A., DROBNE, D., HUMPOLÍČEK, P., RESNIK, M., SCHMUKI, P., MOZETIČ, M. & IGLIČ, A. 2016. Influence of various sterilization procedures on TiO2 nanotubes used for biomedical devices. *Bioelectrochemistry,* 109**,** 79-86.

KARAGEORGIOU, V. & KAPLAN, D. 2005. Porosity of 3D biomaterial scaffolds and osteogenesis. *Biomaterials,* 26**,** 5474-5491.

KAUR, K., DAS, S. & GHOSH, S. 2019. Regulation of Human Osteoblast-to-Osteocyte Differentiation by Direct-Write 3D Microperiodic Hydroxyapatite Scaffolds. *ACS Omega,* 4**,** 1504-1515.

KIM, H.-W., KNOWLES, J. C. & KIM, H.-E. 2004. Hydroxyapatite/poly(ε-caprolactone) composite coatings on hydroxyapatite porous bone scaffold for drug delivery. *Biomaterials,* 25**,** 1279-1287.

KINGERY, W. D., BOWEN, H. K. & UHLMANN, D. R. 1976. *Introduction to ceramics*, John wiley & sons.

KLAWITTER, J. J., BAGWELL, J. G., WEINSTEIN, A. M. & SAUER, B. W. 1976. An evaluation of bone growth into porous high density polyethylene. *J Biomed Mater Res,* 10**,** 311-23.

KMETTY, Á. & LITAUSZKI, K. 2020. Development of Poly (Lactide Acid) Foams with Thermally Expandable Microspheres. *Polymers,* 12**,** 463.

KOKUBO, T. 1991. Bioactive glass ceramics: properties and applications. *Biomaterials,* 12**,** 155-163.

KOKUBO, T., SHIGEMATSU, M., NAGASHIMA, Y., TASHIRO, M., NAKAMURA, T., YAMAMURO, T. & HIGASHI, S. 1982. Apatite-and wollastonite-containg glass-ceramics for prosthetic application.

KRIEGHOFF, J., PICKE, A.-K., SALBACH-HIRSCH, J., ROTHER, S., HEINEMANN, C., BERNHARDT, R., KASCHOLKE, C., MÖLLER, S., RAUNER, M., SCHNABELRAUCH, M., HINTZE, V., SCHARNWEBER, D., SCHULZ-SIEGMUND, M., HACKER, M. C., HOFBAUER, L. C. & HOFBAUER, C. 2019. Increased pore size of scaffolds improves coating efficiency with sulfated hyaluronan and mineralization capacity of osteoblasts. *Biomaterials Research,* 23**,** 26.

KUNJALUKKAL PADMANABHAN, S., GERVASO, F., CARROZZO, M., SCALERA, F., SANNINO, A. & LICCIULLI, A. 2013. Wollastonite/hydroxyapatite scaffolds with improved mechanical, bioactive and biodegradable properties for bone tissue engineering. *Ceramics International,* 39**,** 619-627.

LA CARRUBBA, V., PAVIA, F. C., BRUCATO, V. & PICCAROLO, S. 2008. PLLA/PLA scaffolds prepared via Thermally Induced Phase Separation (TIPS): tuning of properties and biodegradability. *International Journal of Material Forming,* 1**,** 619-622.

LAGOA, A. L., WEDEMEYER, C., VON KNOCH, M., LÖER, F. & EPPLE, M. 2008. A strut graft substitute consisting of a metal core and a polymer surface. *Journal of Materials Science: Materials in Medicine,* 19**,** 417-424.

LAWRENCE, M. & JIANG, Y. 2017. Porosity, Pore Size Distribution, Micro-structure. *Bio-aggregates Based Building Materials.*

LEE, J. A., KNIGHT, C. A., KUN, X., YANG, X. B., WOOD, D. J., DALGARNO, K. W. & GENEVER, P. G. 2015. In vivo biocompatibility of custom-fabricated apatite-wollastonite-mesenchymal stromal cell constructs. *J Biomed Mater Res A,* 103**,** 3188-200.

LEE, J. W., AHN, G., KIM, J. Y. & CHO, D. W. 2010. Evaluating cell proliferation based on internal pore size and 3D scaffold architecture fabricated using solid freeform fabrication technology. *J Mater Sci Mater Med,* 21**,** 3195-205.

LEGEROS, R. Z. 1993. Biodegradation and bioresorption of calcium phosphate ceramics. *Clinical Materials,* 14**,** 65-88.

LEGEROS, R. Z. 2002. Properties of Osteoconductive Biomaterials: Calcium Phosphates. *Clinical Orthopaedics and Related Research®,* 395**,** 81-98.

LI, D., KRANTZ, W. B., GREENBERG, A. R. & SANI, R. L. 2006. Membrane formation via thermally induced phase separation (TIPS): Model development and validation. *Membrane Science,* 279**,** 50-60.

LI, H. & CHANG, J. 2004. Preparation and characterization of bioactive and biodegradable Wollastonite/poly(D,L-lactic acid) composite scaffolds. *Journal of Materials Science: Materials in Medicine,* 15**,** 1089-1095.

LI, M., LIU, W., SUN, J., XIANYU, Y., WANG, J., ZHANG, W., ZHENG, W., HUANG, D., DI, S. & LONG, Y.-Z. 2013. Culturing primary human osteoblasts on electrospun poly (lactic-co-glycolic acid) and poly (lactic-co-glycolic acid)/nanohydroxyapatite scaffolds for bone tissue engineering. *ACS applied materials & interfaces,* 5**,** 5921-5926.

LIM, T. C., CHIAN, K. S. & LEONG, K. F. 2010. Cryogenic prototyping of chitosan scaffolds with controlled micro and macro architecture and their effect on in vivo neo-vascularization and cellular infiltration. *Journal of Biomedical Materials Research Part A,* 94A**,** 1303-1311.

LIN, X., PATIL, S., GAO, Y. G. & QIAN, A. 2020. The Bone Extracellular Matrix in Bone Formation and Regeneration. *Front Pharmacol,* 11**,** 757.

LIN, X., ZHANG, H., HUANG, B. & LIN, S. 2012. Alkaline phosphatase gene sequence characteristics and transcriptional regulation by phosphate limitation in Karenia brevis (Dinophyceae). *Harmful Algae,* 17**,** 14-24.

LIU, P., OYAJOBI, B. O., RUSSELL, R. G. G. & SCUTT, A. 1999. Regulation of Osteogenic Differentiation of Human Bone Marrow Stromal Cells: Interaction Between Transforming Growth Factor-β and 1,25(OH)2 Vitamin D3In Vitro. *Calcified Tissue International,* 65**,** 173-180.

LLOYD, A. W. 2002. Interfacial bioengineering to enhance surface biocompatibility. *Medical device technology,* 13**,** 18-21.

LO RE, G., LOPRESTI, F., PETRUCCI, G. & SCAFFARO, R. 2015. A facile method to determine pore size distribution in porous scaffold by using image processing. *Micron,* 76**,** 37-45.

LOH, Q. L. & CHOONG, C. 2013. Three-Dimensional Scaffolds for Tissue Engineering Applications: Role of Porosity and Pore Size. *Tissue Engineering Part B: Reviews,* 19**,** 485-502.

LU, J. X., FLAUTRE, B., ANSELME, K., HARDOUIN, P., GALLUR, A., DESCAMPS, M. & THIERRY, B. 1999. Role of interconnections in porous bioceramics onbone recolonization in vitro and in vivo. *Journal of Materials Science: Materials in Medicine,* 10**,** 111-120.

MA, P. X. & ZHANG, R. 2001. Microtubular architecture of biodegradable polymer scaffolds. *Journal of Biomedical Materials Research,* 56**,** 469-477.

MAGALLANES-PERDOMO, M., LUKLINSKA, Z. B., DE AZA, A. H., CARRODEGUAS, R. G., DE AZA, S. & PENA, P. 2011. Bone-like forming ability of apatite–wollastonite glass ceramic. *Journal of the European Ceramic Society,* 31**,** 1549-1561.

MANASSERO, M., DECAMBRON, A., GUILLEMIN, N., PETITE, H., BIZIOS, R. & VIATEAU, V. 2016. Coral Scaffolds in Bone Tissue Engineering and Bone Regeneration. Springer International Publishing.

MANAVITEHRANI, I., FATHI, A., BADR, H., DALY, S., NEGAHI SHIRAZI, A. & DEHGHANI, F. 2016. Biomedical Applications of Biodegradable Polyesters. *Polymers,* 8**,** 20.

MANCUSO, E. 2016. *Processing and characterisation of novel bioceramics for load bearing applications.* Newcastle University.

MANCUSO, E., BRETCANU, O. A., MARSHALL, M., BIRCH, M. A., MCCASKIE, A. W. & DALGARNO, K. W. 2017. Novel bioglasses for bone tissue repair and regeneration: Effect of glass design on sintering ability, ion release and biocompatibility. *Materials & Design,* 129**,** 239-248.

MANNELLA, G. 2012. *POLYMERIC POROUS STRUCTURES VIA PHASE SEPARATION.* PhD, Università degl iStudi di Palermo.

MANNELLA, G. A., CARRUBBA, V. L. & BRUCATO, V. 2013. Measurement of cloud point temperature in polymer solutions. *Review of Scientific Instruments,* 84**,** 075118.

MAQUET, V., BLACHER, S., PIRARD, R., PIRARD, J.-P. & JÉRÔME, R. 2000. Characterization of porous polylactide foams by image analysis and impedance spectroscopy. *Langmuir,* 16**,** 10463-10470.

MAQUET, V., BOCCACCINI, A. R., PRAVATA, L., NOTINGHER, I. & JÉRÔME, R. 2003. Preparation, characterization, and in vitro degradation of bioresorbable and bioactive composites based on Bioglass®-filled polylactide foams. *Journal of Biomedical Materials Research Part A: An Official Journal of The Society for Biomaterials, The Japanese Society for Biomaterials, and The Australian Society for Biomaterials and the Korean Society for Biomaterials,* 66**,** 335-346.

MARÍ-BUYÉ, N., LUQUE, T., NAVAJAS, D. & SEMINO, C. E. 2013. Development of a three-dimensional bone-like construct in a soft self-assembling peptide matrix. *Tissue Engineering Part A,* 19**,** 870-881.

MARIEB, E. N. & HOEHN, K. 2007. *Human anatomy & physiology*, Pearson education.

MARTIN, O. & AVÉROUS, L. 2001. Poly(lactic acid): plasticization and properties of biodegradable multiphase systems. *Polymer,* 42**,** 6209-6219.

MARTÍNEZ-PÉREZ, C. A., OLIVAS-ARMENDARIZ, I., CASTRO-CARMONA, J. S. & GARCÍA-CASILLAS, P. E. 2011. Scaffolds for tissue engineering via thermally induced phase separation. *Advances in Regenerative Medicine: InTech***,** 275-294.

MASPERO, F. A., RUFFIEUX, K., MÜLLER, B. & WINTERMANTEL, E. 2002. Resorbable defect analog PLGA scaffolds using CO 2 as solvent: Structural characterization. *Biomedical Materials Research,* 62**,** 89-98.

MAYER, R. P. & STOWE, R. A. 1965. Mercury porosimetry—breakthrough pressure for penetration between packed spheres. *Journal of colloid Science,* 20**,** 893-911.

MC GARRIGLE, M. J., MULLEN, C. A., HAUGH, M. G., VOISIN, M. C. & MCNAMARA, L. M. 2016. Osteocyte differentiation and the formation of an interconnected cellular network in vitro. *Eur Cell Mater,* 31**,** 323-40.

MCMILLAN, P. W. 1979. *Glass-ceramics,* London; New York, Academic Press.

MELO, P., FERREIRA, A.-M., WALDRON, K., SWIFT, T., GENTILE, P., MAGALLANES, M., MARSHALL, M. & DALGARNO, K. 2019. Osteoinduction of 3D printed particulate and short-fibre reinforced composites produced using PLLA and apatite-wollastonite. *Composites Science and Technology,* 184**,** 107834.

MERETOJA, V. V., MALIN, M., SEPPÄLÄ, J. V. & NÄRHI, T. O. 2009. Osteoblast response to continuous phase macroporous scaffolds under static and dynamic culture conditions. *Journal of Biomedical Materials Research Part A,* 89A**,** 317-325.

MIKOS, A. G., SARAKINOS, G., LYMAN, M. D., INGBER, D. E., VACANTI, J. P. & LANGER, R. 1993. Prevascularization of porous biodegradable polymers. *Biotechnol Bioeng,* 42**,** 716-23.

MOUW, J. K., OU, G. & WEAVER, V. M. 2014. Extracellular matrix assembly: a multiscale deconstruction. *Nat Rev Mol Cell Biol,* 15**,** 771-85.

MULLEN, C. A., HAUGH, M. G., SCHAFFLER, M. B., MAJESKA, R. J. & MCNAMARA, L. M. 2013. Osteocyte differentiation is regulated by extracellular matrix stiffness and intercellular separation. *J Mech Behav Biomed Mater,* 28**,** 183-94.

MURPHY, C. M., HAUGH, M. G. & O'BRIEN, F. J. 2010. The effect of mean pore size on cell attachment, proliferation and migration in collagen-glycosaminoglycan scaffolds for bone tissue engineering. *Biomaterials,* 31**,** 461-6.

NASELLO, G., ALAMÁN-DÍEZ, P., SCHIAVI, J., PÉREZ, M. Á., MCNAMARA, L. & GARCÍA-AZNAR, J. M. 2020. Primary Human Osteoblasts Cultured in a 3D Microenvironment Create a Unique Representative Model of Their Differentiation Into Osteocytes. *Frontiers in Bioengineering and Biotechnology,* 8.

NATUREWORKS. 2020. *Ingeo™ Biopolymer 4032D Technical Data Sheet* [Online]. [Accessed 26/04/2020 2020].

NAVARRO, M., GINEBRA, M. P., PLANELL, J. A., ZEPPETELLI, S. & AMBROSIO, L. 2004. Development and cell response of a new biodegradable composite scaffold for guided bone regeneration. *Journal of Materials Science: Materials in Medicine,* 15**,** 419-422.

NOOEAID, P., ROETHER, J. A., WEBER, E., SCHUBERT, D. W. & BOCCACCINI, A. R. 2014. Technologies for Multilayered Scaffolds Suitable for Interface Tissue Engineering. *Advanced Engineering Materials,* 16**,** 319-327.

NORDIN, M. & FRANKEL, V. H. 2001. *Basic biomechanics of the musculoskeletal system*, Lippincott Williams & Wilkins.

NORMAN, M. E., ELGENDY, H. M., SHORS, E. C., EL-AMIN, S. F. & LAURENCIN, C. T. 1994. An in-vitro evaluation of coralline porous hydroxyapatite as a scaffold for osteoblast growth. *Clinical Materials,* 17**,** 85-91.

O'BRIEN, F. J., HARLEY, B. A., WALLER, M. A., YANNAS, I. V., GIBSON, L. J. & PRENDERGAST, P. J. 2007. The effect of pore size on permeability and cell attachment in collagen scaffolds for tissue engineering. *Technology and Health Care,* 15**,** 3-17.

O'BRIEN, F. J., HARLEY, B. A., YANNAS, I. V. & GIBSON, L. J. 2005. The effect of pore size on cell adhesion in collagen-GAG scaffolds. *Biomaterials,* 26**,** 433-41.

OH, D. S., KIM, Y. J., HONG, M.-H., HAN, M.-H. & KIM, K. 2014. Effect of capillary action on bone regeneration in micro-channeled ceramic scaffolds. *Ceramics International,* 40**,** 9583-9589.

OH, S. H., PARK, I. K., KIM, J. M. & LEE, J. H. 2007. In vitro and in vivo characteristics of PCL scaffolds with pore size gradient fabricated by a centrifugation method. *Biomaterials,* 28**,** 1664-1671.

OZDEMIR, F. 2020. Magnetic polymethylmethacrylate cements for hyperthermic cancer treatment.

PANNA, W., WYSZOMIRSKI, P. & KOHUT, P. 2016. Application of hot-stage microscopy to evaluating sample morphology changes on heating. *Journal of Thermal Analysis and Calorimetry,* 125**,** 1053-1059.

PAVIA, F. C., LA CARRUBBA, V., PICCAROLO, S. & BRUCATO, V. 2008. Polymeric scaffolds prepared via thermally induced phase separation: Tuning of structure and morphology. *biomedical Materials Research Part A,* 86A**,** 459-466.

PEREZ, R. A. & MESTRES, G. 2016. Role of pore size and morphology in musculo-skeletal tissue regeneration. *Mater Sci Eng C Mater Biol Appl,* 61**,** 922-39.

PIERANTOZZI, D., SCALZONE, A., JINDAL, S., STĪPNIECE, L., ŠALMA-ANCĀNE, K., DALGARNO, K., GENTILE, P. & MANCUSO, E. 2020. 3D printed Sr-containing composite scaffolds: Effect of structural design and material formulation towards new strategies for bone tissue engineering. *Composites Science and Technology,* 191**,** 108069.

PILIA, M., GUDA, T. & APPLEFORD, M. 2013. Development of composite scaffolds for load-bearing segmental bone defects. *Biomed Res Int,* 2013**,** 458253.

POHANISH, R. P. 2017. Handbook of Toxic and Hazardous Chemicals and Carcinogens (Seventh Edition). *In:* POHANISH, R. P. (ed.) *Sittig's Handbook of Toxic and Hazardous Chemicals and Carcinogens (Seventh Edition).* William Andrew Publishing.

POLAK, S. J., RUSTOM, L. E., GENIN, G. M., TALCOTT, M. & WAGONER JOHNSON, A. J. 2013. A mechanism for effective cell-seeding in rigid, microporous substrates. *Acta Biomater,* 9**,** 7977-86.

POLO-CORRALES, L., LATORRE-ESTEVES, M. & RAMIREZ-VICK, J. E. 2014. Scaffold Design for Bone Regeneration. *Journal of Nanoscience and Nanotechnology,* 14**,** 15-56.

PRASADH, S. & WONG, R. C. W. 2018. Unraveling the mechanical strength of biomaterials used as a bone scaffold in oral and maxillofacial defects. *Oral Science International,* 15**,** 48-55.

PUGLIA, D., CECCOLINI, R., FORTUNATI, E., ARMENTANO, I., MORENA, F., MARTINO, S., ALUIGI, A., TORRE, L. & KENNY, J. M. 2015. Effect of processing techniques on the 3D microstructure of poly (l -lactic acid) scaffolds reinforced with wool keratin from different sources. *Applied Polymer Science,* 132**,** n/a-n/a.

QIU, Z.-Y., CUI, Y. & WANG, X.-M. 2019. Chapter 1 - Natural Bone Tissue and Its Biomimetic. *In:* WANG, X.-M., QIU, Z.-Y. & CUI, H. (eds.) *Mineralized Collagen Bone Graft Substitutes.* Woodhead Publishing.

RADIN, S., REILLY, G., BHARGAVE, G., LEBOY, P. S. & DUCHEYNE, P. 2005. Osteogenic effects of bioactive glass on bone marrow stromal cells. *J Biomed Mater Res A,* 73**,** 21-9.

RAHAMAN, M. N., DAY, D. E., BAL, B. S., FU, Q., JUNG, S. B., BONEWALD, L. F. & TOMSIA, A. P. 2011. Bioactive glass in tissue engineering. *Acta biomaterialia,* 7**,** 2355-2373.

RAJAGOPALAN, S., LU, L., YASZEMSKI, M. J. & ROBB, R. A. 2005. Optimal segmentation of microcomputed tomographic images of porous tissue-engineering scaffolds. *Biomedical Materials Research Part A,* 75A**,** 877-887.

RANUCCI, C. S. & MOGHE, P. V. 1999. Polymer substrate topography actively regulates the multicellular organization and liver-specific functions of cultured hepatocytes. *Tissue engineering,* 5**,** 407-420.

RASBAND, W. 1997. ImageJ. Bethesda, Maryland, USA: U. S. National Institutes of Health,.

RASBAND, W. 2012. ImageJ - Image Processing and Analysis in Java. *Astrophysics Source Code Library,* 1**,** 06013.

RATANAVARAPORN, J., DAMRONGSAKKUL, S., KANOKPANONT, S., YAMAMOTO, M. & TABATA, Y. 2011. Osteogenic differentiation of bone-marrow-derived stem cells cultured with mixed gelatin and chitooligosaccharide scaffolds. *Journal of Biomaterials Science, Polymer Edition,* 22**,** 1083-1098.

RAVAGLIOLI, A., KRAJEWSKI, A., BALDI, G., TATEO, F., PERUZZO, L. & PIANCASTELLI, A. 2008. Glass–ceramic scaffolds for tissue engineering. *Advances in applied ceramics,* 107**,** 268-273.

RAWLINGS, R. D., WU, J. P. & BOCCACCINI, A. R. 2006. Glass-ceramics: Their production from wastes—A Review. *Journal of Materials Science,* 41**,** 733-761.

RAZAK, S. I. A., SHARIF, N. & RAHMAN, W. 2012. Biodegradable polymers and their bone applications: a review. *Int. J. Basic Appl. Sci,* 12**,** 31-49.

REA, S. M., BROOKS, R. A., BEST, S. M., KOKUBO, T. & BONFIELD, W. 2004. Proliferation and differentiation of osteoblast-like cells on apatite-wollastonite/polyethylene composites. *Biomaterials,* 25**,** 4503-12.

REZWAN, K., CHEN, Q. Z., BLAKER, J. J. & BOCCACCINI, A. R. 2006. Biodegradable and bioactive porous polymer/inorganic composite scaffolds for bone tissue engineering. *Biomaterials,* 27**,** 3413-3431.

ROBERT, H., ARAN, R., PATRICK, M. & DAVID, W. Influence of glass composition on nucleation crystallisation microstructure and properties of apatite-mullite glass-ceramics. International Symposium on Crystallization in Glasses and Liquids, 2000. 146-153.

RODRIGUES, N., BENNING, M., FERREIRA, A. M., DIXON, L. & DALGARNO, K. 2016. Manufacture and Characterisation of Porous PLA Scaffolds. *Procedia CIRP,* 49**,** 33-38.

RODRIGUES, N. C. R. 2018. *Materials processing and physical characterisation of a hybrid composite structure for bone replacement applications.* Newcastle University.

ROOHANI-ESFAHANI, S.-I., LIN, K. & ZREIQAT, H. 2017. Fabrication of bioinspired structured glass–ceramics with enhanced fracture toughness. *Journal of Materials Science,* 52**,** 9202-9210.

ROSE, F. R., CYSTER, L. A., GRANT, D. M., SCOTCHFORD, C. A., HOWDLE, S. M. & SHAKESHEFF, K. M. 2004. In vitro assessment of cell penetration into porous hydroxyapatite scaffolds with a central aligned channel. *Biomaterials,* 25**,** 5507-5514.

ROUAHI, M., GALLET, O., CHAMPION, E., DENTZER, J., HARDOUIN, P. & ANSELME, K. 2006. Influence of hydroxyapatite microstructure on human bone cell response. *J Biomed Mater Res A,* 78**,** 222-35.

SAMAVEDI, S., WHITTINGTON, A. R. & GOLDSTEIN, A. S. 2013. Calcium phosphate ceramics in bone tissue engineering: A review of properties and their influence on cell behavior. *Acta Biomaterialia,* 9**,** 8037-8045.

SAUTIER, J. M., KOKUBO, T., OHTSUKI, T., NEFUSSI, J. R., BOULEKBACHE, H., OBOEUF, M., LOTY, S., LOTY, C. & FOREST, N. 1994. Bioactive glass-ceramic containing crystalline apatite and wollastonite initiates biomineralization in bone cell cultures. *Calcified Tissue International,* 55**,** 458-466.

SCHMIDT, C., KASPAR, D., SARKAR, M. R., CLAES, L. E. & IGNATIUS, A. A. 2002. A scanning electron microscopy study of human osteoblast morphology on five orthopedic metals. *J Biomed Mater Res,* 63**,** 252-61.

SCHNEIDER, C. A., RASBAND, W. S. & ELICEIRI, K. W. 2012. NIH Image to ImageJ: 25 years of image analysis. *Nature Methods,* 9**,** 671-675.

SCHUGENS, C., MAQUET, V., GRANDFILS, C., JEROME, R. & TEYSSIE, P. 1996. Biodegradable and macroporous polylactide implants for cell transplantation: 1. Preparation of macroporous polylactide supports by solid-liquid phase separation. *Polymer,* 37**,** 1027-1038.

SERPOOSHAN, V., JULIEN, M., NGUYEN, O., WANG, H., LI, A., MUJA, N., HENDERSON, J. E. & NAZHAT, S. N. 2010. Reduced hydraulic permeability of three-dimensional collagen scaffolds attenuates gel contraction and promotes the growth and differentiation of mesenchymal stem cells. *Acta biomaterialia,* 6**,** 3978-3987.

SHAH, F. A., JOHANSSON, M. L., OMAR, O., SIMONSSON, H., PALMQUIST, A. & THOMSEN, P. 2016. Laser-Modified Surface Enhances Osseointegration and Biomechanical Anchorage of Commercially Pure Titanium Implants for Bone-Anchored Hearing Systems. *PloS one,* 11**,** e0157504-e0157504.

SHELBY, J. E. 2005. *Introduction to Glass Science and Technology - Second Edition,* Cambridge, Royal Society of Chemistry

SHI, G., CAI, Q., WANG, C., LU, N., WANG, S. & BEI, J. 2002. Fabrication and biocompatibility of cell scaffolds of poly(L-lactic acid) and poly(L-lactic-co-glycolic acid). *Polymers for Advanced Technologies,* 13**,** 227-232.

SHUAI, C., ZHUANG, J., HU, H., PENG, S., LIU, D. & LIU, J. 2013. In vitro bioactivity and degradability of β-tricalcium phosphate porous scaffold fabricated via selective laser sintering. *Biotechnology and applied biochemistry,* 60**,** 266-273.

SHUM, A. W. T., LI, J. & MAK, A. F. T. 2005. Fabrication and structural characterization of porous biodegradable poly(dl-lactic-co-glycolic acid) scaffolds with controlled range of pore sizes. *Polymer Degradation and Stability,* 87**,** 487-493.

STEVENSON, G., REHMAN, S., DRAPER, E., HERNÁNDEZ-NAVA, E., HUNT, J. & HAYCOCK, J. W. 2016. Combining 3D human in vitro methods for a 3Rs evaluation of novel titanium surfaces in orthopaedic applications. *Biotechnology and Bioengineering,* 113**,** 1586-1599.

STORY, B. J., WAGNER, W. R., GAISSER, D. M., COOK, S. D. & RUST-DAWICKI, A. M. 1998. In vivo performance of a modified CSTi dental implant coating. *International Journal of Oral and Maxillofacial Implants,* 13**,** 749-757.

STRNAD, Z. 1986. *Glass-ceramic materials : liquid phase separation, nucleation and crystallization in glasses,* New York, Elsevier Science Publishing SNTL, Publishers of Technical Literature, Prague.

TCACENCU, I., RODRIGUES, N., ALHARBI, N., BENNING, M., TOUMPANIARI, S., MANCUSO, E., MARSHALL, M., BRETCANU, O., BIRCH, M., MCCASKIE, A. & DALGARNO, K. 2018. Osseointegration of porous apatite-wollastonite and poly(lactic acid) composite structures created using 3D printing techniques. *Mater Sci Eng C Mater Biol Appl,* 90**,** 1-7.

TERAMOTO, H., KAWAI, A., SUGIHARA, S., YOSHIDA, A. & INOUE, H. 2005. Resorption of apatite-wollastonite containing glass-ceramic and beta-tricalcium phosphate in vivo. *Acta Med Okayama,* 59**,** 201-7.

THALLER, P. H., FURMETZ, J., WOLF, F., EILERS, T. & MUTSCHLER, W. 2014. Limb lengthening with fully implantable magnetically actuated mechanical nails (PHENIX((R)))-preliminary results. *Injury,* 45 Suppl 1**,** S60-5.

THURNER, P. J., ERICKSON, B., JUNGMANN, R., SCHRIOCK, Z., WEAVER, J. C., FANTNER, G. E., SCHITTER, G., MORSE, D. E. & HANSMA, P. K. 2007. High-speed photography of compressed human trabecular bone correlates whitening to microscopic damage. *Engineering Fracture Mechanics,* 74**,** 1928-1941.

TOMLINS, P., GRANT, P., MIKHALOVSKY, S., JAMES, S. & MIKHALOVSKA, L. 2004. Measurement of Pore Size and Porosity of Tissue Scaffolds. *Journal of Astm International,* 1.

TOUMPANIARI, S. 2016. *Apatite-wollastonite glass ceramic scaffolds for bone tissue engineering applications.* Newcastle University.

TRAN, C. T., GARGIULO, C., THAO, H. D., TUAN, H. M., FILGUEIRA, L. & MICHAEL STRONG, D. 2011. Culture and differentiation of osteoblasts on coral scaffold from human bone marrow mesenchymal stem cells. *Cell Tissue Bank,* 12**,** 247-61.

TSIGKOU, O., HENCH, L. L., BOCCACCINI, A. R., POLAK, J. M. & STEVENS, M. M. 2007. Enhanced differentiation and mineralization of human fetal osteoblasts on PDLLA containing Bioglass® composite films in the absence of osteogenic supplements. *Biomedical Materials Research Part A,* 80A**,** 837-851.

TSURUGA, E., TAKITA, H., ITOH, H., WAKISAKA, Y. & KUBOKI, Y. 1997. Pore Size of Porous Hydroxyapatite as the Cell-Substratum Controls BMP-Induced Osteogenesis. *Journal of Biochemistry,* 121**,** 317-324.

TURNBULL, G., CLARKE, J., PICARD, F., RICHES, P., JIA, L., HAN, F., LI, B. & SHU, W. 2018. 3D bioactive composite scaffolds for bone tissue engineering. *Bioact Mater,* 3**,** 278-314.

TZVETANOV, L., NIKOLAEVA, S., MICHAILOV, I. & TIVCHEV, P. 2002. Bone and Ceramic Interaction in the Bone Union Process. *Ultrastructural Pathology,* 26**,** 171-175.

VACANTI, J. P., MORSE, M. A., SALTZMAN, W. M., DOMB, A. J., PEREZ-ATAYDE, A. & LANGER, R. 1988. Selective cell transplantation using bioabsorbable artificial polymers as matrices. *Journal of Pediatric Surgery,* 23**,** 3-9.

VAINIONPÄÄ, S., KILPIKARI, J., LAIHO, J., HELEVIRTA, P., ROKKANEN, P. & TÖRMÄLÄ, P. 1987. Strength and strength retention vitro, of absorbable, self-reinforced polyglycolide (PGA) rods for fracture fixation. *Biomaterials,* 8**,** 46-48.

VAN DE WITTE, P., DIJKSTRA, P., VAN DEN BERG, J. & FEIJEN, J. 1996. Phase behavior of polylactides in solvent–nonsolvent mixtures. *Journal of Polymer Science Part B: Polymer Physics,* 34**,** 2553-2568.

VARLEY, M. C., MARKAKI, A. E. & BROOKS, R. A. 2017. Effect of Rotation on Scaffold Motion and Cell Growth in Rotating Bioreactors. *Tissue Eng Part A,* 23**,** 522-534.

VELASCO, M. A., NARVAEZ-TOVAR, C. A. & GARZON-ALVARADO, D. A. 2015. Design, materials, and mechanobiology of biodegradable scaffolds for bone tissue engineering. *Biomed Res Int,* 2015**,** 729076.

VENUGOPAL, J., LOW, S., CHOON, A. T., SAMPATH KUMAR, T. S. & RAMAKRISHNA, S. 2008. Mineralization of osteoblasts with electrospun collagen/hydroxyapatite nanofibers. *J Mater Sci Mater Med,* 19**,** 2039-46.

WALSH, S., POSPIECH, E. & BRANICKI, W. 2016. Hot on the Trail of Genes that Shape Our Fingerprints. *J Invest Dermatol,* 136**,** 740-742.

WANG, M., PORTER, D. & BONFIELD, W. 1994. Processing, characterisation, and evaluation of hydroxyapatite reinforced polyethylene. *Br. Ceram. Trans,* 93**,** 91-95.

WANG, X., SONG, G. & LOU, T. 2010. Fabrication and characterization of nano composite scaffold of poly(l-lactic acid)/hydroxyapatite. *Material Science,* 21**,** 183-188.

WEI, H.-J., LIANG, H.-C., LEE, M.-H., HUANG, Y.-C., CHANG, Y. & SUNG, H.-W. 2005. Construction of varying porous structures in acellular bovine pericardia as a tissue-engineering extracellular matrix. *Biomaterials,* 26**,** 1905-1913.

WESTHAUSER, F., REHDER, F., DECKER, S., KUNISCH, E., MOGHADDAM, A., ZHENG, K. & BOCCACCINI, A. R. 2020. Ionic dissolution products of Cerium-doped bioactive glass nanoparticles promote cellular osteogenic differentiation and extracellular matrix formation of human bone marrow derived mesenchymal stromal cells. *Biomed Mater*.

WHANG, K., TSAI, D. C., NAM, E. K., AITKEN, M., SPRAGUE, S. M., PATEL, P. K. & HEALY, K. E. 1998. Ectopic bone formation via rhBMP-2 delivery from porous bioabsorbable polymer scaffolds. *Journal of Biomedical Materials Research,* 42**,** 491-499.

WHITE, E. & SHORS, E. C. 1986. Biomaterial aspects of Interpore-200 porous hydroxyapatite. *Dent Clin North Am,* 30**,** 49-67.

WILL, J., MELCHER, R., TREUL, C., TRAVITZKY, N., KNESER, U., POLYKANDRIOTIS, E., HORCH, R. & GREIL, P. 2008. Porous ceramic bone scaffolds for vascularized bone tissue regeneration. *Journal of Materials Science: materials in medicine,* 19**,** 2781-2790.

WIM, G., JAN VAN, K., OLAV, S. & SICCO, D. V. 2010. Processing of Poly(Lactic Acid). *Poly(Lactic Acid).*

WOO, K. M., CHEN, V. J. & MA, P. X. 2003. Nano-fibrous scaffolding architecture selectively enhances protein adsorption contributing to cell attachment. *Journal of Biomedical Materials Research Part A: An Official Journal of The Society for Biomaterials, The Japanese Society for Biomaterials, and The Australian Society for Biomaterials and the Korean Society for Biomaterials,* 67**,** 531-537.

XIAO, K., DALGARNO, K. W., WOOD, D. J., GOODRIDGE, R. D. & OHTSUKI, C. 2008. Indirect selective laser sintering of apatite—wollostonite glass—ceramic. *Proceedings of the Institution of Mechanical Engineers, Part H: Journal of Engineering in Medicine,* 222**,** 1107-1114.

XU, C., SU, P., CHEN, X., MENG, Y., YU, W., XIANG, A. P. & WANG, Y. 2011. Biocompatibility and osteogenesis of biomimetic Bioglass-Collagen-Phosphatidylserine composite scaffolds for bone tissue engineering. *Biomaterials,* 32**,** 1051-1058.

XUE, D., ZHENG, Q., ZONG, C., LI, Q., LI, H., QIAN, S., ZHANG, B., YU, L. & PAN, Z. 2010. Osteochondral repair using porous poly(lactide-co-glycolide)/nano-hydroxyapatite hybrid scaffolds with undifferentiated mesenchymal stem cells in a rat model. *Biomedical Materials Research Part A,* 94A**,** 259-270.

YAMADA, S., NAKAMURA, T., KOKUBO, T., OKA, M. & YAMAMURO, T. 1994. Osteoclastic resorption of apatite formed on apatite- and wollastonite-containing glass-ceramic by a simulated body fluid. *Journal of Biomedical Materials Research,* 28**,** 1357-1363.

YANG, Y., ZHAO, Y., TANG, G., LI, H., YUAN, X. & FAN, Y. 2008. In vitro degradation of porous poly(l-lactide-co-glycolide)/β-tricalcium phosphate (PLGA/β-TCP) scaffolds under dynamic and static conditions. *Polymer Degradation and Stability,* 93**,** 1838-1845.

YAO, R. & WONG, J. Y. 2015. The effects of mechanical stimulation on controlling and maintaining marrow stromal cell differentiation into vascular smooth muscle cells. *J Biomech Eng,* 137**,** 020907.

YOUNG, M. F. 2003. Bone matrix proteins: their function, regulation, and relationship to osteoporosis. *Osteoporosis international,* 14**,** 35-42.

YUE, Y., KEDING, R. & RÜSSEL, C. 1999. Oriented calcium metaphosphate glass-ceramics. *Journal of materials research,* 14**,** 3983-3987.

YUSTE, I., LUCIANO, F. C., GONZÁLEZ-BURGOS, E., LALATSA, A. & SERRANO, D. R. 2021. Mimicking bone microenvironment: 2D and 3D in vitro models of human osteoblasts. *Pharmacological Research,* 169**,** 105626.

ZELTINGER, J., SHERWOOD, J. K., GRAHAM, D. A., MÜELLER, R. & GRIFFITH, L. G. 2001. Effect of pore size and void fraction on cellular adhesion, proliferation, and matrix deposition. *Tissue engineering,* 7**,** 557-572.

ZHANG, H., YE, X.-J. & LI, J.-S. 2009. Preparation and biocompatibility evaluation of apatite/wollastonite-derived porous bioactive glass ceramic scaffolds. *Biomedical Materials,* 4**,** 045007.

ZHANG, J., ZHAO, S., ZHU, M., ZHU, Y., ZHANG, Y., LIU, Z. & ZHANG, C. 2014. 3D-printed magnetic Fe3O4/MBG/PCL composite scaffolds with multifunctionality of bone regeneration, local anticancer drug delivery and hyperthermia. *J Mater Chem B,* 2**,** 7583-7595.

ZHANG, K., FAN, Y., DUNNE, N. & LI, X. 2018. Effect of microporosity on scaffolds for bone tissue engineering. *Regen Biomater,* 5**,** 115-124.

ZHANG, X., GUO, X., ZHANG, J., FAN, X., CHEN, M. & YANG, H. 2021. Nucleation, crystallization and biological activity of Na2O-CaO-P2O5-SiO2 bioactive glass. *Journal of Non-Crystalline Solids,* 568**,** 120929.

ZHAO, X. 2011. Bioactive materials in orthopaedics. Elsevier.